THÈSE

UNIVERSITÉ DE PAU ET DES PAYS DE L'ADOUR

École Doctorale des Sciences Exactes et leur Applications (ED SEA)

Par **Mª Lourdes MARTÍNEZ DE BAÑOS**

pour obtenir le grade de docteur
de l'Université de Pau et des Pays de l'Adour
Spécialité : Physico-Chimie

MECHANISMS OF FORMATION AND DISSOCIATION OF CYCLOPENTANE HYDRATES

(MÉCANISMES DE FORMATION ET DISSOCIATION D'HYDRATES DE CYCLOPENTANE)

MEMBRES DU JURY

PRÉSIDENT
- Christophe DICHARRY — Professeur / UPPA

RAPPORTEURS
- Didier DALMAZZONE — Professeur / ENSTA ParisTech
- Jean-Baptiste SALMON — CNRS Research Scientist / LOF UMR5258

EXAMINATEURS
- Ross BROWN — Directeur de Recherche CNRS / UPPA
- Anh Minh TANG — Chargé de recherche / École des Ponts ParisTech
- Wenceslao GONZALEZ-VIÑAS — Maître de Conférences / Universidad de Navarra

DIRECTEUR
- Daniel BROSETA — Professeur / UPPA

CO-ENCADRANT
- Patrick BOURIAT — Maître de Conférences / UPPA

UNIVERSITÉ DE PAU ET DES PAYS DE L'ADOUR

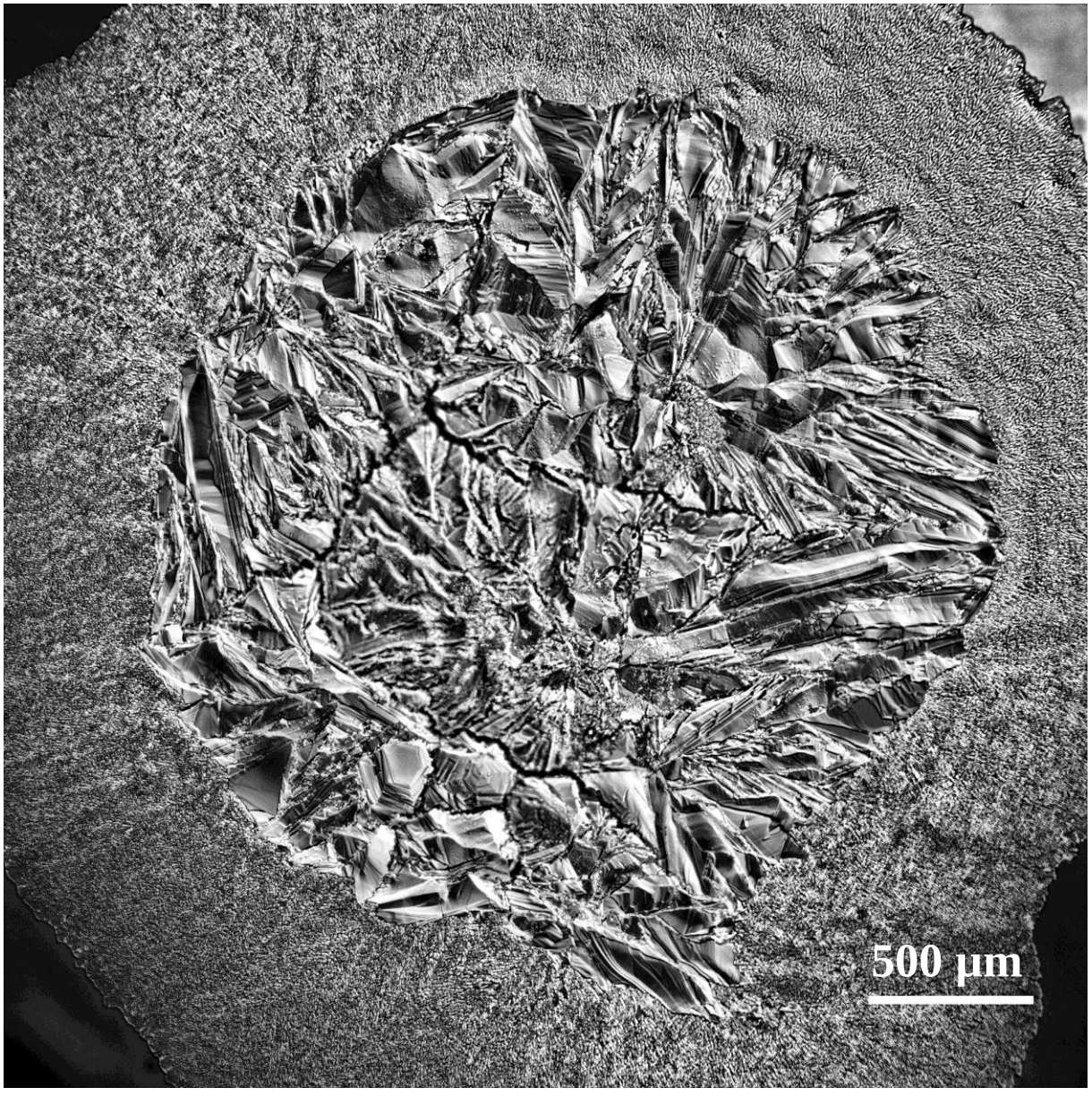
500 µm

To my husband

“Caminante, no hay camino,
se hace camino al andar”.

Antonio Machado

Acknowledgements

Cuando te embarcas en la aventura de una tesis, puede que creas saber cómo va a empezar, pero nunca sabes cómo va a terminar. Por eso yo lo llamo aventura. La tesis es todo menos un camino fácil. Durante todo este camino encuentras innumerables obstáculos que tratan de detenerte y desmotivarte, pero eso es precisamente lo que hace de una tesis algo emocionante. Si en lugar de ver obstáculos ves retos, entonces en lugar de detenerte, continuas y los afrontas. He disfrutado con todas y cada una de las cosas nuevas que he aprendido durante estos tres años y que distan tanto de la formación inicial con la que llegué a Francia. Todas ellas, junto con las espectaculares imágenes que he tenido el privilegio de observar gracias a la microscopía, me han hecho sentirme muy realizada y han hecho el trabajo agradable y placentero.

First of all I would like to thank my PhD supervisor Mr. Daniel Broseta for his insistence and excitement in addressing new challenges and in always trying to carry on new experiments and discoveries. Without him I would not have been able to last long and to finish this work.

Also, I want to thank my co-supervisor Mr. Patrick Bouriat for all the time spent with me in the lab, for his creativity and for all the discussions about physics and more things, always with a huge touch of humor.

Thank you too, Mr. Ross Brown, for the perseverance, the huge curiosity and desire to always learn new things, and for showing me everything about the microscope and the care with which it has to be treated. I have just fallen in love with microscopy!

I want to thank the members of the jury: Mr. Wenceslao González-Viñas, Mr. Anh Minh Tang, Mr. Patrick Bouriat, Mr. Ross Brown, Mr. Christophe Dicharry and Mr. Daniel Broseta; and also the reporters of the jury of this thesis: Mr. Jean-Baptiste Salmon and Mr. Didier Dalmazzone, for having accepted to read and evaluate my work. Thank you.

I would like to thank some other members of the group: Mr. Jean-Philippe Torré, Mr. Christophe Dicharry and Mr. Patrice Creux, for the always interesting scientific and not scientific discussions and for their support.

A big thank you to all the people that have helped me in some way, in the administrative or the experimental work, during these three years: Ms. Catherine Urrea and all the members of the “École Doctorale”; Mr. Laurent Marlin and all the members of the workshop.

I would also want to thank the post doctoral students that have helped me in my research: Odile Carrier and Nelly Hobeika; and my colleagues from the second floor office -doctoral students and ‘stagiers’- that have helped me in some way all along this time: Marfa, Luigi, Lele, Henry, Romuald, Hafid, Laura, Matt and Tanguy. Thank you for making the office a nice place to go to every day, for the music and for the laughs.

No puedo terminar sin dar las gracias a Bruno y a Nicolás. Ellos han sido las personas que han cuidado y se han preocupado por mí durante todo este tiempo; los que han hecho mi día a día más feliz, las personas con las que he podido compartir conversaciones sobre música y cine, entre otras, y los que han hecho mis comidas de todos los días más divertidas y agradables. Muchas gracias a los dos por vuestro sentido del humor y por hacerme sentir como en casa. Nunca os olvidaré.

Y, ¡cómo no! ‘The Spanish team’. Muchas gracias María y José por aportar esa chispa española que tanta falta nos hace cuando estamos lejos y que tan unidos nos ha mantenido durante todo el tiempo que hemos coincidido. Gracias por ser el apoyo más grande. Gracias por saber escuchar cada una de las tristezas y alegrías que traía para compartir con vosotros. Gracias por estar ahí cada vez que os he necesitado. Siempre estaréis en mi corazón.

Por último quería dar las gracias a mi familia por el apoyo en la distancia y por haber confiado tanto en mí y en mis capacidades. Vosotros sabíais que podía hacerlo, y no os habéis equivocado. Gracias padres, gracias hermanos.

No tengo palabras para dar las gracias a mi marido. Supongo que nunca podré agradecerle como se merece todo el apoyo que me ha dado y todas las cosas que ha aguantado y soportado conmigo y sin mí en la distancia, que no han sido pocas. Gracias por no dejarme sola ni un momento y por tu paciencia; por confiar y creer en mí y por haber hecho que el tiempo pasase más rápido. Llego el día. Siempre llega. Gracias.

ABSTRACT

The mechanisms of formation and dissociation of cyclopentane (CP) hydrates, which form at ambient pressure and temperatures between 0°C and 7°C, have been observed in/on/near water drops immersed in CP at scales ranging from a few nanometers to the millimeter by a variety of techniques including macrophotography and optical microscopy under various modes: bright field, differential interference contrast (DIC), fluorescence and confocal reflectance. The substrates used are either hydrophobic or hydrophilic.

In a first series of experiments, a simple millifluidic method is implemented. It allows to generate, store and monitor at the same time almost a hundred of regularly-spaced water droplets of equal volume (in the µl range) separated by the guest (CP) phase in a transparent fluorinated polymeric (PFA) (hydrophobic) tubing, each droplet behaving as an independent reactor for hydrate crystallization. Insights into the 'memory effect' are gained by measuring the statistics of hydrate nucleation events in these reactors when chilling below 7°C the water drops. The method also allows the visualization of single-drop events such as hydrate birth and growth, and the formation of a CP-in-water emulsion upon hydrate melting, especially when an additive such as an inhibitor is added to the water. In a second series of experiments, a single water droplet in CP, either sitting or hanging from a glass substrate, is observed by microscopy under various cooling and heating sequences. Hydrate crystallization (nucleation and growth) is observed to strongly depend on subcooling at the water drop/CP interface. Two novel phenomena are visualized in detail:

(i) the propagation, from the contact line of the water drop, of a hydrate halo along the glass/CP interface.

(ii) hydrate crystallization in a two-dimensional CP-in-water emulsion.

The two types of tools developed in this thesis open new perspectives for elucidating the mechanisms of hydrate formation and dissociation in presence of additives (promoters and inhibitors) and in the presence of a mineral substrate. Applications include hydrates in sedimentary environments, flow assurance, gas separation, etc.

Keywords: cyclopentane hydrate, millifluidics, memory effect, emulsion, crystallization, subcooling, hydrophilic surface, halo, percolation-type process.

RÉSUMÉ

Les mécanismes de formation et dissociation d'hydrates de cyclopentane (CP), qui forment á pression ambiante et á des températures entre 0ºC et 7ºC, ont été observés dans/sur/proche des gouttes d'eau immergées dans du CP á des échelles qui vont du micron jusqu'au millimètre. Plusieurs techniques d'observation ont été utilisées, telles que la macrophotographie et la microscopie optique en champ clair, par contraste interférentiel différentiel (CID), par fluorescence et par réflectance confocale. Des substrats hydrophiles et hydrophobes ont été utilisés.

Dans une première série d'expériences, un procédé millifluidique simple a été mis au point. Il permet de générer, stocker et surveiller simultanément une centaine de gouttelettes de même volume (de l'ordre de µl), régulièrement espacées. Elles sont séparées par la phase 'invité' (CP) dans un tuyau en polymère fluoré (PFA) transparent. Chacune d'elles se comporte comme un réacteur indépendant. Une vision sur l'effet mémoire est obtenue en menant des mesures statistiques sur la nucléation des hydrates quand les gouttes d'eau sont refroidies au-dessous de 7°C. Cette méthode permet aussi de visualiser des événements dans des gouttes individuelles, tels que la naissance et la croissance de l'hydrate (surtout lorsqu'un additive tel qu'un inhibiteur est rajouté dans l'eau), ainsi que la formation d'une émulsion de CP dans l'eau pendant la dissociation de l'hydrate. Dans une deuxième série d'expériences, une seule goutte d'eau est posée ou pendue d'un substrat en verre et immergée dans du CP. Elle est observée par microscopie sous des séquences différentes de refroidissement – échauffement. Il a été observé que la cristallisation d'hydrates dépend fortement du sous-refroidissement. Deux nouveaux phénomènes ont été observés:

(i) la propagation d'un « halo » d'hydrate le long de l'interface verre/CP depuis la ligne de contact de la goutte d'eau.
(ii) cristallisation de l'hydrate dans une émulsion 2D de CP dans l'eau.

Les deux types d'outils développés dans cette thèse ouvrent des nouvelles perspectives pour élucider les mécanismes de formation et dissociation d'hydrates en présence d'additives (promoteurs et inhibiteurs) et en présence d'un substrat minéral. Les applications comprennent les hydrates dans des environnements sédimentaires, séparation de gaz, etc.

Mots-clé: hydrate de cyclopentane, millifluidique, effet mémoire, émulsion, cristallisatiosous-refroidissement, surface hydrophile, halo, processus de percolation.

List of Figures

List of Tables

TABLE OF CONTENTS

I. INTRODUCTION

INTRODUCTION

The interest for gas hydrates is growing at a very fast pace. For decades, petroleum (oil and gas) applications have been the main incentives for investigating these materials, starting in the 1930s with the transport of natural gas in flow lines (tubing, pipelines, valves…). How to avoid the plugging of these lines by gas hydrates has been the main motivation for studies on the thermodynamics and kinetics of hydrate formation and on processes or additives that inhibit this formation. This application – flow assurance in natural gas transport – is now a mature technology. Gas hydrates are also of interest to the oil and gas industry for at least two other reasons: one is related to the production of deep-offshore oil and gas fields, which are often located below hydrate-bearing sediments, and the other one is the possibility of recovering the natural gas present in enormous amounts (probably larger than all the fossil energy produced to date) in these sediments. The recovery of these highly unconventional fossil resources presents however enormous technical challenges and is still at a very exploratory stage. Other potential applications of gas hydrates in the energy sector include gas storage and transport, CO_2 capture and storage, and secondary refrigeration. Potential applications in the non-energy sector include the desalination of salted water and the purification of waste water.

These perspectives are motivating research efforts in various areas, from the characterization of interactions between sediments and natural gas hydrates to the kinetics of hydrate crystallization, which depending on the application need to be either accelerated or slowed down by means of appropriate additives. Progresses in these areas will stem from the development and implementation of novel experimental and modelling tools and methods. The length and time scales that have been mostly investigated so far are either microscopic or macroscopic. Microscopic scales are accessed experimentally, e.g., by diffraction and spectroscopic methods, which give for instance information as to gas hydrate structures, and numerically by molecular simulation tools, which are limited to a few nanometers and nanoseconds. Macroscopic scales are accessed by conventional experiments in instrumented cells, for instance, where the temperature, pressure and composition variations can be monitored in the course of the hydrate formation and dissociation processes; these variations are used to construct thermodynamic models, among other things.

The experimental work described in this thesis focuses for a large part on some mesoscopic features of gas hydrate formation and dissociation processes. Intermediate - mesoscopic - length scales, from roughly the micron to the millimeter; have been much less investigated than the microscopic and macroscopic scales [1]. Most if not all investigations at these mesoscopic scales have been concerned with the properties of the single crystals and of the polycrystalline crusts that form and grow at the interfaces between water and the guest phase (e.g., methane): for a review, see [2]. In particular, the microporous and slowly annealing structure of these crusts has been revealed, together with their consequences on the kinetics of hydrate formation [3]. Other important topics have been barely investigated, and are the subject of this thesis:

(i) The role of a substrate, such as a mineral substrate, in gas hydrate formation and growth.

(ii) Gas hydrate formation and growth in an emulsion.

Topic (i) is of interest for understanding the behavior of gas hydrate-bearing sediments, in which mineral phases are ubiquitous. Some authors [4] have shown experimental evidence that gas hydrates grow on these mineral (hydrophilic) phases as a “halo” that propagates from a reservoir of water (e.g., a water drop) along the mineral/gas interface, in a manner analog to the creeping of salt solutions on glass caused by evaporation [5]. Topic (ii) is of interest in the context of the transport of water, oil and gas (where these phases often form an emulsion)

[6] and also for fundamental reasons: understanding the hydrate formation and growth mechanisms in an assembly of droplets or bubbles.

The favorite tool for investigating mesoscopic scales is optical microscopy. Surprisingly, the statement made in 1997 by Smelik and King that "optical microscopy has not been fully exploited in hydrate research" [7] is still true today. This thesis exploits optical microscopy and some of its observation modes, such as differential interference contrast (DIC), fluorescence and confocal reflectance which, to the best of our knowledge, have not been used in gas hydrate research yet.

The other topic investigated in this thesis is one of the most fascinating features encountered in gas hydrate research, referred to as the 'memory effect', which describes the fact that gas hydrate nucleation is facilitated by using a water that has experienced shortly before some previous ice or hydrate formation and dissociation. Because hydrate nucleation is a stochastic process, the experimental investigation of this 'memory effect' requires many experiments to be carried out under the same conditions, which is cumbersome and unpractical: in practice, the number of repeat experiments done in kinetic studies of gas hydrate formation rarely exceed a few units. This difficulty is alleviated by using another experimental tool which, to the best of our knowledge, has never been used in gas hydrate research either: microfluidics, and more precisely, droplet-based microfluidics, also called millifluidics when the size of the objects (droplets) is in the millimeter range as is the case in this thesis. This tool allows the generation of many identical droplets acting as independent reactors for crystallization, which can then be monitored *collectively*, e.g., for gaining insights for instance into the statistics of crystal (here, hydrate) formation as a function of various fluid or thermodynamic parameters, as well as *individually*, for determining some particular crystalline form or crystal growth/melting process. In this thesis, we use the first aspect (the simultaneous monitoring of a collection of individual reactors for gas hydrate crystallization) for gaining insights into the 'memory effect'. We use the second aspect (the monitoring of an individual reactor) to figure out how gas hydrates form, grow and melt at the water/guest interface (i.e., at the surface of these droplets) in the presence or absence of additives such as hydrate inhibitors.

The guest (or hydrate-former) molecule chosen is cyclopentane (CP). CP hydrates are considered a proxy of natural gas hydrates because CP, similarly to these mixtures of low

molecular-weight alkanes, is sparingly soluble in water and forms structure II hydrates. The interest of CP hydrates, which are stable below the dissociation temperature $T_{dis} \approx 7°C$ (T_{dis} is the temperature of coexistence between CP hydrate, liquid water and liquid CP), is that they form at ambient pressure, which considerably eases the experimental work.

The manuscript is organized as follows. Chapter 1 is devoted to the state of the art, not only in the crystalline characteristics and kinetic properties of gas hydrates, but also in the field of microfluidics. Chapter 2 presents an overview of the optical characterization techniques that are used in this thesis: dark and bright field, differential interference contrast, fluorescence and confocal reflectance. Chapter 3 reports an experimental investigation (recently published in Chemical Engineering Science, Vol. 123, 2015) on the 'memory effect' by a droplet-based millifluidic technique. It also examines the growth and melting of CP hydrate in an individual drop with a resolution of a few microns. Chapter 4 examines at the same resolution the effect of inhibitors on CP hydrate formation and melting. In the following chapters, the optical resolution is considerably enhanced not only by the optical setup and imaging modes but also by the addition of fluorescent particles and dyes in water: CP hydrate formation, growth and melting is observed in/on/near a single sub-millimetric water drop in CP. Chapter 5 examines CP hydrate growing (as a polycrystalline crust) and melting (as an emulsion of CP droplets) on the water drop surface, i.e. at the water/CP interface. Some properties such as the loci of CP hydrate nucleation, crust growth velocity and crystal morphologies are studied in detail. Chapter 6 is devoted to the study of the hydrate halo that forms on the mineral (quartzitic) substrate near the water drop. Chapter 7 explains the types of crystallization of CP hydrates that occur in a CP-in-water emulsion: conventional crystallization and dendritic hydrate growth. The last chapter presents the conclusions and prospects of this work.

REFERENCES

[1] Sloan, E. D., **2003**. Clathrate hydrate measurements: microscopic, mesoscopic, and macroscopic. Journal of Chemical Thermodynamics *35* (1), 41-53.

[2] Sun, C. Y., Peng, B. Z., Dandekar, A., Ma, Q. L., Chen, G. J., **2010**. Studies on hydrate film growth. Annual Reports on the Progress of Chemistry, Section C (Physical Chemistry) *(106)*, 77-100.

[3] Davies, S. R., Sloan, E. D., Sum, A. K., Koh, C. A., **2010**. In Situ Studies of the Mass Transfer Mechanism across a Methane Hydrate Film using High Resolution Confocal Raman Spectroscopy. Journal of Physical Chemistry C *114* (2), 1174-1180.

[4] Beltrán, J. G. and Servio, P., **2010**. Morphological Investigations of Methane - Hydrate Films formed on a Glass Surface. Crystal Growth & Design *10* (10), 4339-4347.

[5] Shahidzadeh, N., Schut, M. F. L., Desarnaud, J., Prat, M., Bonn, D., **2015**. Salt stains from evaporating droplets. Scientific Reports *(5)*.

[6] Zerpa, L. E., Salager, J. L., Koh, C. A., Sloan, E. D., Sum, A. K., **2011**. Surface Chemistry and Gas Hydrates in Flow Assurance. Industrial Engineering Chemistry Research *50* (1), 188-197.

[7] Smelik, E. A. and King Jr., H. E., **1997**. Crystal-growth studies of natural gas clathrate hydrates using a pressurized optical cell. American Mineralogist *(82)*, 88-98.

CHAPTER 1

STATE-OF-THE-ART

The objective of this first chapter is to introduce clathrate hydrates. The first part explains in the detail the generalities about clathrate hydrates such as the different structures they can adopt, the characteristics of the guest molecules, the analogies with ice, etc. The second part of this chapter is devoted to the hydrate formation (nucleation and growth) and dissociation ("memory effect") processes. Then we focus on cyclopentane hydrates and we clear up the reason why we have chosen them as the object of our study. In the next section we give some generalities about hydrate inhibitors and we explain why the gas and oil industry is so interested in their study. Finally, microfluidics is introduced as a new tool for the study of hydrate formation and dissociation processes. As far as we know, this droplet-based microfluidic tool has never used before for the study of hydrates.

1.1. Clathrate hydrates

1.1.1. Background

The term « clathrate », from the Greek word khlatron, means barrier, and indicates crystalline inclusion compounds in which small guest atoms or molecules are physically trapped in host cavities. These cavities are formed by hydrogen-bonded molecules, called host molecules, creating a tridimensional lattice [1]. When these host molecules are water molecules, the crystalline inclusion compounds are called "clathrate hydrates", and when in addition the guest molecules are gases like methane, ethane, propane, etc., they are called gas hydrates, leaving the word "clathrate" for the cases where another molecule apart from water takes part of the tridimensional lattice. These ice-like compounds are stable in a domain of low enough temperatures (typically, below a few °C) and high enough pressures (often above a few bar) that depend on the particular guest molecule (or hydrate-former). The most widespread gas hydrates are the natural gas hydrates encountered in geological settings such as permafrost regions and deep marine sediments. The hydrate-former of natural gas hydrates is natural gas, which contains predominantly methane and a small amount of other gases. These structures will be introduced below.

The discovery of clathrate hydrates was made by Sir Humphrey Davy in 1810. Over a long period, the interest of these structures was purely academic and they remained a laboratory curiosity. It was later, in the 1930s, when natural gas hydrates were observed by oil and gas producers to form an ice-like material blocking pipelines exposed to cold temperatures (Figure 1.1). Research programs were initiated in order to avoid the formation of such structures inside the pipelines.

Figure 1. 1. Natural gas hydrates blocking a pipeline due to the cold temperatures and high pressures.

In the 1960s scientists found naturally occurring gas hydrates for the first time. This was in the Messoyakha gas field in western Siberia. Natural gas hydrates also occur on continental margins and shelves worldwide from Polar Regions to the tropics, and their energy content is estimated to exceed that of all other fuel sources combined. Gas hydrates are considered as an unconventional fossil fuel resource of energy. Indeed, one volume of methane hydrate yields upon dissociation 164 volumes (at standard temperature and pressure) of gaseous methane. However, gas hydrate exploitation is a distant objective for now, as many technical challenges need to be addressed first [2].

Apart from being a potentially huge energy source, the use of clathrate hydrates is being considered in a lot of applications such as carbon dioxide capture and sequestration [3], storage and transportation of natural gas [4], refrigeration applications such as cold storage or air conditioning due to their high latent heats of dissociation [5], [6], [7], etc.

The research in this area has experienced an increase in the last years because the industry is interested in these kinds of structures, whether to avoid hydrate formation in the oil and gas pipelines or to produce them for the applications mentioned above.

1.1.2. Hydrate cavities and structure of clathrate hydrates

As mentioned above, clathrate hydrates are inclusion compounds based on a three-dimensional ice-like framework of hydrogen-bonded water molecules. This framework consists of several polyhedral cavities of different dimensions where a (guest) molecule of the right size will go and act to stabilize the structure, thanks to the Van der Waals forces between the water molecules that form the cavity and the guest molecule itself.

All common natural gas hydrates belong to the three crystal structures, cubic structure I (sI), cubic structure II (sII) and hexagonal (sH) [8]. The formation of one structure or the other depends on several factors, such as the size of the guest molecule.

1.1.2.1. The cavities in hydrates

The hydrate structures are composed of five different polyhedra made up of water molecules linked by hydrogen bonds (Figure 1.2). The nomenclature n_i^m is used, where n is the number of edges in the face type "i" and m is the number of faces with n_i edges. This section is inspired from chapter 2 of reference [8].

- The pentagonal dodecahedron (5^{12}) is the basic building block and the smallest cavity in all known hydrate structures. It is a 12-sided cavity in which all the faces are pentagons with equal edge length and equal angles. As all pentagons share sides, just 20 molecules are needed to build a 5^{12} structure instead of 60. As shown in Table 1.1, the 5^{12} cavity is almost spherical with a radius of 3.95 and 3.91Å in sI and sII structures, respectively. Although this is the smallest cavity in hydrate structures, it has been confirmed that the smallest molecules are not necessarily stabilized in it. Helium, hydrogen and neon are the smallest molecules with diameters less than 3Å. At first they were considered too small to stabilize any cage; however, new research has confirmed that they can stabilize either big or small cages at high pressures [9], [10], [11], [12].

- The tetrakaidecahedron (5^{12} 6^2) is a 14-sided cavity and is composed of 12 pentagonal and 2 hexagonal faces. This cage is formed by 2 facing hexagons with 12 connecting pentagons. This is the most nonspherical cavity in sI or sII. The average radius is 4.33Å and is large enough to contain molecules smaller than 6Å in diameter. This is the stabilizing structure for molecules that form structure I.

- The hexakaidecahedron (5^{12} 6^4) is a 16-sided cavity and contains, apart from 12 pentagonal faces, 4 hexagonal ones. The hexagonal faces are symmetrically arranged so that the normal to the center of each face form the vertices of a tetrahedron. There is not a hexagon sharing edges with another because each one of them is entirely surrounded by pentagonal faces. This is the most spherical cavity known, and can contain molecules with diameters of 6.6Å.

As shown in Figure 1.2, there exist some other types of cavities, which form structure H (Table 1.1). This structure is beyond our study (see reference [8] for more information).

In Table 1.1 we observe the characteristics of structure I and II with respect to the number of cages of each type that each unit cell contains, the average radium for each cavity and the number of molecules needed to form each cage.

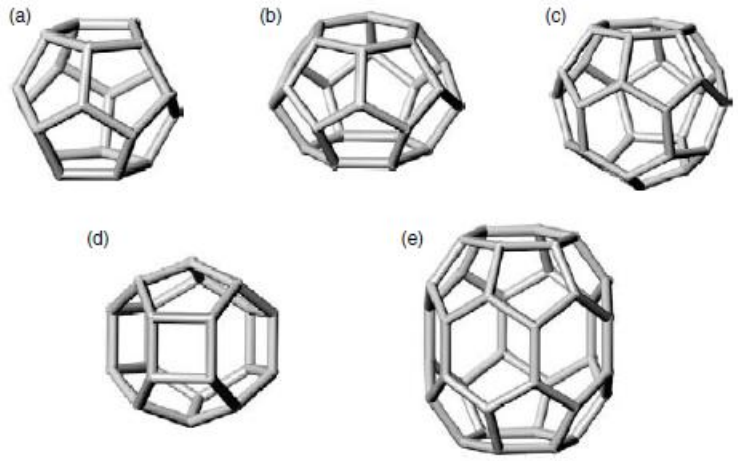

Figure 1. 2. Cavities that form hydrates type I, II and/or H. a) 5^{12}, b) $5^{12}\,6^2$, c) $5^{12}\,6^4$, d) $4^3 5^6 6^3$, e) $5^{12}6^8$.

Hydrate crystal structure	I		II		H		
Cavity	Small	Large	Small	Large	Small	Medium	Large
Description	5^{12}	$5^{12}6^2$	5^{12}	$5^{12}6^4$	5^{12}	$4^3 5^6 6^3$	$5^{12}6^8$
Number of cavities/unit cell	2	6	16	8	3	2	1
Average cavity radius (Å)	3.95	4.33	3.91	4.73	3.94	4.04	5.79
Variation in radius (%)	3.4	14.4	5.5	1.73	4.0	8.5	15.1
No. of water molecules/cavity	20	24	20	28	20	20	36

Table 1. 1. Geometry of the cages that form hydrates, adapted from [8].

1.1.2.2. Hydrate crystal cells

There exist three common types of gas hydrate structure: sI, sII and sH, which differ in the number and size of the cages and in their unit cells. All the hydrate structures are composed of two or more types of water cavities packed within the crystal lattice (Figure 1.3). In hydrate formation not all the cages need to be filled. A lot of times just the big cages are occupied and the small ones remain empty, and the hydrate is formed and stable.

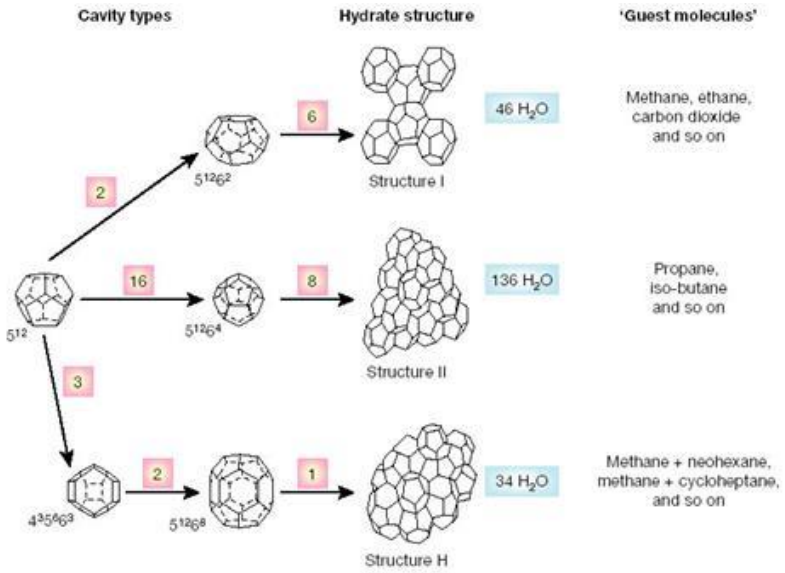

Figure 1. 3. Scheme of the formation of the three more common hydrate structures with respect to the cavity type.

- ***Structure I*** contains two types of cavities. These are 2 small cages 5^{12} and 6 big cages 5^{12} 6^2 [13], and the unit cell contains a total of 46 water molecules (Figure 1.4a). Pentagonal dodecahedra share vertices within the cubic unit cell. There is no direct contact between the faces of this cavity. The vertices of the 14-hedra are arranged in columns in which pentagonal dodecahedra occupy the space between each pair of 14-hedra, as shown in Figure 1.4b. The dimension of the lattice parameter *a* is 12Å.

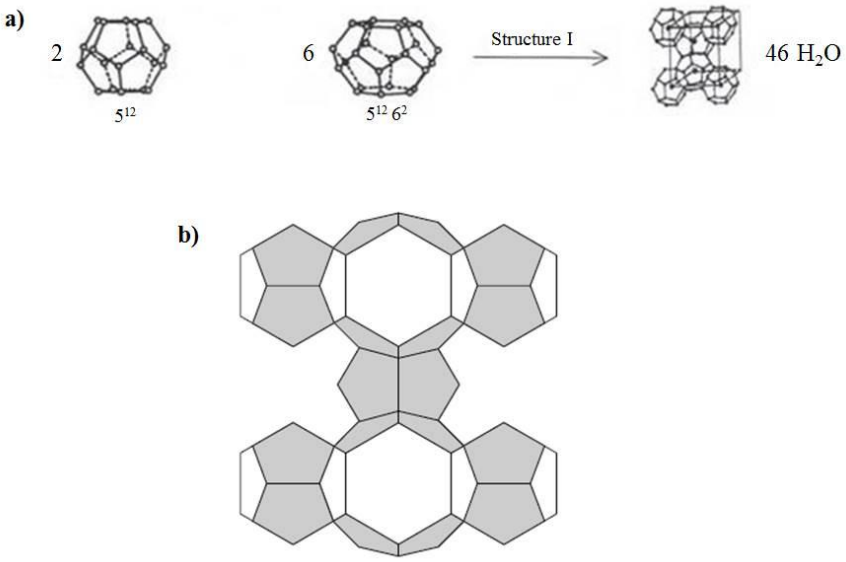

Figure 1. 4. a) Formation of the unit cell of a structure I hydrate. b) Linking five 5^{12} polyhedra by two 5^{12} 6^2 polyhedra to form structure I hydrates [8].

- ***Structure II***. This type of structure is formed by two types of cavities: 16 small cavities 5^{12} and 8 big cavities 5^{12} 6^4. The total number of water molecules per unit cell is, in this case, 136 (Figure 1.5a). The crystal consists of a face-centered cubic lattice, which fits in a cube of 17.3Å on a side. In this case, the crystal structure is completely defined by the vertices of the 5^{12} cavities. In Figure 1.5b we present a layer of structure II in which many face-sharing 5^{12} are arranged so that the residual voids are $5^{12}6^4$ (which share all hexagonal faces). Layers in this structure are stacked in a pattern ABCABC so that the centers of the 16-hedra form a diamond lattice within a cube, with shared hexagonal faces.

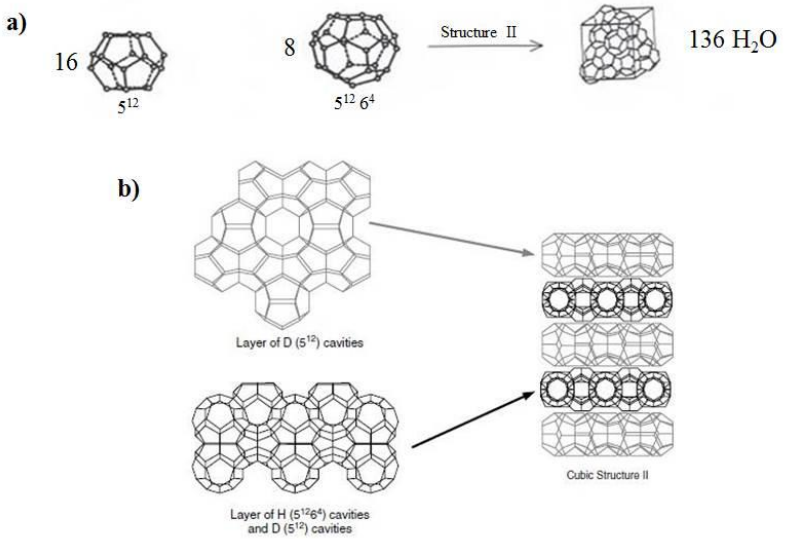

Figure 1. 5. a) Formation of the unit cell of a structure II hydrate. b) In sII hydrates, face-sharing 5^{12} are arranged so that the residual voids are $5^{12}6^4$ (which share all hexagonal faces).

For a better understanding of chapter 5 it is helpful to remember here that a cube is a highly symmetrical body, as it contains 23 elements of symmetry. An octahedron has the same 23 elements of symmetry so, despite the difference in outward appearance, there is a definite crystallographic relationship between these two forms. Figure 1.6 shows the passage from the cubic (hexahedral) to the octahedral form by a progressive and symmetrical removal of the corners. There exist 13 semiregular solids which are called combination forms, i.e. combinations of a cube and an octahedron. Crystals exhibiting combination forms are commonly encountered [14].

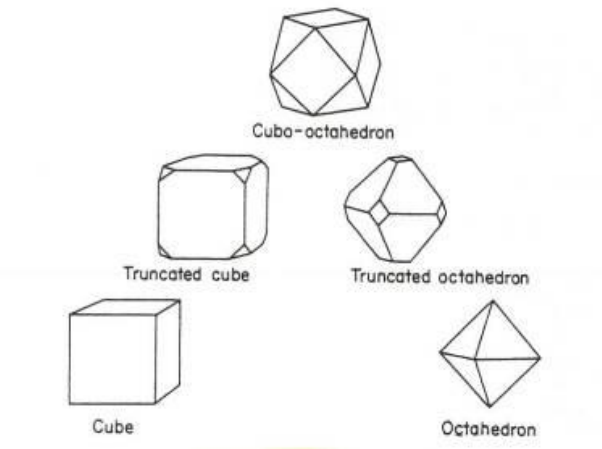

Figure 1. 6. Combination forms of cube and octahedron, result of the passage from the cubic (hexahedral) to the octahedral form by a progressive and symmetrical removal of the corners [14].

1.1.2.3. Analogies with ice

The most common solid form of water is known as ice Ih (hexagonal ice). The tetrahedral O-O-O angle of 109.5° is the most stable because there is almost no geometrical distortion. In ice, the tetrahedrally hydrogen-bonded water molecules form nonplanar "puckered" hexagonal rings, rather than planar sheets. The typical distance between oxygen nuclei is 2.76Å, covalently bonded protons are about 1Å from an oxygen nucleus and the hydrogen-bond length comprises the remaining 1.76Å. The ice crystal structure consists of water molecules hydrogen-bonded in a solid lattice.

A high quantity of water is involved in hydrate formation so it seems logical to do a comparison between the properties of both structures. Davidson (1973) [15] notes that hydrate hydrogen bonds average only 1% longer than those in ice and the O-O-O angles differ from the ice tetrahedral angles by 3.7° and 3.0° in structures I and II, respectively. A hydrate cavity is normally larger than that of the ice.

For a long time it has been believed that empty hydrates (with no guest molecules present in the structure) could not be stable and therefore they could not exist. It was not until 2009 that an empty hydrate of structure II was predicted by Conde et al. [16] by means of molecular simulation. Very recently, a completely empty type sII clathrate hydrate has been synthesized in the laboratory for the first time [17]. This new form of ice has been called ice XVI, according to the current ice nomenclature, and is expected to be the stable low

temperature phase of water at negative pressures, i.e. under tension. They have found the empty hydrate structure to exhibit negative thermal expansion below about 55K and to be mechanically more stable than the filled hydrate. Also, it presents larger lattice constants at low temperatures.

A lot of similarities between ice and hydrate structure are identified. These are related to mechanical, thermodynamic and thermal properties [8].

1.1.2.4. Characteristics of guest molecules

One way of classifying hydrates is by considering the guest molecules. This classification is a function of two factors: the chemical nature of the guest molecule and its geometry (shape and size).

1.1.2.4.1. Chemical nature of guest molecules

This whole section is based on chapter 2 of [8]. The first classification of guest molecules depending on their chemical nature was made by Stackelberg in 1956. This scheme was a combination of both size and chemical nature. The second one was proposed by Jeffrey and McMullan in 1967 [18], who split guest molecules into four groups: a) hydrophobic compounds, b) water-soluble acid gases, c) water-soluble polar compounds and d) water-soluble ternary or quaternary alkylammonium salts. The latter group does not give rise to hydrates (or clathrate hydrates) in the sense that the guest molecules are also part of the host structure together with water molecules: the corresponding clathrates formed by these salts and water are referred to as semi-clathrates.

Later, in 1984, Jeffrey stated that the guest molecule must not contain any single strong hydrogen-bond group or several moderately strong hydrogen-bonding groups [19]. Note that most of the natural gas components that form hydrates are hydrophobic (except from hydrogen sulfide and carbon dioxide), so they are included within the first two groups of Jeffrey and McMullan classification.

1.1.2.4.2. Geometry of guest molecules

This characteristic can be divided into size and shape of guest molecules. The shape plays a minor role in the properties and structure of sI and sII hydrates, but it is particularly important in hydrates of type sH.

The influence the size of guest molecules has on the formation of one type of hydrate structure or the other is explained through the study in the way hydrate cages are filled. In these three structures, each cavity can contain at most one guest molecules except in the case of small guest molecules such as argon, nitrogen, or hydrogen, among others, which exhibit multiple occupancy of the large cavity of sII hydrates at high pressures. Firstly we explain what the ratio of guest molecules to host cavities is, for a better understanding of how a certain cavity of one of the hydrate structures is either filled or not.

In general it is said that at normal pressures, molecules below 3.5Å are very small to stabilize any cavity, while above 7.5Å they are too big to fit into any cavity of sI or sII structures. In 1971, Davidson indicated that all molecules between 3.8Å (size of argon) and 6.5Å (size of cyclobutanone) can form sI and sII hydrates, if the restrictions of chemical nature are respected [20]. Ripmeester et al. [21] noted that the largest molecule that forms sII hydrates is tetrahydropyran (THP) with a diameter of 6.95Å. Udachin et al. [22], on the other hand, stated that molecules of size between 7.1 and 9Å can occupy sH cavities (if they obey the shape restrictions). It is important to note that the lattice size tends to depend on the guest size [22]. For example, trimethylene oxide, chloroform, THP and benzene, which present an increasing Van der Waals diameter of 6.01, 6.50, 6.95 and 7.07Å show increasing lattice parameters of 17.182, 17.236, 17.316 and 17.363Å, respectively, at 263K. This has a significant effect on thermodynamic parameters. Increases in lattice parameter with guest size, i.e. increasing unit cell volume, may change significantly the free energy [23], the hydrate formation pressure [24] or others. The average cavity diameter, hence the lattice parameter depends on temperature, pressure and guest composition.

In order to determine the upper and lower size limit of each cavity available for a certain guest, the ratio of guest molecules to host cavities was defined. Davidson suggested the subtraction of the van der Waals radius of the water molecule from the average cage radius previously given. This parameter is about 0.76 for the lower size ratio, indicating that below this value, the molecular attractive forces are too low and contribute less to the cavity stability. The upper limit is 1.0, meaning that above this value guest molecules are too large to enter any cavity without distortion. Note that any guest molecule capable to occupy the 5^{12} cavity of any of the structures will also fit in the large cavity of that structure. For example, in methane hydrates, methane molecules can occupy both the small and large cages of structure I. The methane diameter ratio to the 5^{12} cavity is 0.86 for structure I whereas it is 0.87 for

structure II hydrates (Table 1.2). Apparently it is a small difference but structure I hydrates gain stability by guest occupying the 5^{12} 6^2 cavity [20]. Nitrogen is known to stabilize the small cavities of sII hydrates (size ratio of 0.82) and so the big cavities of the structure. It does not provide a big stability to the big cages of either sI (5^{12} 6^2) or sII (5^{12} 6^4) structures (size ratios of 0.70 and 0.62, respectively), but as it is a very small molecule, more than one molecule could occupy the big cavities. The reason why nitrogen prefers to occupy the large cavities of sII hydrates instead of those of sI is because structure II has almost three times the number of 5^{12} cages per unit volume (0.0033/Å^3 in sII vs. 0.0012/Å^3 in sI) and that helps to stabilize the structure.

From the natural gas components that form hydrates, nitrogen, propane and iso-butane are known to form sII hydrates whereas methane, ethane, carbon dioxide and hydrogen sulfide form sI as simple hydrates. Natural gases form sII hydrates, even though the majority component is methane.

		Molecular diameter / cavity diameter for cavity type			
Guest hydrate former		**Structure I**		**Structure II**	
Molecule	**Diameter (Å)**	**5^{12}**	**$5^{12}6^2$**	**5^{12}**	**$5^{12}6^4$**
N_2	4.1	0.804	0.700	0.817	0.616
CH_4	4.36	0.855	0.744	0.868	0.655
H_2S	4.58	0.898	0.782	0.912	0.687

Table 1. 2. Ratio of molecular diameters to cavity diameters for some of the natural gas hydrate formers.

In summary, there are some general "rules" that help the characterization of guest molecules:

- At normal pressures, molecules below 3.5Å become too small to stabilize any cavity and above 7.5Å molecules are too big to fit into any cavity of sI or sII.

- Some molecules only stabilize the large cavity of sII, like propane or iso-butane.

- When a molecule stabilizes the small cavities of a structure it will also fit into the big cavities of that structure.

- It is well known that the smallest guest molecules (argon, krypton, nitrogen and oxygen) form sII hydrates rather than sI hydrates.

- Molecules with a size within the grey zones of Figure 1.7 exhibit the most non stoichiometry (the cages are not completely filled, i.e. the filling occupancy is less than 100%).

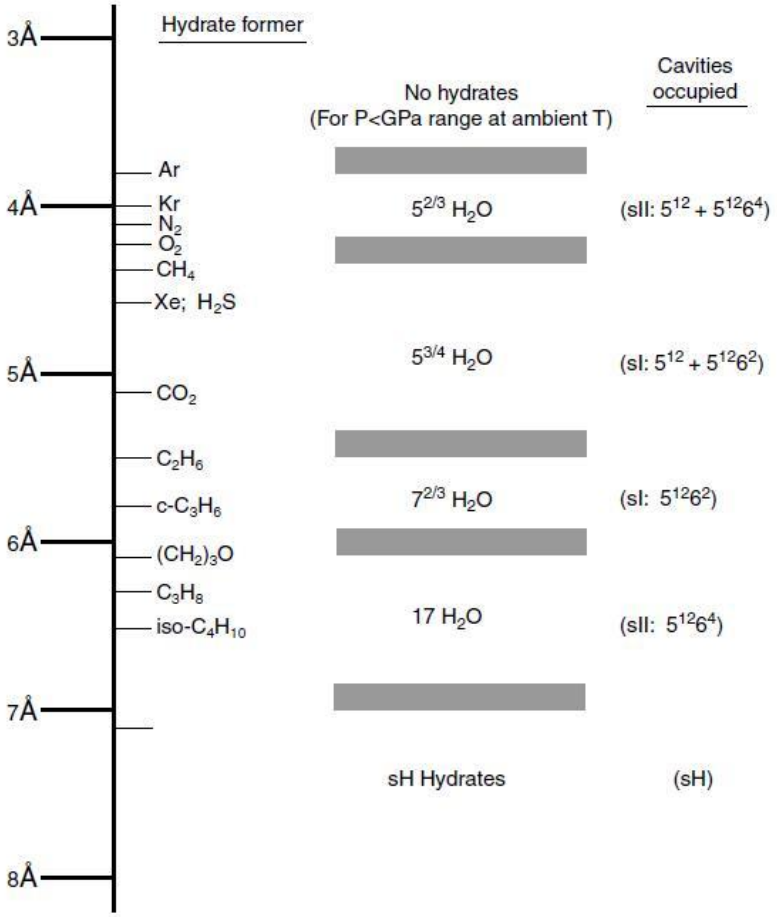

Figure 1. 7. Comparison of guest molecule sizes and cavities occupied as simple hydrates [8].

1.2. Hydrate formation and dissociation

One of the most challenging questions about hydrates is how they form, dissociate and are either inhibited or promoted elapsed with time. This section is also inspired from reference [8] and only takes into account the time-dependent properties of structures I and II, because of the lack of these data for structure H. The hydrate formation - dissociation process can be divided into three steps: hydrate nucleation, hydrate growth and hydrate dissociation. In Figure 1.8 we observe the typical path in a temperature - pressure diagram of the processes of methane hydrate formation and dissociation. It has to be noted that all the experiments made in order to obtain these kinds of diagrams are usually carried out at the macroscopic scale, meaning that the fluid volume is large (at least a few milliliters): this volume is typically that of a cell instrumented with temperature and pressure sensors, and sometimes equipped with see-through windows. In these experiments, the liquid water + gas system is first cooled down (path AB in Figure 1.8) to a temperature low enough for forming the hydrates: this formation is manifested by the drop in pressure (BC). The system is then heated up slowly (path CDA) to dissociate the hydrate: the equilibrium conditions are determined along this path, which meets path AB at point D. Path DB during the hydrate formation (cooling) process corresponds to a range of metastable conditions, where the system does not form a new hydrate phase and remains in two - phase (liquid water + gas) conditions even though the temperature and pressure conditions for hydrate stability are reached. Metastability is observed in all crystal-forming systems, and it is more developed for small volumes.

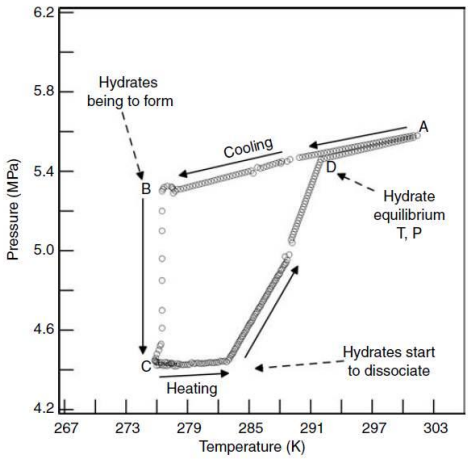

Figure 1. 8. Temperature – pressure trace for formation and dissociation of simple methane hydrates [25]. Normally hydrate formation takes place when the host and the guest molecules meet at low temperature (higher than 0°C) and high pressure (over 1 atm), although there are some hydrate that form at atmospheric pressures, as we will see later.

Hydrate formation normally takes place when the host and the guest molecules meet at low temperature (higher than 0°C) and high pressure (over 1atm), although there are some hydrates that are formed at atmospheric pressures, as we will consider later on. The driving force is used to define how far from equilibrium conditions the (metastable) system is located. This driving force can be rigorously defined in terms of a difference in chemical potentials, but in practice it is considered equal to the difference in temperature between the equilibrium (or dissociation) temperature at the experimental pressure and the temperature of the experiment [26]. This difference is also referred to in this manuscript as the subcooling degree. The larger this driving force or subcooling degree, the smaller the induction time and the faster the subsequent growth will be. The induction time is the time taken for hydrates to be detected macroscopically, once given conditions of T, P have been attained. It is the sum of the nucleation time, that is, the time for having a nucleus of size large enough to grow further (see below), and the time necessary for this nucleus to grow to a size large enough to be detected (see Figure 1.9). During this time, temperature and pressure conditions are within the hydrate stability region and the macroscopic characteristics of the system will not change significantly. However, hydrates do not form because of metastability, i.e., the ability of a non-equilibrium state to persist for a long period of time.

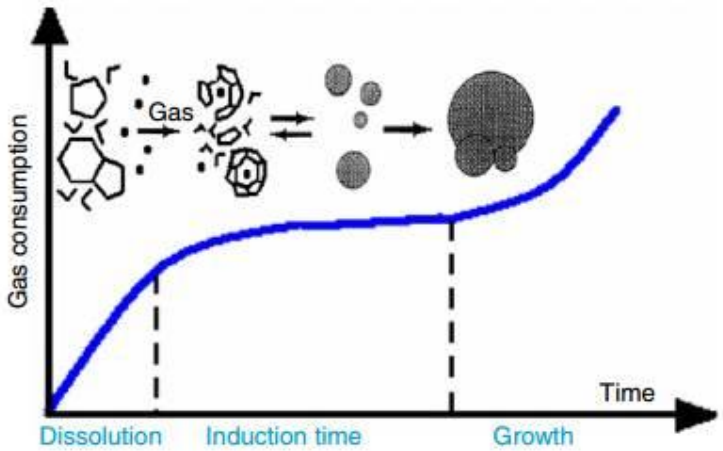

Figure 1. 9. Typical gas consumption plot showing the induction time [28].

1.2.1. Hydrate nucleation process

1.2.1.1. Fundamentals of hydrate nucleation

Hydrate nucleation is the process during which small clusters (hydrate nuclei) grow and disperse in order to achieve a critical size for continuing the growth. This step is a microscopic phenomenon involving tens to thousands of molecules [14] and is difficult to observe experimentally. In the case of strongly salted aqueous solutions, metastability is driven by supersaturation, which describes the state of a solution containing more dissolved salt than the equilibrium solubility limit: when the salt crystal forms id because this limit is reached in the solution. A supersaturated solution is one in which the liquid (solvent) contains more dissolved solute than can be ordinarily accommodated at that temperature. The greater the degree of supersaturation, the greater the number of salt crystal nuclei that will form in solution. In the case of hydrate-forming water/gas system, supersaturation is replaced by the difference between the chemical potentials of the molecules in a hydrate building unit in the solution and in the hydrate crystal, which itself is roughly proportional to the difference between the temperature of the experiment and that of equilibrium conditions at the experimental pressure, as we will see below.

This difference in chemical potentials - or driving force - favors the aggregation of water and guest molecules in order to form a hydrate embryo. There exists a limit of metastability, called the thermodynamic spinodal, which is characteristic of each host - guest couple [27] but it is not know precisely where the spinodal line occurs. Hydrate nucleation and growth normally take place within the metastable region before entering the spinodal region.

Figure 1.10 shows a normal hydrate crystallization curve with the AB equilibrium and the CD spinodal (supersaturation limit) curves. The crystallization regions are as follows:

1. There is a stable zone to the right of the AB equilibrium curve where crystallization does not take place.

2. The metastable region is located between the AB equilibrium and the CD spinodal curve. In this area, spontaneous crystallization is improbable but it can be helped by adding a hydrate seed, for instance. The place in which the CD spinodal curve is placed is not known for hydrates.

3. In the unstable zone to the left of the CD spinodal line, nucleation takes place spontaneously because of the very high driving forces.

Two types of nucleation are going to be considered hereafter: homogeneous and heterogeneous nucleation.

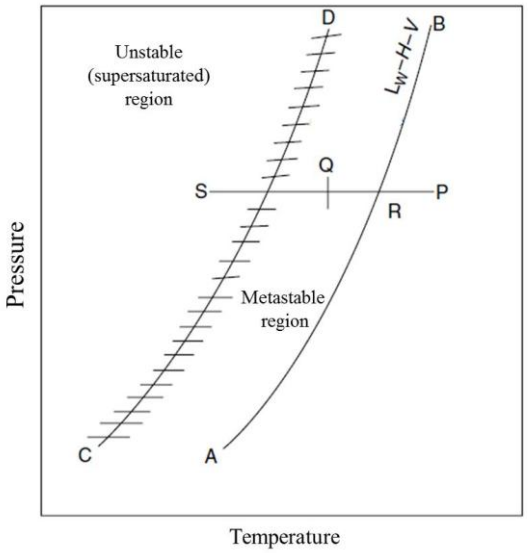

Figure 1. 10. Hydrate formation as a function of subcooling relative to the AB equilibrium line and the CD spinodal line (supersaturation limit, if we make the analogy with salted aqueous solutions).

1.2.1.1.1. Homogeneous nucleation

This type of nucleation is hard to find in nature because it requires the absence of impurities. The way through which this nucleation takes place is by sequential formation of clusters (embryos) within the liquid. This cluster increases its size by adding more molecules in the bulk metastable liquid until the critical size is reached. This critical cluster size or critical nucleus is the cluster size that must be reached before nuclei/clusters can grow spontaneously. This spontaneous growth can be explained by the excess Gibbs free energy (ΔG) between a small solid particle of solute and the solute in solution. ΔG is equal to the sum of the surface excess free energy ΔG_s (for solute particles becoming part of the surface of the crystal nuclei) and the volume excess free energy ΔG_v (for solute molecules ending up in the bulk / interior of the crystal nuclei):

$$\Delta G = \Delta G_S + \Delta G_V 4\pi r^2\sigma + \frac{4}{3}\pi r^3 \Delta g_v,$$

where Δg_v is the free energy change per unit volume and σ is the surface tension of the crystal - liquid interface. In Figure 1.11 we see that ΔG_s and ΔG_v have opposite sign and are different functions of *r*, which is the radius of the solid particle. The addition of both effects (surface and volume) causes a maximum (ΔG_{crit}) where r_c is the radius of the critical nucleus. The free energy must be higher than the free energy barrier ΔG_{crit} in order to form a cluster of critical size beyond which the nuclei/clusters grow spontaneously. By differentiating the precedent equation we obtain:

$$r_c = \frac{-2\sigma}{\Delta g_v}$$

$$\Delta G_{crit} = \frac{4\pi\sigma r_c^2}{3}$$

The rate at which clusters of critical size will form depends on the height of the free energy barrier (ΔG).

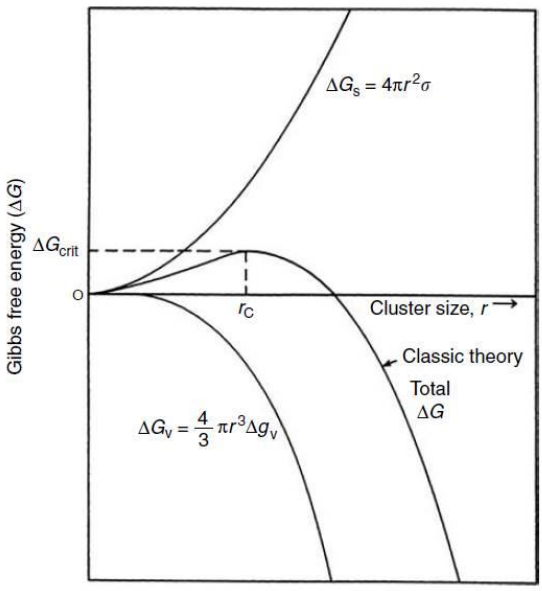

Figure 1. 11. Comparison of surface excess free energy (ΔG_S) and volume excess free energy (ΔG_V) as functions of cluster size.

1.2.1.1.2. Heterogeneous nucleation

We have already said that homogeneous nucleation is very difficult to achieve because the fact of not having any impurity in the system is almost impossible. The most usual nucleation is the heterogeneous one, which occurs in the presence of a foreign body or surface, at smaller driving force or subcoolings (some authors use the term 'supercooling') than those required for homogeneous nucleation [29]. From a free energy point of view, it is more probable to grow an ice or hydrate nucleus on a two-dimensional surface (a wall or a dust particle, for instance) than in a three-dimensional surface-free volume of water. The effect of the surface is to lower the free energy barrier $\Delta G'_{crit}$ compared to the free energy barrier for homogeneous nucleation (see preceding equation). The former ($\Delta G'_{crit}$) is smaller than the latter (ΔG_{crit}) by a factor Φ (smaller than 1) related to the contact angle θ between the hydrate crystal and a surface as follows:

$$\Delta G'_{crit} = \Phi \cdot \Delta G_{crit}$$

$$\Phi = \frac{[(2 + \cos\theta)\,(1 - \cos\theta)^2]}{4}$$

The last equation shows that for a contact angle $\theta = 180°$ (complete nonwetting of the substrate: nucleation occurs in the bulk, i.e. homogeneously), $\Delta G'_{crit} = \Delta G_{crit}$ and when $\theta = 0°$ then $\Delta G'_{crit} = 0$. The kinetics of nucleation of gas hydrates in aqueous solution has been analyzed by Kashchiev and Firoozabadi [30]. It has to be noted that hydrate formation normally takes place at the vapor - liquid interface. This is like this not only because the interfaces lower the Gibbs free energy of nucleation but also because the interface is the place where host and guest molecules are at their higher concentrations.

According to Sear, heterogeneous nucleation is still easier at a triple line [31]: the energy required for forming a critical nucleus is still lower than that required for forming it at an interface due to the disappearance of three different interfaces, all of which can cost free energy.

1.2.1.2. Stochastic nature of heterogeneous nucleation

The differences between stochastic and deterministic properties are shown in Figure 1.12. A deterministic property is any common thermodynamic property such as temperature (vertical line of the figure). This means that there is a certainty of observing a specific

temperature for a specific equilibrium state, for example. On the other hand, there are some properties for which the probability of observation is distributed over a range of values. It is the same to say that the observation of a certain value cannot be predictable. Curves with uncertainty in the observed value are called stochastic. After studying the macroscopic measurements to date, it is known that the hydrates induction time (nucleation and beginning of growth) is stochastic, mainly at low driving forces in the metastable region. When the driving force is higher, the stochastic nature of the system becomes less pronounced.

In summary, the magnitude of the driving force affects the stochastic behavior of crystal nucleation: the smaller the driving force (low subcooling conditions), the more stochastic (less deterministic) the nucleation process will be.

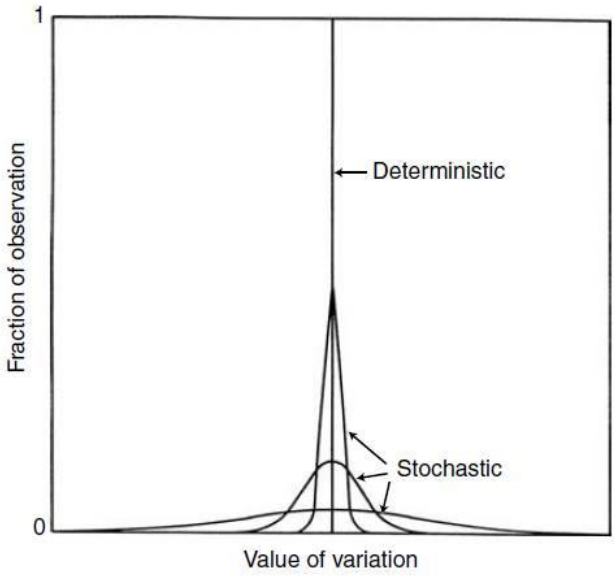

Figure 1. 12. Comparison of stochastic and deterministic properties [8].

1.2.1.3. The "memory effect"

All hydrate researchers have come to the conclusion that hydrates retain a "memory" of their structure when they are dissociated or melted at moderate temperatures above the equilibrium temperature and/or for a moderate amount of time above this temperature. As a consequence, metastability is less pronounced: hydrates form more easily once they have been previously formed, i.e. when they form from "fresh" melted solutions of host and guest molecules (hydrate history). If the melting temperature is very high compared to the

equilibrium temperature at a given pressure, this effect can be lost. There are two different hypotheses that try to explain this phenomenon:

1. Hydrate structure (not visible to the naked eye) remains in solution after hydrate dissociation as a residual structure [28], [32], [33], [34] consisting of partial hydrate cages or polyhedral clusters (short-range ordered structure) for a certain time period or as persistent hydrate crystallites (long-range ordered structure), which probably remain in solution for several hours after increasing the temperature above the hydrate dissociation temperature. To the best of our knowledge, these persistent structures have not yet been observed experimentally.

2. Dissolved guest molecules remain in solution after the hydrate has been dissociated [35]. The aqueous phase solution is therefore supersaturated with the guest molecules; very often a guest-in-water emulsion is formed.

The memory effect clearly exists and it is very important in practice for promoting hydrate formation, but it is still far from being understood due to the limited number of investigations. The precise characterization of the stochastic (or deterministic) character and of the memory effect is very difficult because it requires a significant number of identical hydrate formation experiments to be carried out in order to have a relevant statistics. The droplet-based microfluidic methods that are introduced below and used in this thesis allow such a characterization.

1.2.2. Hydrate growth process

Once the stochastic hydrate crystal nucleation takes place, the crystal will continue growing. However, data about this hydrate growth after nucleation is shortage. There are a lot of important parameters in hydrate growth such as displacement from equilibrium conditions, water history, gas composition, etc. But the most important ones are mass and heat transfer. Hydrate growth is a combination of three factors:

1) Kinetics of crystal growth at the hydrate surface.

2) Mass transfer of components to the growing crystal surface.

3) Heat transfer of the exothermic heat of hydrate formation away from the growing crystal surface. If heat transfer is not fast enough, the global growth velocity can be limited.

There is a wide variety of kinetic theories based on mass and heat transfers that try to explain the hydrate crystallization process, but the most important ones, which are based on theoretical concepts, are that of Englezos et al. (1987) [36], [37] and the one Skovborg and Rasmussen proposed in 1994 [38]. The first one divides hydrate growth into three different steps and base the model on crystallization theory and on the double layer model for mass transfer at the interfaces. Another important crystallization model is the one Skovborg and Rasmussen proposed. They affirmed that the only responsible for the limitation in hydrate growth velocity is the resistance to the transfer due to the gas diffusion from the bulk to the host-guest interface. These are affirmations taken from experiments carried out in macroscopic dimensions.

In this section we are just going to explain the crystal growth molecular concepts modified by Elwell and Scheel in 1975 [39] and the hydrate crystal growth processes for a single crystal and for a hydrate film that grows at the water/hydrocarbon interface.

1.2.2.1. Crystal growth molecular basis

The crystal growth model is divided into several steps, shown in Figure 1.13:

a) Once the nucleation has taken place, a guest in a temporal water cluster is transported to the growing crystal surface. The driving force for this to happen is the lower Gibbs free energy existing at the crystal surface.

b) The growing crystal exerts a force field into the fluid that makes the cluster adsorb on the surface.

c) Then a diffusion process takes the cluster from the solid crystal surface to a step in the crystal. The adsorbed clusters just can diffuse in two dimensions because the force field exerted from the crystal surface is perpendicular to it.

d) The cluster is attached to the crystal surface. The step is a favorable place for the cluster to get attached because there are two solid faces that make a force (two surface-reactant interactions) instead of just one force field exerted by the flat surface (only one surface-reactant interaction).

e) Here there is only one movement possibility of the attached cluster which is along the step. The cluster will move in order to find a defect point in the step.

f) The cluster is then adsorbed at the defect point. This place is attractive because three or more solid faces exert a larger force field than the two forces exerted by the step. Finally, the cluster is immobilized in three dimensions.

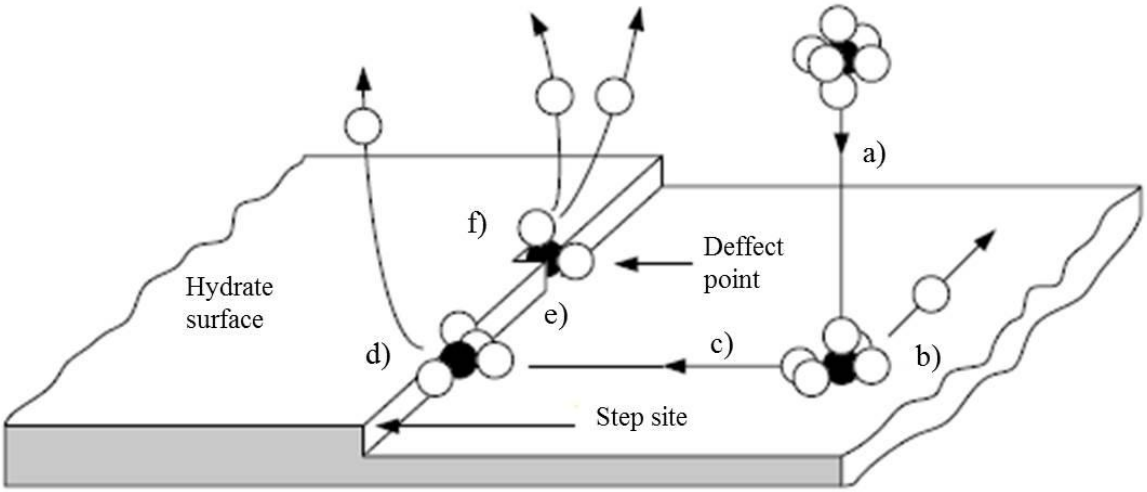

Figure 1. 13. Hypothesis picture of hydrate growth at a crystal, adapted from [39].

In the above process, not all the molecules progress in a deterministic way. With so many particles in motion, every combination can be possible. For example, some clusters can adsorb directly to a defect point without any apparent diffusion. Some other clusters can detach from the surface and diffuse away in contrast to our macroscopic observations of growth. A few molecular ways for crystal growth are highly preferred over others, and this can make the hydrate growth process predictable, in contrast to the stochastic nucleation step.

1.2.2.2. Hydrate crystal growth processes

There are several different types of hydrate crystal growth, but here we are going to highlight just two of them: single crystal growth and hydrate film/shell growth at the water-hydrocarbon interface.

1.2.2.2.1. Single crystal growth

It is relatively easy to obtain single hydrate crystals when the hydrate former is completely miscible in water, such as tetrahydrofuran or ethylene oxide. In contrast, single

crystals of gas hydrates are harder to obtain and isolate. There are few studies about them [40].

In single crystal growth, the slowest-growing planes are observed [25], while rapidly growing single crystal planes disappear (as we will see in chapter 5). This is why single crystals show {110} and {111} crystal planes for structures I and II, respectively. It is hypothesized that the {111} plane in sII grows slower because it contains a predominance of hexagonal faces relative to other crystal planes in sII. Crystal planes containing hexagonal faces grow slower because the hexagonal faces are more strained (120° between O-O-O angles) than pentagonal ones (108°), relative to the tetrahedral O-O-O angle (109°) or the water angle (H-O-H of 104.5°). The same could be deduced for the {110} plane of sI.

1.2.2.2.2. Hydrate film growth at the water-hydrocarbon interface

It is well known that hydrate growth is typically initiated at the water-hydrocarbon interface. According to wide documentation, mostly based on macrophotography, show that morphology changes during hydrate growth are similar independently of the hydrate former, making the subcooling degree (or driving force) responsible for the morphology observed.

Growth studies at water-hydrocarbon interfaces show the hydrate film grows laterally across the entire interface. Then, over time, the hydrate layer thickens to a final thickness that depends on the subcooling degree. The hydrate film thickness and growth rate have been determined using gas consumption coupled with video imaging [41], [42], or from micrometer measurements [43]. For instance, an initial 12μm film thickness was measured for cyclopentane hydrate. This thickness then increases very slowly with elapsed time. From the experiments, the proposed mechanism of hydrate growth is based on the guest molecule diffusion from the bulk aqueous phase to the hydrate film formed at the water-hydrocarbon interface. In Figure 1.14 we observe a conceptual picture of the hydrate growth mechanism not only for a flat surface but also for a water droplet (both analyzed in this thesis). In either case, the hydrate growth mechanism is the same. The first step is the propagation of a thin porous hydrate film/shell across the hydrocarbon-water interface, or around the water droplet. Then the film develops to finally solidify. In the case of the water droplet, once the shell has completely covered the surface, a droplet bulk conversion into hydrate takes place at a very low rate compared to that required for forming the thin hydrate film/shell across the interface.

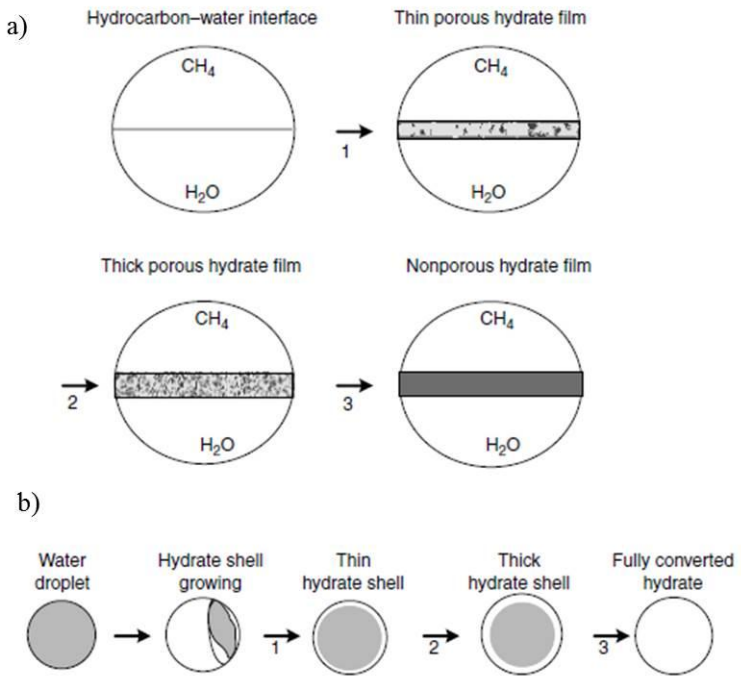

Figure 1. 14. a) Schematics of the proposed mechanism for hydrate film formation at a hydrocarbon-water interface. b) Schematics of the proposed mechanism for hydrate film formation on a water droplet. [8]

1.3. Cyclopentane hydrates

The interest in the study of cyclopentane (CP) hydrates, which are structure II hydrates, has increased over the last years. One reason for this interest is that these hydrates, in the presence of pressurized gases such as CH_4, CO_2, N_2, act as promoter of other types (i.e. structure I) of hydrates [44], [45], [46], [47]. The other reason is that cyclopentane hydrates are a model of natural gas hydrates (the water and the guest are sparingly miscible in each other, and they form structure II hydrates) and stable below the dissociation temperature of about 7°C and ambient pressure, which ease the experiments. The presence of a 'help gas' at moderate pressures (a few bars to tens of bars) has for effect to increase the dissociation temperature of the structure II hydrate and to expand the hydrate stability domain. The structure II CP hydrate acts then at still higher pressures to promote the formation of structure I hydrate according to ill-understood mechanisms.

Due to its size and shape cyclopentane (C_5H_{10}) occupies the big cavities (5^{12} 6^4) of structure II hydrates, leaving the small ones (5^{12}) empty. There also exist mixed hydrates

CP+H_2O+gas in which big cavities are occupied by the CP and the gas, whereas the small cavities trap just the gas molecules such as CH_4, CO_2 or N_2, among others.

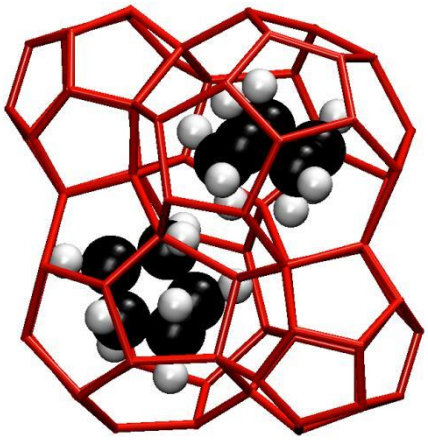

Figure 1. 15. Occupation of the big cavities (5^{12} 6^4) of sII by the guest molecule (CP) in CP hydrate.

The equilibrium temperature at atmospheric pressure has been studied by several groups and the results were in between 7°C and 7.9°C. Fan et al. [48] were the first in determining the quadruple point of the CP + H_2O system at a temperature of 280.22K and at 0.0198MPa. The phases present in the system at the quadruple point are CP hydrate (H), liquid water (L_W), liquid CP (L_{HC}) and saturated vapor (G).

1.4. Inhibitors

1.4.1. Background

The study of the effect of inhibitors on the formation and dissociation conditions of clathrate hydrates is essential, mainly because of the interest in avoiding their formation in gas and oil transport pipelines. The formation is very favored in there due to the high pressures and low temperatures present, as we have already explained. This is a disadvantage for the industry as these offshore flow-lines transporting hydrocarbons are considered the principal concern for flow assurance engineers [49].

The hydrate formation process starts by having something as simple as two interfaces of water and a hydrate forming compound, and the good temperature and pressure conditions.

Figure 1.16 illustrates a proposed model for hydrate formation in a multiphase flow system containing water, oil, and gas, where hydrates form at the interface of water droplets contained in the oil phase, and/or from gas bubbles entrained in the water phase [50]. In the oil phase, these hydrate-encrusted water droplets can agglomerate into larger hydrate masses, leading to an increase in the slurry viscosity, which can eventually form a plug. The surface of water droplets in water-in-oil (W/O) emulsions is a critical location for the formation and agglomeration of hydrates.

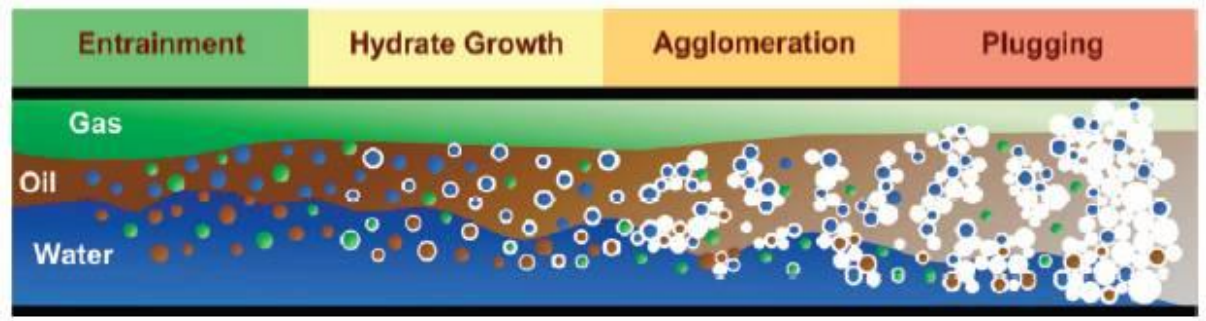

Figure 1. 16. Model for hydrate formation in a multiphase flow system containing water, oil, and gas [50].

Hydrate formation prevention can be attacked from various flanks. Hydrate formation could be stopped from the beginning (avoiding hydrate crystals to grow or even nucleate) or from another posterior step (agglomeration), allowing hydrate crystals to nucleate and grow, but preventing them from agglomerating. Depending on what to avoid, two types of synthetic compounds have been studied, apart from the natural inhibitors, present in the crude. The first synthetic molecules are called thermodynamic inhibitors and the others are "low dosage hydrate inhibitors" (LDHIs). These LDHIs have been researched and developed over the past 15 years as an alternative method to control gas hydrates [51]. They are now established tools for the prevention of gas hydrate plugging of oil and gas pipelines and gas wells. In this wide group there are two types of inhibitors that act in two different moments of hydrate formation. They are anti-agglomerants and kinetic inhibitors. All of them present some benefits and some disadvantages, and have their own "working mode".

Motivated by these affirmations, we realize about the importance of a deep study of the action mechanisms of these compounds, in order to give a clue about which one could be more appropriate, taking into account all the pros/cons factors. In this thesis we have focused

on just one type of inhibitors: the kinetic inhibitors (KHIs), because their mechanism of action is still poorly understood, and we would like to provide with scientific explanations by getting into it.

1.4.2. Thermodynamic hydrate inhibitors (THIs)

The main way of action of these compounds is that they shift the hydrate equilibrium curve towards higher pressure and lower temperature, so that the formation conditions are more difficult to achieve [49], i.e. lower subcoolings are required to obtain hydrates. The addition of THIs is a widely used way to prevent pipes plugging due to hydrate agglomeration. This is because of the fact that the amount of free water available to form hydrates is reduced because it is present forming hydrogen-bonds with the inhibitors [52]. This causes a shift in the equilibrium diagram, and that is why lower temperatures and higher pressures are required to form hydrates. Therefore, the system can be operated safely outside the hydrate stability region.

Some examples of THIs are methanol, mono-ethylene glycol (MEG) and other alcohols and diols. The most used THIs are methanol and MEG. Salts are also considered as THIs because water links to ions from deionized salts and Coulombic bonds are greater than hydrogen ones. Hydrate formation is inhibited because water is attracted to ions more than water is attracted to the hydrate structure [8]. The next diagrams show how the two more common THIs affect the equilibrium curve depending on the quantity we add. From the graphs shown in Figure 1.17 we can say that methanol has higher inhibition performance than MEG for the same amount of inhibitor added. Also, the inhibiting action increases when the percentage of inhibitor in the mixture increases.

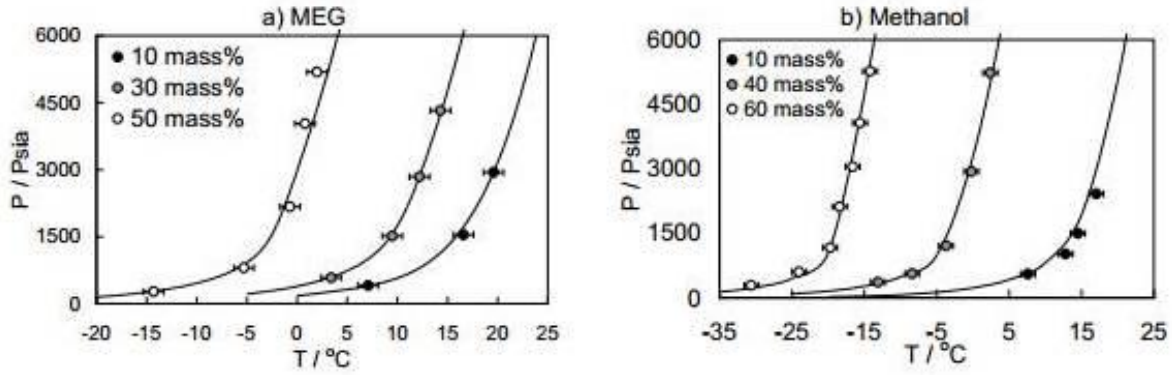

Figure 1. 17. Experimental and predicted hydrate phase boundary for natural gas in the presence of a) MEG and b) methanol aqueous solutions, taken from [53] and [54].

But the drawback with THIs is that they have to be added in very big quantities (20 - 50 wt%) [51] and they present high toxicity to the environment. Also, there exists the difficulty of recovering or recycling them post-addition, so there are some financial implications, both to treat and to transport them to the oilfield site. This is why the industry is moving towards other possible compounds that can avoid this hydrate formation.

Although the study of these THIs is very interesting, they are not the object of our research.

1.4.3. Low Dosage Hydrate Inhibitors (LDHIs)

The use of some surfactants to avoid hydrate formation in wells was first discovered by a Russian engineer called Kuliev in the early 1970s, who experienced the gas hydrate formation problem in his gas wells [55]. He observed that, by adding some commercial surfactants, the problem of hydrate formation disappeared. After that, no works on LDHIs have been reported until the 1980s, and from then their use has increased a lot.

The basic action mechanism of this kind of compounds is that they act in the early stages of hydrate formation, i.e. nucleation and/or growth. In contrast to THIs, LDHIs do not change the equilibrium conditions and it is possible to work in the hydrate stability zone. One of the main advantages in the use of these substances is that not big amounts of them are required, as their own name indicates, in contrast to THIs. We are talking about 0.1 - 1.0 wt% for LDHIs compared to 20 - 50 wt% for THIs [51], as it is said above. The use of low quantities of LDHIs for avoiding hydrate formation makes them a more investment cost saving option. Another benefit is that, in contrast to methanol (THI), these compounds are a lot less volatile and flammable, so Health, Safety and Environment (HSE) risks are reduced [56].

We can classify these LDHIs into two groups, depending on the moment of the hydrate formation at which they are effective: Kinetic hydrate inhibitors (KHIs) and anti-agglomerants (AAs: also called dispersant additives). Both types of compounds are going to be explained in the next pages, but the ones that have drawn our attention are the Kinetic Hydrate Inhibitors. The reason why we decided to study them (their effect on hydrate formation and dissociation) is that they have been less investigated and their action mechanism is still poorly understood. We expect to be able to give some insights into their

action mechanism by studying the addition of two different KHIs to our hydrate system water+cyclopentane.

1.4.3.1. Anti-Agglomerants (AAs)

Hydrate agglomeration is the stage just previous to pipe plugging, as it can be observed in Figure 1.16. This agglomeration process is due to the formation of inter-particle capillary bridges that increase their cohesion forces. This is why agglomeration could be avoided by reducing these "bridges".

AAs are normally surface active products mixed in a solvent. They can be water or oil soluble, depending on the technology used [56]. They are generally amphiphilic compounds, being ammonium quaternary salts the most typical, with a polar head and a hydrophobic part. Their mechanism of action is thought to be as follows: tiny hydrate crystals are formed when the good hydrate formation conditions are achieved (nucleation) but the polar heads of these AAs are adsorbed to the hydrate structure, preventing them to grow. The nonpolar part of these compounds stays in the oil phase, creating a steric repulsion between the small hydrate crystals, as shown in Figure 1.18.

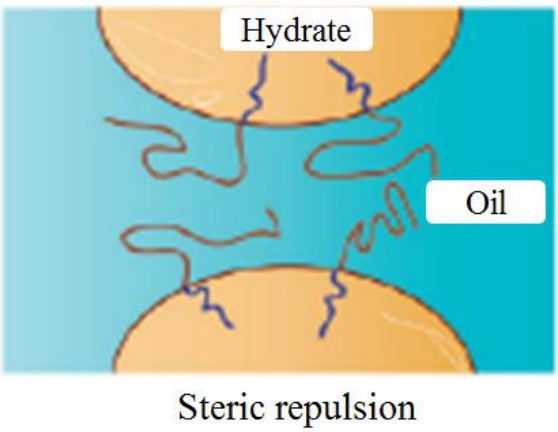

Figure 1. 18. Steric repulsion created between small hydrate crystals due to the nonpolar part of AAs, which stays in the oil phase (adapted from [50]).

Instead of inhibiting the crystallization of hydrates, these compounds prevent the agglomeration of small clathrate hydrates crystallites and ensure that free-flowing slurry is maintained [57] (Figure 1.19). There is a disadvantage, which is the necessity for the presence

of a liquid hydrocarbon phase for these AAs to work, so they are not suitable for all field site applications. The principal advantages of using this kind of compounds is that performance at high subcooling is superior to that of KHIs and also smaller quantities are required (0.1 - 1 wt%).

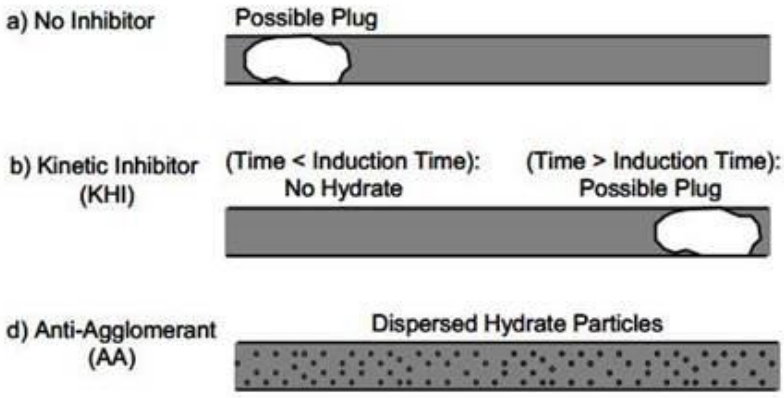

Figure 1. 19. Simplified methods by which LDHIs prevent hydrate plug formation [58].

1.4.3.2. Kinetic hydrate inhibitors (KHIs)

In contrast to AAs, KHIs do not prevent the aggregation of small hydrate crystals, but they inhibit the rate of nucleation and/or the growth of clathrate crystals. KHIs are water-soluble polymers that can either delay the onset of hydrate nucleation or the growth of hydrate crystals for periods long enough to ensure transport of the fluid without pipeline blockage [57]. The induction time (nucleation) is the most critical factor, and is dependent on the subcooling (ΔT) in the system, as we have already explained.

In nature we can find some compounds that act as inhibitors of ice and ice-like materials crystallization in the form of natural antifreeze proteins. The regular array of hydrophilic amino acid residues is thought to interact with the growing surface of an ice crystal. Some studies report that the mechanism of action is possibly due to a surface adsorption and the resulting Kelvin effect [59]. Celik et al. suggested that AFPs adsorb to the ice surface forming “patches” and so they change the curvature radius of the growing crystals [60] [61]. This change in the curvature produces a difference in pressure between the crystal inside and outside, which can be the reason why some structures like ice or hydrates, need to

be superheated in order to dissociate or melt, as we will explain below. This is called the Gibbs-Thomson effect.

But the problem of these structures is that they are quite expensive to synthesize so other possibilities are taken into consideration. It has been proved that some synthetic KHIs as poly(N-vinyl pyrrolidone) (PVP) or polyvinyl-caprolactam (PVCap) give some results in the inhibition of nucleation and crystal growth comparable to those of AFPs [57].

In contrast to thermodynamic inhibitors, the use of KHIs and AAs is increasing because they can be used in much lower dosages, as we have already said. KHIs are becoming a good option for inhibiting hydrate formation, for obvious economic and pollution reasons. In Figure 1.20 we can observe some of the most kinetic inhibitors used.

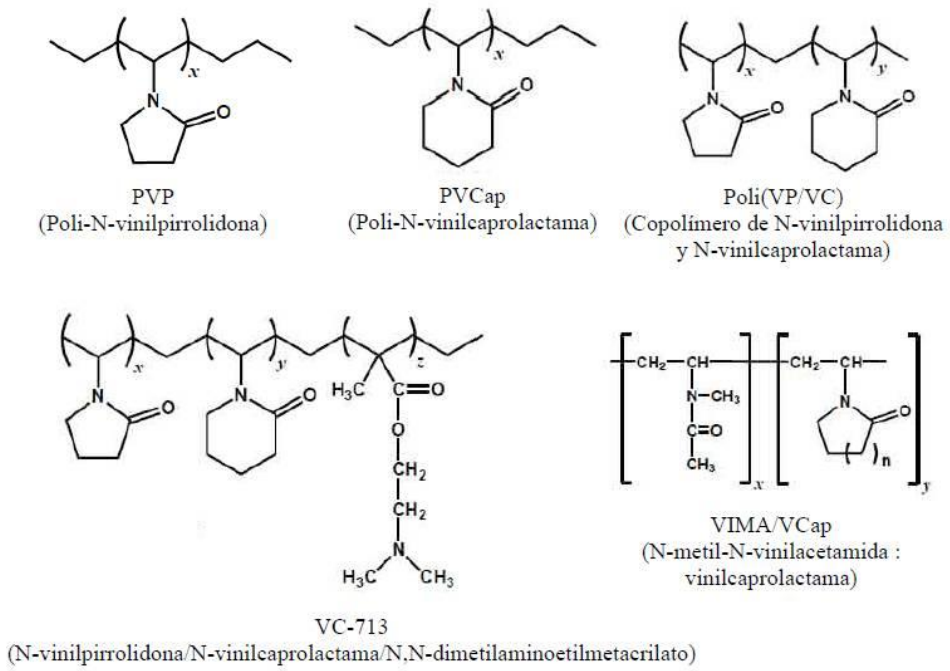

Figure 1. 20. Some of the kinetic inhibitors used in the inhibition of hydrate formation industry.

1.5. Microfluidics

Miniaturization has become more and more important in the last years and a lot of progresses have been done. All kinds of systems can be miniaturized nowadays to the sub-micrometric scale: mechanical, fluidic, electromechanical or thermic. The discipline that

studies the behavior of fluid flows in these conditions is called microfluidics, and is the purpose of this section [62]. Microfluidics is the science and technology of systems that process or manipulate small (10^{-9} to 10^{-18} liters) amounts of fluids, using channels with dimensions ranging from a few nanometers to the millimeter [63]. The terms nanofluidics and millifluidics are sometimes preferred when the dimensions are in the nanometric range or in the millimetric range, respectively. It is still not very clear the reason why people started to use microfluidic technologies in their studies. In the 1980s, Michael Widner thought it was more interesting to reduce the scale of the experimental setups used in the lab [64]. Later on, some other advantages of using microfluidic devices started to make them more and more interesting. The first Lab-on-a-Chip (LOC) or microfluidic device was conceived by Michael Widner at Ciba-Geigy (now Novartis), but it was not until 1990 that it was described conceptually by Manz et al. An extensive work about this was published in 1992 [65]. In the 1990s further development in microfluidics as a new area of discovery was carried out. An example of a microfluidic device is showed in Figure 1.21.

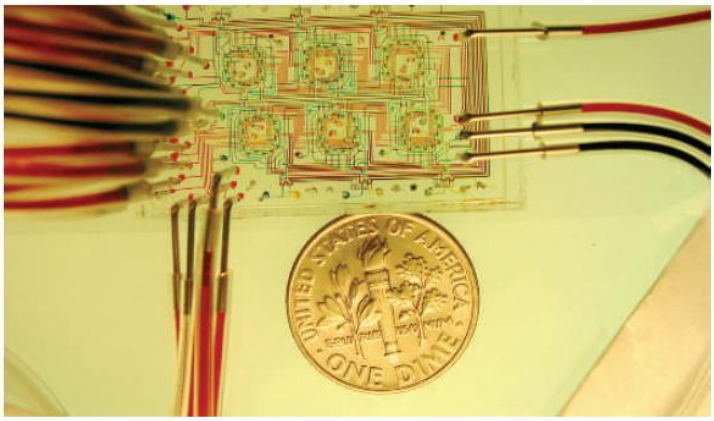

Figure 1. 21. A microfluidic chemostat used to study the growth of microbial populations. The colors are dyes introduced to trace the channels [70].

As far as we know, nobody has studied the phenomenon of formation and dissociation of hydrates at the micrometric scale. This with all the advantages micrometric systems provide pushed us to study the process of hydrate formation and dissociation in order to obtain many more details than when using macroscale reactors. Following what R. Feynman said in 1959 in his conference "*There is plenty of room at the bottom"* [66] we seek to study the curious and strange phenomena that take place at scales in the micron-to-millimeter range

and that have not been observed before in the formation and dissociation processes of gas hydrates.

1.5.1. Why should we use microfluidics to study our system?

There are some important differences between working at the micro or the macroscale which make microfluidic technologies very interesting nowadays. Gravity and inertia dominate the "macrophysics" but, in contrast to that, if we reduce the size of the channels where the fluid is confined other parameters such as the diffusivity, the interfacial tension or the viscosity become more important and predominate. Microfluidics deals then with the behavior, precise control and manipulation of fluids that are geometrically constrained to small, typically submillimeter, scales. The fact of miniaturizing offers a precise control of the transport phenomena: mixing, thermal transfer, strict control over spatial and temporal concentration distributions, rapid heat exchange, mass transfer and homogeneous reaction environments [67]. All these features make the conditions of a reaction easier to control.

Miniaturization is very important in the scientific research because it reduces the expenses and the environmental research impacts, as very low quantities of reactants are required (typical volumes are between 1pl and 1µl, and velocities between 10µm/s and 1cm/s). At this small length scales (small volumes), surface effects are important and confinement plays a role. Microfluidics is then important in order to study these kinds of parameters, more difficult otherwise. Also, high throughput, resolution and sensitivity can be obtained with small amount of liquids and in very short times of analysis.

One of the main advantages of microfluidics is that it allows fast analysis of fluid samples. This is just because the diffusion distances are short and there are very small volumes, which increase the surface area to volume ratio. This is the principal characteristic of microfluidic devices. The other thing is the reduction in cost, because a very low quantity of reagents is needed to perform an experiment. This last factor reduces the environmental pollution, and it is one of the reasons why microfluidics is interesting as well. Another important thing is that numerous experiments can be carried out simultaneously if we optimize the experiment conditions, which allows us to gain a lot of time. Turbulences can be avoided by using these devices and working in laminar flow is possible. This is one of the improvements that this technique allows: at large scales, fluids mix convectively and inertia is normally more important than viscosity. But in microsystems, two fluids do not mix

convectively: they flow in parallel and the only parameter that makes them mix is not the turbulences, but the diffusion of molecules across the interface that separates them.

1.5.2. Applications

The importance of microfluidics is not only the demonstration of principles, but also using it in the resolution of problems. This is why microfluidic systems are being more and more used in old applications and starting to be used in new applications. By seeing Figure 1.22 we can conclude that the research area where the majority of microsystems are used is the pharmaceutical and health care for diagnostics, and growing. A big number of conditions can be screened when using a microfluidic device: pH, ionic strength and composition, co-solvents and concentration, which is very desirable and important for protein crystallization.

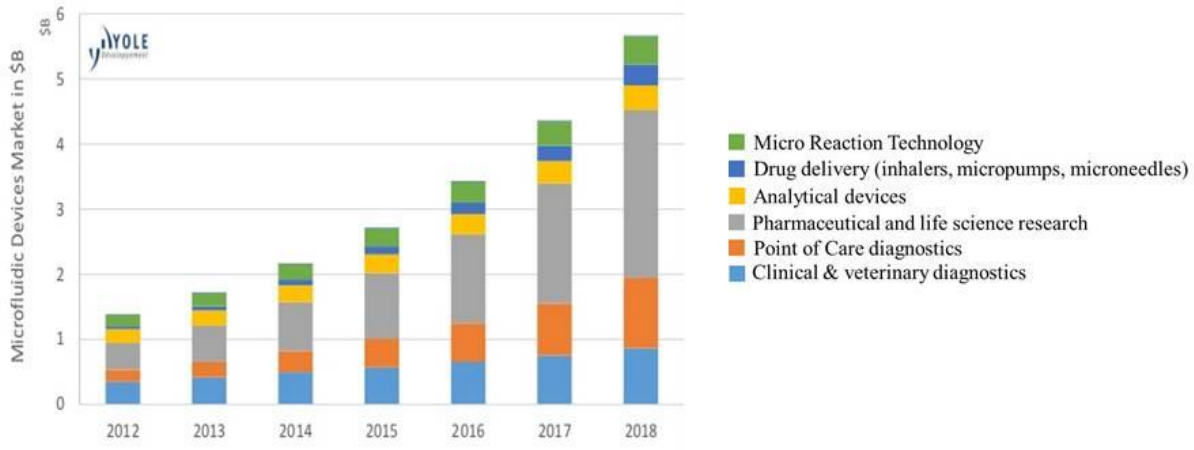

Figure 1. 22. Microfluidic Applications Market 2013 Report. Yole Développement SA [68].

Another important characteristic of microfluidic devices is that they allow us to create bubbles or droplets of a dispersed gas or liquid phase in a continuous liquid stream. This suggests new ways to synthesize polymers, particles, emulsions, foams, etc., and study them in more detail or even get insights into the formation. For example, droplets can act as different compartments where a reaction takes place. We can see them as miniaturized reactors for applications ranging from biological and material analysis to material synthesis to medical diagnostics [69].

In summary, even though microfluidics is at its starting point, it is growing more and more, and many different fields are using it for their research.

1.5.3. Droplet-based microfluidic crystallization

In the first part of this work, a microfluidic system is used in order to assist the investigation of cyclopentane hydrates crystallization. As we explained above, crystallization in general is a complex process involving nucleation and growth until at least one germ is visible, and thus couples kinetics to thermodynamics [70]. We already know that there are no accurate theories that substitute empirical approaches yet. The crystallization process deals with both thermodynamic and kinetic features. Thermodynamic data are the solubility lines, the presence of metastable phases, polymorphs, liquid - liquid separation…, and they depend on multiple parameters such as the temperature, pH, solvent, impurities, etc. On the other hand, kinetic trajectories in the phase diagram are relevant to control most of the final properties of the synthesized crystals. The path followed in the diagram controls the nucleation and growth of the crystals, and thus their number, size, and morphology.

The benefits of using microfluidics to study crystallization are in relationship with the specific objectives crystallization one seeks. The objective of crystallization is to either collect thermodynamic/kinetic data or to grow good crystals for diffraction purposes [70]. The first objective needs experiments to be multiplied, which can be achieved thanks to microfluidics because several experiments are carried out at the same time and a good statistics is this obtained. The second objective can also be achieved thanks to microfluidics and a good optical system, because a focus on a specific point to unveil fundamental mechanisms is required. Both of the general objectives of crystallization can be achieved through microfluidic systems. One of the aims of this work is to obtain a good statistics of the kinetics of hydrate formation and also to gain insights into the fundamentals of the mechanisms of gas hydrate formation and dissociation by using microfluidic devices.

In general, a microfluidic system must have a series of generic components: a method of introducing reagents and samples, normally as fluids, methods for moving these fluids around on the chip and for combining and mixing them (if it is the case), and various other devices (such as detectors for most microanalytical work, and components for purification of products for systems used in synthesis). Millifluidic devices are based on the same schema.

The microfluidic system we have used in the first part of this thesis for the study of hydrate formation is also based on this schema.

REFERENCES

[1] Chatti, I., Delahaye, A., Fournaison, L., Petitet, J. P., **2005**. Benefits and drawbacks of clathrate hydrates: a review of their areas of interest. Energy Conversion and Management *(46)*, 1333-1343.

[2] Grauls, D., **2001**. Gas hydrates: importance and applications in petroleum exploration. Marine and Petroleum Geology *(18)*, 519-523.

[3] Lee, S., Liang, L., Riestenberg, D., West, O.R., Tsouris, C., Adams, E., **2003**. CO_2 hydrate composite for ocean carbon sequestration. Environmental Science & Technology *(37)*, 3701-3708.

[4] Sloan, E. D., **2000**. Clathrate hydrates: the other common solid water phase. Industrial & Engineering Chemical Research *(39)*, 3123-3129.

[5] Tanasawa, I. and Takao, S., **2002**. Fourth International Conference on Gas Hydrates, Yokohama, Japan, p. 963.

[6] Fournaison, L., Delahaye, A., Chatti, I., Petitet, J.P., **2004**. CO_2 hydrates in refrigeration processes. Industrial & Engineering Chemistry Research *(43)*, 6521-6526.

[7] Eslamimanesh, A., Mohammadi, A., H., Richon, D., Naidoo, P., Ramjugernath, D., **2012**. Application of gas hydrate formation in separation processes: A review of experimental studies. The Journal of Chemical Thermodynamics *(46)*, 62-71.

[8] Sloan, E. D. and Koh, C. A., **2008**. Clathrate Hydrates of Natural Gases, 3rd edition (H. Heinemann, ed.), CRC Press, Boca Raton, Florida.

[9] Manakov, A.Y., Voronin, V.I., Teplykh, A.E., Kurnosov, A.V., Goryainov, S.V., Ancharov, A.I., Likhacheva, A.Y., **2002**. Fourth International Conference on Gas Hydrates, Yokohama, Japan, p. 630.

[10] Mao, W.L., Mao, H.K., Goncharov, A.F., Struzhkin, V.V., Guo, Q.Z., Hu, J.Z., Shu, J.F., Hemley, R.J., Somayazulu, M., Zhao, Y.S., **2002**. Hydrogen Clusters in Clathrate Hydrate. Science *(297)*, 2247-2249.

[11] Lokshin, K.A., Zhao, Y., Lobanov, M.V., Greenblatt, M., **2005a**. Fifth International Conference on Gas Hydrates, Trondheim, Norway, p. 2005.

[12] Lokshin, K.A., Zhao, Y., Mao, W.L., Mao, H., Hemley, R.J., Lobanov, M.V., Greenblatt, M., **2005b**. Fifth International Conference on Gas Hydrates, Trondheim, Norway, p. 5024.

[13] Koh, C. A., **2002**. Towards a fundamental understanding of natural gas hydrates. Chemical Society Reviews *(31)*, 157-167.

[14] Mullin, J. W., **2001**. Crystallization, 4th edition. Butterworth-Heinemann, Oxford, U. K.

[15] Davidson, D.W., **1973**. Water: A Comprehensive Treatise, vol. 2 (F. Franks, ed.), Plenum Press, New York, 115-234.

[16] Conde, M. M., Vega, C., Tribello, G. A., Slater, B., **2009**. The phase diagram of water at negative pressures: Virtual ices. The Journal of Chemical Physics *(131)*, 034510.

[17] Falenty, A., Hansen, T. C., Kuhs, W. F., **2014**. Formation and properties of ice XVI obtained by emptying a type sII clathrate hydrate. Nature *(516)*, 231-233.

[18] Jeffrey, G.A. and McMullan, R.K., **1967**. Progress in Inorganic Chemistry, vol. 8 (F. A. Cotton, ed.), Wiley & Sons, Inc., 43-108.

[19] Jeffrey, G.A., **1984**. Inclusion Compounds (J.L. Atwood, J.E.D. Davies, D.D. MacNichol, eds.), Academic Press, 135.

[20] Davidson, D.W., **1971**. The Motion of Guest Molecules in Clathrate Hydrates. Canadian Journal of Chemistry *49* (8), 1224-1242.

[21] Ripmeester, J.A., Ratcliffe, C.I., Tse, J.S., **1988**. The nuclear magnetic resonance of ^{129}Xe trapped in clathrates and some other solids. Journal of the Chemical Society, Faraday Transactions 1 *(84)*, 3731-3745.

[22] Udachin, K.A., Ratcliffe, C.I., Ripmeester, J.A., **2002**. Fourth International Conference on Gas Hydrates, Yokohama, Japan, p. 604.

[23] Tse, J.S., **1987**. Thermal expansion of the clathrate hydrates of ethylene oxide and tetrahydrofuran. Journal De Physique *(48)*, 543-549.

[24] Kini, R.A., Huo, Z., Jager, M.D., Bollavaram, P., Ballad, A.L., Dec, S.F., Sloan, E.D., **2002**. Fourth International Conference on Gas Hydrates, Yokohama, Japan, p. 867.

[25] Ouar, H., Cha, S.B., Wildeman, T.R., Sloan, E.D., **1992**. The Formation of Natural-Gas Hydrates in Water-based Drilling-Fluids. Chemical Engineering Research & Design (Trans IChemE) *(70A)*, 48.

[26] Arjmandi, M., Tohidi, B., Danesh, A., Todd, A. C., **2005**. Is subcooling the right driving force for testing low-dosage hydrate inhibitors? Chemical Engineering Science *(60)*, 1313-1321.

[27] Miers, H. A. and Isaac, F., **1907**. The spontaneous crystallization of binary mixtures. Proceedings of the Royal Society *(A79)*, 322-351.

[28] Lederhos, J.P., Long, J.P., Sum, A., Christiansen, R.L., Sloan, E.D., **1996**. Effective kinetic inhibitors for natural gas hydrates. Chemical Engineering Science *(51)*, 1221.

[29] Pruppacher, H. R., **1994**. A new look at homogeneous ice nucleation in supercooled water drops. Journal of the Atmospheric Sciences *52* (11), 1924-1933.

[30] Kashchiev, D. and Firoozabadi, A., **2002**. Nucleation of gas hydrates. Journal of Crystal Growth *243* (3), 476-489.

[31] Sear, R. P., **2007**. Nucleation at contact lines where fluid–fluid interfaces meet solid surfaces, Journal of Physics: Condensed Matter *(19)*, 466106.

[32] Takeya, S., Hori, A., Hondoh, T., Uchida, T., **2000**. Freezing-memory effect of water on nucleation of CO_2 hydrate crystals. J. Phys. Chem. B, *104* (17), 4164-4168.

[33] Ohmura, R., Ogawa, M., Yasuoka, K., Mori, Y.J., **2003**. Statistical study of clathrate–hydrate nucleation in a water/hydrochlorofluorocarbon system: search for the nature of the "memory effect". The Journal of Physical Chemistry B *(107)*, 5289-5293.

[34] Buchanan, P., Soper, A.K., Westacott, R.E., Creek, J.L., Koh, C.A., **2005**. Search for memory effects in methane hydrate: structure of water before hydrate formation and after hydrate decomposition. The Journal of Chemical Physics *123* (16), 164507.

[35] Rodger, M., **2000**.Gas Hydrates: Challenges for the Future. Annals of the New York Academy of Sciences *(912)*, 474.

[36] Englezos, P., Kalogerakis, N., Dholabhai, P.D., Bishnoi, P.R., **1987a**. Kinetics of formation of methane and ethane gas hydrates. Chemical Engineering Science *42* (11), 2647-2658.

[37] Englezos, P., Kalogerakis, N., Dholabhai, P.D., Bishnoi, P.R., **1987b**. Kinetics of Gas Hydrate Formation from Mixtures of Methane and Ethane. Chemical Engineering Science *42* (11), 2659-2666.

[38] Skovborg, P., Rasmussen, P., **1994**. A mass transport limited model for the growth of methane and ethane gas hydrates. Chemical Engineering Science *(49)*, 1131-1143.

[39] Elwell, D. and Scheel, H.J., **1975**. Crystal Growth from High Temperature Solutions. Academic Press, London (Chapters 4 - 6), p. 273.

[40] Udachin, K.A., Ratcliffe, C.I., Ripmeester, J.A., **2002**. Single Crystal Diffraction Studies of Structure I, II and H Hydrates: Structure, Cage Occupancy and Composition. Journal of Supramolecular Chemistry *(2)*, 405-408.

[41] Freer, E., Selim, M.S., Sloan, E.D., **2001**. Methane hydrate film growth kinetics. Fluid Phase Equilibria *185* (1-2), 65-75.

[42] Taylor, C.J., Miller, K. T., Koh, C. A., Sloan Jr., E. D., **2006**. Macroscopic investigation of hydrate film growth at the hydrocarbon / water interface. Chemical Engineering Science *(62)*, 6524-6533.

[43] Makogon, Y., Makogan, T., Holditch, S., **1998**. Japan National Oil Conference,Tokyo, p.259.

[44] Tohidi, B., Dancsh, A., Todd, A.C., Burgass, R.W.,**1997**. Hydrate-free zone for synthetic and real reservoir fluids in the presence of saline water. Chemical Engineering Science *(52)*, 3257-3263.

[45] Du, J., Liang, D., Li, D., **2010**. Experimental Determination of the Equilibrium Conditions of Binary Gas Hydrates of Cyclopentane plus Oxygen, Cyclopentane plus Nitrogen, and Cyclopentane plus Hydrogen. Industrial & Engineering Chemistry Research *49* (22), 11797-11800.

[46] Mohammadi, A. H. and Richon, D., **2011**. Phase equilibria of binary clathrate hydrates of nitrogen + cyclopentane/cyclohexane/methyl cyclohexane and ethane + cyclopentane/cyclohexane/methyl cyclohexane. Chemical Engineering Science *(66)*, 4936-4940.

[47] Galfre, A., **2014**. Captage du CO_2 par cristallisation de clathrate hydrate en présence de cyclopentane : étude thermodynamique et cinétique. M. Sc. Thesis, Ecole Nationale Supérieur des Mines, Saint Etienne.

[48] Fan, S. S., Liang D. Q., Guo, K. H., **2001**. Hydrate Equilibrium Conditions for Cyclopentane and a Quarternary Cyclopentane-Rich Mixture. Journal of Chemical & Engineering Data *(46)*, 930-932.

[49] Cha, M., Shin, K., Kim, J., Chang, D., Seo, Y., Lee, H., Kang, S. P., **2013**. Thermodynamic and kinetic hydrate inhibition performance of aqueous ethylene glycol solutions for natural gas. Chemical Engineering Science *(99)*, 184-190.

[50] Zerpa, L. E., Salager, J. L., Koh, C. A., Sloan, E. D., Sum, A. K., **2011**. Surface Chemistry and Gas Hydrates in Flow Assurance. Industrial Engineering Chemistry Research *50* (1), 188-197.

[51] Kelland, M. A., **2006**. History of the Development of Low Dosage Hydrate Inhibitors. Energy Fuels *20* (3), 825-847.

[52] Azarinezhad-Mohammadi, R., **2010**. A chemical based wet cold flow approach for addressing hydrate flow assurance problems. M. Sc. Thesis, Heriot-Watt University; Institute of Petroleum Engineering.

[53] Haghighi, H., Chapoy, A., Burgess, R., Mazloum, S., Tohidi, B., **2009**. Phase Equilibria for Petroleum Reservoir Fluids Containing Water and Aqueous Methanol Solutions: Experimental Measurements and Modelling Using the CPA Equation of State. Fluid Phase Equilibria *(278)*, 109-116.

[54] Haghighi, H., Chapoy, A.,Tohidi, B., **2009**. Experimental and Thermodynamic Modelling of Systems Containing Water and Ethylene-glycol: Application to Flow Assurance and Gas Processing. Fluid Phase Equilibria *(276)*, 24-30.

[55] Kuliev A. M. et al., **1972**. Surfactants Studies as Hydrate-Formation Inhibitors. Gazov. Delo. *(10)*, 17-19.

[56] Peytavy, J. L., Glenat, P., Bourg, P., **2008**. Qualification of Low Dose Hydarte Inhibitors (LDHIs): Field Cases Studies Demonstrate the Good Reproducibility of the Results Obtained from Flow Loops. 6th International Conference on Gas Hydrates (ICGH), Vancouver, British Columbia, Canada.

[57] Perrin, A., Musa, O. M., Steed, J. W., **2013**. The chemistry of low dosage clathrate hydrate inhibitors. The Chemical Society Review *(42)*, 1996-2015.

[58] Frostman, L. M., **2000**. Anti-Agglomerant Hydrate Inhibitors for Prevention of Hydrate Plugs in Deepwater Systems. SPE Annual Technical Conference and Exhibition, Dallas, Texas.

[59] Zeng, H., Moudrakovski, I. L., Ripmeester, J. A., **2006**. Effect of Antifreeze Protein on Nucleation, Growth and Memory of Gas Hydrates. AIChE Journal *52* (9), 3304-3309.

[60] Celik, Y., Graham, L. A., Mok, Y. F., Bar, M., Davies, P. L., Braslavsky, I., **2010**. Superheating of ice crystals in antifreeze protein solutions. Proceedings of the National Academy of Sciences *(107)*, 5423-5428.

[61] Celik, Y., Drori, R., Pertaya-Braun, N., Altan, A., Barton, T., Bar-Dolev, M., Groisman, A., Davies, P. L., Braslavsky, I., **2013**. Microfluidic experiments reveal that antifreeze proteins bound to ice crystals suffice to prevent their growth. Proceedings of the National Academy of Sciences *(110)*, 1309-1314.

[62] Tabeling, P., **2003**. Introduction à la microfluidique. Editions Belin (Collection Echelles), Paris.

[63] Whitesides, G. M., **2006**. The origins and the future of microfluidics. Nature *(442)*, 368-373.

[64] Alarishi, B. and Bach, C., **2014**. The Future of Laboratory Work Lab-On-Chip Device: An Overview. International Journal of Innovation and Applied Studies *6* (2), 187-191.

[65] Harrison, D. J., Manz, A., Fan, Z., Ludi, H., Widmer, H. M., **1992**. Capillary electrophoresis and sample injection systems integrated on a planar glass chip. Analytical Chemistry *(64)*, 1926-1932.

[66] Feynman, Richard P., **1960**. There's Plenty of Room at the Bottom. Engineering and Science *23* (5), 22-36.

[67] Nguyen, L. T. and Yang, K-L., **2014**. Uniform cross-linked cellulase aggregates prepared in millifluidic reactors. Journal of Colloid and Interface Science *(428)*, 146-151.

[68] Microfluidic Applications Market **2013** Report. Yole Développement S.A.

[69] Wang, W. S. and Vanapalli, S. A., **2014**. Millifluidics as a simple tool to optimize droplet networks: Case study on drop traffic in a bifurcated loop. Biomicrofluidics *(8)*, 064111.

[70] Leng, J. and Salmon, J-B., Lab Chip, **2009**. Microfluidic crystallization. Lab on a Chip *(9)*, 24-34.

II. CHARACTERIZATION TECHNIQUES

CHAPTER 2

OPTICAL MICROSCOPY

2.1. Introduction

A big part of this work requires the knowledge of some specific optical techniques that allow a fine observation of transparent samples (hydrates). These techniques cannot be understood without knowing the fundamentals of microscopy. This is why a review of the optical phenomena that have a relationship with the optical techniques we use here is first presented. Then some fundamentals about optical microscopy are introduced, such as magnification or resolution (they are the most important parameters to take into account). In the following section we present the different imaging and contrast generation modes that allow us to observe transparent samples (hydrates). Those used in the performance of our experiments are: bright and dark field imaging mode, differential interference contrast (DIC), fluorescence and confocal reflectance microscopy. This chapter ends with the introduction of

a technique that allows us to study thin films (thickness, roughness, etc.) of inhibitors deposited on hydrophilic surfaces (in our case). This is the so-called ellipsometry method.

2.2. Optical phenomena contributing to image quality and contrast

The operation mode of a microscope depends on several geometrical and wave optics considerations that are going to be introduced below. We will discuss briefly factors of each kind of optics influencing the final quality of the images obtained.

2.2.1. Geometrical optics

Light is one of the electromagnetic energy ways present in nature and interacts with matter in many different ways. When radiation is incident at the boundary between two media (diopter) with different refractive indexes n_1 and n_2, energy is reflected, transmitted (or refracted) and/or scattered.

Geometrical optics teaches that two types of reflection can take place: specular and diffuse. In both types of reflection, a part of the radiant flux is reemitted without any variation in the wavelength after striking a surface. If the diopter is flat a specular reflection is produced (Figure 2.1a), i.e. a single incident beam produces a unique reflected beam and the incident angle θ_1 between the normal and the incident beam is equal to the reflection angle between the normal and the reflected beam (Snell-Descartes law). In the case of specular reflection, the incident beam, the reflected rays and the normal of the diopter are placed in the same plane. On the other hand, if the diopter is not uniform and presents some irregularities diffuse reflection takes place and a unidirectional incident beam is deflected into many directions (Figure 2.1b) [1]. Diffusion takes place when the characteristic size l of the irregularities is higher than the wavelength λ of the incident beam. But if l is lower or similar to λ then diffraction can also occur and the wave aspects of light have to be taken into account, as we will see below.

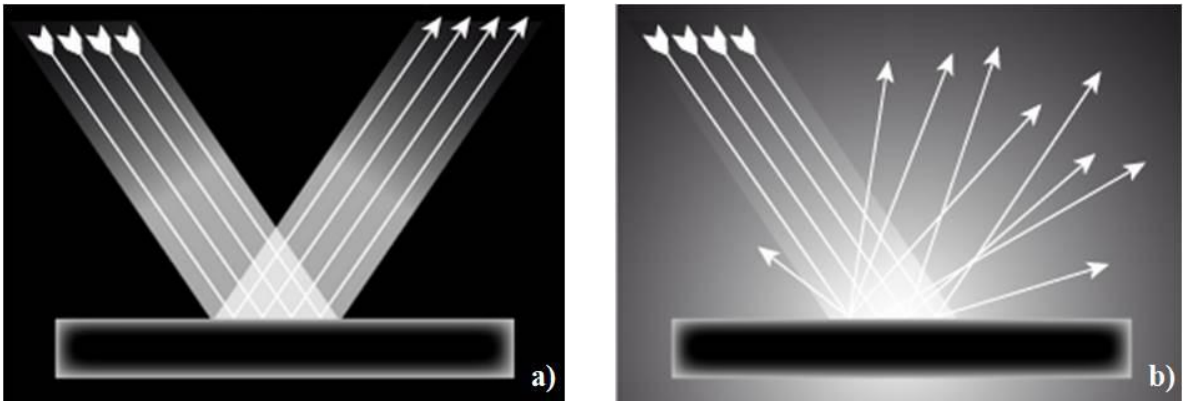

Figure 2. 1. a) Specular reflection: reflected rays and the normal of the diopter are in the same plane. b) Diffuse reflection: a unidirectional incident beam is deflected into many directions.

In the same way, transmission is observed when flat diopters are used. The transmitted beams follow the Snell's refraction law (Figure 2.2): $n_1 \cdot \sin \theta_1 = n_2 \cdot \sin \theta_2$. On the other hand, diffuse refraction is observed when diopters are rough.

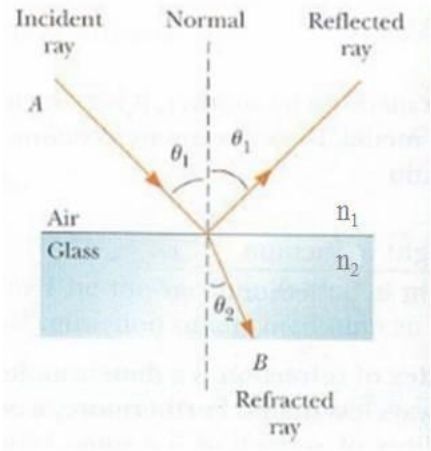

Figure 2. 2. Angles involved in the Snell's law.

The amount of reflected and transmitted light depends on the refractive indexes of the two media and on the incident angle: the more the difference between n_1 and n_2, the more the light is reflected (power). In the same way a bigger difference between n_1 and n_2 means a higher deviation of the refracted beam. For example, a gas bubble in water will be much more visible than an oil droplet in water because of the larger difference in the refractive index.

Microscopes enhance our sense of sight: they allow us to look directly at things that are far too small to view with the naked eye. For achieving the most important objective of a microscope, which is the possibility to resolve the small details of an object [2], some of the parameters that affect its performance have to be optimized. The most important ones are magnification and resolution.

This section is divided into two parts: magnification and optical aberrations. Both of them are very important for obtaining good quality images.

2.2.1.1. Magnification

Magnification is the property of a microscope of increasing the image size in relationship with the real size of an object. It is defined as the ratio between the distance from the objective to the object and the focal length (distance from the objective to the eyepiece). The higher this ratio the higher the magnification will be. Historically, the focal length was fixed (160 mm), and it was the distance between the object and the objective what was changed.

We can distinguish between simple and compound microscopes:

- *Simple microscopes* are composed by a short focal length lens or magnifier in order to obtain a virtual and upright image, higher than the object, which is placed inside the focus. The magnification in this type of microscopes is given by:

$$M = \frac{h_i}{h_0}$$

The purpose of a microscope is to increase the value of ß (Figure 2.3), in order to obtain a greater image:

$$tan\,ß = \frac{h_0}{u} = \frac{h_i}{D}$$

Considering a very small object, tan ß ~ ß so, rearranging:

$$\frac{h_i}{h_0} = \frac{D}{u}$$

$$M = \frac{D}{u}$$

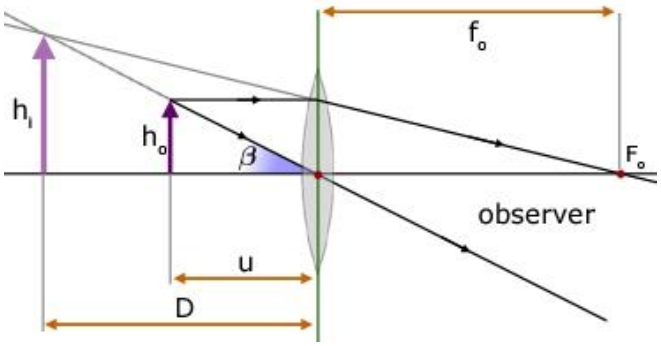

Figure 2. 3. Basic concepts of a simple microscope: there is a magnifier that produces a virtual and upright image (h_i), higher than the object (h_o), which is placed inside the focus.

When the power of the simple microscope is to be increased, the focal length must be reduced. For reducing the focal length, a reduction in the diameter of the lens is required. But the problem is that when the lens diameter gets smaller and smaller, it reaches a point where it becomes difficult to see through it, and the performance is affected by the aberrations. To solve this problem, the compound microscope was invented.

The compound microscope is composed by two (at least) or more lenses (see Figure 2.4). The lens nearest to the object is the objective and produces a real and inverted image (I_1) at a point inside the principal focus (f_e) of the other lens, called eyepiece. This real image serves as "object" for the eyepiece, which produces another image (I_2), larger than the previous one (magnified) but virtual, and visible to the eye of the observer. The eyepiece acts as a simple microscope and produces further magnification. The total magnification depends on the magnification of the objective and that of the eyepiece. The product of the eyepiece and the objective lens magnification is called magnifying power.

However, some disadvantages can be found in this microscope arrangement. First of all, the eye is not relaxed. It should focus to infinity instead of focusing on the near point. This makes the difference between finite and infinity optical systems, explained below. Another disadvantage is that changing the distance between the objective and the eyepiece can produce a change in magnification. Finally, these systems are not designed for including additional optical elements such as filter cubes or intermediate tubes into the optical pathway between the objective and the eyepiece without introducing spherical aberration. This would require focus corrections, apart from creating other image problems.

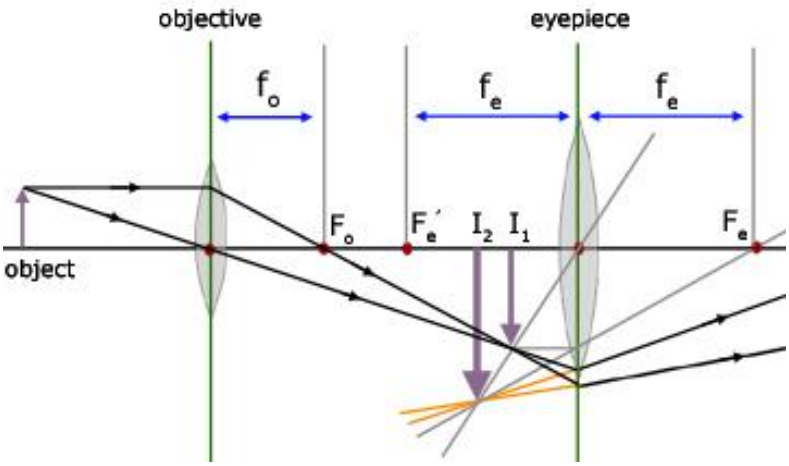

Figure 2. 4. Basic concepts of a compound microscope: the objective produces a real and inverted image (I_1) at a point inside the principal focus (f_e) of the eyepiece. This real image serves as "object" for the eyepiece, which produces another image (I_2), larger than the previous one (magnified) but virtual, and visible to the eye of the observer.

In a fixed tube length finite optical system, light passes through the objective and converges in the intermediate image plane (located at the front focal plane of the eyepiece) in order to produce an image. "Finite" means that the focal plane is fixed. The image is formed by the objective lens itself. On the other hand, in infinity optical systems, another lens (tube lens) is added between the objective and the eyepiece (Figure 2.5). The light beam becomes parallel after passing through the first lens (objective) and is projected at the infinity along the optical axis of the microscope towards the tube lens. All the light is then focused at the intermediate image plane producing a real image with a magnification given by next equation, and finally enlarged by the eyepiece.

$$M = \frac{f_{tube}}{f_{objective}}$$

As the light beam between the objective and the tube lens is parallel, in theory the distance can be extended flexibly, and that is why the word "infinity" is used. The benefit of using this kind of system is that additional optical elements like vertical illuminators, DIC prisms, polarizers, retardation plates, etc., can be introduced. Also, the magnification can be increased as it depends on the tube length, around 160 mm for finite optical systems and between 160 and 200 mm for infinity ones (depending on the company).

These days nearly all observation is done by electric cameras (CCD, CMOS…). The camera does not have its own objective. The detector chip is placed at the focus of the tube lens.

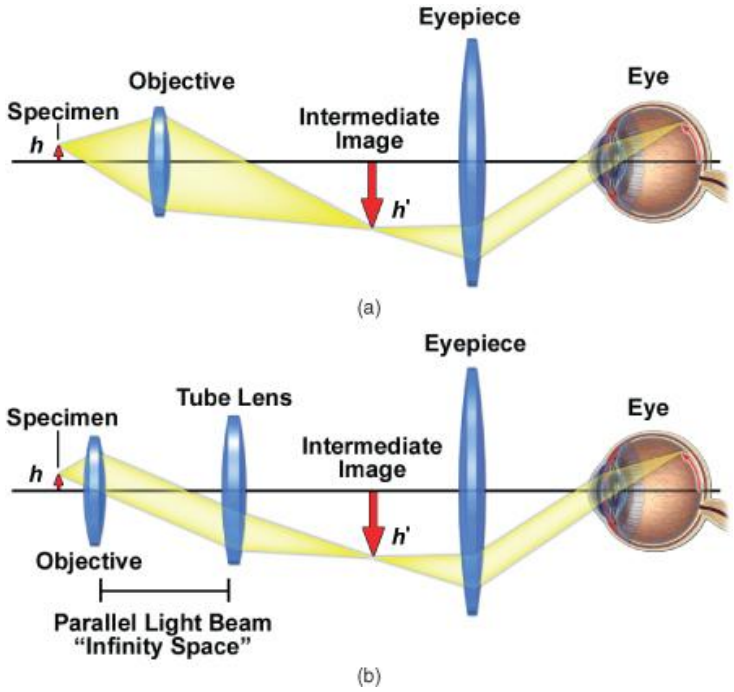

Figure 2. 5. Principle of finite optical systems (upper): the focal plane is fixed and the image is formed by the objective lens itself, and infinite optical systems (lower): the light beam becomes parallel after passing through the objective and is projected at the infinity along the optical axis of the microscope towards the tube lens [2].

2.2.1.2. Optical aberrations

Optical aberrations are caused by artifacts that appear from the interaction of light with glass lenses or with thick samples [3]. Depending on the lens quality these aberrations can be reduced or not, but note that these errors are always there, and result in an inability of delivering perfect imaging. They can be introduced by the sample, if it is very thick or curved [1], [2], [3]. There are two principal causes of aberration: geometrical or spherical aberrations, related to the spherical nature of the lens and chromatic aberrations that appear due to the variations in the refractive indices of the wide range of frequencies found in the visible light:

- ***Spherical aberration*** occurs because light waves that pass through the periphery of the lens are refracted to a greater degree than the ones that pass near the center (Figure 2.6). This generates different focal points along the optical axis, meaning that there is not a well-

defined image plane. For an extended object not the whole image is sharp, being the periphery the most blurred parts.

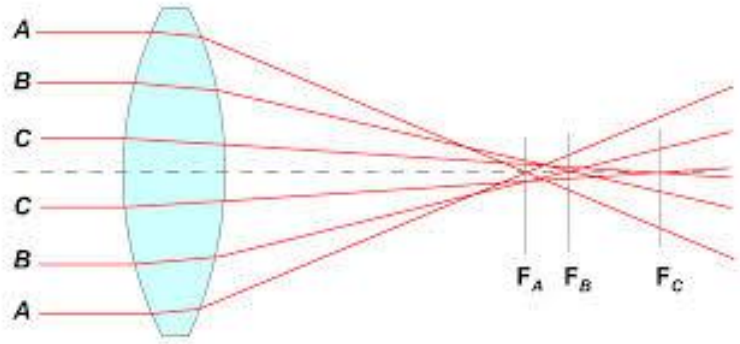

Figure 2. 6. Schematics of the spherical aberration: light waves that pass through the periphery of the lens are more refracted than those that pass near the center. The image is distorted.

- ***Geometrical aberrations*** include a variety of effects:

- Astigmatism and comatic aberrations are very similar. They are off-axis aberrations and appear when rays from an object point pass through the vertical and horizontal diameter of a lens and are focused as a short streak at two different focal planes (Figure 2.7). This streak appears as elliptical, elongated spots for the horizontal and the vertical directions at both sides of the best focus, where the focused image of a point appears as an extended circular patch. Astigmatism is also caused by asymmetric lens curvature due to mistakes in the fabrication.

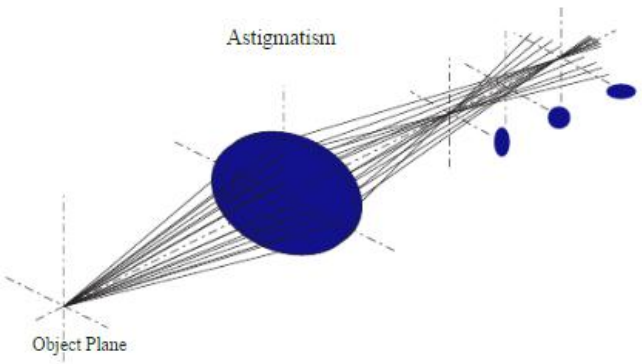

Figure 2. 7. Schematics of the astigmatism aberration [1]: the rays from an object point pass through the vertical and horizontal diameter of a lens and are focused as a short streak at two different focal planes, producing circular patches.

- Curvature of field is and off-axis aberration and is the natural result of using lenses that have curved surfaces. When visible light is focused through a curved lens, the image plane produced by the lens will be curved. As a result, different zones of the image can be brought into focus, but the whole image cannot be focused simultaneously on a flat surface (Figure 2.8).

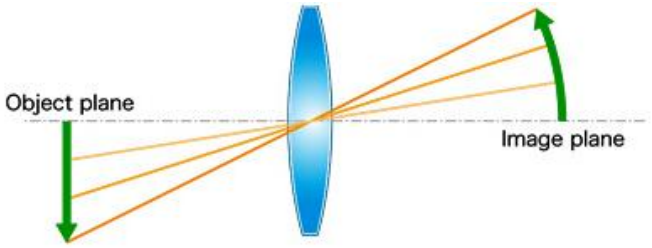

Figure 2. 8. Schematics of the curvature of field aberration: when visible light is focused through a curved lens, the image plane produced by the lens will be curved.

- Geometric distortion is an aberration that causes the focus position of the object image to shift laterally in the image plane (Figure 2.9). The consequence is a radial variation of magnification that will image a square as a pincushion or barrel.

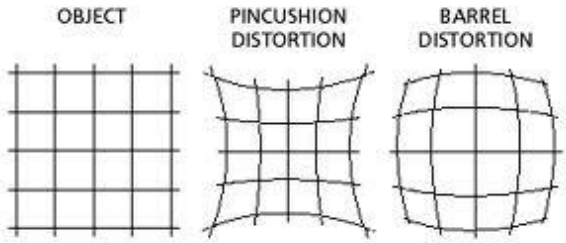

Figure 2. 9. Schematics of the geometric distortion aberration: the focus position of an object image is shifted laterally in the image plane.

- ***Chromatic aberration*** is due to the dispersion of light of the optical materials used for fabricating lenses. White light is composed of different wavelengths. When a beam of white light passes through a lens with a refractive index, all the different wavelengths are refracted differently, according to their frequencies. That is why blue wavelengths are focused in an image plane closer to the lens than the image plane for red wavelengths. The inability of

lenses to bring all the colors into a common focus results in a slightly different image size and focal point for each predominant wavelength group. Even at the best focus, point sources are surrounded by color halos. We can distinguish between the transverse (lateral) and the axial (longitudinal) chromatic aberration. The first one is an off-axis imaging of colors at different locations of the image plane (Figure 2.10a), whereas the second appears because some wavelengths are focused at different distances behind the optical system (Figure 2.10b).

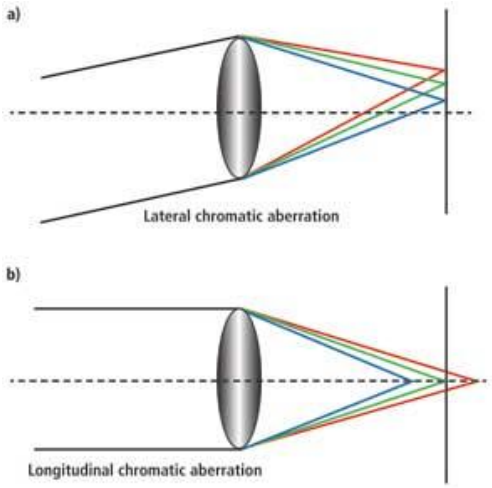

Figure 2. 10. Schematics of a) lateral chromatic aberration, which results in different frequencies of light being in focus along different points in the optical axis and b) longitudinal chromatic aberration, which results in different frequencies of light being in focus at different points along the optical axis [4].

Almost all the aberrations produced by lenses are corrected in microscopes of high quality but they are still present due to the sample thickness because:

- Most of the objectives of a microscope are made for observing the surface of an object assuming there is air between the objective and the surface of the object. A lot of times this is not the case (for instance, there may be a glass wall in between, as we will see below) and the objective has to be corrected in order to avoid the aberration.

- If we focus the incident beam on a transparent sample the peripheral rays are refracted in a different way depending on the distance to the axis (Figure 2.11). This happens when we look through something with an important transparent thickness. The two main consequences of aberration at planar sample interfaces are:

(i) Axial smearing of the focal point, resulting in loss of resolution and contrast.

(ii) The approximate focal point is deeper in the sample than deduced from the depth scaleof the microscope: $z_{real} = n_{sample} \cdot x \cdot z_{apparent}$

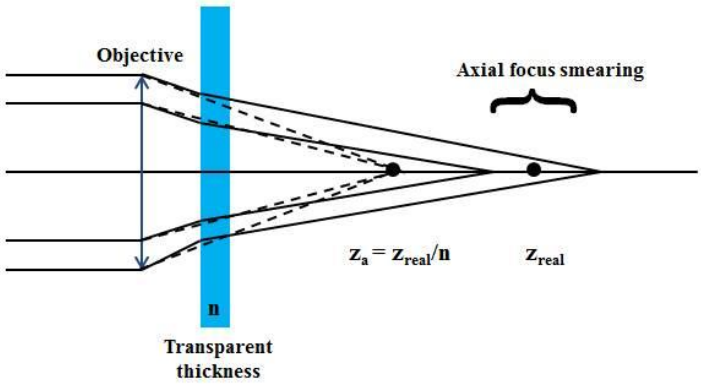

Figure 2. 11. Schematics of the aberration produced when light traverses a transparent thickness.

2.2.2. Wave optics

Apart from the phenomena that can happen to light when it is incident on a surface, i.e. geometrical optics, there are some other factors that can affect the images quality and which are related to the wave nature of the light. They are going to be discussed below.

2.2.2.1. Diffraction of light

The process of diffraction involves the spreading of light waves when they pass through apertures or around screens. The effect is strong if the size of the diffracting object is comparable to the wavelength. Thus, the image of an object self-luminous point obtained with a microscope is not a point but an intricate diffraction pattern of a bright central spot and concentric bright rings, formed by the interference of the waves diffracted by the objective aperture (Abbe's theory). This diffraction pattern is referred to as an Airy disk. When this pattern is magnified, it results in a central bright spot or diffraction disk containing ~84% of the light from the source, surrounded by a series of concentric diffraction rings with gradually decreasing intensities (Figure 2.12 upper a). Diffraction needs to be taken into account when we talk about ***resolution***. Resolution is limited by both geometrical (size of the camera pixels: points projected into the same pixel will not be resolved) and wave optics factors. Microscope

resolution *s* is the shortest distance between two separate points in a microscope's field view that can be distinguished as individual entities. Rayleigh criterion states that two points are resolved when the maximum of diffraction of one point coincides at least with the first minimum of a second point (Figure 2.12 lower b).

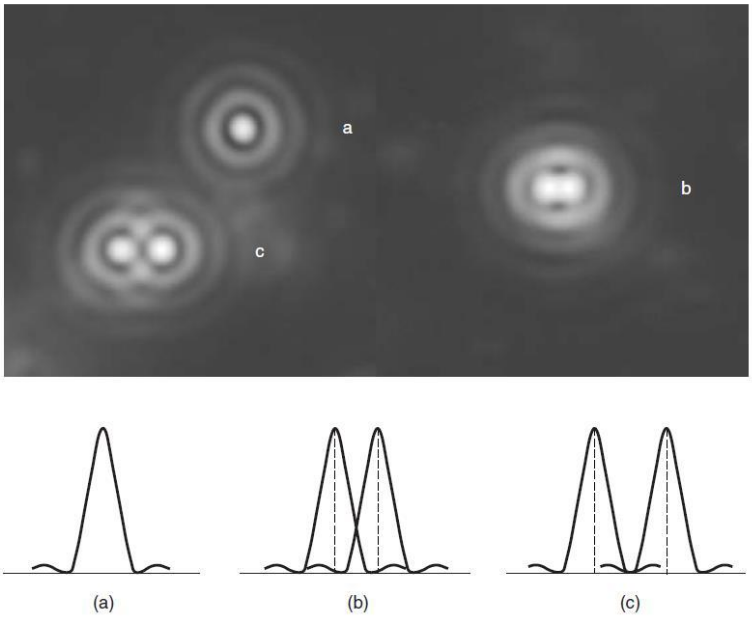

Figure 2. 12. Upper: Diffraction of light through a circular pupil. Lower: Rayleigh criterion. Diffraction patterns of a) a single source, b) two sources hardly separated and c) two sources well separated.

The size of the central spot in the Airy pattern is related to the wavelength of light and the aperture angle of the objective, described by the numerical aperture (NA). In terms of resolution, the radius of the diffraction Airy disk in the lateral (x,y) image plane is defined by the following formula:

$$Abbe\ resolution_{x,y} = \frac{\lambda}{2 \cdot NA}$$

The numerical aperture of an objective lens is defined as the ability of the lens to gather light and resolve a point at a fixed distance from the lens. The aperture diaphragm of the optical system determines the angle at which rays emerge from the axial object point and, after refraction, pass through the optical system. NA is defined as follows:

$$NA = n \cdot \sin \theta$$

where *n* is the refractive index between the object and the optical system and θ the aperture angle, i.e. the half angle over which the objective can gather light from the specimen. The higher the refractive index the greater NA and more light will be gathered (refraction angles at the interfaces will be reduced) (Figure 2.13). This results in a better resolution. Water or immersion oil are media with higher refractive index (see Table 2.1) than that of the air, and are the most used ones for optical systems. Our system contains inspection windows to see through, so long working distance objectives were needed, but it was not possible to immerse them in any liquid in order to improve the NA because of the low temperatures needed to perform the experiments, and the condensation produced.

Media	Refractive Index
Air	1
Water	1.33
Oil	1.45 - 1.6 (1.515 is typical)

Table 2. 1. Refractive indices for different media.

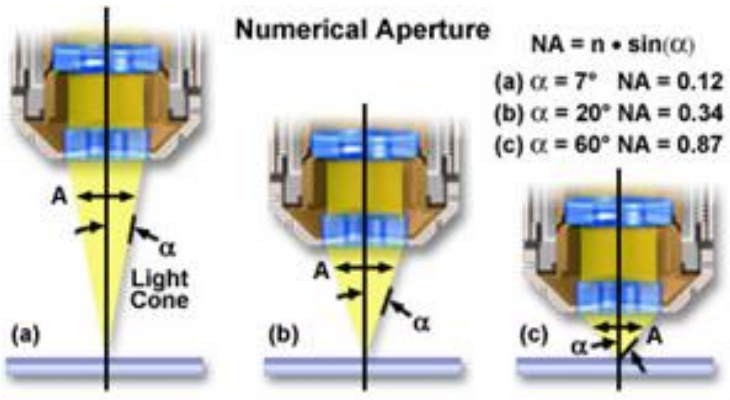

Figure 2. 13. Influence of the working distance (aperture angle α) on the numerical aperture NA [5].

2.2.2.2. Polarization of light

It is well known that sunlight and other natural and artificial illumination forms produce non-polarized light, thus, light waves whose electric field vectors *E* vibrate in all planes that are perpendicular to the direction of propagation. If the electric field vectors are restricted to a unique plane by filtration of the beam, then linearly polarized light is obtained. The *E* vector is always orthogonal to the direction of light wave propagation (z), and can be described by two harmonic oscillations along *x* and *y*. These oscillations have the same frequency, but generally different amplitude and phase. As a result, at a fixed point in the space the *E* vector moves along an ellipse in a planes perpendicular to the direction of light wave propagation. Elliptically polarized light is a state between linear and non-polarized light and the most general state of polarization. If the phase of *x* and *y* oscillation is equal, the resulting ellipse degenerates into a straight line. If the phase difference is +/- 90° the ellipse becomes a circle. Thus, the linear and the circular polarizations are limiting cases of the general elliptical state.

2.2.2.3. Interference of light

Several phenomena in this thesis depend on interference of reflected light waves. In general, reflection itself depends on light polarization and on the incident angle of the light beam.

The process of interference describes the recombination and summation of two or more superimposed wavefronts [6], [7]. Interference of light plays an important role in all aspects of image formation. The conditions for two waves to interfere in one point are: 1) both waves have to be monochromatic, i.e. they must have the same wavelength and 2) they have to be coherent, i.e. the must be in constant phase.

We frequently observed interference fringes due to interferences between waves reflected off close, nearly parallel interfaces. The amplitude of the reflected waves depends in general on the polarization and angle of incidence. Although illumination under the microscope, particularly in confocal microscopy, involves a spread of incidence angles, a simple theory based on the assumption of normal incidence (vanishing angle of incidence) works remarkably well for deducing the thickness of thin films.

Under illumination the image of a non-opaque object results from light reflected at interfaces between media of different refractive indices *n*. The Fresnel reflection coefficient (r) at the boundary between media with refractive indices n_1 and n_2 (Figure 2.14) for an incident beam normal to the surface is:

Eq. 2. 1. $$r_{12} = \frac{n_1 - n_2}{n_1 + n_2}$$

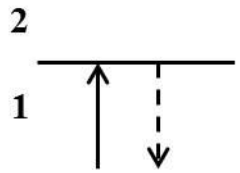

Figure 2. 14. Reflection of a wave at a boundary interface.

In general, the reflection coefficient for waves that are polarized in the plane of incidence (90°) vanishes at a particular angle, i.e. Brewster angle (see ellipsometry section). The intensity of the reflected beam (I_r) is proportional to $I_i \cdot r^2$, being I_i the intensity of the incident beam and r the amplitude of the reflected wave. Note that in Equation 2.1, for $n_1 < n_2$ (e.g., air/glass), $r_{12} < 0$, meaning the wave undergoes a π phase change, equivalent to a $\lambda/2$ path difference.

Reflection occurs in every interface between media of different refractive index. In Figure 2.15 we analyze the reflections that take place in our system and how they interfere. A beam of monochromatic light (λ = 532 nm) strikes a glass surface. This light beam finds in its way two interfaces: 1) glass (n_G = 1.52) / water (n_w = 1.33) and 2) water/cyclopentane (n_{CP} = 1.41).

The incident light beam first finds a glass/water interface. As the refraction index of water is lower than that of glass, the reflected wave 1 does not suffer any change in its phase when it is reflected. The refracted part of the incident beam continues its way through the water to finally find a new interface water/CP (CP has a higher refraction index than that of the water). The emergent wave 2 suffers two reflections of different nature.

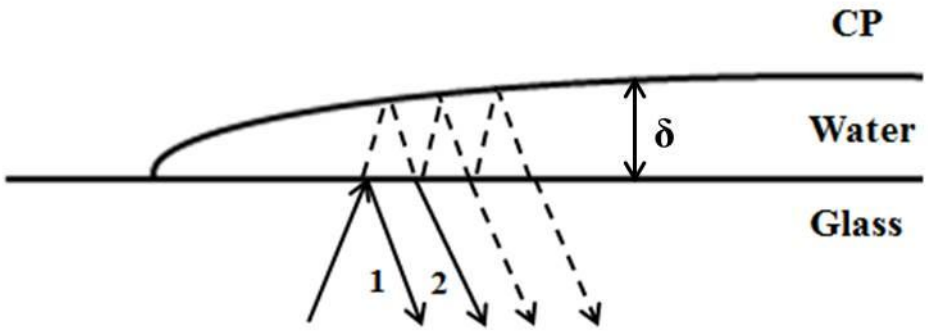

Figure 2. 15. Reflections that take place in our system after the incident light beam strikes the two interfaces present. The reflected ray 1 suffers a reflection of one type: glass/water, whereas the reflected ray 2 is the result of two different reflections: glass/water and water/CP.

The optical path difference $\Delta\delta$ is given by $\Delta = 2 \cdot n_m \cdot d \cdot \cos\theta$, where n_m is the refractive index of the medium, d is the distance between the interfaces and θ is the angle of refraction in the medium. When $\Delta\delta = N \cdot \lambda$, a dark fringe will be produced whereas there will be a bright one when $\Delta\delta = (N + ½) \cdot \lambda$. With monochromatic incident light these interferences result in bright and dark zones compared to the background. This can give us information about the sample thickness because the distance δ between two dark or bright fringes is related to it. Depending on the order of the refractive indices, there may be 0, 1 or 2 reflections off a more refractive medium. In that case, $\lambda/2$ has to be added to the path length, before deciding if the zeroth fringe (where the thickness vanishes) is to be expected bright or dark.

2.3. Contrast generation and imaging modes

What makes a specimen visible in optical microscopy is the difference in intensity and/or color. This creates image contrast. As a general rule best contrast is obtained in methods which provide a small signal on a theoretical vanishing background. Contrast is the difference in light intensity between the image and adjacent background relative to the overall background intensity. The generation of a good contrast is essential in microscopy, not only for making objects visible but also for observing and measuring individual details, characteristics or just a specific part of a specimen. However, there are a lot of unstained objects for which the images generate very little contrast and then they remain almost invisible, regardless of the ability of the objective to resolve details. This is why some

different contrast enhancing techniques have been developed. In this section just the techniques that have been used in this work are explained.

2.3.1. Bright field

It is the most elementary form of microscope illumination techniques. It receives this name because the specimen is dark and contrasted by the surrounding bright viewing field. In transmission bright field microscopy image contrast appears due to the absorption of amplitude (naturally colored or stained), reflecting and diffuse (fibers, hairs, etc.) specimens.

2.3.2. Dark field

In bright field microscopy all the rays are gathered by the objective lens and contribute to image formation. Both the diffused (rays that interact with the specimen) and the non-diffused incident rays (the ones that do not interact with the object and pass non-deviated through or around the specimen) take part in image formation.

In order to remove the non-deviated rays and obtain much more contrasted images an annular diaphragm is placed in the condenser. The cone shaped sheet of light (Figure 2.16) produced has such an opening that the non-deviated rays by the object are expelled around the objective. The only rays received by the objective are those diffused by the object. As a result the specimen appears as brightly illuminated on a dark background, which is different from what we observe in bright field mode (Figure 2.17) [1], [5].

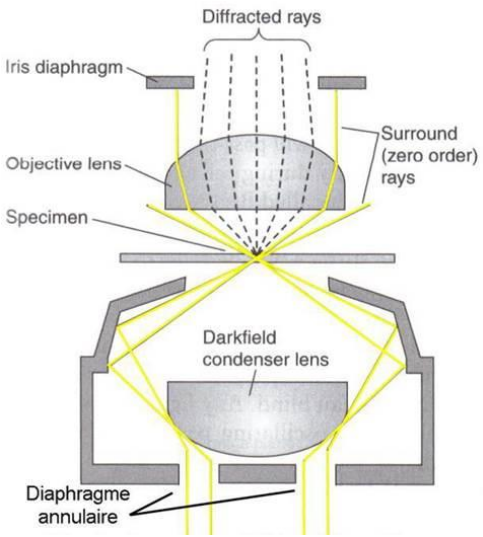

Figure 2. 16. Principle of the dark field mode: the non-deviated rays by the object are expelled around the objective. The only rays received by the objective are those diffused by the object.

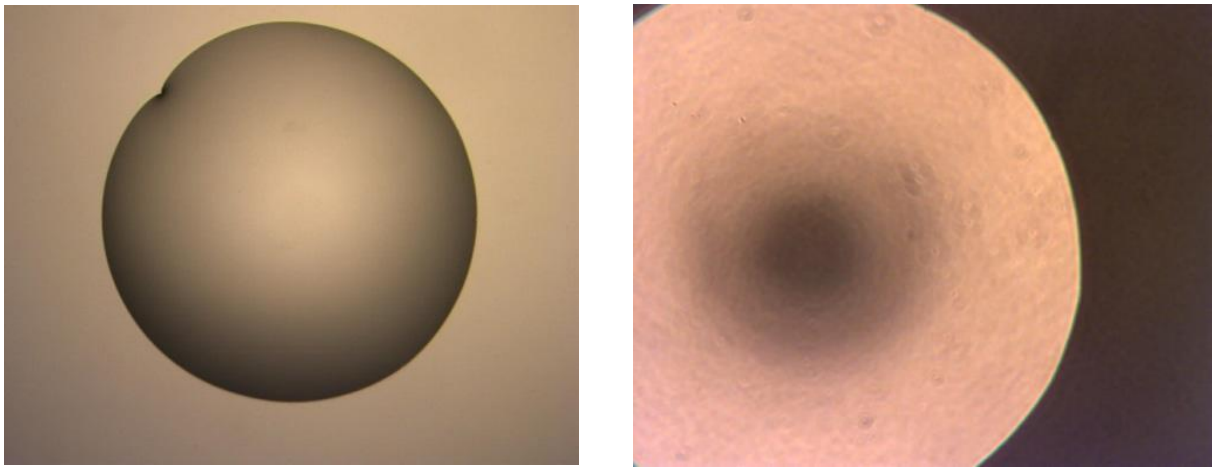

Figure 2. 17. Left: a water drop viewed in bright field mode. Right: a water drop viewed in dark field mode.

2.3.3. Differential interference contrast (DIC or Nomarski phase contrast)

There exist a lot of unstained specimens that are invisible to the eye because they do not absorb light but alter the phase of the diffracted light (phase objects). Therefore, many different contrast methods have been developed in order to see such phase objects. These methods use a local variation of the refractive index or thickness (or both) of the specimen to generate some contrast, very difficult otherwise. The result is that the details of the image appear lighter against a darker background. One of these methods, widely used is differential interference contrast (DIC).

DIC uses two Wollaston prisms in its most used and simple design (Figure 2.18) [13]. After passing through a polarizer 45° inclined with respect to the Wollaston, light enters the first Wollaston prism, which splits the light beam into two of equal intensity. These two beams have their own polarization directions that are perpendicular between them and travel nearly parallel to each other. The distance between both rays is called shear and is very small (less than the resolving ability of the objective). Then both beams interact with the specimen and their wave paths are altered depending on its varying thickness, refractive indices or slopes. When the two beams get out the objective they are recombined by the second Wollaston (inverted) prism.

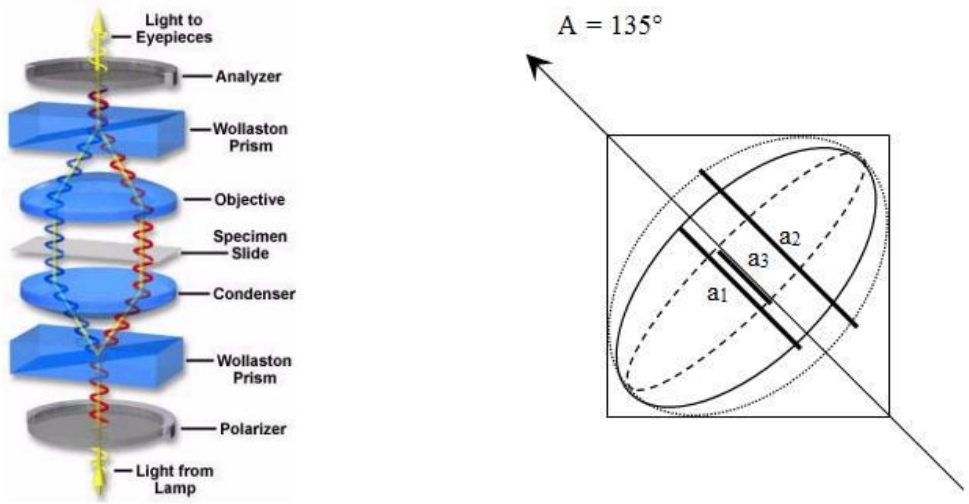

Figure 2. 18. Principle of a DIC imaging mode. Left: experimental setup. Right: the different elliptic forms obtained for various local phase shifts in the specimen and the corresponding amplitudes measured by the analyzer. In the figure, a_1 is the amplitude with no phase shift, a_2 when the phase shift is positive and a_3 when the phase shift is negative.

If the specimen did not introduce any path difference, the beam recombined by the second Wollaston is the same as the beam who was split by the first Wollaston, i.e. it is linearly polarized at 45°. On the other hand, if the specimen presents some refractive index or thickness gradient, the recombined beam is no more linearly polarized but elliptic.

An analyzer is placed after the second Wollaston prism and perpendicular to the polarizer in order to stop the zero path beams and to bring vibrations of the elliptic beams into the same axis so that they can interfere (they have been vibrating perpendicular to each other and could not produce interference). The problem with this setup is that it is not possible to differentiate positive from negative phase shifts. To resolve this problem, a positive phase shift is imposed to the system (e.g., by rotating one of the Wollaston) in order to produce an elliptic vibration even in absence of phase shifts in the specimen. Then, depending on the sign of the phase shift (that depends on the sign of the refractive index gradient) induced by the specimen, both the ellipse and the amplitude (given by the projection of the ellipse on the analyzer direction) will be more or less pronounced. Therefore, the resulting intensity will be brighter or less bright than in the cases where the gradient is null (Figure 2.18 right). The light passes then through the eyepiece to be observed as differences in intensity. One side of the detail appears bright (positive gradient of the refractive indexes or increasing thickness) whereas the other is darker (negative gradient of the wave path). This effect allows detecting

the shapes of the objects very precisely and gives the specimen a three-dimensional appearance (Figure 2.19).

Overall DIC images show bright features on a dark background, wherever there is a gradient of the optical path (gradient of refractive index or variation of the sample thickness).

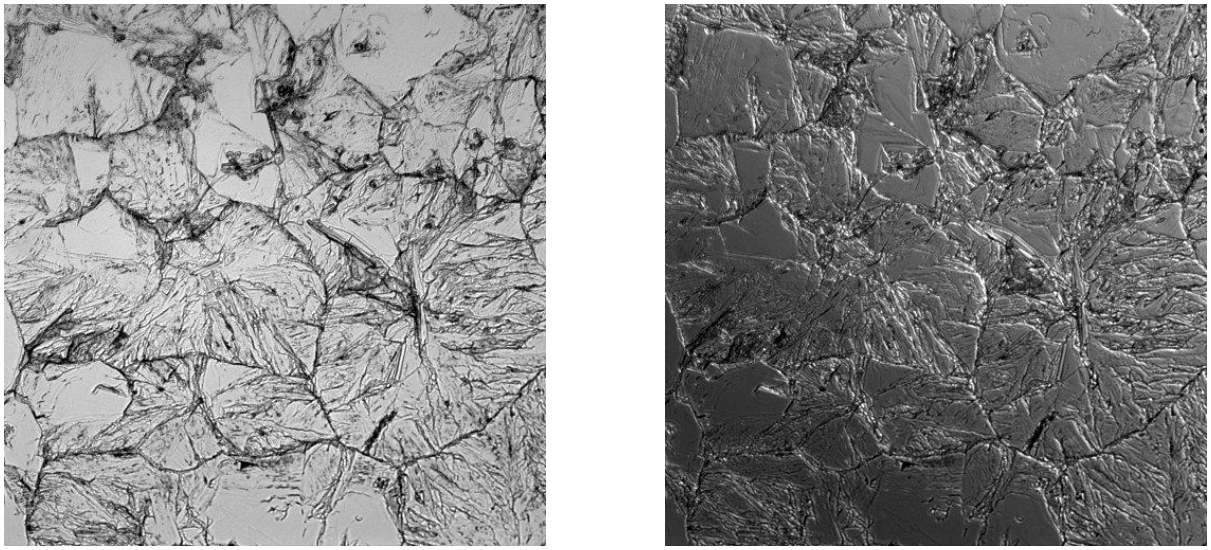

Figure 2. 19. Cyclopentane hydrate at the water/cyclopentane interface. Left: bright field mode. Right: DIC mode. The three-dimensional appearance is easily observed.

2.3.4. Fluorescence

Fluorescence is the process by which a specimen absorbs and subsequently reradiates light [8]. The fluorescence process occurs nearly simultaneously with light absorption because the time delay between a photon is absorbed and reemitted is less than a microsecond.

Fluorescent molecules or photo-sensitizers are also called fluorophores and are necessary to perform the fluorescence microscopy experiments. These molecules typically absorb light in a determined wavelength and then emit photons in a longer wavelength. More precisely, a fluorescent molecule can be excited from a vibrational level in the electronic ground state (S_0) to one of the many vibrational levels in the electronic excited state (S_n), when it absorbs a photon of the appropriate energy. Excited molecules return to the ground energy levels through several steps (Figure 2.20):

1. The molecule quickly loses energy non-radiatively through collision with other molecules in order to reach the lowest vibrational level ($\nu = 0$) of its excited state S_n (vibrational relaxation).

2. The molecule keeps dissipating part of its energy and reaches the lowest vibrational level of the lowest excited singlet state (S_1) by internal conversion IC ($S_n \rightarrow S_{n-1} \rightarrow \ldots \rightarrow S_1$). This process occurs in picoseconds and only between energy levels of the same spin state.

3. The molecule then goes back to the ground state S_0 in some possible different ways:

- When the molecule returns to the electronic ground state by emitting a photon, fluorescence occurs. This photon has a longer wavelength than the incident radiation. Emission typically occurs within nanoseconds. The rest of the energy is released as heat (IR radiation).

- Radiationless transitions make the molecule return to the ground state by releasing heat.

- Before reaching the ground state S_0, a molecule can pass from S_1 to T_1 (excited triplet state, where the excited electron has been reversed) by intersystem crossing (ISC). This is a radiationless transition between two excited states of different spin. The triplet state is of lower electronic energy than the excited singlet state, and exists for each one of the existing excited singlet states. A second ISC $T_1 \rightarrow S_0$ can occur, by which the molecule reaches the electronic ground state through the necessary vibrational relaxations.

- If the molecule in the excited triplet state T_1 loses its energy by emitting a photon when it goes back to S_0, phosphorescence occurs. This process takes between 10^{-7} and 10^{-5} seconds at T ~ 300K and is less probable than a transition $S_1 \rightarrow S_0$. The emitted photon will be less energetic than the one emitted in fluorescence because the excited triplet state T_1 is lower in energy than S_1.

Fluorescence microscopy uses this process to generate contrast in image formation. This is a very used technique nowadays not only because autofluorescent specimens can be studied, but also because of the use of a huge number of fluorophores is possible (secondary fluorescence). These molecules are excited when irradiated with light and attach to visible or sub-visible structures. They then relax emitting light of useful intensity. As the development of these kinds of molecules is increasing and their respective absorption-emission curves are

being obtained, the use of this technique is becoming more and more important, apart from being relatively easy to use and of great specificity.

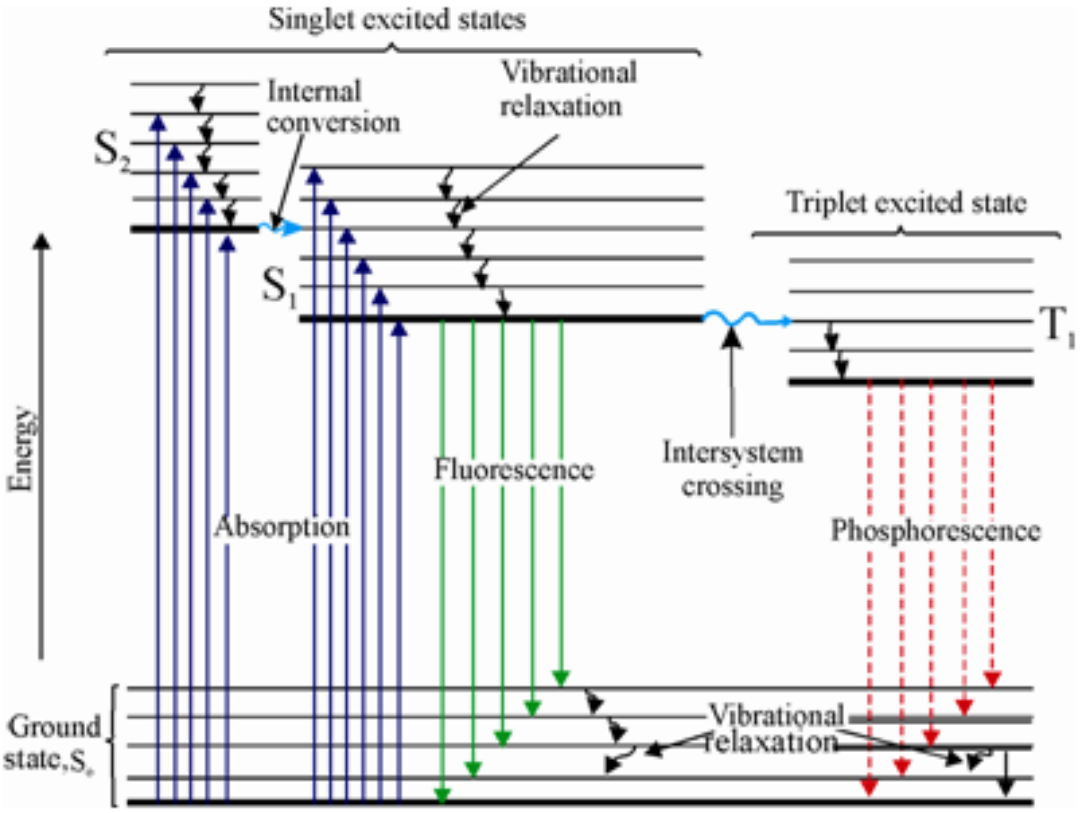

Figure 2. 20. Jablonski diagram showing all the possible relaxation ways of an electron after energy absorption.

The basic operation mode of fluorescence microscopes is to first excite the specimen with a selected wavelength or a set of wavelengths and then separate the weaker reradiating fluorescent light from the much brighter excitation light. This is necessary for allowing just the emission light to reach the detector. For achieving this, fluorescence microscopes are modified and several filters are included. The exciting light comes from a lamp or another light source and light of a specific wavelength or set of wavelengths is produced after passing through the first filter, called excitation filter. The desired wavelength is reflected by a dichroic filter and directed towards the objective and then the specimen. This dichroic beamsplitting mirror allows the long wavelengths (those that will form an image of the specimen in the image plane) emitted by the specimen to pass through efficiently and reflects shorter wavelength light (exciting light), making it go back to the light source. Once the

specimen fluoresces and after passing through the dichroic mirror, the emitted light passes through another filter, called barrier or suppression filter. This filter blocks any residual excitation light and passes just the desired longer emission wavelengths before they reach the eyepiece. In most systems the three filters are incorporated in a cube (Figure 2.21). One example of the images we can obtain is shown in Figure 2.22.

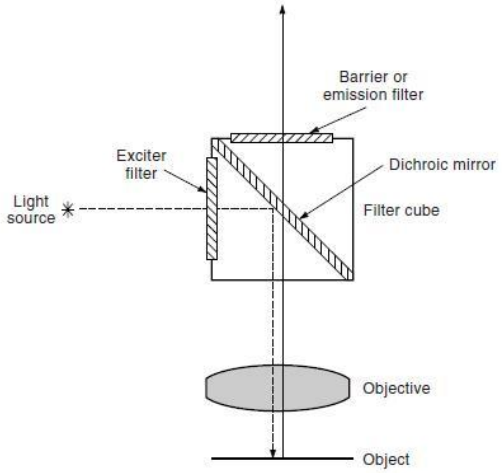

Figure 2. 21. Principle of a filter cube used in fluorescence microscopy: the desired wavelength is reflected by a dichroic filter and directed towards the objective and then the specimen. Once the specimen fluoresces and after passing through the dichroic mirror, the emitted light passes through another filter, called barrier or suppression filter.

Figure 2. 22. Hydrate crystal at the interface water/cyclopentane using the fluorescence imaging mode. DASPI molecules are added to the water with a concentration $2 \cdot 10^{-6}$ M.

In some of our experiments we used a molecular probe responding to a constrained molecular environment, as when a molecule is physisorbed on an interface (liquid/liquid as well as solid/liquid) or is dissolved in a very viscous solvent. Trans- 4-[4-(dimethylamino)-styryl]-1-methylpyridinium iodide (4-DASPI) was used as fluorophore (Figure 2.23). 4-DASPI is one of the hemicyanine dyes in which the dimethyl amino group is an electron donor and the methylpyridinium group is an electron acceptor.

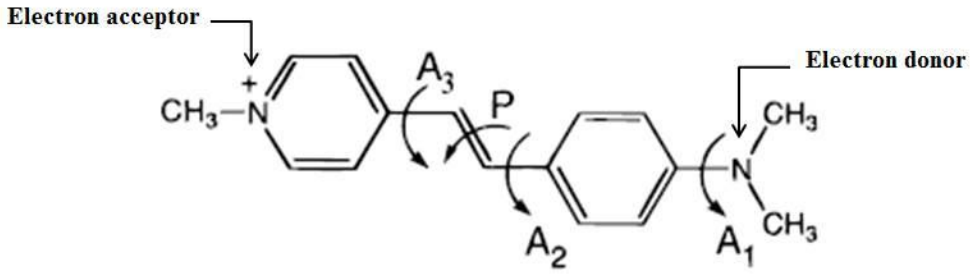

Figure 2. 23. Several possibilities of twisted conformations of *p*-DASPI.

This fluorophore is a planar molecule in its ground state but is susceptible to be twisted through different rotations (see Figure 2.23) when it is excited and the charge transfer occurs [9]. The molecule could twist around one or both of the single bonds placed near the double bond (A_2 or A_3). Anyway, it has been reported from calculations [10], [11], [12] that twisting of the phenyl group (A_2) is the dominant process in the excited state because there is a potential barrier for twisting of the methylpyridinium ring (A_3), which is higher than the thermal energy at room temperature. But no experimental evidences have been reported yet. Therefore it is admitted that the twisting generally occurs around the double bond. In order to get the twisted intramolecular charge transfer (TICT) state a process governed by the potential surface (Figure 2.24) [9] takes place during the excitation. The TICT state is non-fluorescent.

The twisting process in more detail would be as follows: after excitation of the planar molecule (ICT state), the molecule undergoes an internal rotation to the TICT state by twisting its olefinic double bond towards an angle of 90°, corresponding to the most stable excited conformation. This excited state P^* is a little lower in energy than the excited planar state (Figure 2.25) [13]. But the ground state energy of the twisted molecule is much higher than that of the plane molecule and the relaxation to the state energy of the twisted molecule

is much less energetic. Strehmel et al. showed in 1997 that the deactivation of this excited state is radiationless.

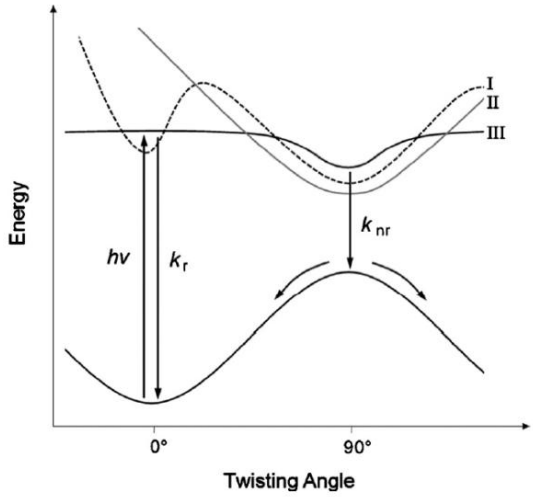

Figure 2. 24. The possible potential energy surfaces of a molecular rotor. The rate processes in the excited state are governed by the potential surface: I) activated potential case, II) inverse potential case and III) flat potential case [9].

When an external constraint prevents the twisting of 4-DASPI after excitation, the TICT state cannot be reached. Therefore, the only conformation the molecule can adopt in the excited state is the planar one which is, at the same time, the one that emits the most (E^* in Figure 2.25). This is why an increase of fluorescence is observed when the molecule is in a viscous or solid medium (quartz), in comparison with when it is dissolved in water, where not only the planar configuration of the molecule is possible in the excited state, but also the TICT conformation, leading to a reduced fluorescence.

In any case, and notwithstanding continuing debate in the literature on the twisting process of DASPI and similar molecules, we can expect a stronger emission when it is absorbed or blocked on a solid surface because the molecular conjugation is broken.

Apart from the experiments carried out with DASPI, other types of experiments were performed with fluorescent microscopy. In this case, fluorescent latex beads (27 nm diameter) containing rhodamine 6G [14], [15] were added to the system, as we will see below. We used them as tracers of water free flow.

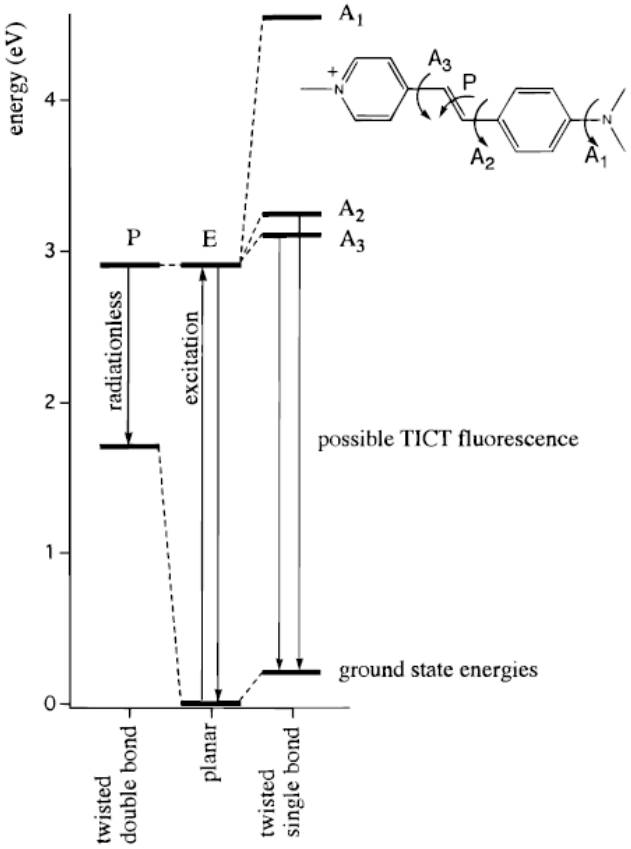

Figure 2. 25. Calculated absolute energies of the different conformations of *p*-DASPI by using the calculated ground state energies (AM1) in conjunction with the excitation energies [13].

2.3.5. Confocal reflectance microscopy

Confocal microscopy uses optical imaging to create a virtual slice or plane, many micrometers deep, within the sample. It provides very high-quality images with fine detail and more contrast than conventional microscopy [16], [17], [18]. In addition, the imaging technique allows for reconstruction of virtual three-dimensional (3D) images of the sample when multiple sections are combined. Confocal microscopy is usually performed either in an epi-fluorescence mode or a bright-field reflection mode. The basis of the latter imaging mode is as follows: a beam of incoming light (the excitation beam) is focused through the microscope objective on a small spot inside the sample, which can be almost as small in diameter as the wavelength of light itself - about 0.5μm. The same objective gathers the reflected light coming back from the sample, but unlike conventional light microscopy, this light is projected and not directly viewed. In conventional light microscopy, although only a

small field of the sample is illuminated at one time, some of the reflected light scatters, which could blur or obscure the image. Confocal microscopy overcomes this problem using a small pinhole aperture in a screen that allows only the light emitting from the desired focal spot to pass through. Any light outside of the focal plane (the scattered light) is blocked by the screen. In optical terms, the pinhole is placed in a conjugate focal plane as the sample (hence the designation "confocal") (Figure 2.26). A sensitive light detector, such as a photomultiplier tube, on the other side of the pinhole is used to detect the confocal light. This technique allows the specimen to be imaged one "point" at a time. To generate a complete image, the spot is moved over the specimen and the image built point by point.

The most important aspect of confocal microscopy is that parts of the specimen that are not at the focal point contribute very little to the in-focus image, contrary to conventional light microscopy, in which all of the light collected by the objective lens is detected.

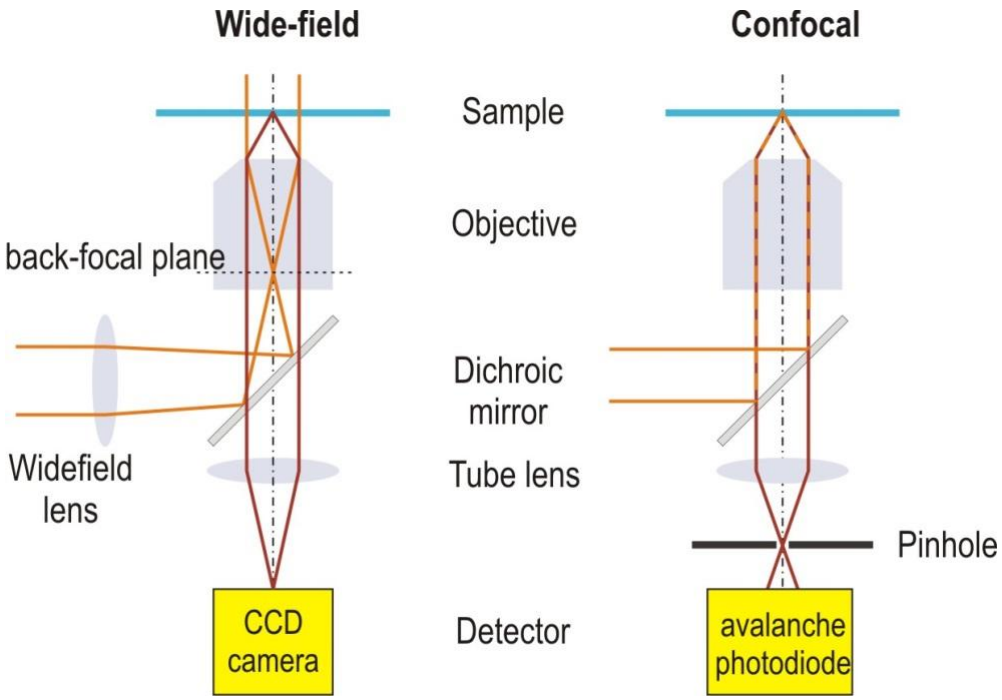

Figure 2. 26. Confocal microscope setup (right) in contrast to the conventional light microscope (left). In the confocal setup a pinhole is placed in order to block any light outside of the focal plane (the scattered light).

In addition, the confocal technique can be combined with any imaging mode of conventional microscopy, including dark-field, polarization, Nomarski DIC, and interference microscopy [7]. Interference of light has already been explained and is the basis of the

functioning of this imaging mode. It can give us information about the thickness of the sample, which is very important for us. An example of the type of images obtained is sown in Figure 2.27 right. From the number of adjacent dark (or bright) fringes ($m \sim 10$) between the edge and the center of the drop, we deduce a height of $h=ml/2n_W = 2\mu m$, with $n_W = 1.33$ the refractive index of water and $l = 532$ nm the wavelength of the laser.

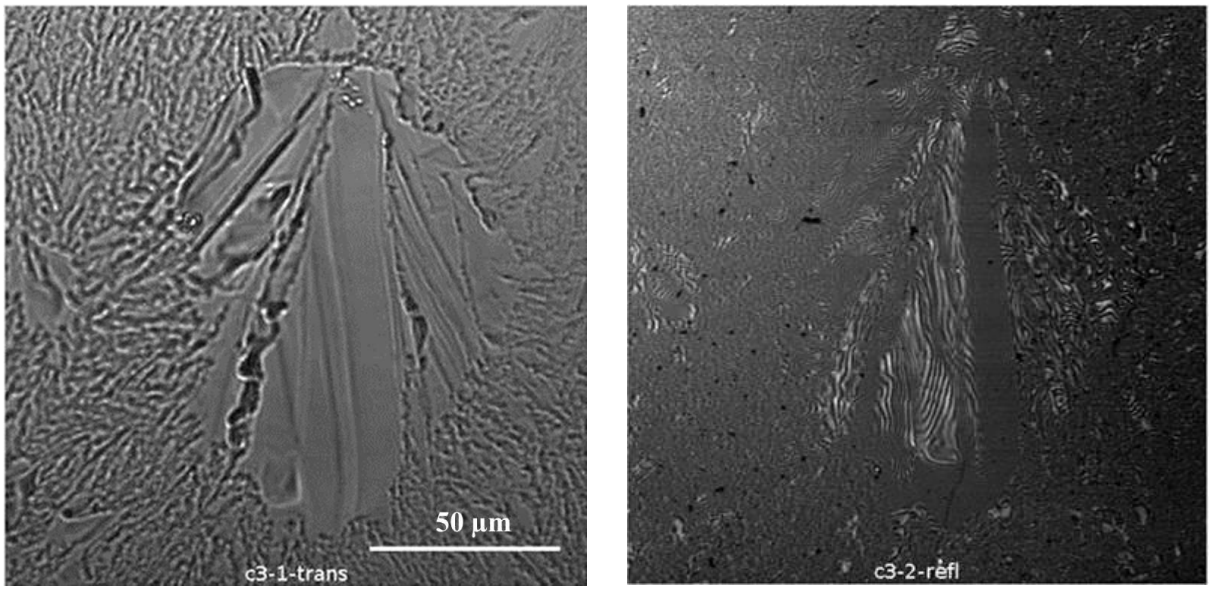

Figure 2. 27. CP hydrate crust over a water drop. Left: Transmission imaging mode. Right: confocal reflectance imaging mode.

2.3.6. The microscopes used in this work

In this section we give a detailed description of the instrumentation used for the development of our studies and its characteristics. We used as inverted microscopes an AE21 Motic™ in preliminary observations and the other part the work was carried out on an inverted Nikon Ti Eclipse microscope. It is designed for transmission, DIC phase contrast, wide-field fluorescence, video microscopy, confocal fluorescence and reflectance, including *z*-scanning, TCSPC, FLIM and confocal emission spectroscopy. In table 2.2 we show the objectives used in our experiments. Note that the objective x20 is corrected for avoiding axial smearing of the focus, i.e. spherical aberrations induced in thick samples. In this particular case the aberrations are produced by the 1.5 mm-thick quartz wall. Wide-field images were recorded with two cameras: (i) a ProEM 512B camera (Prinston Instruments) which is an

electron multiplying charged coupled device (EMCCD) with a 512^2 pixels matrix (16μm pixels) and (ii) a SCMOS camera (ORCA -4.0, Hamamatsu), with 6.5μm pixels. The microscope is equipped with an effective tube extender (x1.5). A sub-micron resolution is obtained for the highest magnification (i.e. with the x20 objective and the tube extender). The lamp used for transmission and DIC is a 120 watt filament lamp while the source for widefield-fluorescence is a 505 nm LED. The filter cube used in our experiments contains a 494 nm/51 exciter filter, in order to excite either the 4-DASPI fluorophore we have used (Kim and Lee find the absorption maximum of DASPI in water at 452 nm) or fluorescent latex beads (27 nm diameter [14], [15]), containing rhodamine 6G. We did have to use in all our experiments an IR filter in order to avoid the local heating of the samples, which could lead us to errors. For the confocal reflection microscopy, the wavelength used was 532 nm. Assuming normal incidence, the separation between two consecutive dark stripes in the images is equal to $½ \cdot \lambda \cdot n$; in this case $½ \cdot 532 \cdot 1.33 = 350$ nm.

Objective	**Focal length (mm)**	**NA**	**Working Distance (mm)**	**EMCCD field (μm)**	**α (°)**
x4	50	0.13	17.2	2047.6	7.5
x4 x1.5				1334.8	
x10	20	0.30	16	821.8	17.5
x10 x1.5				546.5	
x20 (corrected)	10	0.45	8.2	423.1	26.7
x20 x1.5				284.4	
x50	4	0.6	11	164.8	36.9
x50 x1.5				109.7	

Table 2. 2. Objectives of the Nikon Ti Eclipse microscope used in our experiments. Note that the objective x20 is specially corrected for spherical aberrations in thick samples.

2.4. Ellipsometry and Brewster angle microscopy (BAM)

Ellipsometry is a very sensitive optical method, used to obtain information about thin films developed on flat surfaces. This is a noninvasive technique with very high accuracy (of the order of 1 nm). This technique uses the change in the polarization state of light when a light beam is reflected from a surface covered with a thin film. The component *x* is parallel to the plane of incidence of the light beam (*p* polarization) and the component *y* is perpendicular to the incident plane (*s* polarization). The amplitude and phase of each component are altered after reflection due to the structure of the surface.

2.4.1. Fresnel's laws of reflection at surfaces and Brewster's angle

Experiments show that when the incident angle i_1 (Figure 2.28) does not exceed the limit angle, there is not only refraction but also a reflection that becomes more pronounced as the incident angle increases. Moreover, it was observed that the fraction of energy reflected or transmitted depends on the direction of polarization of the light [19]. In particular, two directions of polarization were studied: one in the *p* plane that corresponds to the incident plane and the other in the *s* plane, which is perpendicular to the *p* plane.

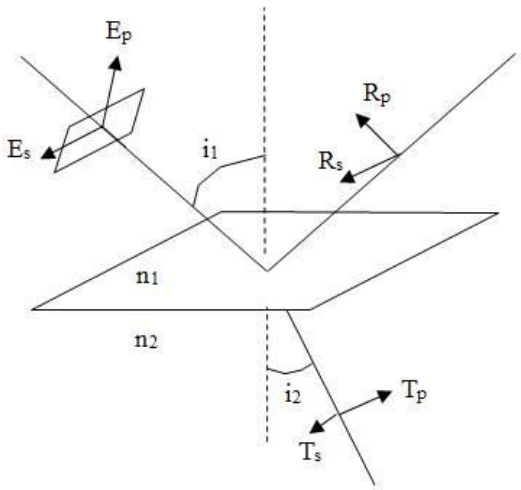

Figure 2. 28. Decomposition of the electrical field vectors in *p* plane and in *s* plane. E refers to the incident beam, R to the reflected beam and T to the refracted beam.

Fresnel solved this problem and developed several equations that describe the reflection and transmission coefficients of the amplitudes of electric field in the *p* and *s* plane:

$$r_p = \frac{R_p}{E_p} = \frac{n_1/\cos i_1 - n_2/\cos i_2}{n_1/\cos i_1 + n_2/\cos i_2}, \; r_s = \frac{R_s}{E_s} = \frac{n_1 \cos i_1 - n_2 \cos i_2}{n_1 \cos i_1 + n_2 \cos i_2}$$

$$t_p = \frac{T_p}{E_p} = \frac{n_1}{n_2}\left(1 - r_p\right), \; t_s = \frac{T_s}{E_s} = \left(1 + r_s\right)$$

We see that $r_p = 0$ when $i_1 + i_2 = \pi/2$. This occurs at the Brewster angle $i_1 = i_B$ at which $\tan i_B = \frac{n_2}{n_1}$. Therefore, an incident beam polarized in the *p* direction will be completely extinguished because only *s* polarized rays can be reflected. This phenomenon is exploited in Brewster angle microscopy, where the specimen is observed through the reflection of a *p* incident beam and the analyzer in the *p* direction. The reflection of *p* rays by an interface makes them disappear while those reflected by a thin layer are generally elliptically polarized and are then visible.

2.4.2. Principle of an ellipsometric measurement

Light is reflected by the surface of the sample. When a polarized light beam strikes a surface, the *p* and *s* components suffer an alteration in their phases and amplitude and exhibit different reflectivities. Therefore, a change in the form and size of the ellipse of polarization is observed. This change can be traduced as a measure of the properties of the optical system. Figure 2.29 shows the different components that are necessary to perform an ellipsometric measurement by the nulling technique. A beam of non-polarized light (a) enters a linear polarizer, allowing the light to become polarized in the desired direction P. The *p* and *s* components of the electric field vector E have the same phase (b). This linearly polarized light then arrives to the compensator formed with a quarter wave plate, where the amplitude and phase of the two components are shifted, converting the linear polarized light into an ellipse (c). The elliptically polarized light strikes the surface (d) and the objective is to achieve a linear polarized light (e) after reflection of the light on the thin layer. To achieve this, in general the quarter wave plate is set to an angle C = 45° and the polarizer is turned to the

desired P angle producing a linear polarized light after reflection from the thin layer. An analyzer (f) is placed just before the receptor and it is turned to an angle A to extinguish the beam in order to determine the direction of polarization of the beam after reflection. This is called "nulling" and corresponds to the fact of finding a minimum of the signal in the photodetector. The knowledge of the three angles P, C and A, allows to directly determining the ellipsometric angles ψ and δ, which are related to the ratio of the complex reflection coefficients of *p* and *s* polarizations:

$$\frac{r_p}{r_s} = \tan\psi \exp(i\delta) = -\tan A \frac{\tan C - i\tan(C-P)}{1 + i\tan C \tan(C-P)},$$

where ψ is the angle whose tangent gives the ratio of the change in amplitude for the *p* and *s* components and δ is the relative phase shift between the *p* and *s* component upon reflection. These values are then treated through a complex optical model in order to obtain the film properties.

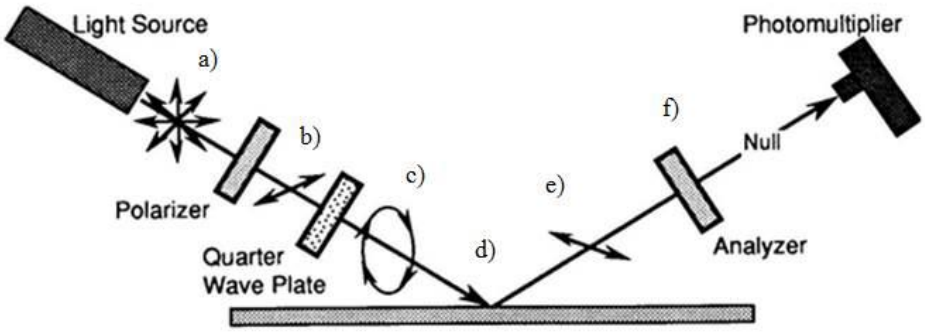

Figure 2. 29. Components of a nulling ellipsometer (see text).

2.4.3. Ellipsometer characteristics

We used an auto-nulling imaging ellipsometer (Nanofilm Surface Analysis) with 0.001° resolution for the angles δ and ψ. The light source is an internal 532 nm solid-state laser and instead of a photometer, a CCD camera with 768 x 572 pixels allowed to get images of the interface. In order to get the most precise results one has to use an incident angle close to the Brewster angle because it is close to this angle where δ and ψ vary the most with

respect to the layer thickness. It is reasonable to state that the uncertainty of our measurements is about 1 nm concerning the determination of the layer thickness.

REFERENCES

[1] Tkaczyk, T. S., **2010**. Field Guide to Microscopy (J. E., Greivenkamp, ed.); SPIE Field Guides, Vol. FG13, Bellinghman, Washington, USA.

[2] Murphy, D. B., **2001**. Fundamentals of Light Microscopy and Electronic Imaging. Wiley-Liss (a John Wiley & Sons, Inc., Publication), New York, USA.

[3] Abramowitz, M., Davidson, M. W. The Microscopy (http://microscopy.fsu.edu/primer).

[4] www.vision-systems.com

[5] www.microscopyu.com

[6] Izzard, C. S. and Lochner, L. R., **1976**. Cell-to-substrate contacts in living firoblasts: an interference reflexion study with an evaluation of the technique. Journal of Cell Science *21*, 129-159.

[7] Verschueren, H., **1985**. Interference reflection microscopy in cell biology: methodology and applications. Journal of Cell Science *74*, 279-301.

[8] Spring, K. R. Fluorescence Microscopy (www.microscopyu.com).

[9] Jee, A. J., Bae, E., Lee, M., **2010**. Internal motion of an electronically excited molecule in viscoelastic media. The Journal of Chemical Physics *(133)*, 014507.

[10] Kim, J. and Lee, M., **1999**. Excited-State Photophysics and Dynamics of a Hemicyanine Dye in AOT Reverse Micelles. The Journal of Physical Chemistry A *103* (18), 3378–3382.

[11] Ephardt, H. and Fromherz, P., **1991**. Anilinopyridinium: solvent-dependent fluorescence by intramolecular charge transfer. The Journal of Physical Chemistry *95* (18), 6792–6797.

[12] Fromherz, P. and Heilemann, A., **1992**. Twisted Internal Charge-Transfer in (Aminophenyl) Pyridinium. The Journal of Physical Chemistry *(96)*, 6864-6866.

[13] Strehmel, B., Seifert, H., Rettig, W., **1997**. Photophysical Properties of Fluorescence Probes. 2. A Model of Multiple Fluorescence for Stilbazolium Dyes Studied by Global Analysis and Quantum Chemical Calculations. The Journal of Physical Chemistry B *(101)*, 2232-2243.

[14] Cerdán, L., Gartzia-Rivero, L., Enciso, E., Bañuelos, J., López-Arbeloa, I., Costela, A., García-Moreno, I., **2013**. Focusing on charge-surface interfacial effects to enhance the laser properties of dye-doped nanoparticles. Laser Physics Letters *11*, 015901.

[15] Enciso, E., Costela, A., García-Moreno, I., Martin V., Sastre, R., **2010**. Conventional Unidirectional Laser Action Enhanced by Dye Confined in Nanoparticle Scatters. Langmuir *26*, 6154-6157.

[16] Nwaneshiudu, A., Kuschal, C., Sakamoto, F. H., Anderson, R., Schwarzenberger, K., Young, R. C., **2012**. Introduction to Confocal Microscopy. Journal of Investigative Dermatology *(132)*.

[17] www.olympusmicro.com

[18] Sheppard, C. J. R. Scanning Confocal Microscopy.

[19] Tompkins, H. G. and McGahan, W. A., **1999**. Spectroscopic Ellipsometry and Reflectometry: A User's Guide, 1sr edition. Wiley-Interscience (a John Wiley & Sons, Inc., Publication).

III. RESULTS AND DISCUSSION

CHAPTER 3

STATISTICS OF HYDRATE NUCLEATION AND GROWTH

The text of this chapter has recently been published under the title "Droplet-based millifluidics as a new tool to investigate hydrate crystallization: Insights into the memory effect" in Chemical Engineering Science. This paper is reproduced below.

Abstract

A simple millifluidic method is used for studying hydrate crystallization. Regularly – spaced water drops of equal volume in the ml range separated by the guest (hydrate-former) phase are placed in transparent plastic tubing. Temperature and/or pressure are controlled. In one experiment several tens of water drops behaving as independent reactors are video-monitored for hydrate formation and melting events. This method is used here to gain insights into the 'memory effect'. The hydrate-former chosen is cyclopentane (CP), which forms

hydrates at ambient pressure and temperatures below T_{eq} = 7.2°C, the three-phase (CP, water, hydrate) equilibrium temperature. The statistics of hydrate nucleation events when chilling the water drops below T_{eq} is observed to depend strongly on the thermal history, e.g., prior CP hydrate formation and subsequent melting at various prescribed temperatures (above 7.2°C) and durations. When one or two of these parameters (melting temperature and duration) increase, the 'memory' of the hydrate previously formed fades: the subcoolings required for hydrate formation increase and are more scattered, i.e. they differ more from one drop to the other. The method also allows the visualization of single-drop events such as hydrate birth and growth. The results complement those obtained from more conventional methods and show the promises of using this method for investigating the kinetics of hydrate crystallization and melting.

3.1. Introduction

Clathrate hydrates (hereafter abbreviated as hydrates) consist of hydrogen-bonded water (host) molecules forming a crystalline lattice stabilized by hydrate-former (guest) molecules (CO_2, low molecular-weight alkanes, etc.) present in some of its cavities. These ice-like compounds are stable in a domain of low enough temperatures (typically, below a few °C) and high enough pressures (often above a few bar) that depend on the particular hydrate-former. Hydrate crystallization, long considered to be a nuisance (still to be avoided in oil and gas transportation lines), is now being considered for an increasing number of applications including gas storage, refrigeration processes, CO_2 separation from natural gas, water purification and desalination, etc [1], [2]. Research activity is booming, mostly aimed at characterizing and controlling the kinetics of hydrate crystallization, which shall be either accelerated or inhibited, depending on the application. Such kinetic control is often ensured by appropriate molecules dissolved in very small amounts (with concentrations typically in the 0.1 wt% range and below) in the water phase and/or (in some rare instances) in the guest phase. The mechanisms by which these additives promote or inhibit crystallization are still poorly understood: some additives act mainly upon the first step of crystallization, i.e. nucleation (e.g., in the case of some inhibitors, by increasing the nucleation time), whereas others act mainly upon the second step of crystallization, i.e., hydrate growth (e.g., in the case of hydrate-promoting additives, by ensuring a rapid and massive conversion of water and guest molecules into hydrates). These two steps often are examined in separate sets of experiments. The nucleation (or induction) step, which is stochastic in nature, needs to be

appreciated from several experiments conducted under identical conditions (for a recent review, see [3]). The number of such experiments rarely exceeds a few units [4], [5], except when using dedicated methods [6] or working (e.g., by means of micro - DSC) with a water-in-oil emulsion where each water drop is considered to behave as an independent reactor for hydrate formation/dissociation [7], [8]. The hydrate growth step can be evaluated by calorimetry, by measurements of temperature and pressure (for gas hydrates forming in a closed vessel) and/or by direct visualization of water/guest interfaces [9], [10]. We present a simple experimental setup and procedure inspired from the milli- and micro-fluidic approaches used for investigating in a precise and controlled fashion the nucleation and growth steps in crystal - forming systems: concentrated salt solutions, molecules of biological and pharmaceutical interest, etc. (for a review see [11]). To the best of our knowledge, these fluidic tools have not been used yet to investigate this important class of crystal-forming systems, namely hydrates. They are used here to gain insights into the 'memory effect' as well as into the morphology and growth of hydrates in a simple hydrate-forming system: water + cyclopentane (CP). 'Memory effect' refers here to the fact that hydrates form more easily when chilling a water phase that has already contained ice or hydrates. Zylyftari et al. [12] have recently reviewed possible explanations for this phenomenon (see also chapter 3 from [9]). One of these is the persistence of residual H-bonded molecular structures, but these structures have eluded experimental observation. Like many other hydrate-formers, CP is sparingly soluble in water, and its hydrate is considered a model of hydrates of practical interest such as gas hydrates [13], while being easier to manipulate because it forms at atmospheric pressure in a fairly large range of temperatures below T_{eq} = 7.2°C. CP is, in fact, used as hydrate-former in many fundamental studies of the hydrate formation and dissociation processes, and CP hydrate formation has been characterized from various viewpoints: calorimetric [14], [15], [16], morphological [17], spectroscopic [18], rheological [19], [20], etc. Attempts to understand the hydrate promoting or -inhibiting mechanisms of various electrolytes, surfactants, polymers and particles have also been made with CP as a hydrate former [21], [22], [23], [17], [20], [24]. In a recent experimental study of CP hydrate formation from ice, Zylyftari et al. [12] argued that hydrate nucleation takes place heterogeneously at the triple lines (CP, water and ice) that arise at the interfaces between CP and ice when the latter phase melts. In the case of CP hydrate formation from an aqueous (liquid) phase that previously contained hydrates (but not ice), the hydrate formation that takes place when the water + CP system is chilled again depends on the thermal history and

particularly on the conditions of dissociation of the previous hydrates, but the physical origin is less clear. A systematic study of the impact of these conditions on the memory effect in CP hydrate formation has recently been published by Sefidroodi et al. [25]. These authors formed CP hydrate in water + CP systems with prior histories of CP hydrate formation and dissociation. The temperature T_{dis} (> T_{eq}) and duration t_{dis} of this dissociation step was systematically varied and found to have a strong effect on the subsequent hydrate formation: lower and more scattered temperatures of CP hydrate formation were observed for more severe melting conditions (higher T_{dis} and/or t_{dis}). These authors used laboratory glassware (ml-sized beakers) as reactors, which limited the number of data points (to 8, as there were 4 beakers per experiment, which was often duplicated) and therefore the information on the statistics of hydrate formation. The method introduced here alleviates this limitation. The outline of this paper is as follows. The experimental setup and procedure used for this study are presented in next section. The following section presents and discusses the observations of the kinetics of CP hydrate formation in systems with various histories of CP hydrate formation and dissociation (melting). The last section is devoted to the perspectives of using millifluidic tools and methods in the area of hydrate crystallization.

3.2. Experimental setup and procedure

The experimental setup consists of a spiral capillary tube containing initially (i.e. at the beginning of the experiment) a train of water drops dispersed in the hydrate-former (guest), here CP, as showed in Figure 3.1 (with more than 98% purity, purchased from Sigma-Aldrich). This train of drops is generated by co-injecting water and CP at constant rates through a co-flow junction located upstream of the capillary entry (Figure 3.2). The capillary is sandwiched between a sapphire window at the top and an aluminum holder at the bottom, which is itself in contact with the cold side of a Peltier element driven by a temperature controller (Accuthermo ATEC302). The heat produced in the hot side of the Peltier element is evacuated through a cooling circuit in which a mixture of water and glycol circulates at the temperature of -2°C. An insulating jacket is placed around the setup in order to minimize heat losses. The imaging system consists of a camera mounted on a zoom system (x16, Qioptiq) allowing the visualization and video-recording either of the whole collection of drops (Figure 3.1.left), or of a single drop (Figure 3.1.right). Most of the videos and images are acquired using as lighting system a 4" LED ring light (Edmund) positioned below the zoom system. Coaxial lighting is used only in a few cases, as indicated below.

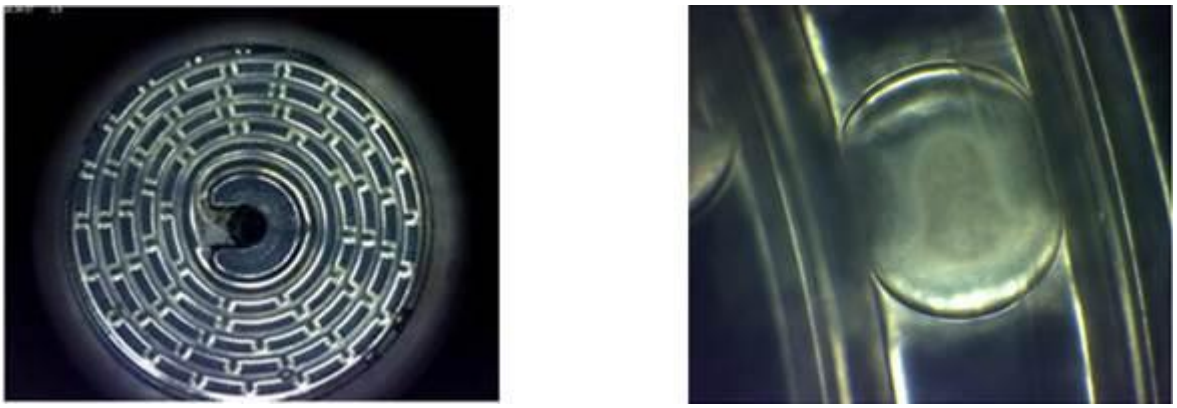

Figure 3. 1. Left: Overview of the spiraled capillary tube containing the immobile water drops dispersed in CP, i.e. at the start of the experiment. The inner diameter of the capillary is 1 mm. Right: Zoomed in view of a single water drop in CP inside the tube at ambient T.

In the experiments reported here, the capillary tube is an optically transparent perfluoroalkoxy-alkane (PFA) tube (Dupont^{R}) with an outer diameter (OD) of 1.59 mm (1/16") and an inner diameter (ID) of 1 mm. This capillary tube is connected to a syringe pump (Harvard) that delivers CP at a fixed flow rate, and is open at the other end. It is immersed in ethanol whose refractive index is very close to that of PFA, which renders the capillary tube almost invisible. The inner capillary tube of the co-flow assembly is a fused silica capillary of OD = 350 µm and ID = 250 µm (Polymicro^{TM}) connected to another syringe pump that delivers water at fixed rate. The tube dimensions and flow rates (30 ml/hour for water and 100 ml/hour for CP) ensure that water drops are generated in a 'dripping' regime characterized by regularly-spaced drops with similar volumes. Once the train of water drops is generated, the two syringe pumps are stopped, that is, the water drops are immobilized, for the whole duration of the experiment.

To the best of our knowledge, these fluidic tools have not been used yet to investigate this important class of crystal-forming systems, namely hydrates.

This experimental setup is very versatile and can be used with a variety of commercially available tube dimensions. The above choice of tube dimensions is the result of the following compromise: water drops must be numerous enough to provide relevant statistics of the nucleation events, and large enough for visualization of crystal features and evolution within each drop. Here, drop volumes are in the µl-range, and an average of around 70 water drops can be stored in the spiral capillary (Figure 3.1).

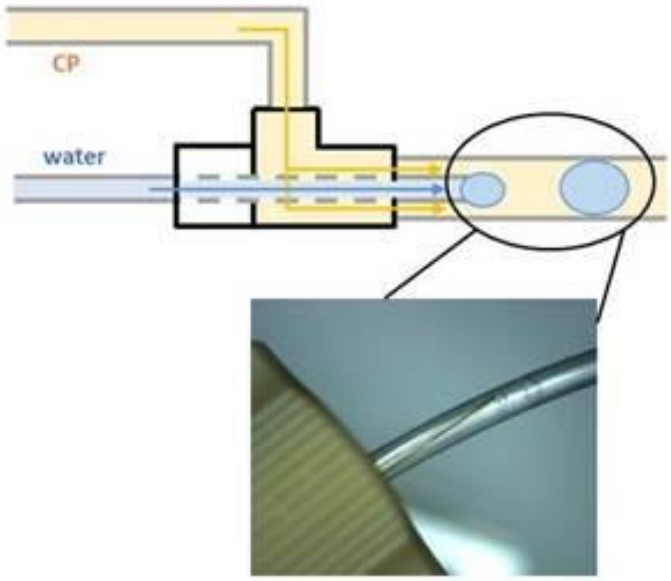

Figure 3. 2. Schematics of the drop generation system, with a zoomed-in view of the co-flow junction.

Experiments are carried out at constant (atmospheric) pressure (the capillary tube is open at one end), but a pressure control can easily be added, e.g., by means of a back pressure regulator, and the setup is thus suited to the study of more conventional gas hydrates such as light hydrocarbon or CO_2 hydrates: work along these lines will be reported elsewhere.

The continuous CP phase in these experiments has two functions: (i) to generate and carry the train of water drops into the capillary (as explained above) and then, when the drops are immobile and the temperature T is low enough, (ii) to react with water and form CP hydrates. Like many other hydrates of sparingly water-soluble guests, CP hydrate nucleates at the water/guest (CP) interfaces and then grows rapidly laterally along these interfaces as a polycrystalline film that acts as a barrier for subsequent growth normal to the interface [10], due to the slow mass transfer. According to the interferometric measurements of Taylor et al. [26], this film reaches thicknesses in the range 10 - 30 µm (depending on the subcooling $\Delta T_{sub} = T_{eq} - T$) within a few minutes, that remain then fairly constant over hours. Only a small proportion of the CP and water molecules serve as reactants: each water drop thus behaves as an independent reactor with respect to hydrate formation or dissociation. In a few instances, we did observe coalescence between two neighboring water drops. These data are excluded from the analysis because nucleation rates are known to increase with reactor size.

3.2.1. Sequences of temperature variations

As explained in chapter 1, hydrate formation in quiescent systems is not spontaneous and takes an extremely long time, even under strong subcooling. The only thing we can do with this setup is to first form ice that is then transformed into hydrate at its interfaces with the guest (hydrate-former) phase by heating slightly above 0°C [4], [12]. Figure 3.3 shows a typical thermal cycle. The first step in all experiments consists in quickly (within a few minutes) driving the temperature down to T = -26°C in order to transform all water drops into ice 'drops'. One of these is shown in Figure 3.4. These freezing temperatures are somewhat higher than those expected for homogeneous nucleation (-33 to -35°C for mm-sized free water drops cooled at similar rates, see [27]), showing that ice nucleation proceeds heterogeneously: freezing starts at the CP/water interface and/or is promoted by impurities. Frozen water drops are opaque due to small air bubbles excluded from the ice and exhibit the remains of fracturing events (see white arrow in Figure 3.4a), which occur upon freezing when the inwards growth of the ice shell compresses the remaining water inside the drop and at some point causes explosive shattering (this phenomenon is well known for 'free' water drops [28], [29]).

The second step in all experiments is to drive T from -26°C to slightly above 0°C in order to form CP hydrate from ice (first hydrate formation). This is done by increasing T quickly to -5°C and then slower to 2°C, where ice 'drops' are left for 10 min allowing them (or at least their outer shell) to transform into CP hydrate: see the faceted polycrystalline shell in Figure 3.4b. This step is further discussed in section 3.2, where the observations are compared with those obtained with CP replaced by n-hexane, a non-hydrate former.

The next step is the hydrate dissociation step, which differs from one experiment to the other. It consists in increasing the temperature to a certain dissociation (or melting) temperature T_{dis} above the equilibrium temperature T_{eq} and then keeping this temperature constant for a certain duration t_{dis}. The equilibrium temperature T_{eq} is measured ~ 7.2°C, in agreement with Sakemoto et al. [30] and Zylyftari et al. [20]. An example of the drop appearance during this dissociation step is shown in Figure 3.4c. The origin of the turbidity observed at the top of the water drop - a stable CP-in-water emulsion resulting from hydrate melting - is addressed in section 3.3.

The next (and last) step is identical in all experiments: the system is slowly chilled down to slightly above 0°C (cooling rate: 0.2°C/min) in order to form again CP hydrates (second hydrate formation). Hydrate formation events in this last step are detected as explained in subsection 3.1.2. Figure 3.4d shows a drop where second hydrate formation has just occurred. In the example in Figure 3.3 the hydrate melting step at T_{dis} = 8.8°C lasts t_{dis} = 20 min.

The above procedure for characterizing 'memory effects' in hydrate-forming systems was introduced in 2003 by Ohmura et al. [5] and then widely used in many laboratories including our own [31], mainly for characterizing the effect of inhibitors added to the water phase. Variations in the last step (second hydrate formation) include step-like (rather than continuous) temperature decreases, or a very quick decrease to a target temperature that subsequently remains constant [32].

The procedure followed here is the same as that employed by Sefidroodi et al. [25]. In particular, the cooling rates during the second hydrate formation are nearly identical: 0.2°C/min in this work vs. 0.18°C/min in Sefidroodi's work [33]. The cooling rate is constant and identical in all experiments, hence elapsed time (since the start of the temperature descent) and subcooling $\Delta T = T_{eq} - T$ are proportional.

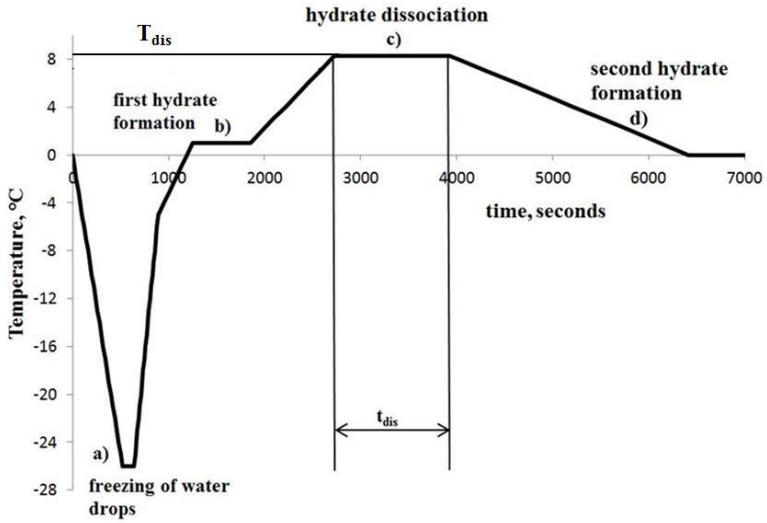

Figure 3. 3. Sequence of temperature variations in a typical experiment.

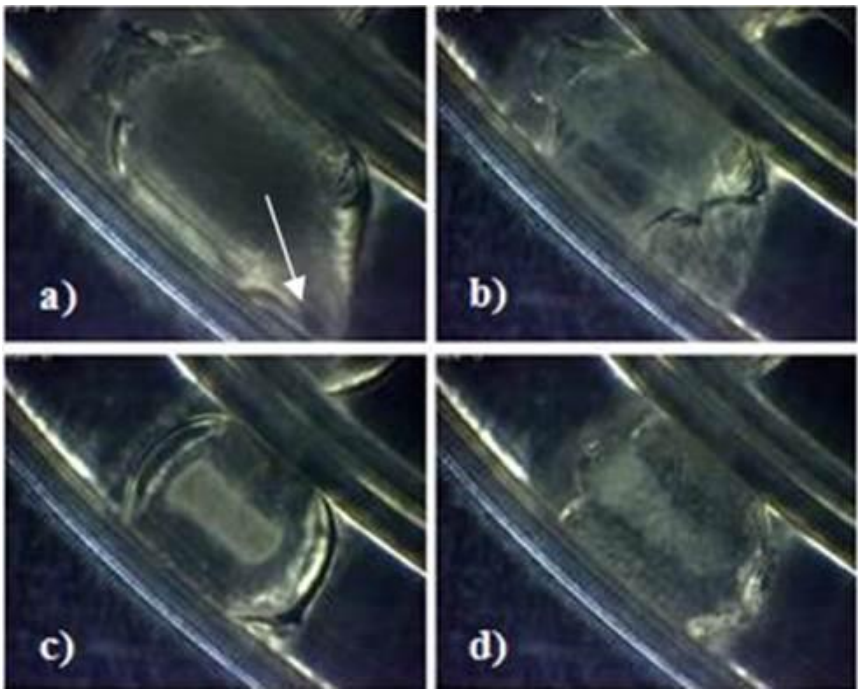

Figure 3. 4. Zoomed-in views of a single drop (obtained by using the zoom x16) at various stages of the experiment indicated in Figure 3.3. a) T = -25°C. The white arrow indicates the location of the ice shell breaking upon freezing. b) T = 2.4°C, c) T = 8.8°C and d) T = 0.6°C.

3.2.2. Image analysis: identification of the hydrate conversion events

Conversion events correspond to the moments when the presence of hydrate crystals becomes visible within the resolution of the optical setup. These events are posterior to the nucleation events, which correspond to the initial formation of hydrate crystals of size large enough - but not visible yet - to grow further (smaller crystals are not stable). It is usually assumed that the statistical behavior of both types of events is similar. Conversion events in the last step of the experiment (second hydrate formation, see Figure 3.3) are identified in each water drop from the video recordings by means of an appropriate treatment carried out using ImageJ routines. First, the background, i.e. the blank image of the capillary fully saturated with CP, is subtracted from all images. The contrast is then optimized and each drop is analyzed for changes in grey levels. At the scale of the spiralled capillary (Figures 3.1 and 3.5), which is the scale at which we have carried out the analysis of conversion events, these changes are first apparent at an apex of the drop (see Annexe A: Detection of the apparent onset and end of hydrate formation in a single drop), whereas at the smaller scale of a single drop conversion events often appears to start a few seconds earlier, in the turbid region of the

drop, i.e. in a more central region of the drop (see below Section 3.4). These changes then propagate to the other apex of the drop and cease shortly after reaching this apex. For a given water drop (or reactor), the conversion time (corresponding to a particular temperature T or subcooling T_{eq} - T) is defined as the time when changes become apparent within the drop, and the growth time as the duration of apparent changes in that drop. Dividing the drop length by the growth time gives the hydrate growth velocity. Figure 3.5 shows two images of the train of drops (with background subtracted and optimized contrasts) at two moments in the second hydrate formation step: at the start of the temperature descent, when all water drops are liquid (left), and at the end of the temperature descent, when almost all water drops have been converted into hydrate (right).

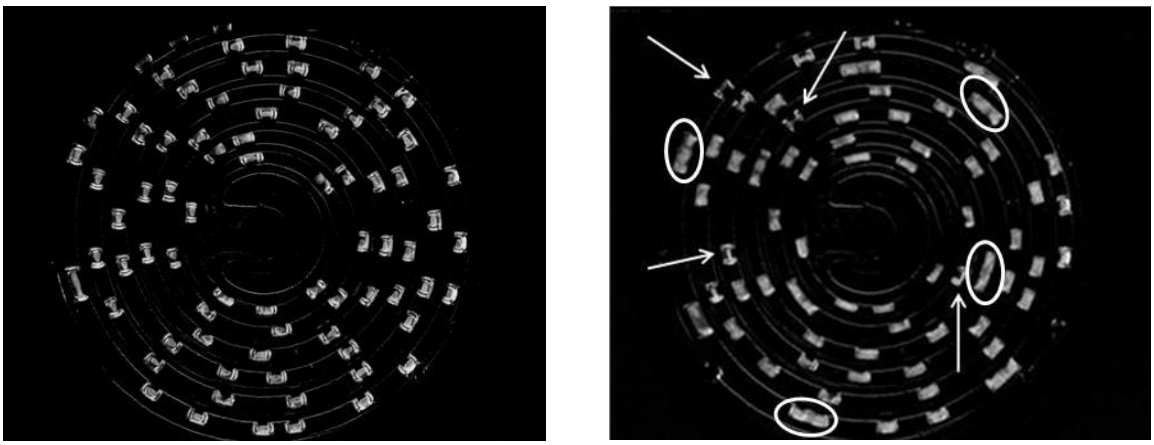

Figure 3. 5. Processed images of one of the experiments (second hydrate formation, conditions of dissociation: T_{dis} = 8.8°C and t_{dis} = 20 min). Left: all water drops are liquid (T above 3°C). Right: conversion has occurred in almost all drops (T ~ 0°C). Some of the drops that have not started conversion are pointed with arrows. Ovals show couples of neighboring drops that have merged into a single drop and therefore are not considered in the analysis.

3. 3. Results and discussion

In this section, the results on the first hydrate formation that occurs when ice is melted (T raised slightly above 0°C) are presented and discussed first: the observations are compared to those obtained under similar conditions with a non-hydrate-former, n-hexane. Then, the results for the second hydrate formation are presented for various melting conditions of the first hydrate. Finally, an attempt is made to characterize the turbidity - a CP-in-water

emulsion - that forms upon hydrate melting and understand its role in the subsequent hydrate formation process.

3.3.1. Comparison of the ice-melting step in hydrate-forming and non-hydrate forming systems

Experiments were also conducted with n-hexane as the continuous phase as an example of a non-hydrate former, in order to be sure about the fact that we were obtaining a hydrate (with CP) or not (with n-hexane). The water drops generated with the setup and procedures described above (flow rates equal to 30 ml/h for water and 100 ml/h for hexane) are slightly bigger in n-hexane than in CP. Similar freezing behaviour of the water drops is observed during the ice formation step: in particular, the breaking of the ice shell is observed in both systems (as shown in Figure 3.6).

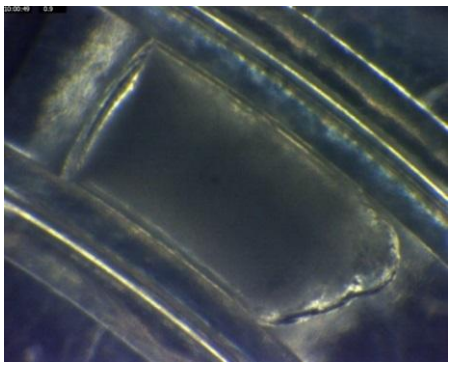

Figure 3. 6. Breaking of the ice shell during the ice formation step in a water drop in n-hexane.

We focus hereafter on the second step (ice-melting). Snapshots of the ice melting process in CP and in n-hexane at temperatures rising from slightly above 0°C (0.8 - 0.9°C) to 2.6 - 2.7°C are shown in Fig. 3.7. Ice ‘drops’ look very similar in CP and n-hexane (leftmost images) at 0.8 - 0.9°C, just before the start of ice melting, which then proceeds from the drop edges (near the PFA wall) inwards. The drops then evolve in a very different manner in CP and in n-hexane: in CP the drop surface has the faceted appearance characteristic of a polycrystalline (hydrate) layer, whereas in n-hexane the drop surface has the constant curvature of a liquid/liquid interface.

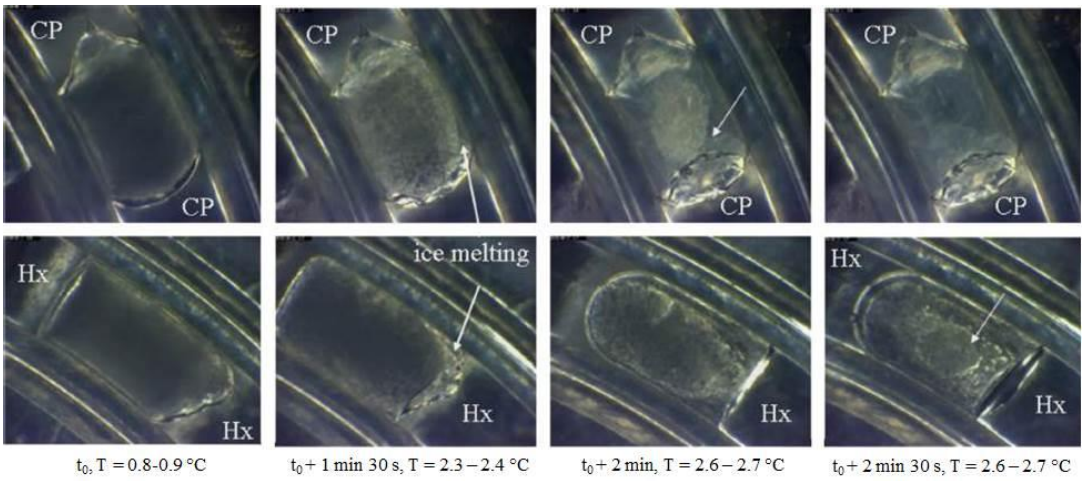

Figure 3. 7. Ice melting in cyclopentane (CP) and n-hexane (Hx): T is raised at a rate of 1°C/min from 0.8 - 0.9°C (leftmost images) to 2.6 - 2.7°C and then left at this temperature (two rightmost images). Ice melting starts at drop edges near the PFA walls (white arrows) and then proceeds radially inwards (arrows in the two rightmost images). In CP, ice is replaced at the drop surface by a polycrystalline hydrate layer, whereas in Hex the drop surface has the constant curvature of a liquid - liquid interface. Small air bubbles are apparent in the water drop in Hx (rightmost image).

The nucleation of CP hydrate from ice has been recently investigated from single drop experiments by Zylyftari et al. [12], who heated ice drops immersed in CP from -5 to 0.2°C at various rates and observed nucleation times (at constant T = 0.2°C) that increased with the heating rate. Since heating at lower rates produces more fragmented ice, these authors argued that the amount of triple line (CP, water and ice) might play a key role (for an analysis of facilitated nucleation at a triple line, see [34]).

Another possible mechanism has recently been proposed by Poon and Peters [35], who showed from a simple model that the increased solute (here: CP) concentration due to solvent (water) freezing is likely to trigger nucleation due to the much higher CP supersaturation in the remaining (unfrozen) water. Following this idea, the water supersaturated with CP produced when ice forms is expected to produce nuclei entrapped in the ice defects. Once the ice melts, the nuclei exposed to both CP and water are again able to grow.

3.3.2. Second hydrate formation: conversion curves for various thermal histories

The experiments conducted have consisted, once the first two steps are accomplished (freezing the water drops and then forming the first hydrate, see 3.1.1 and 3.2.1), in melting the first hydrate at various temperatures and times (T_{dis} and t_{dis}) in the intervals of 7.8 to 9.7°C

and 20 to 120 minutes, respectively, and then in lowering the temperature at an identical rate down to slightly above 0°C. For each set of dissociation conditions (T_{dis} and t_{dis}), the conversion curve is extracted as well as information about the hydrate growth velocity during the second hydrate formation. The conversion curve is the fraction of drops as a function of subcooling $\Delta T = T_{eq} - T$ in which conversion events have been detected (see 3.1.2).

These curves are plotted in Figure 3.8. Following the lowest dissociation temperature T_{dis} = 7.8°C, the subcoolings necessary to trigger hydrate formation in the water drops are the lowest (50% of the water drops have started conversion at $\Delta T_{50\%}$ = 3.7°C) and fall in the narrowest range (90% of the drops experience conversion in the interval from 3.1 to 4.3°C). Dissociation time t_{dis} (20 or 120 min) has however little impact on hydrate formation. For T_{dis} = 8.8°C (and t_{dis} = 20 min), the subcoolings required for conversion have increased to $\Delta T_{50\%}$ = 4.6°C and they are more scattered (90% of the water drops have started conversion in the interval from 3.9 to 5.5°C). Clearly, when melting conditions get more severe, the memory effect is attenuated, i.e. hydrate formation is a more stochastic/less deterministic process that needs a larger subcooling or elapsed time to be triggered. Unlike what is observed at T_{dis} = 7.8°C, a strong impact of t_{dis} on the memory effect is observed at the melting temperatures T_{dis} = 8.8 and 9.7°C. For the most severe hydrate melting conditions displayed in Figure 3.8 (T_{dis} = 8.8 and 9.7°C, t_{dis} = 120 min) a significant fraction of the drops is still unconverted when T reaches 0°C (but is eventually converted at later times). For the strongest dissociation conditions investigated (T_{dis} = 9.7°C and t_{dis} = 120 min) all drops turn out to be unconverted at 0°C (hence, the conversion curve is not represented in Figure 3.8).

These trends are identical to those previously observed by Sefidroodi et al. [25], who investigated a range of dissociation conditions T_{dis} = 8.3 to 12.1°C and t_{dis} = 20 min to 20 hours in reactors with volumes 3 - 4 orders of magnitude larger than our µl-sized water drops. These authors observed conversion for subcoolings systematically lower - by at least 0.5°C - than ours. It is a well-known feature of nucleation phenomena that the metastability range is enlarged for smaller sample volumes. Interestingly, our observations for the lowest dissociation temperature T_{dis} = 7.8°C are in line with those of Sefidroodi et al., who did not notice any impact of the dissociation time (in the interval from 20 to 120 minutes) on the conversion temperatures for the lowest dissociation temperature investigated, T_{dis} = 7.8°C.

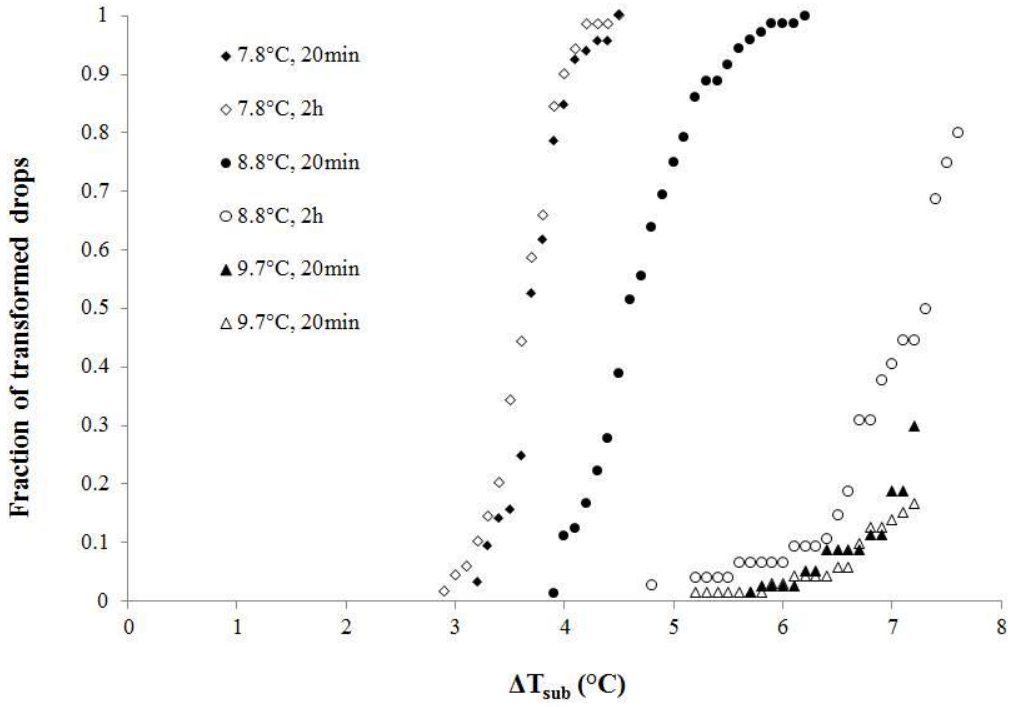

Figure 3. 8. Conversion curves: fraction of converted drops vs. subcooling ΔT (2nd hydrate formation, with various melting conditions of the first hydrate). There are two experiments for the same melting conditions T_{dis} = 9.7°C, t_{dis} = 20 min.

3.3.3. Lateral growth of the polycrystalline CP hydrate film at the water drop surface

The image analysis allows to detect not only the apparent onset of hydrate formation in each drop but also its end, corresponding to the completion of lateral growth of the polycrystalline CP hydrate at the surface of the water drop (see 3.1.2). Any further change in the water drops is imperceptible with our imaging system over the time scale (less than one hour) of the observations. As already emphasized, the hydrate shell that is formed around the drop strongly limits the transfer of water and guest (CP) molecules required for forming some new hydrate, and hydrate growth in the direction normal to the surface (i.e., shell thickening) is therefore very slow in comparison to the preceding lateral growth. As explained above an estimate of the lateral growth rate is obtained by dividing the drop length by the duration of lateral growth. Growth durations (and hence lateral growth rates) are observed to depend primarily on subcooling and to range from about 7 minutes for onset subcoolings equal to 3°C to about 2.5 min for the maximum onset subcooling of 7.2°C, corresponding to lateral growth rates of respectively 2.2 and 6.7µm/s. We will see below how this subcooling has an

effect not only on the lateral growth rates but also on the size and shape of the hydrate crystals. Such growth rate values are consistent with the values observed in other systems with low guest solubilities in water [36]. Lateral growth rates are known to be controlled primarily by heat transfer processes at the edge of the advancing hydrate film [37]: they strongly increase with subcooling as the heat generated by the hydrate formation is evacuated more efficiently. A quantitative comparison with existing models is not attempted here for two reasons. First, temperature varies slightly over the duration of drop conversion events (which lasts as long as 7 minutes, corresponding to a variation of 1.4°C). Second, the CP film that is sandwiched between the water drop and the PFA wall presumably plays a role (since the CP feeds hydrate growth along the water/CP interface); unfortunately, the properties of this film (such as its thickness) are not accessible.

3.3.4. Is the CP-in-water emulsion responsible for the memory effect?

We attempt here to provide (partial) answers to the (difficult) question of the origin of the memory effect in hydrate formation. This question has recently been tackled experimentally by Zylyftari et al. [12] for hydrate formation from melting ice (called here 'first formation'), but the concern here is hydrate formation from a system that has contained the hydrate shortly before (called 'second formation'). One obvious possible cause for facilitated hydrate second formation is the CP-in-water emulsion that appears as turbidity at the top of water drops where CP hydrate has been previously formed and then melted (see Figure 3.4c) (we will study this subject in more detail afterwards). Another view of this emulsion is given in Figure 3.9, which is obtained by using both the LED ring and coaxial lightings. This emulsion, which results from the melting of the CP hydrate polycrystalline layer initially covering the water drop, is fairly stable: the turbidity persists over long periods of time, meaning that the coalescence between oil (CP) droplets is a very slow process. Even after heating some time at 22°C, the CP-in-water emulsion is still there and remains stable. In all of our single-drop observations of second hydrate formation, the hydrate turns out to appear in the turbid region of the drop surface - that is, where some CP-in-water emulsion is present at the drop surface. This can be seen in Figure 3.10, which shows snapshots of a water drop (with a CP-in-water emulsion at the top) undergoing the hydrate conversion process: first, a grey spot (shown by an arrow) appears in the emulsion, which gets darker and bigger and moves a few seconds later (about 17 in this example) towards the apex of the drop, where then hydrate growth proceeds over the whole drop surface. Indeed, these regions contain a

large quantity of CP/water interfaces (the high surface/volume ratio of each CP-in-water drop enhances the probability of hydrate formation), as well as residual clusters or structured water (associated with melted hydrate) that have been invoked to play a role in hydrate nucleation, but are still to be observed and verified experimentally.

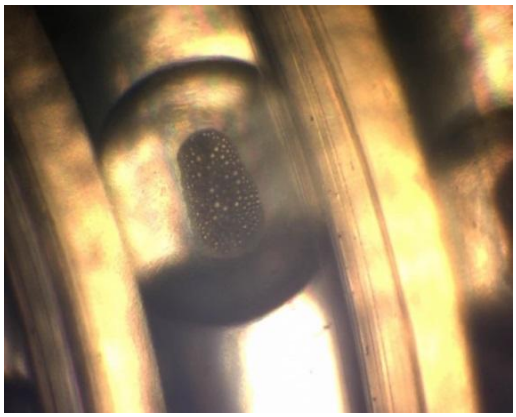

Figure 3. 9. Zoomed in view of the CP-in-water emulsion at the top of the water drop (following hydrate melting at 8.8°C during about 1h). Small oil (CP) droplets are visible.

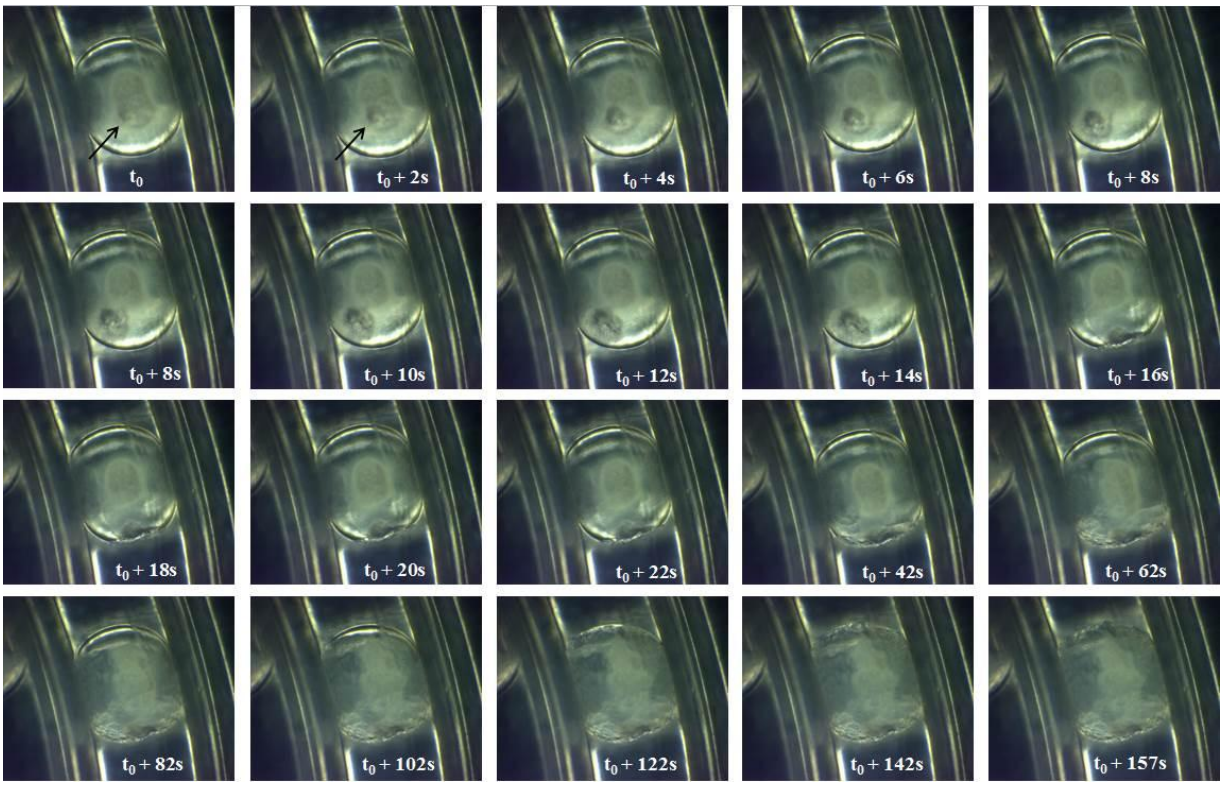

Figure 3. 10. Snapshots of (second) hydrate formation in a single water drop (melting conditions of the first hydrate: T_{dis} = 8.8°C, t_{dis} = 2 h). CP hydrate appears at t_0 (T ~ 2°C) as a darker spot (black arrow) in the emulsion, which then moves slowly and reaches the drop apex at t_0 + 17.4 s; then hydrate grows and covers the whole drop surface within about 2.5 min.

The water used in all experiments reported above is pure deionized water. Waters of low ionic strength and simple oils are able to form stable emulsions - e.g., by ultrasonication - because of the negative electrical charges carried by the water/oil interface at pH higher than about 3 [38]. In order to check and verify that the turbidity on top of the water drops (Figure 3.4c) is a CP-in-water emulsion stabilized by the electrical charges at the water/CP interfaces, and to assess whether this emulsion really plays a role in hydrate reformation, one experiment has been carried out using weak brine (NaCl 0.1 M) instead of pure water: the addition of this electrolyte is expected to screen the repulsive interactions between the CP droplets and therefore to promote their coalescence, i.e. destroy the emulsion. As shown in Figure 3.11, water drops resulting from CP hydrate melting (at T_{dis} = 8.8°C and t_{dis} = 20 min) are transparent, meaning that, unlike its pure water counterpart, the CP-in-weakly salted water emulsion is not stable (as expected).

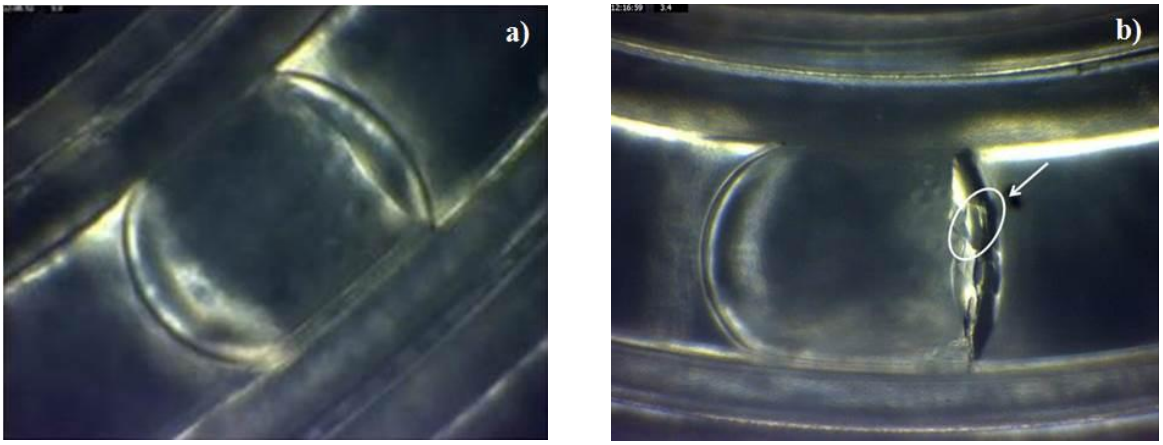

Figure 3. 11. Zoomed in views of a) a single 0.1 M NaCl water drop in CP after hydrate melting at T_{dis} = 8.8°C (the drop is transparent: compare with Figure 3.4c) and b) in the course of 2nd hydrate formation (see text). A hexagonal plate is clearly apparent in the oval on the right.

The corresponding conversion curve is displayed in Figure 3.12, together with the conversion curve of its pure water/CP counterpart for the same dissociation conditions. An inhibiting effect of the electrolyte (NaCl) is apparent: the subcoolings required to trigger hydrate formation in the weakly salted water drops are larger by about 0.5°C than in the pure water/CP system (the equilibrium temperatures T_{eq} have been considered to be the same in both systems, which is a reasonable approximation for such low salinity, cf. Sakemoto et al. [30]). An analysis of hydrate lateral growth rates shows considerable slowing down in the

weakly salted water/CP system, where a rate half that in the pure water/CP system is measured (this slowing down might be due to a thinner CP film in-between the water drop and the PFA wall due to a change in the wettability, with therefore lesser CP feeding hydrate growth along the water drop surface).

A close-up view of hydrate formation in a single weakly-salted water drop (Figure 3.11b) shows a somewhat different morphology from the case of pure water (Figure 3.4d), with hydrate growth being hindered by the tube walls. Hydrates appear first at one of the two apex of the water drop, where they form large hexagonal plates, and possibly octahedra (Figure 3.13), as has already been observed with other structure II hydrates [39].

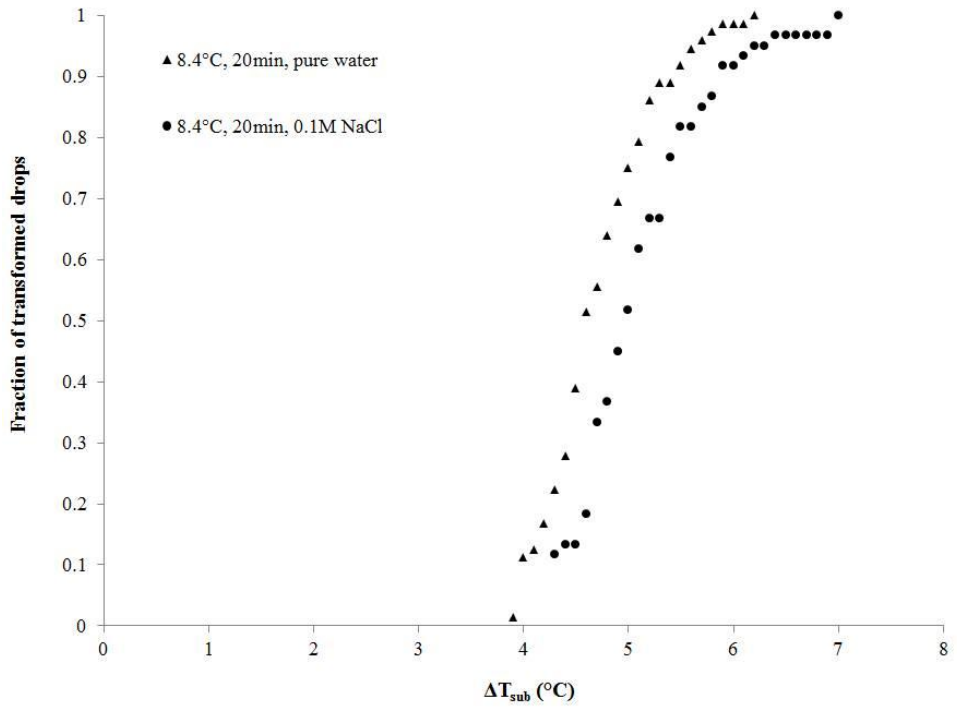

Figure 3. 12. Conversion curves (2nd hydrate formation) vs. subcooling $\Delta T = T_{eq} - T$: effect of water salinity.

As a partial answer to the question raised above, it can be stated that the existence of a CP-in-water emulsion can have an effect on the second hydrate formation but is not totally responsible of the observed memory effect because its presence does not mean that the second formation is going to take place. We are sure about this affirmation because when heating at

22°C the emulsion is still present, but a second hydrate formation is impossible. From the other hand, hydrate reformation and memory effects are still present in hydrate-forming systems such as CP and weakly-salted water where CP-in-water emulsions are not stable, so we cannot say that the emulsion is absolutely necessary for the formation of hydrates. This CP-in-water emulsion will be studied in more detail in the following chapters. In addition, the effects of solid-like impurities (particles) that are always present and trapped at interfaces (here, the water/CP interfaces) cannot be overlooked: the pits, pores and scratches of these particles might be able to stabilize hydrate nuclei beyond their melting temperature, as shown by theoretical analysis [40], [41].

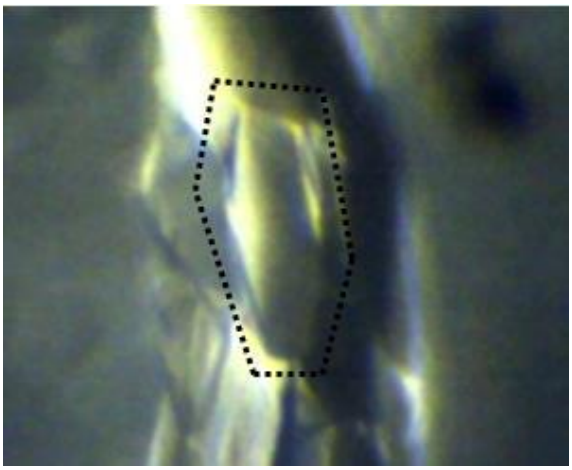

Figure 3. 13. Close-up view of CP hydrate at the interface between CP and weakly-salted (0.1 M NaCl) water: a hexagonal plate is visible in the front and (possibly) octahedra at the rear.

3.4. Conclusions

Droplet-based millifluidic methods, which have been widely used for studying crystallization of a wide range of molecules in various solvents, can also be successfully adapted and implemented to the study of the kinetics of hydrate crystallization. Because they are run rapidly and need small amounts of sample, these are low-cost and versatile methods that nonetheless give insights not only into crystal growth and morphology, but also and simultaneously, into features that are otherwise hard to access, such as the nucleation step of crystallization. The work presented here is focused on the memory effect, which is one of the most studied (and perhaps controversial) aspects of hydrate crystallization kinetics in recent

years. Results are in line with recent data obtained by conventional methods, but with the improvement of providing better statistics (due to the much larger number of reactors) while allowing crystal growth and other phenomena, such as the production of stable emulsions from hydrate melting in pure water, to be investigated, questioned for their role in hydrate reformation and visualized on the scale of a few microns. To the best of our knowledge, this is the first time that millifluidic methods are being used for the studying hydrate crystallization. Opportunities for future developments include the understanding of the mechanisms by which additives act as promoters or inhibitors of hydrate crystallization, as we will see in the next chapter and, on a more practical side, the high throughput testing of additives as well as the evolution of the above setup and procedure towards higher pressures allowing the study of gas hydrates of practical interest.

REFERENCES

[1] Chatti, I., Delahaye, A., Fournaison, L., Petitet, J. P., **2005**. Benefits and drawbacks of clathrate hydrates: a review of their areas of interest. Energy Conversion and Management *(46)*, 1333-1343.

[2] Eslamimanesh, A., Mohammadi, A.H., Richon, D., Naidoob, D., Ramjugernath, D., **2012**. Application of gas hydrate formation in separation processes: a review of experimental studies. The Journal of Chemical Thermodynamics *(46)*, 62-71.

[3] Vekilov, P.G., **2010**. Nucleation. Crystal Growth & Design *10* (12), 5007-5019.

[4] Takeya, S., Hori, A., Hondoh, T., Uchida, T., **2000**. Freezing-memory effect of water on nucleation of CO_2 hydrate crystals. The Journal of Physical Chemistry B *(104)*, 4164-4168.

[5] Ohmura, R., Ogawa, M., Yasuoka, K., Mori, Y.H., **2003**. Statistical study of clathrate-hydrate nucleation in a water/hydrochlorofluorocarbon system: search for the nature of the "Memory Effect". The Journal of Physical Chemistry B *(107)*, 5289-5293.

[6] Maeda, N., Wells, D., Becker, N.C., Hartley, P.G., Wilson, P.W., Haymet, A.D.J., Kozielski, K.A., **2011**. Development of a high pressure automated lagtime apparatus for experimental studies and statistical analyses of nucleation and growth of gas hydrates. Review of Scientific Instruments *(82)*, 065109.

[7] Dalmazonne, D., Hamed, N., Dalmazonne, C., Rousseau, L., **2006**. Application of high pressure DSC to the kinetics of formation of methane hydrate in water-in-oil emulsion. Journal of Thermal Analysis and Calorimetry *(85)*, 361-368.

[8] Davies, S.R., Hesterb, K.C., Lachance, J.W., Koh, C.A., Sloan, E.D., **2009**. Studies of hydrate nucleation with high pressure differential scanning calorimetry. Chemical Engineering Science *(64)*, 370-375.

[9] Sloan, E.D. and Koh, C.A., **2008**. Clathrate Hydrates of Natural gases, 3rd ed. CRC Press, Boca Raton, Florida.

[10] Sun, C.Y., Peng, B.Z., Dandekar, A., Maa, Q.L., Chen, G.J., **2010**. Studies on hydrate film growth. Annual Reports Section "C" (Physical Chemistry) *(106)*, 77-100.

[11] Leng, J., Salmon, J.B., **2009**. Microfluidic crystallization. Lab on a Chip *(9)*, 24-34.

[12] Zylyftari, G., Ahuja, A., Morris, J.F., **2014**. Nucleation of cyclopentane hydrate by ice studied by morphology and rheology. Chemical Engineering Science *(116)*, 497-507.

[13] Dirdal, E.G., Arulanantham, C., Sefidroodi, H., Kelland, M.A., **2012**. Can cyclopentane hydrate formation be used to rank the performance of kinetic hydrate inhibitors? Chemical Engineering Science *(82)*, 177-184.

[14] Zhang, Y., Debenedetti, P.G., Prud'homme, R.K., Pethica, B.A., **2004**. Differential scanning calorimetry studies of clathrate hydrate formation. The Journal of Physical Chemistry B *(108)*, 16717-16722.

[15] Whitman, C.A., Mysyk, R., White, M.A., **2008**. Investigation of factors affecting crystallization of cyclopentane clathrate hydrate. The Journal of Chemical Physics *(129)*, 174502.

[16] Karanjkar, P.U., Lee, J.W., Morris, J.F., **2012a**. Calorimetric investigation of cyclopentane hydrate formation in an emulsion. Chemical Engineering Science *(68)*, 481-491.

[17] Karanjkar, P.U., Lee, J.W., Morris, J.F., **2012b**. Surfactant effects on hydrate crystallization at the water–oil interface: hollow-conical crystals. Crystal Growth & Design *(12)*, 3817-3824.

[18] Lo, C., Zhang, J., Somasundaran, P., Lee, J.W., **2010**. Raman spectroscopic studies of surfactant effect on the water structure around hydrate guest molecules. The Journal of Physical Chemistry Letters *(1)*, 2676-2679.

[19] Peixinho, J., Karanjkar, P.U., Lee, J.W., Morris, J.F., **2010**. Rheology of hydrate forming emulsions. Langmuir *(26)*, 11699-11704.

[20] Zylyftari, G., Lee, J.W., Morris, J.F., **2013**. Salt effects on thermodynamic and rheological properties of hydrate forming emulsions. Chemical Engineering Science *(95)*, 148-160.

[21] Zhang, J.S., Lo, C., Couzis, A., Somasundaran, P., Wu, J., Lee, J.W., **2009**. Adsorption of kinetic inhibitors on clathrate hydrates. The Journal of Physical Chemistry C *(113)*, 17418-17420.

[22] Li, X., Negadi, L., Firoozabadi, A., **2010**. Anti-agglomeration in Cyclopentane Hydrates from Bio- and Co-surfactants. EnergyFuels *(24)*, 4937-4943.

[23] Nakajima, M., Ohmura, R., Mori, Y.H., **2008**. Clathrate hydrate formation from cyclopentane-in-water emulsions. Industrial & Engineering Chemistry Research *(47)*, 8933-8939.

[24] Cha, M., Baek, S., Morris, J., Lee, J.W., **2014**. Hydrophobic particle effects on hydrate crystal growth at the water/oil interface. Chemistry: An Asian Journal *(9)*, 261-269.

[25] Sefidroodi, H., Abrahamsen, E., Kelland, M.A., **2013**. Investigation into the strength and source of the memory effect for cyclopentane hydrate. Chemical Engineering Science *(87)*, 133-140.

[26] Taylor, C.J., Miller, K.T., Koh, C.A., Sloan, E.D., **2007**. Macroscopic investigation of hydrate film growth at the hydrocarbon/water interface. Chemical Engineering Science *(62)*, 6254-6533.

[27] Pruppacher, H.R., **1995**. A new look at homogeneous ice nucleation in supercooled water drops. Journal of the Atmospheric Sciences *(52)*, 1924-1933.

[28] Johnson, D.A., Hallett, J., **1968**. Freezing and shattering of supercooled water drops. Quarterly Journal of the Royal Meteorological Society *(94)*, 468-482.

[29] King, W.D., Fletcher, H.D., **1973**. Pressures and stresses in freezing water drops. Journal of Physics D: Applied Physics *(6)*, 2157-2173.

[30] Sakemoto, R., Sakamoto, H., Shiraiwa, K., Ohmura, R., Uchida, T., **2010**. Clathrate hydrate crystal growth at the seawater/hydrophobic –guest– liquid interface. Crystal Growth & Design *10* (3), 1296-1300.

[31] Duchateau, C., Glénat, P., Pou, T-E., Hidalgo, M., Dicharry, C., **2010**. Hydrate precursor test method for the laboratory evaluation of kinetic hydrate inhibitors. Energy Fuels *24* (2), 616.

[32] del Villano, L., Kelland, M.A., **2011**. An investigation into the laboratory method for the evaluation of the performance of kinetic hydrate inhibitors using super- heated gas hydrates. Chemical Engineering Science *(66)*, 1973-1985.

[33] Kelland, M., **2014**. Personal Communication.

[34] Sear, R.P., **2007**.Nucleation at contact lines where fluid–fluid interfaces meet solid surfaces. Journal of Physics: Condensed Matter *(19)*, 466106.

[35] Poon, G.G., Peters, B., **2013**. A stochastic model for nucleation in the boundary layer during solvent freeze-concentration. Crystal Growth & Design *(13)*, 4642-4647.

[36] Saito, K., Sum, A.K., Ohmura, R., **2010**. Correlation of hydrate-film growth rate at the guest/liquid – water interface to mass transfer resistance. Industrial & Engineering Chemistry Research *(49)*, 7102-7103.

[37] Mochizuki, T., Mori, Y.H., **2006**. Clathrate-hydrate film growth along water/hydrate-former phase boundaries - numerical heat-transfer study. Journal of Crystal Growth *(290)*, 642-652.

[38] Marinova, K.G., Alargova, R.G., Denkov, N.D., Velev, O.D., Petsev, D.N., Ivanov, I.B., Borwankar, R.P., **1996**. Charging of oil–water interfaces due to spontaneous adsorption of hydroxyl ions. Langmuir *(12)*, 2045-2051.

[39] Knight, C.A., Rider, K., **2002**. Free-growth forms of tetrahydrofuran clathrate hydrate crystals from the melt: plates and needles from a fast-growing vicinal cubic crystal. Philosophical Magazine A *(82)*, 1609-1632.

[40] Sear, R.P., **2012**. The non-classical nucleation of crystals: microscopic mechanisms and applications to molecular crystals, ice and calcium carbonate. International Materials Reviews *(57)*, 328-356.

[41] Christenson, H.K., **2013**. Two-step crystal nucleation via capillary condensation. CrystEngComm *(15)*, 2030-2039.

CHAPTER 4

INHIBITION OF CYCLOPENTANE HYDRATE FORMATION AND DISSOCIATION

4.1. Introduction

In this chapter, we investigate the effects of a few water-soluble polymers (listed below) known to be good hydrate inhibitors at low concentrations (100 ppm) on the formation and melting of CP hydrate. We use the setup described in the preceding chapter in its zoom mode to observe one single reactor (drop). Dirdal et al. [1] used some inhibitors in order to study the effect on hydrate formation for the water/CP hydrate forming system. Three of the inhibitors they used have also been studied by other authors and have been chosen and analyzed in this work. They are: poly(N-vinyl pyrrolidone) (PVP), vinyl pyrrolidone : vinyl-caprolactam copolymer (VP/VCap) and polyvinyl-caprolactam (PVCap). Their structures are shown in Figure 4.1.

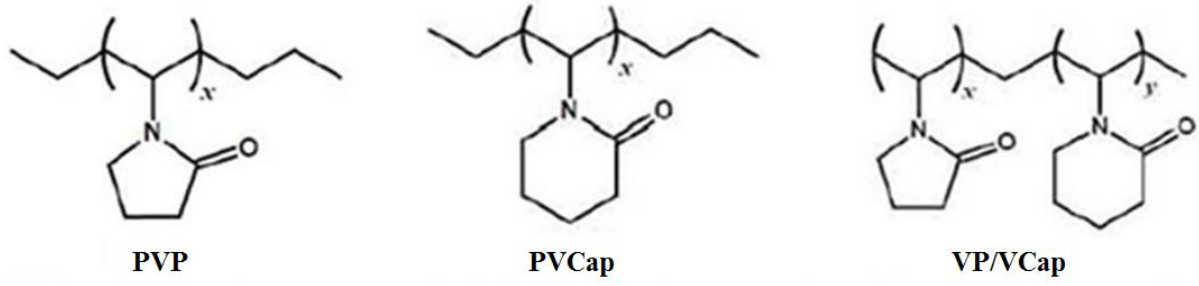

Figure 4. 1. Structure of the inhibitors used in our experiments: PVP, PVCap and VP/VCap.

The chapter is divided as follows. The first part explains the experimental setup and classifies the differences found when working with inhibitors with respect to the pure system. The 'Results' section first introduces the new experimental procedure and temperature sequence used in these experiments and then shows the experimental results obtained for the first hydrate formation, the melting process and the second hydrate formation. These results are obtained from the observation of one single drop. In the 'Discussion' section we analyze the possible adsorption mechanisms of inhibitors on the hydrate surface, the superheating phenomenon observed when melting, which led us to design and perform some ellipsometric experiments, and the morphology of the hydrate layer, which depends on the type of inhibitor adsorbed to the surface. Finally the conclusions are shown.

4.2. Experimental procedure

First of all we prepared the aqueous polymer solutions. In line with the authors cited above, a concentration of 100 ppm was chosen, as this concentration has been observed to be sufficient for inducing an inhibiting effect on hydrate formation. PVP (40000 Mw) was obtained from Sigma-Aldrich while PVCap (low molecular weight) and VP/VCap (55000 Mw) were provided by BASF.

The experimental setup is exactly the same as the one explained in chapter 3. Drops of the above aqueous polymer solutions in cyclopentane (CP) are created in the same way than for the pure system: in particular, the injection rates of these two fluids are 30 ml/hour for water and 100 ml/hour for CP, in order to create a train of regular water drops. Here, the focus is one single drop, which is visualized by using the zoom x16.

We initially tried to study the effect of these inhibitors on the induction time and the velocity at which the hydrate film grew all along the water drops. But we encountered some difficulties not observed with the pure water/CP system (chapter 3), which we finally decided to address. While performing the experiments with the procedure described in chapter 3 (1^{st} formation, dissociation and 2^{nd} formation), we noted two differences with respect to the observations made with the pure water/CP system:

i) when melting the ice drop at about 2°C no CP hydrate (or very little) was formed on the water drop surface over time scales of a few hours, whereas this formation is instantaneous in the case of pure water (cf. Figure 3.7 upper).

ii) once the first hydrate is formed (in a way that is going to be explained below), its melting by raising the temperature slightly above 7.2°C (T_{dis} of the pure system water + CP) does not occur.

To address these differences, we designed a procedure which slightly differs from that used in chapter 3, and which is described at the beginning of the Results section.

4.3. Results

4.3.1. New experimental procedure and temperature sequence

(i) First hydrate formation. The first part of the experiment is exactly the same as that described in chapter 3. Water drops need to first be transformed into ice, which is then melted in order to obtain a water drop covered with a CP hydrate crust. For this purpose, temperature is decreased down to -26°C, then raised fast to -5°C and finally slower to 2°C. When we use inhibitors, in the first hydrate formation step (at about 2°C) hydrate formation at the surface of the water drop is not spontaneous, unlike what was observed with pure water: no CP hydrate (or very little) is detected at the surface of the water drop over time scales of some hours, i.e. the 100 ppm of polymer added to the water has an inhibiting effect on hydrate formation (Figure 4.2). In order to form the CP hydrate crust at the surface of the water drop temperature had to be decreased from 2°C down to 0°C.

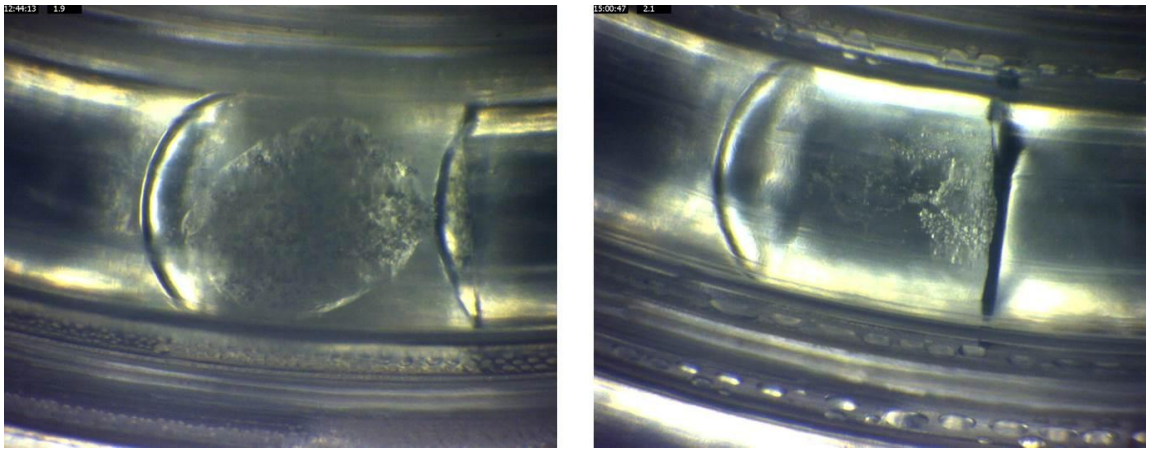

Figure 4. 2. Left: Ice melting of the water + VP/VCap (100 ppm)/CP system (T slightly above 0°C): a liquid/liquid interface is observed. Right: only a small part of the water drop surface appears to be covered with grains and possibly a hydrate film after spending 3 hours at T = 2°C.

(ii) CP hydrate melting. Once CP hydrates have been formed, as we do not know the exact melting temperature T_{dis} when inhibitors are added to the pure system, the train of water drops is submitted to a temperature ramp of 0.5°C/min up to 7.2°C (the value of T_{dis} in the absence of inhibitor) and from there temperature is raised by steps. Drops are left during 30 minutes at each temperature in order to see whether the hydrate melt at this temperature.

The next and last step is the second hydrate formation, which is achieved by decreasing the temperature from just above the melting temperature to 0°C through a 0.2°C/min ramp.

4.3.2. Experimental results

In this section, the results of the first hydrate formation for drops of an aqueous phase containing 100 ppm of the inhibitors listed above are first presented. A comparison is made with the pure system water + CP. Then the results of the melting of this first hydrate are presented, followed by the observations of a second hydrate formation, compared again with those of the pure system.

4.3.2.1. First hydrate formation

We present here the observations made for the three inhibitors tested. After ice melting we usually observe white spots that gather at the surface of the water drop (Figure 4.3). We hypothesize that these spots are hydrate nuclei that are formed after ice melting but, since

inhibitors are present and possibly adsorb on these nuclei, the later growth is very difficult. However, by decreasing temperature down to 0ºC, the driving force for hydrate growth is increased and a hydrate film is formed all over the drop surface.

In some experiments, we skipped the latter step (decrease in temperature from 2 to 0°C) and increased the temperature to about 10°C for a few minutes, and then decreased the temperature to 0°C at the same rate (0.2°C/minute). These white spots were visible all over the temperature sequence. Surprisingly, the water drop covered itself with a hydrate film, meaning that the above white spots were effectively hydrate nuclei. The only reason why the latter hydrate formation could take place easily is that stable hydrate nuclei were present all the time. But why are these nuclei stable at a temperature that high (10°C)? This point will be addressed below.

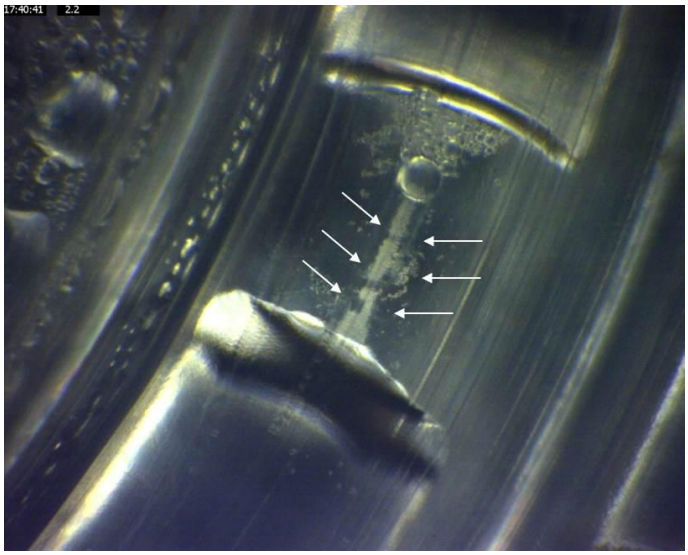

Figure 4. 3. White spots (‘hydrate nuclei’) present on top of the water drop after ice melting (T = 2°C) of the system with VP/VCap. These white spots do not disappear when temperature is raised up to 10°C for some minutes and hydrate second formation can be possible when T is lowered back to 0°C.

4.3.2.2. Hydrate melting

First of all, we show the observations of the melting process made for each system. As we have said before, the time we spend at each temperature step is 30 minutes. Note that all the images in Figures 4.4, 4.5, 4.6 and 4.7 are taken when the set temperature has just been reached, i.e. at the beginning of the step, except from the last one (h), which is taken 15 minutes after reaching the last temperature (9.5°C). In all cases some little changes are

apparent as soon as temperature exceeds 7.2°C, but the significant changes, i.e. the complete hydrate melting, are observed at higher temperatures.

- *Pure system water/CP:* in Figure 4.4 we have a sequence of images of the CP hydrate melting when we work with the pure system. As we observe, the CP hydrate is completely melted at 8.5°C (e) (a liquid/liquid interface, which is smooth and has a constant curvature, is easily observed).

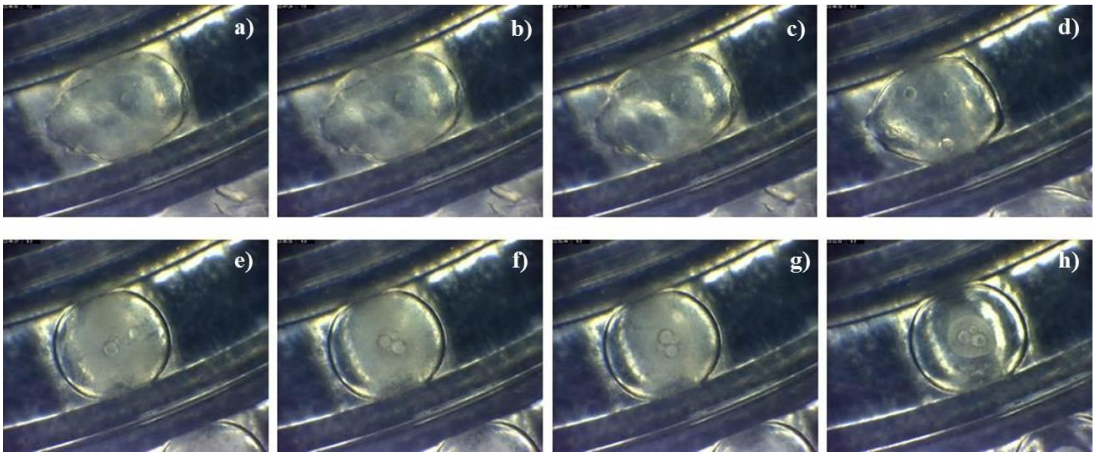

Figure 4. 4. Dissociation of the pure system water + CP. a) 7.2°C, b) 7.5°C, c) 7.7°C, d) 8°C, e) 8.5°C, f) 9°C, g) 9.5°C and h) 9.5°C 15min . The hydrate is completely melted at 8.5°C.

- *Water + PVP (100 ppm)/CP:* in Figure 4.5 the temperature sequence characteristic of this system is shown. In this case the CP hydrate is not completely melted at 8.5°C but at 9°C (at least) (f), which is the moment where we start to observe the liquid/liquid interface.

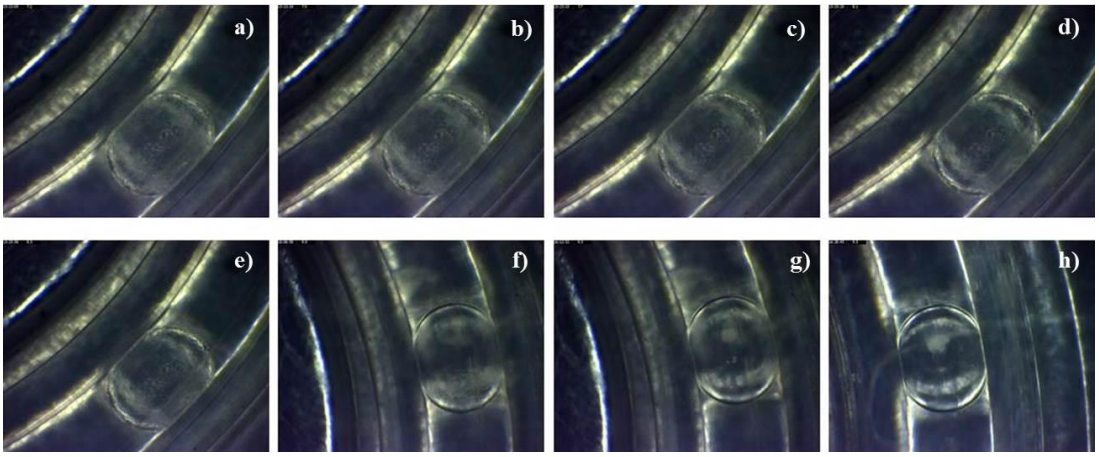

Figure 4. 5. Dissociation of the water + PVP (100 ppm)/CP system. a) 7.2°C, b) 7.5°C, c) 7.7°C, d) 8°C, e) 8.5°C, f) 9°C, g) 9.5°C and h) 9.5°C + 15min. The hydrate is completely melted at 9°C

- *Water + VP/VCap (100 ppm)/CP:* the hydrate with VP/VCap is more difficult to melt, as observed in Figure 4.6. We do not see it melting during all the temperature sequence shown in the image, i.e. it does not melt even staying at 9.5°C during 15 minutes. In this case, for melting the hydrate the temperature needs to be raised up even more, as we will see below. This agrees with what Bruusgaard et al. observed in their study of the effect of VP/VCap, among others, on the morphology of methane hydrates [2]. VP/VCap produces a slower dissociation than the pure system despite the thicker appearance of the hydrate skin on the pure water droplet.

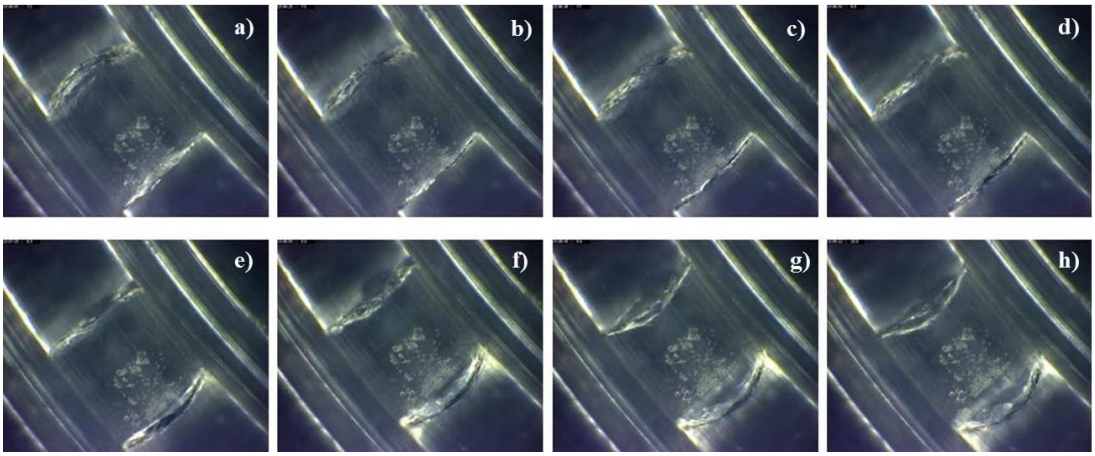

Figure 4. 6. Dissociation of the water + VP/VCap (100 ppm)/CP system. a) 7.2°C, b) 7.5°C, c) 7.7°C, d) 8°C, e) 8.5°C, f) 9°C, g) 9.5°C and h) 9.5°C + 15min. The hydrate is not completely melted after 15minutes at 9.5°C.

- *Water + PVCap (100 ppm)/CP:* this system is even more difficult to melt than the previous one (VP/VCap), as we will see below. We observe in Figure 4.7, as we do for the previous system, that the hydrate is not melted after all the temperature sequence and temperature needs to be raised up in order to completely melt it.

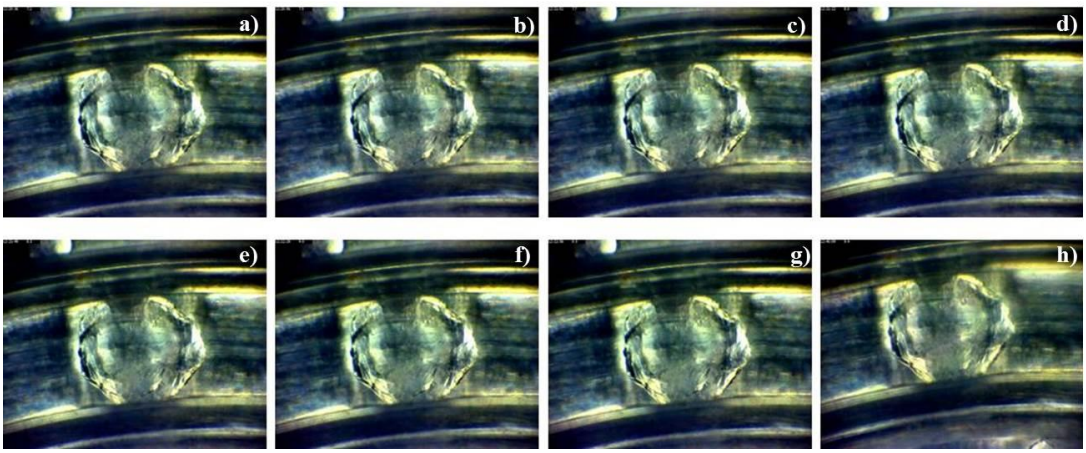

Figure 4. 7. Dissociation of the water + PVCap (100 ppm)/CP system. a) 7.2°C, b) 7.5°C, c) 7.7°C, d) 8°C, e) 8.5°C, f) 9°C, g) 9.5°C and h) 9.5°C + 15min. The hydrate is not melted at all after 15min at 9.5°C.

After analyzing the results, we could say that the two stronger inhibitors of hydrate melting are VP/VCap and PVCap, since the hydrate is not melted after 15 minutes at 9.5°C for none of them. In Figure 4.8 we compare VP/VCap with PVCap in order to observe any evidence of one of them melting later than the other. The temperature has just continued being increased by steps of 0.5°C and kept during 30 minutes.

- *VP/VCap:* at 11-11.5°C (Figure 4.8 left c and d) the liquid/liquid interface can be clearly observed so we conclude that the hydrate is completely melted.

- *PVCap:* we cannot say that the hydrate is completely melted at 11.5°C (Figure 4.8 right d). The interface is not a liquid/liquid interface yet. For this system the temperature continued to be raised in order to find the temperature at which the liquid/liquid interface (complete hydrate melting) was observed. The first temperature at which we observe a smooth surface is around 13°C, as we observe in Figure 4.9.

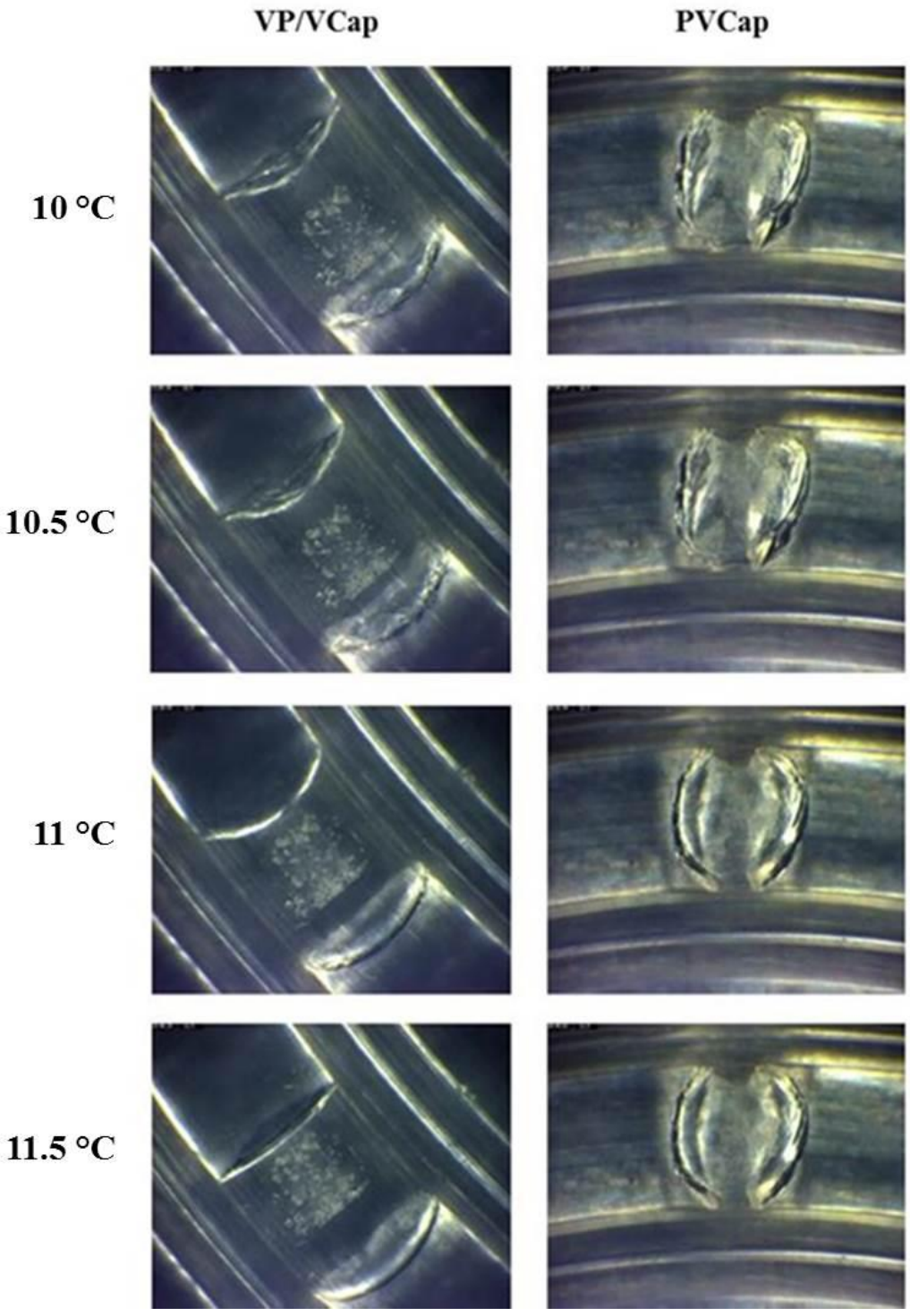

Figure 4. 8. Comparison of hydrate dissociation for the system with VP/VCap (100 ppm) and that with PVCap (100 ppm). Both systems need a temperature higher than 9.5°C to completely dissociate. Note that at 11.5°C the hydrate with VP:VCap is completely melted but the hydrate with PVCap is not.

Figure 4. 9. Complete dissociation of the hydrate system water + PVCap (100 ppm)/CP at 13°C. See that a liquid/liquid interface is observed.

Therefore, we conclude that there exists a kind of superheating effect in these systems since they end up melting at temperatures much higher than the equilibrium temperature of the pure system (7.2 °C) (Table 4.1). The superheating $\Delta T_{superheating}$ is defined as the temperature difference between the end of the melting process and the melting temperature of the pure water/CP hydrate system, i.e. T_{dis} = 7.2 °C.

Inhibitor	**$\Delta T_{superheating}$**
PVP	2.3°C
VP/VCap	4.3°C
PVCap	5.8°C

Table 4. 1. Difference between the dissociation temperature of CP hydrates with each inhibiting system and the equilibrium temperature 7.2°C.

In presence of 100 ppm of PVCap and VP/VCap, the melting of the CP hydrate requires to heat the system by more than 4 degrees above the dissociation temperature of the pure system. In presence of 100 ppm of PVP this interval is reduced to around 2 degrees. This agrees with the observations by Duchateau et al. [3], who observed in their studies (not with

CP but with other guest gases) a minimum superheating of 4.6 to 5.6°C with PVCap. It thus appears that these additives are not only kinetic inhibitors but can be considered as thermodynamic inhibitors as well.

In fact it appears that it is difficult to give a precise melting temperature to the hydrate crystal as it is the case for the pure system where T_{dis} = 7.2°C. In presence of inhibitors the hydrate melts step by step between 7.2 °C and a maximum temperature given by 7.2°C plus the superheating temperature given in Table 4.1. This peculiar phenomenon is discussed below.

4.3.2.2.1. The superheating phenomenon

The "superheating phenomenon" occurs in our experiments during hydrate melting in the presence of some inhibitors. This phenomenon could be explained thanks to the Gibbs-Thomson effect, as we will see below. The superheating effect has been documented for antifreeze proteins added to ice crystals: these proteins have also an effect on the ice melting temperature, which is slightly increased by a few tenths of °C [4], [5]. As stated by the authors, the melting is very progressive: "After half of the ice crystals melted (around 0.22 ºC above T_{melt}), we maintained the temperature without change for 1h. During the initial 10 minutes of temperature maintenance, half of the remaining crystals melted, but further melting was not observed in the following 50 minutes at this T." We observe a similar phenomenon in our experiments, with ice being replaced by CP hydrate. Part of the hydrate crystal melts at one temperature but after some time (around 5 minutes) no further melting is observed (during 30 minutes) unless the temperature is increased by at least 0.5°C more (as has been observed to various extents for all three inhibitors). By increasing temperature above T_{dis} we see how drops start moving (meaning that melting has started), but just during a short time. They move again when higher temperature is applied, etc. In the end, we reach a temperature, corresponding to T_{dis}+ $\Delta T_{superheating}$, where the crystal is completely melted.

4.3.3. Second hydrate formation

After the determination of the melting temperature, we have studied the second hydrate formation for the pure system water + CP and with two inhibitors: PVP and VP/VCap, with the objective of determining the growth velocity of the hydrate crust. The same hydrate formation temperature is set for all the systems. The procedure consists of

decreasing the temperature at 0.2°C/min from the melting temperature previously determined to 0.2°C – 0.5°C. Some aspects like the induction time and growth velocity of the hydrate layer are analyzed below. Our second hydrate formation experiments are performed after a complete melting of the first hydrates (appreciated by the liquid/liquid nature of the interface), contrary to the experiments by Lederhos et al. (1996) [6], who performed second hydrate formation experiments by re-cooling the system prior to complete dissociation of the methane hydrates to characterize the inhibition effect of PVCap. We aim to study both hydrate nucleation and growth processes, so complete hydrate melting is first required. Two sets of experiments have been carried out, one for studying hydrate nucleation and the other for studying the hydrate growth process. In the nucleation experiments, the first CP hydrate is melted at (or just above) the melting temperature previously determined for each system. In the growth experiments, the experiments carried out with inhibitors are compared to one with pure water in which the melting temperature of the first CP hydrate is high enough to ensure that the second hydrate does not start forming before reaching 0°C.

4.3.3.1. Second hydrate nucleation

In order to compare the nucleation process of the different systems, the same least severe melting conditions are set (i.e. the minimum melting temperature at which the hydrate is completely melted, taking into account that it is different for each system, as explained before). For the hydrate forming system with PVP and VP/VCap, the second hydrate formation experiments have been performed after dissociating the first hydrate just above their melting temperatures: 9.5°C and 11.5°C during 20 minutes, respectively. For the system with inhibitors, we first performed some second hydrate formation experiments at low subcooling but hydrate formation was very hard (we did not get to form them).They not only need to reach 0 - 0.5°C for starting the second hydrate formation but also to wait some time at this temperature before something is observed.

The data for the second hydrate formation of the pure system, taken from chapter 3, are those in which the first hydrate is melted at the least severe conditions (just above T_{dis} = 7.2°C): 7.8°C during 20 minutes. In these conditions, we do not need to reach 0 - 0.5°C and wait some time to start observing the second formation because it is achieved before. Between 4.3°C and 3.1°C, 90% of the water drops are reconverted into hydrate, as we have explained

in chapter 3. Moreover, the 100% of the water drops are reconverted into hydrate before reaching 0°C.

In Table 4.2 we show the temperature at which the second hydrate formation starts for the pure system water + CP and also the time needed for the system with inhibitors to start being observed after reaching 0.5°C.

KHI	**T (°C)**	**t (min) at T = 0.5°C**
Pure system	4.3	-
PVP	-	4
VP/VCap	-	17

Table 4. 2. Second hydrate nucleation. Average temperature at which the second hydrate formation starts (for the pure system previously melted at T= 7.8°C during 20 minutes). For the system with inhibitors (T_{dis} = 9.5°C for PVP and T_{dis} = 11.5°C for VP/VCap), the temperature at which the second hydrate formation starts is always 0 – 0.5°C. We show the time needed to start observing the second hydrate formation after reaching 0.5°C. We see here that VP/VCap is a better inhibitor of hydrate formation.

This is in agreement with what other authors have observed. Dirdal et al. [1] studied the induction times of CP hydrate formation in batch for subcoolings ΔT_{sub} = 7.8°C and found that the best inhibitor was PVCap. The induction time for this inhibitor was about twice the time needed when they used VP/VCap which, at the same time, was seven times larger than the induction time observed for PVP (our measured times obey the same trend). May et al [7] studied the effect of PVP and VP/VCap on hydrates of a synthetic gas (CH_4, C_2H_6, C_3H_8, i-C_4H_{10}, n-C_4H_{10}, N_2 and CO_2) too. They found VP/VCap to be a more performant inhibitor because the subcooling (driving force) required for forming hydrates was higher (13.1K) compared to 8.4K for PVP (in our two experiments the temperature is fixed at T = 0 - 0.5°C). Duchateau et al. [3] made a comparison between the subcoolings (ΔT_{sub}) measured with and without additives at methane/propane hydrate reformation and found that higher subcoolings were needed for reforming hydrates with PVCap than for those that had PVP.

4.3.3.2. Second hydrate growth

Once nucleation takes place and we start to see the beginning of the hydrate growth, measurements of the hydrate crust growth velocity are carried out.

In this type of experiments, the same hydrate formation temperature needs to be set in all systems (as we have already seen in chapter 3, ΔT_{sub} plays an important role on the growth velocity so the hydrate formation temperature has to be the same) for having a comparable measurement of the hydrate film growth velocity. We have seen that the hydrate forming systems with inhibitors (PVP and VP/VCap) need the hydrate formation temperature to be 0.5°C (at least) to start forming after melting them at 9.7°C and 11.5°C during 20 minutes, respectively.

The same hydrate formation temperature needs to be set for the pure system in order to make a good comparison. We saw in chapter 3 that by melting the first CP hydrate at 9.7°C during 20 minutes most of the drops started the second hydrate formation at 0 – 0.5°C and not before, so these are the melting conditions chosen in this experiment.

Table 4.3 shows the growth times and velocities for a drop 1.4 mm average length. In Figure 4.10 the hydrate film growth for the system with VP/VCap after melting the hydrate at 11.5°C during 20 minutes is shown. It takes the hydrate film about 15 minutes to completely cover the water drop. Data were extracted through visual analysis of the differences between consecutive images. A decrease in translucency is clearly observed over time between the first and the last image, meaning that the liquid drop is covered with a hydrate crust.

KHI	Melting T (t = 20 minutes) (°C)	Growth time (approx., minutes)	Growth velocity (µm/s)
Pure system	9.7	4	6.6
PVP	9.7	8	2.8
VP/VCap	11.5	15	1.6

Table 4. 3. Growth velocities of the hydrate layer on the water surface after dissociation for the pure system, the system with PVP and the system with VP:VCap. For all of them, the temperature of hydrate reformation is 0°C. Note that VP/VCap is better inhibitor than PVP.

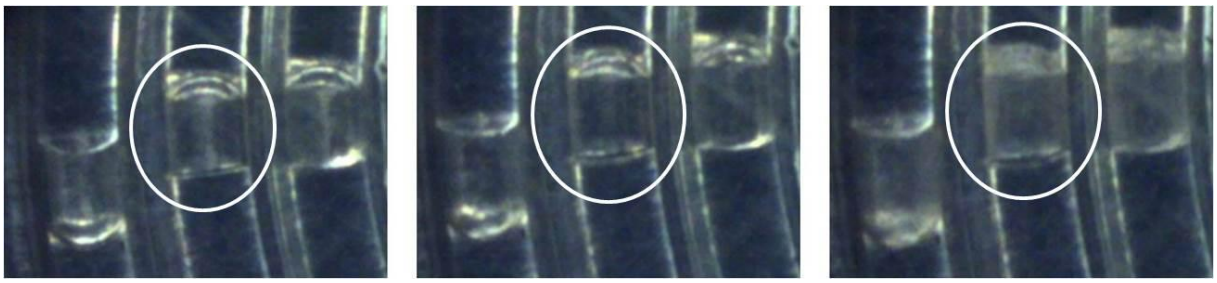

Figure 4. 10. Second hydrate formation for the system with VP/VCap after a dissociation at 11.5°C during 20min. a) Liquid drop (T > 0.5°C). b) Hydrate film starts growing (t_0, T = 0.3°C). c) End of the hydrate film growth (t_0 + 15min, T = 0.5°C).

4.4. Discussion

4.4.1. Possible chemical inhibiting processes

In the literature we find different views about the possible action mechanisms of inhibitors. A lot of authors agree with the fact that the action mechanism is related to the adsorption of these inhibitors on the hydrate crystals already nucleated, not allowing them to reach a critical size for a later growth. Two different mechanisms are proposed found in the literature and are summarized in Figure 4.11: the polymers either adsorb onto the hydrate surface and form a steric barrier (Figure 4.11b) that prevents the mass transfer between CP molecules and the hydrate surface, or create a perturbation of the local water molecules organization, by linking them through hydrogen bonds, thus preventing hydrate growth (Figure 4.11c). Perrin et al. suggest a mechanism of irreversible inhibition. They believe that there are many pendant groups all along the polymer length when the adsorption to the hydrate is considered [8]. To them, this adsorption occurs through hydrogen bonding between the amide functionality (through the carbonyl group) and the hydrate surface, and this is why growth becomes more difficult. In order to fully desorb, this would require the many pendant groups to all simultaneously desorb from the surface, and this is why the adsorption is considered as irreversible, because that would be quite difficult.

Lederhos et al. [6] suggest that lactam rings adsorb to the hydrate surface during hydrate growth through hydrogen bonding by the amide group, sterically blocking the hydrate growth, as shown in Figure 4.11b. Also, as polymers form a network around hydrate nuclei, agglomeration and further growth is more difficult. Zhang et al. performed some experiments in order to relate the type of adsorption of these polymers on cyclopentane hydrates with the

superior performance of the PVCap, compared with PVP [9]. The adsorption isotherms give a Langmuir type for PVP, i.e. monolayer adsorption, while PVCap follows a BET type, i.e. the polymer is adsorbed in a multiple-layer way. They affirm that "the larger molecule size and its multiple-layer adsorption of PVCap give rise to a larger thickness of adsorption layer compared to the adsorption case of PVP".

There are also some experiments that assure that the hydrogen bond network between water molecules and the inhibitor is perturbed (Figure 4.11c). Davenport et al. propose a two-step mechanism of KHI action that involves a) disruption of local water order in liquid water by KHIs and b) inhibitor binding to the growing crystal surface [10].

Another possible explanation could fit with what Zylyftari et al. suggest in [11]. They study the salt effects on the thermodynamic and rheological hydrate properties. To them, NaCl acts as a thermodynamic inhibitor, and one of the possible mechanisms by which the formation temperature is lowered (more subcooling is required) is because the salt ions interact with the water molecules preventing formation of hydrate cages. If we think in the same way for inhibitors, we could suggest that the amide hanging groups interact with the water molecules, and this avoids the hydrate cages to be formed (in accordance with the perturbation inhibition theory by Lederhos et al. [6]).

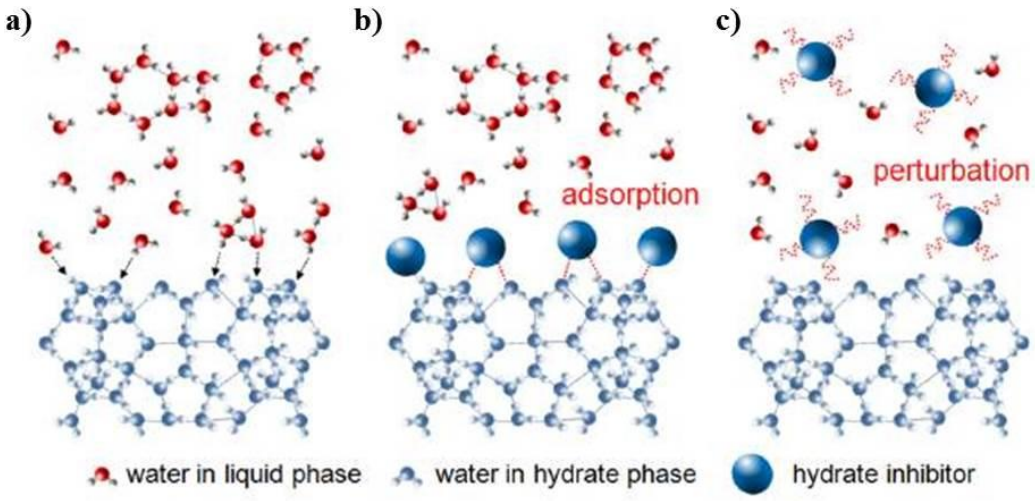

Figure 4. 11. Schematic diagram showing hydrate formation and the possible inhibition process [12]. a) In the pure system, liquid water molecules that are close to the hydrate surface participate in hydrate formation. b) The adsorption inhibition theory involves the adsorption of inhibitors on the hydrate surface, preventing it to grow. c) The perturbation inhibition theory involves the perturbation of the organization of the local water molecules, preventing hydrate growth.

These are just some possible explanations about the hydrate inhibition process that could fit with our observations, because it is very difficult for us to observe at smaller scales with high resolution. However, microscopic experiments will be done in the future trying to get insights into these inhibition mechanisms. But all these theories are not valid for explaining the superheating effect discussed above and the reason why the adsorption of inhibitors on the hydrate surface would increase the melting temperature. In next section we argue that the Gibbs-Thomson effect and a 'patchy' (by clumps) polymer adsorption might be responsible for superheating phenomenon.

4.4.2. Superheating of hydrate crystals: a consequence of patchy polymer adsorption?

Here we present a mechanism that has been invoked for explaining why and how anti-freeze proteins (AFPs) act not only to decrease the freezing temperature of water, but also to raise the ice melting temperature. This mechanism has been recently observed experimentally: Celik and coworkers [4], [5] and others [13] have shown that these AFPs adsorb onto the ice crystals and prevent them (i) from growing to a macroscopic size when T is decreased a few degrees below 0°C, and (ii) from melting when T is raised slightly above the ice melting temperature, i.e. 0°C. The latter phenomenon is the superheating phenomenon mentioned above, which has been shown to exist for hydrate melting in presence of some polymers as well (see the experimental results reported above). In the case of ice, Celik and coworkers measured superheating values as high as 0.44°C for some hyperactive AFPs.

The explanation proposed by Celik et al. is the following. AFPs adsorb onto the ice surface at some attachment sites (i.e. in a 'patchy' configuration) and suppress ice growth or melting locally. In the growth process, the crystal may bulge between the attachment sites, and the freezing point is decreased by the Gibbs-Thomson effect, namely, that a curved surface has a lower freezing point than a flat one. In the melting process, however, the crystal surface is curved as well, but the curvature is in the opposite sense (Figure 4.12): the melting point is increased by virtue of the Gibbs-Thomson effect. This effect is based on the Gibbs free energy equation for closed systems at the equilibrium. Our system is composed by a solid (CP hydrate) and a liquid phase (liquid CP):

$$dG = VdP - SdT$$

In the equilibrium the Gibbs free energy of the liquid and the solid phase must be equal:

$$dG_S = dG_L$$

$$V_S dP_S - S_S dT = V_L dP_L - S_L dT$$

The pressure of the liquid phase P_L does not suffer any change: $V_L dP_L = 0$

$$dP_S = \frac{(S_S - S_{L)}}{V_S}\, dT$$

The second law of thermodynamics says that $dS = \frac{\delta Q}{T}$, so:

$dP_S = -\frac{Q}{T_0 V_S} dT$ $(S_S - S_L < 0)$, being T_0 the equilibrium temperature.

The pressure of the solid phase P_S changes and is determined by the Laplace equation at curved interfaces: $dP_S = \frac{2\gamma}{R}$, being γ the interfacial tension between both phases and R the curvature radius of the solid/liquid interface.

$$\frac{2\gamma}{R} = -\frac{Q\ (T - T_0)}{T_0 V_S}$$

$$R = -\frac{2\gamma T_0 V_S}{Q\ (T - T_0)}$$

When R < 0 (Figure 4.12) T > T_0, which is the case of the increase in temperature (superheating) with respect to the equilibrium temperature we observe when melting hydrates with inhibitors.

So, according to the Gibbs-Thomson condition, the mean curvature is related to the relative shift in melting temperature. For our system, γ = 30 mN/m, T_0 = 280K, T – T_0 = 5K (for the most performing inhibitor) and $Q_{CP\ hydrate}$ = ~284 kJ/kg [14], so the curvature radius R between two clumpsof inhibitor adsorbed on the hydrate surface should be around 12 nm.

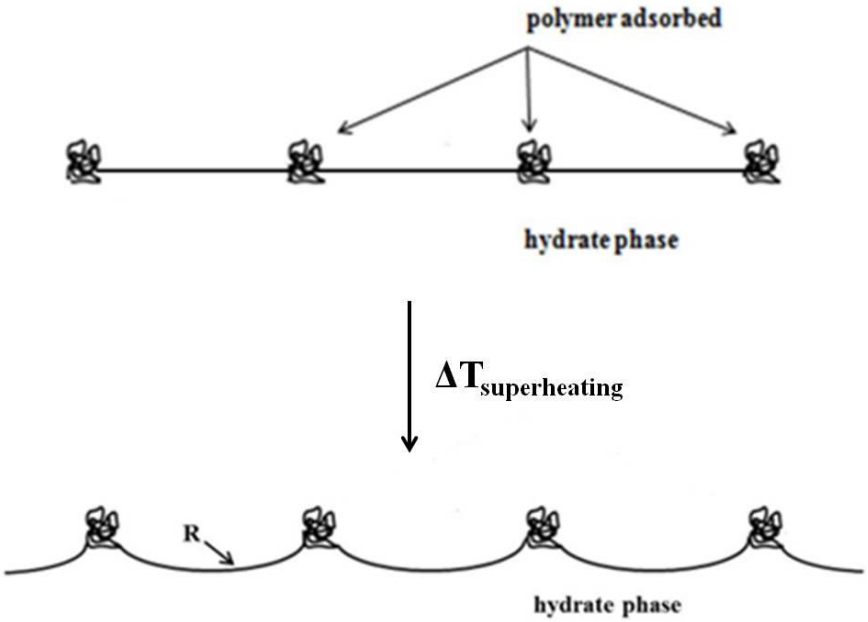

Figure 4. 12. Schematics of the polymer adsorption onto the hydrate surface and the curvature produced during the melting process. A curved surface (with radius R) like that in the scheme has higher melting point than a flat one.

But how can we relate the way inhibitors adsorb to the hydrate surface with the Gibbs-Thomson effect? We present here our view about how the process is. One hypothesis is that these inhibitors act with repect to hydrate melting in the same way as AFPs act with respect to ice melting. The adsorption of inhibitors onto the hydrate surface not only slows down hydrate growth but also produces some irregularities and inhomogeneities on the hydrate surface (this could be related with what Bruusgaard et al. observe [2]. See Apendix 2). We do not know whether inhibitors adsorb onto the surface by patches or linearly, but the inhibitor concentration (100 ppm) is so low that it is unlikely that the whole hydrate surface is covered with polymer layer(s). Therefore a reasonable hypothesis is that these polymers adsorb onto the hydrate surface as patches (or clumps). The concentration at the surface is principally controlled by the monomer/surface interaction whereas further out the layer is controlled by the chain length [15]. Unfortunately, we cannot estimate the adsorption density because the specific surface of the hydrate phase is not known.

Since we have only some parts of the hydrate surface covered with the inhibitor, when we increase the temperaure above 7.2°C the hydrate present between two inhibitor adsorption sites or ‘patches’ is going to suffer a certain curvature as the melting process takes place.

There will be a maximum curvature or superheating at which the hydrate will melt completely for each system as given by the Gibbs-Thomson relationship. As discussed above, we have calculated this curvature to be around 12 nm for a superheating of about 5.6ºC..

The ellipsometric experiments presented below address the question of whether polymers adsorb as patches or more uniformly on hydrate surfaces by considering strongly hydrophilic silica rather than hydrate. Silica wafers are flat surfaces that allow the use of ellipsometry to investigate polymer adsorption on the surface.

4.4.2.1. Adsorption of inhibitors on solid hydroxylated surfaces

Experiments by ellipsometry have been carried out in order to obtain more information about the adsorption of inhibitors on the hydrate surface. Unfortunately, the surface of CP hydrates is not smooth enough to allow the measurement of thin films thickness by ellipsometry. We then decided to study the adsorption of inhibitors on a silicon wafer. Silicon is oxidized in contact with air and a silica (SiO_2) multilayer is formed on top of the wafer surface.

The surface properties of amorphous silica depend on the presence of silanol groups [16]. At a sufficient concentration these groups render the surface hydrophilic. The idea is to provide the silica surface with hydroxyl groups (OH groups) by treating it with water or aqueous solutions (Figure 4.13).

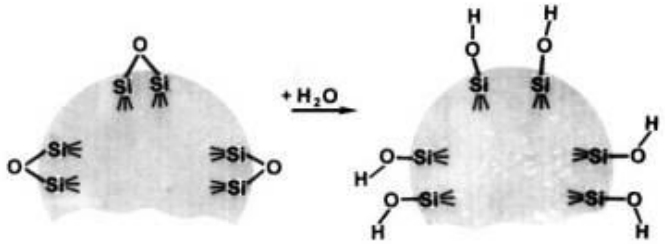

Figure 4. 13. The formation of silanol groups on the silica surface [16].

The silica surface now contains –OH groups, exactly like hydrate surfaces. The hydrogen of the –OH group is susceptible to form hydrogen bonds with any electronegative atom, so we can make the similarity and use the silanol groups (Si-OH) as if they were a piece of hydrate (Figure 4.14).

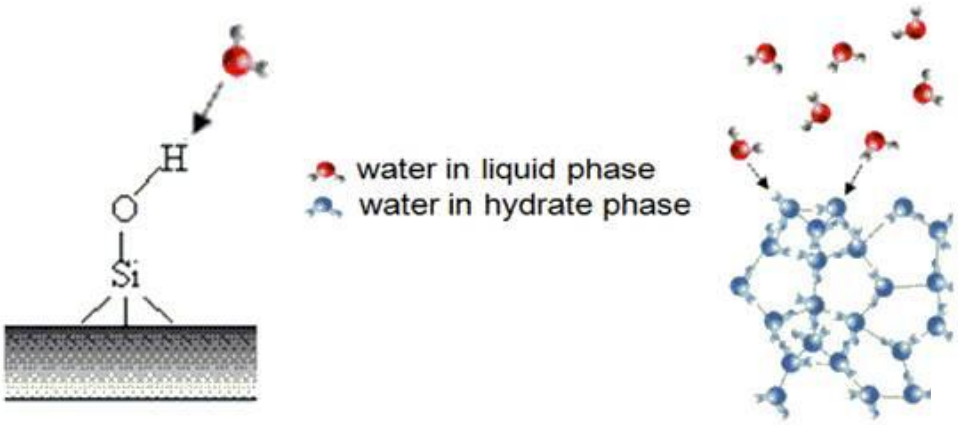

Figure 4. 14. Analogy between a silicon wafer surface and a hydrate surface. Both surfaces have the possibility of forming hydrogen-bonds with liquid water molecules that may be around, due to the free –OH group present in both systems (we cannot know the quantity of free –OH groups there will be in a silicon wafer and on a hydrate surface, but the analogy can be made).

We cleaned the silicon wafers with piranha solution during 10 minutes, in order to have the maximum number of groups –OH on the surface and then washed with pure water. Once dry, we immersed one of them into the solution containing 100 ppm of the first inhibitor during 15 minutes, and the same with the others. This time is enough for the inhibitor to be adsorbed to the silanol groups present on the surface. Then we let them drain the excess of polymer solution, we rinsed with distilled water and finally we dried them before being placed on the ellipsometer.

Figure 4.15 shows the raw Brewster angle microscopy images (taken at an incident angle of 76.8°) of the silicon wafers without any inhibitor adsorbed, and after immersing them in the different polymeric solutions. The color code varies from black (nothing is adsorbed) to white passing through brown, red and yellow. A dark surface can be considered as uncovered and the clearer it appears the thicker the adsorbed film. In Figure 4.15b we observe that PVP adsorbs on the wafer surface (the image is clearer than Figure 4.15a which is that of the uncovered surface) and forms a thin film of uniform thickness (the dark and bright horizontal lines are wafer scratches). Figure 4.15c and 4.15d show the adsorption of VP/VCap and PVCap, respectively. Bright spots reveal the presence of polymeric grains, probably resulting from a non-homogeneous, ‘patchy’ adsorption.

Ellipsometric measurements also allow determining thickness maps of the analyzed surfaces. For that, many photographs are taken at different polarizer and analyzer angles in order to determine the ellipsometric angles δ and ψ of each image pixel. This allows the ellipsometer software to produce a 3D map by using a model that simulates the layer deposited on the silicon surface. The silicon is ideally treated as a medium of refractive index n_{Si} = 4 surrounded by air (n_{air} = 1). The resulting thin film after inhibitor adsorption takes place is composed of the silica layer covering the silicon surface and the polymeric layer adsorbed on top. This global thin film is simulated as forming a single layer of refractive index n_{layer} = 1.46. This coarse approximation is acceptable since both the polymeric material and silica have more or less the same refractive index value.

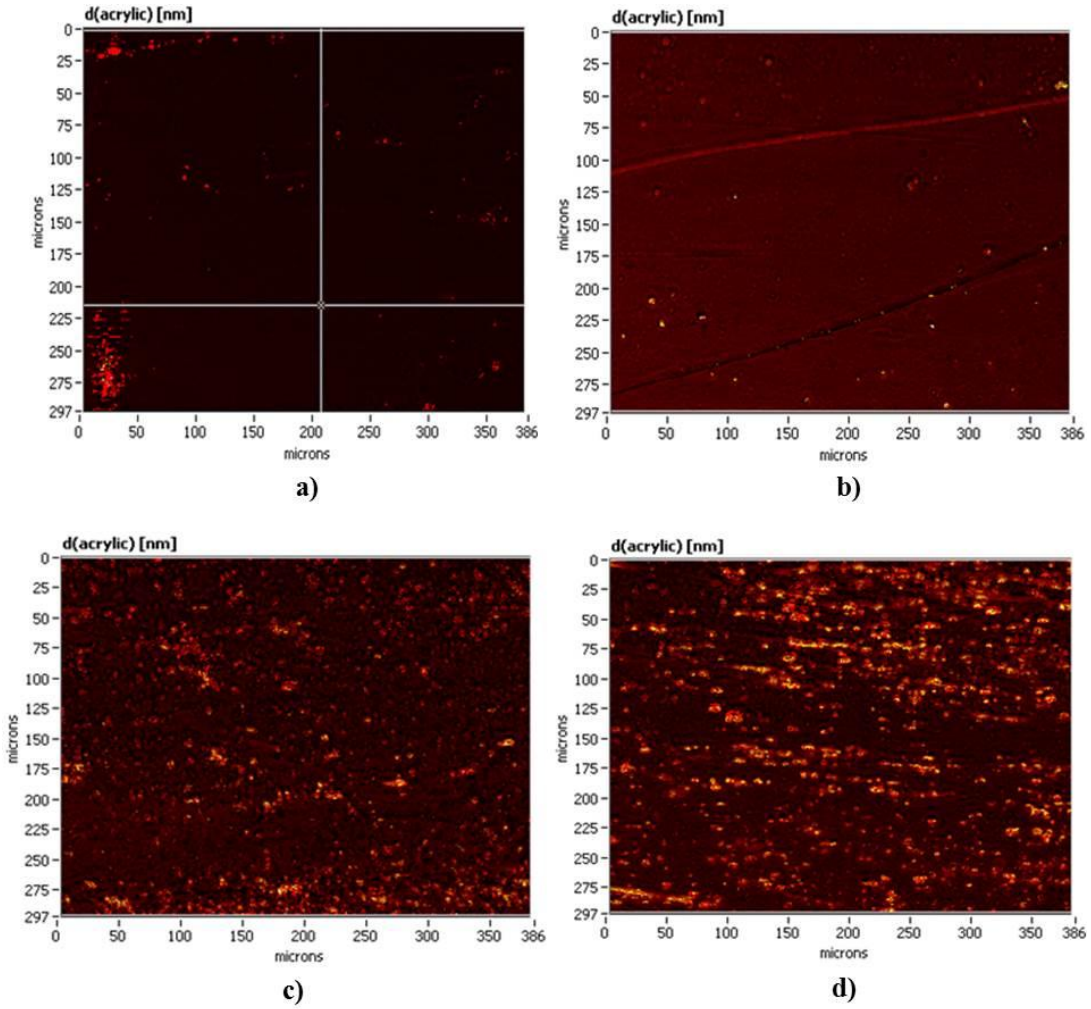

Figure 4. 15. Brewster angle microscopy images of the silicon wafers with: a): no inhibitor, b) PVP, c) VP/VCap, d) PVCap.

Figure 4.16 presents the raw data given by the software, i.e. the thickness of the model layer that simulates both the polymeric layer and also the silica layer. Figure 4.16a shows that without any polymer adsorbed, a layer of about 1 - 2 nm is observed. This layer corresponds to the silica formed on the silicon surface in presence of water as we discussed before. Figure 4.16b shows a uniform thickness layer of about 3 - 4 nm revealing that PVP forms a more or less homogeneous film of about 2 nm all over the surface (the peaks are considered as impurities).

In contrast to this homogeneity, the adsorption of VP/VCap and PVCap do not produce homogeneous layers. VP/VCap forms a film with comparable thickness to that of PVP (about 2 nm) but with local inhomogeneities with thicknesses up to 6 - 8 nm (Figure 4.16c). PVCap shows the same behavior but the thickness of the patches is higher (about 10 – 16 nm) (Figure 4.16d). For PVCap the film inbetween the patches has more or less the same thickness as the films observed for the two others inhibitors. Note that the maps shown in Figure 4.16 are smothed by a numerical procedure, so the patch extents are overestimated in the interfacial plane. For having a more realistic information about the lateral extent of these patches one has to reffer to Figure 4.15.

In summary, PVCap is the most compatible inhibitor (and VP/VCap to a less extent) with the ‘patchy model’ because it forms the most inhomogeneous film onto the hydrate surface. The result is that PVCap is observed to be the best inhibitor of hydrate formation. Further experiments will be done in this field.

This technique has allowed us to determine the way the inhibitors adsorb on a silicon wafer, which we assimilate to the adsorption to a hydrate surface. Unfortunately the resolution is not high enough for giving us the separation between two patches of inhibitor adsorbed, which is related tothe curvature radius of the surface between two clumps, so the calculation presented abovewhere we find ~12 nm as the curvature radius cannot be verified. We show the morphology of the CP hydrate crusts with the three different inhibitors adsorbed with respect to the observations made in the ellipsometric experiments in Annexe B.

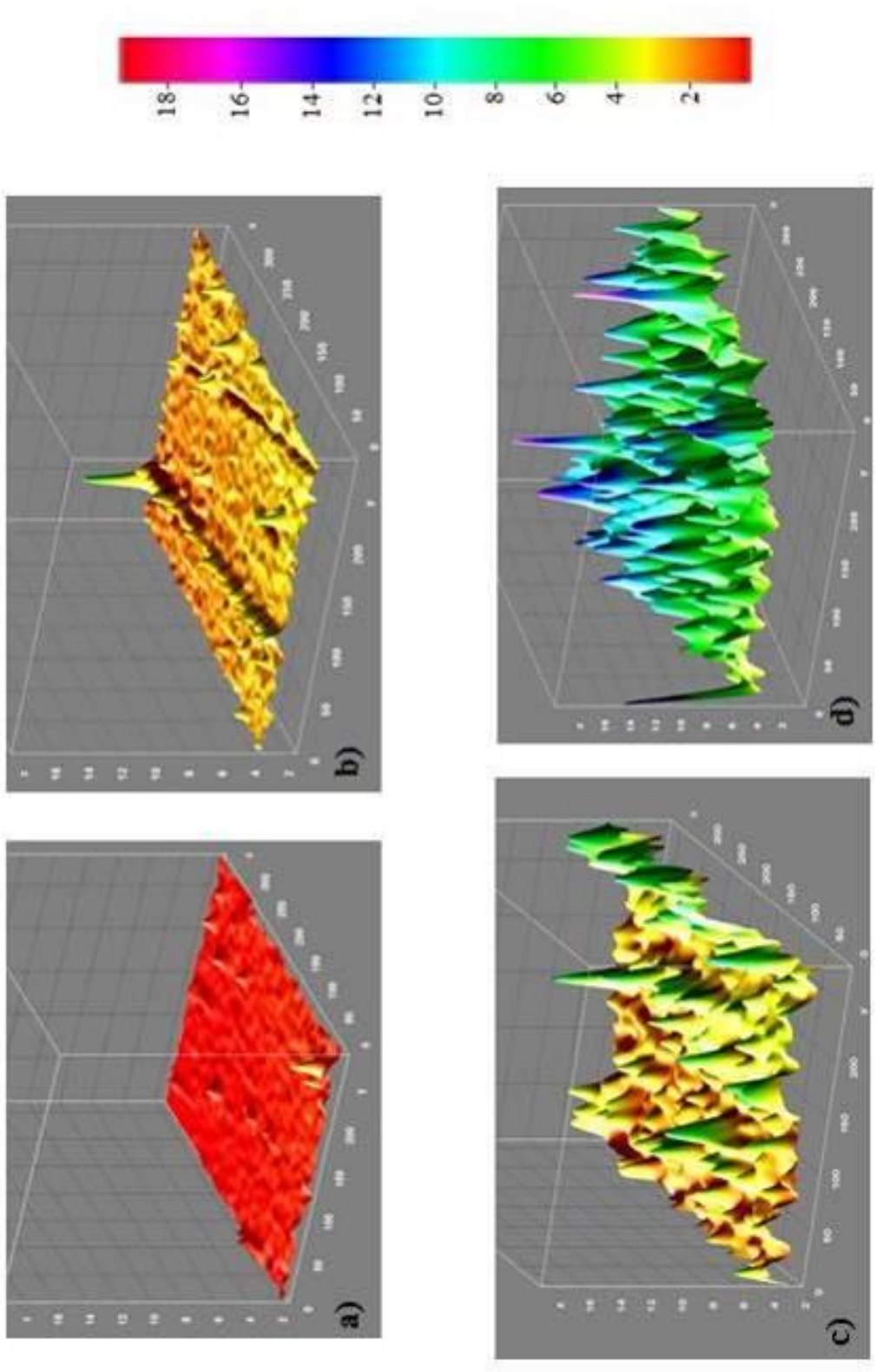

Figure 4. 16. 3D maps showing the thickness of polymeric layers deposited on silicon wafers with: a) no inhibitor, b) PVP, c) VP/VCap, d) PVCap. The color code is common to all images to allow direct comparison between experiments. It represents layer thicknesses comprised between 0 and 20 nm.

4.5. Conclusions

The experimental setup of the preceding chapter in its zoom mode has been very useful for the study of the effect of some kinetic inhibitors on CP hydrate formation and dissociation.

In the early stages of this investigation, we realized that these inhibitors not only have an effect on hydrate formation, but also on hydrate dissociation. This last topic has therefore been the main focus of our investigation. The inhibitors investigated act by raising the melting temperature up to 5.6°C, possibly due to the Gibbs-Thomson effect. By adsorbing as patches at the hydrate/water interface, these polymers or at least the most active of them, promote a curvature in the crystal surface during the melting process; this curvature stabilizes the hydrate phase above the normal melting temperature. The more patchy-like adsorption of PVCap (and VP/VCap to a less extent) seems to be supported by the ellipsometric measurement on hydrophilic silica, considered here to be representative of the hydrate/water interface.

We have also checked the inhibiting power of two of these polymers (PVP and VP/VCap) during the second hydrate formation. The effect of the inhibitors is to decrease the formation temperature and to slow down the hydrate crust growth velocity. We have observed that lower temperatures (higher T_{sub}) are needed when we use inhibitors compared to the pure system. Once reached the maximum subcooling, VP/VCap is more performing than PVP: the induction time, i.e. the time we have to wait at that maximum subcooling until we detect the onset of hydrate formation, is about four times higher with VP/VCap than with PVP. We have also compared the hydrate crust growth velocities, which is about four times lowerwith PVP and 2.5 times lower with VP/VCap as with the pure system (for the maximum possible subcooling, i.e., 7°C).

The ellipsometric experiments had led us to the conclusion that PVP adsorbs to the hydrate surface in a homogeneous manner (thickness = 2 nm), whereas VP/VCap and PVCap form a film that possesses in addition local inhomogeneities (‘patches’) extending from the surface at distances up to 6 - 8 nm and about 10 – 16 nm, respectively.

All these results suggest that the inhibiting power of these polymers, that is, their ability to prevent the growth of CP hydrate crystals when temperatures is lowered below the

melting temperature T_{dis}, is related to their ability to prevent the melting of the same hydrates when heating above T_{dis}. We observe that the ranking of these inhibitors with respect to the two effects is the same: PVP < VP/VCap < PVCap, being PVCap the strongest inhibitor.

REFERENCES

[1] Dirdal, E. G., Arulanantham, C., Sefidroodi, H., Kelland, M. A., **2012**. Can cyclopentane hydrate formation be used to rank the performance of kinetic hydrate inhibitors? Chemical Engineering Science *(82)*, 177-184.

[2] Bruusgaard, H., Lessard, L. D., Servio, P., **2009**. Morphology Study of Structure I Methane Hydrate Formation and Decomposition of Water Droplets in the Presence of Biological and Polymeric Kinetic Inhibitors. Crystal Growth & Design *9* (7), 3014-3023.

[3] Duchateau, C., Glénat, P., Pou, T-E., Hidalgo, M., Dicharry, C., **2010**. Hydrate Precursor Test Method for the Laboratory Evaluation of Kinetic Hydrate Inhibitors. Energy Fuels *24* (1), 616-623.

[4] Celik, Y., Graham, L. A., Mok, Y-F., Bar, M., Davies, P. L., Braslavsky, I., **2010**. Superheating of ice crystals in antifreeze protein solutions. Proceedings of the National Academy of Sciences *(107)*, 5423-5428.

[5] Celik, Y., Drori, R., Pertaya-Braun, N., Altan, A., Barton, T., Bar-Dolev, M., Groisman, A., Davies, P. L., Bralavsky, I., **2013**. Microfluidic experiments reveal that antifreeze proteins bound to ice crystals suffice to prevent their growth. Proceedings of the National Academy of Sciences *110* (4), 1309-1314.

[6] Lederhos, J. P., Long, J. P., Sum, A., Christiansen, R. L., Sloan Jr., E. D., **1996**. Effective kinetic inhibitors for natural gas hydrates. Chemical Engineering Science *51* (8), 1221-1229.

[7] May, E. F., Wu, R., Kelland, M. A., Aman, Z. M., Kozielski, K. A., Hartley, P. G., Maeda, M., **2014**. Quantitative kinetic inhibitor comparisons and memory effect measurements from hydrate formation probability distributions. Chemical Engineering Science *107* (0), 1-12.

[8] Perrin, A., Musa, O. M., Steed, J. W., **2013**. The chemistry of low dosage clathrate hydrate inhibitors. Chemical Society Reviews *42* (5), 1996-2015.

[9] Zhang, J. S., Lo, C., Couzis, A., Somasundaran, P., Wu, J., Lee, J. W., **2009**. Adsorption of Kinetic Inhibitors on Clathrate Hydrates. The Journal of Physical Chemistry C *(113)*, 17418-17420.

[10] Davenport, J. R., Musa, O. M., Paterson, M. J., Piepenbrock, M-O. M., Fucke, K., Steed, J. W., **2011**. A simple chemical model for clathrate hydrate inhibition by polyvinylcaprolactam. Chemical Communications *(47)*, 9891-9893.

[11] Zylyftari, G., Lee, J. W., Morris, J. F., **2013**. Salt Effects on Thermodynamic and Rheological Properties of Hydrate Forming Emulsions. Chemical Engineering Science *(95)*, 148-160.

[12] Sa, J-H., Kwak, G-H., Lee, B. R., Park, D-H., Han, K., Lee, K-H., **2013**. Hydrophobic amino acids as a new class of kinetic inhibitors for gas hydrate formation. Scientific Reports *(3)*.

[13] Haridas, V. and Naik, S., **2013**. Natural macromolecular antifreeze agents to synthetic antifreeze agents. RSC Advances *(3)*, 14199-14218.

[14] Nakajima, M., Ohmura, R., Mori, Y. H., **2008**. Clathrate hydrate formation from cyclopentane-in-water emulsions. Industrial & Engineering Chemistry Research *(47)*, 8933-8939.

[15] Clément, F. and Johner, A., **2000**. Adsorption of neutral polymers : loops and tails. Comptes Rendus de l'Académie des Sciences Paris *1* (Série IV), 1135-1142.

[16] Zhuravlev, L. T., **2000**. The surface chemistry of amorphous silica. Zhuravlev model. Colloids and Surfaces A: Physicochemical and Engineering Aspects (*173)*, 1-38.

CHAPTER 5

CHARACTERISTICS OF THE POLYCRYSTALLINE HYDRATE CRUST

5.1. Introduction

In this chapter we try to give insights into the characteristics (growth rate, morphology, etc.) of the polycrystalline hydrate crust that forms at the water/CP interface of a water drop by means of microscopy. First of all we will explain the setup and experimental procedure used for carrying out this kind of experiments. In the Results section, we will first analyze the possible nucleation places in our system. Then we will study the hydrate growth rates and the morphology of a CP hydrate crust formed at the interface of a water drop and how the driving force (subcooling degree) has an effect in these properties. The effect of temperature cycling is also going to be explained and the chapter will finish with the conclusions.

5.2. Experimental setup and procedure

In all experiments, a water drop with volumes in the 0.03 - 1µl range is deposited on a (horizontal) quartz substrate previously immersed in the guest fluid (CP) (Figure 5.1). The CP was previously equilibrated with water at room temperature (≈ 20°C). The quartz substrate is the inner wall of a Hellma rectangular cell with a 2 mm-optical path (QS-110-2-40). The Hellma cell is inserted into a cylindrical aluminum (AU4G) cell holder with a rectangular aperture in its center (Figure 5.2) allowing the observation by light transmission microscopy of the glass/CP and glass/water interfaces and their vicinity. This cell-holder is in contact on one side with a cylindrical Peltier element and a cooling system (both with a central hole) allowing a precise temperature control in the Hellma cell (temperature controller Accuthermo ATEC302). We employed as inverted microscopes an AE21 Motic™ in preliminary observations, and then an inverted Eclipse Ti Nikon™ used in various modes, principally bright and dark field, differential interference contrast (Nomarski), fluorescence and confocal reflectance. The objectives used range from x4 to x20, the latter corrected for spherical aberrations induced by the 1.5 mm-thick glass wall. The camera is equipped with an effective tube extender (x1.5). A sub-micron resolution is obtained for the highest magnification (i.e., with the x20 objective and the tube extender). The cameras used are either a colour camera Ueye SE1240 (IDS) or a PROEM 512B Excelon (Princeton Instruments).

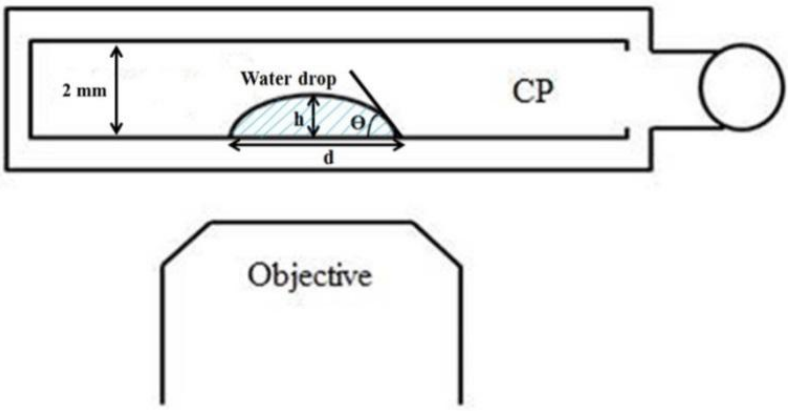

Figure 5. 1. Schematics of the experimental setup adapted to the inverted microscope, where a water drop is introduced in a Hellma cell filled with CP. The cell holder and the temperature control system are not shown here.

Figure 5. 2. Experimental setup. Left: Cylindrical aluminum cell holder where the Hellma cell is inserted. Right: Complete experimental setup on the Motic microscope: cell holder with the Hellma cell inside, Peltier element and cooling system.

The experimental procedure is very similar to the one used in chapter 3 (Figure 5.3). The objective is to first convert the water drop into ice for inducing hydrate formation afterwards. Therefore, temperature is lowered to -20°C and then raised up rapidly to -5°C. Then, we increase it slowly above 0°C in order to melt the ice and form a hydrate crust at the water drop surface. Once all the hydrate is formed, we raise the temperature slightly above the equilibrium temperature 7.2°C (8 - 9°C, generally) at 1°C/min. Dissociation time is not taken into account in this type of experiments, so an average of 5 min is chosen. We consider this time long enough for completely melt the hydrate crust and short enough for not losing the memory effect that will help the second hydrate formation afterwards. Finally, temperature is decreased at 1°C/min to the desired temperature: higher (3.5 – 5.5°C) if we want to do the experiments at low subcooling and lower (0.5°C) if we want to carry them out at high subcooling. Contrary to what we studied in chapter 3, here we play with the last part of the graph (Figure 5.3) and not with the dissociation time and temperature. The objective is to study the effect of the subcooling degree on the crystalline characteristics of the hydrate layer.

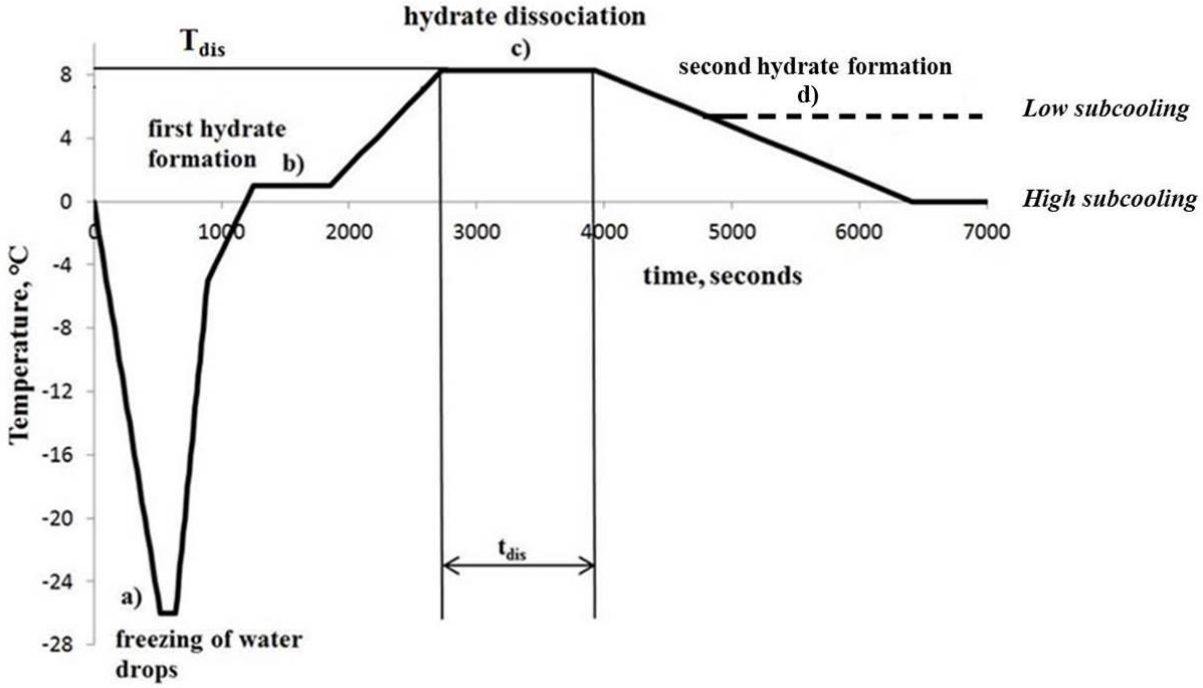

Figure 5. 3. Experimental temperature profile. The ΔT_{sub} at which we perform the second hydrate formation is the important step in these experiments: low or high subcooling.

5.3. Results and discussion

5.3.1. Nucleation places

Before talking about the different places where nucleation takes place, we have to remind that a CP-in-water emulsion is created during the dissociation of the CP hydrate crust at the surface of the water drop (cf. chapter 3). As the CP droplets are lighter than water, when the water drop is placed upwards, i.e. sitting on the substrate (Figure 5.1), which is the typical way of working in chapters 5 and 6, they tend to go to the upper part of the water drop, where they accumulate (Figure 5.4).

5.3.1.1. Nucleation in the CP-in-water emulsion

The CP-in-water emulsion is a very good place for crystals to nucleate due to the huge quantity of water/CP interfaces. As we explained above, interfaces are a favorable place for nucleation to occur because it is the place where more quantity of host-guest molecules is in contact. Nucleation can take place via several processes. We have observed that tiny crystals

can nucleate either at the water drop surface far from a CP droplet (Figure 5.5), or from a single CP droplet the water (Figure 5.6), or from an aggregate of CP droplets (Figure 5.7).

The density of CP hydrate is equal to 0.97 g/cm^3 as calculated from the volume of a structure II crystal unit (17.3 x 17.3x 17.3 Å^3) and the weight of its 136 molecules of water and 8 molecules of CP (see section 1.1.2.2). The CP hydrate crystals are therefore expected to float at the surface of a sitting water drop in CP, as is indeed observed experimentally.

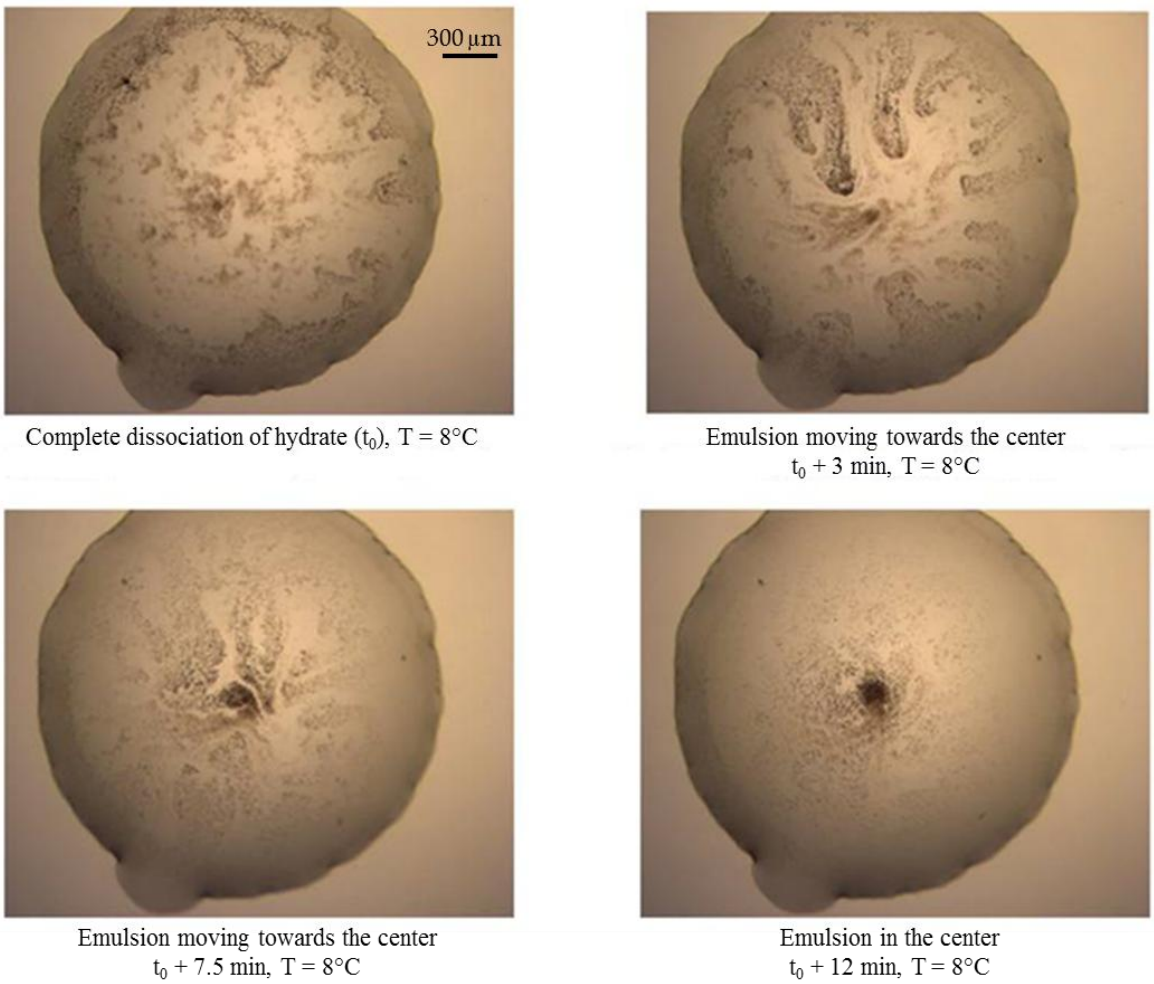

Figure 5. 4. Movement of the CP-in-water emulsion in a water droplet sitting on the substrate. After hydrate dissociation, the emulsion tends to go towards the center of the water drop since it is lighter than water. The black dots correspond to CP microdroplets. Bright field imaging mode. Experiment 2014/10/31.

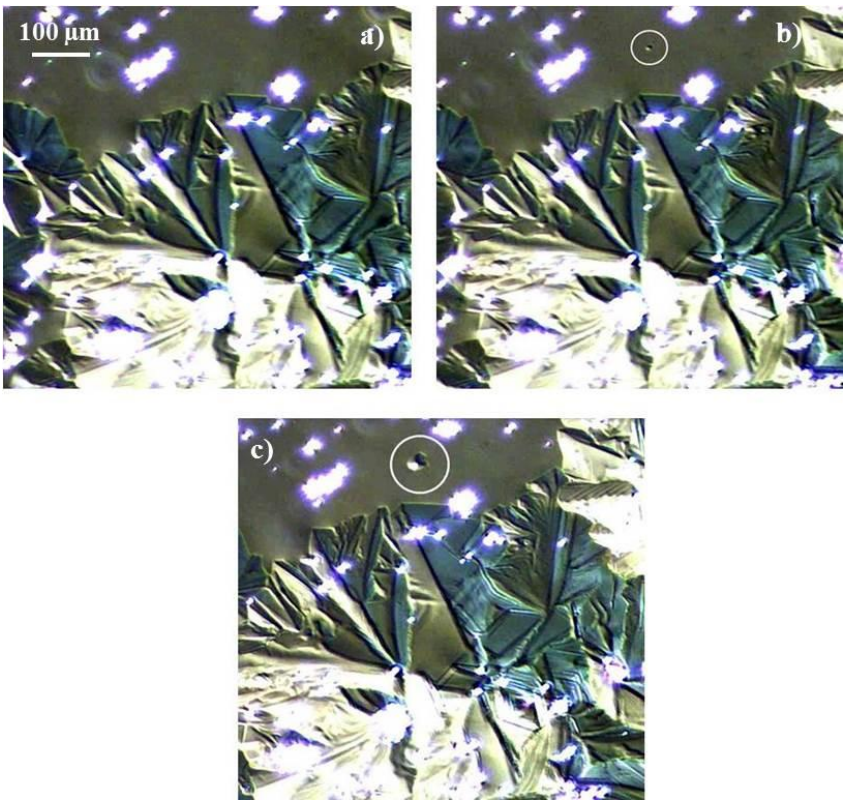

Figure 5. 5. Nucleation of a tiny crystal (white circle) at the water drop surface far from a CP droplet (T = 0°C). a) t_0, b) t_0 + <1s, c) t_0 + 1s. DIC imaging mode. Experiment 2014/11/17.

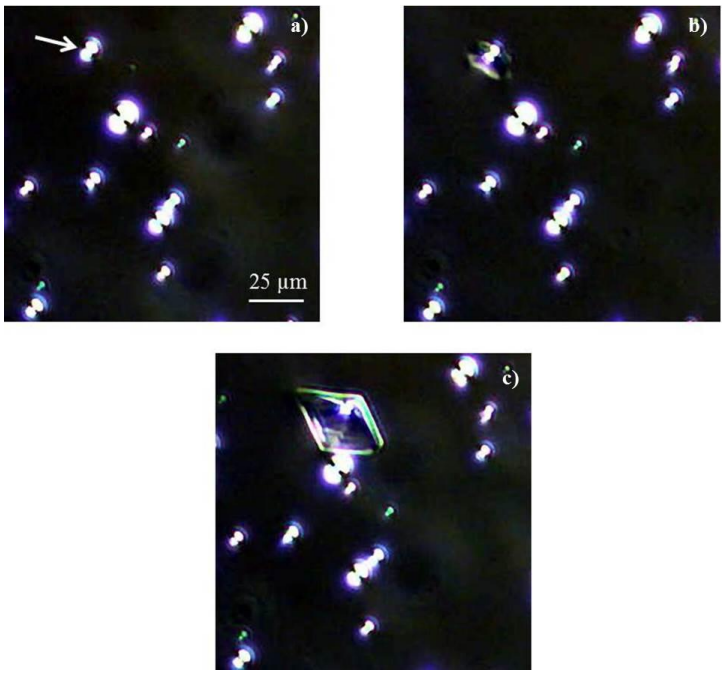

Figure 5. 6. Nucleation of a tiny hydrate crystal on a CP droplet (white arrow in (a)) at the surface of the water drop and subsequent crystal growth over 1s (T = 0°C): a) t_0, b) t_0 + <1s, c) t_0 + 1s. The CP droplets appear as bright dots. The imaging mode (DIC) is responsible for the splitting of the bright dots in planes that are slightly out of focus. Experiment 2014/11/17.

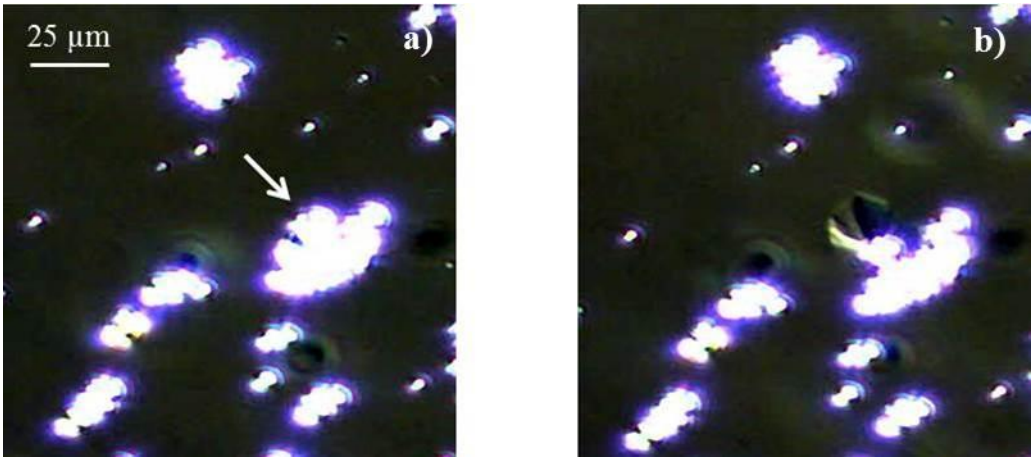

Figure 5. 7. Nucleation of a hydrate crystal from an aggregate of CP droplets (white arrow in (a)) at the surface of the water drop and subsequent growth over an interval of less than 1s (T = 0°C): a) t_0, b) t_0 + <1s. DIC imaging mode. Experiment 2014/11/17.

5.3.1.2. Nucleation at the triple line

Sear explains in his review [1] that at a contact line, three interfaces meet and so when a nucleus forms there, it replaces more interface than when it forms just at a vapor/liquid interface, for example, where it can only replace one interface. This is our case here. Nucleation at the contact line glass/water/CP is favored because when the crystal forms it is going to replace three interfaces instead of just one: water/CP (case of the emulsion).

Depending on the subcooling degree and on the quantity of emulsion present after dissociation, sometimes both types of nucleation can take place at the same time. We have observed that when less emulsion is present (less volume of water/CP interfaces) nucleation tends to take place at the triple line (three interfaces can be replaced) (Figure 5.8), whereas when there is higher quantity of emulsion on top of the water drop, nucleation occurs preferentially in the emulsion (more interface can be replaced) or there is competition between both places (Figure 5.9).

5.3.2. Hydrate growth and morphology

When nucleation takes place in the emulsion at the surface of the water drop, as soon as crystals are formed and reach a certain size, most of the times they are ejected towards the triple line to continue growing there (Figure 5.9 right, 5.10 and 5.11). This fact is independent on the subcooling degree at which we work.

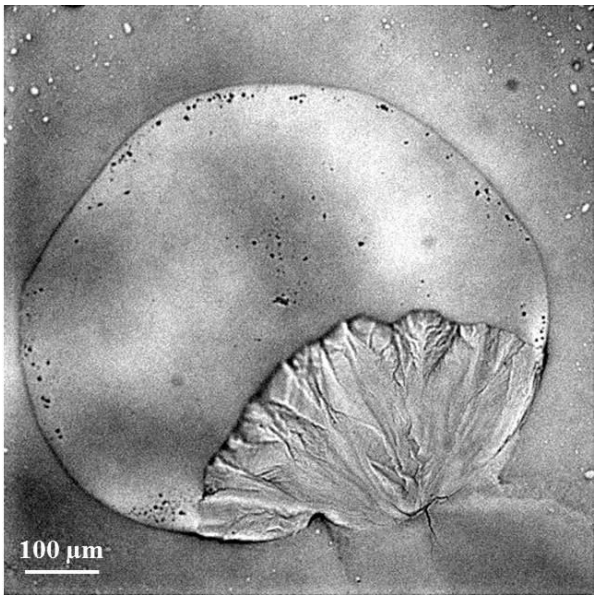

Figure 5. 8. Low quantity of emulsion present at the water drop surface after the first hydrate dissociation: nucleation takes place at the triple line (T = 0°C). Bright field imaging mode. Experiment 2015/06/03.

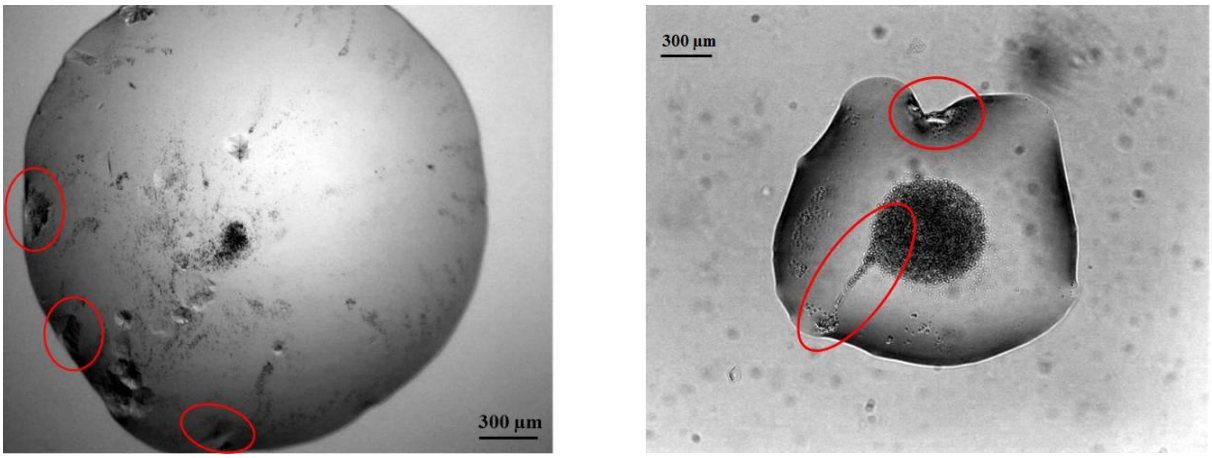

Figure 5. 9. High quantity of emulsion present after the first hydrate dissociation. Competition between nucleation in the emulsion and at the triple line (T = 0°C). Bright field imaging mode. Left: Experiment 2014/10/31. Right: Experiment 2014/10/23.

In case of having several nucleation points, the growing hydrate crystals move along the water/CP interface, find other smaller or bigger crystals nearby and are attracted to finally merge together in order to form a bigger crystal (we call it 'crystal front') that always finish by moving towards the triple line. A 'crystal front' grows by merging with small hydrate crystals and other crystal fronts.

When hydrate nucleation takes place at the triple line, hydrate crystals just stay there and grow (Figure 5.8). The CP hydrate crust grows by attracting and adding to the structure other crystals already formed in other places of the water drop surface or by incorporating CP and water molecules which just feed the only existing hydrate front and make it grow. In case of having several nucleation points at the triple line, each hydrate front grows independently to finally meet somewhere of the water drop surface.

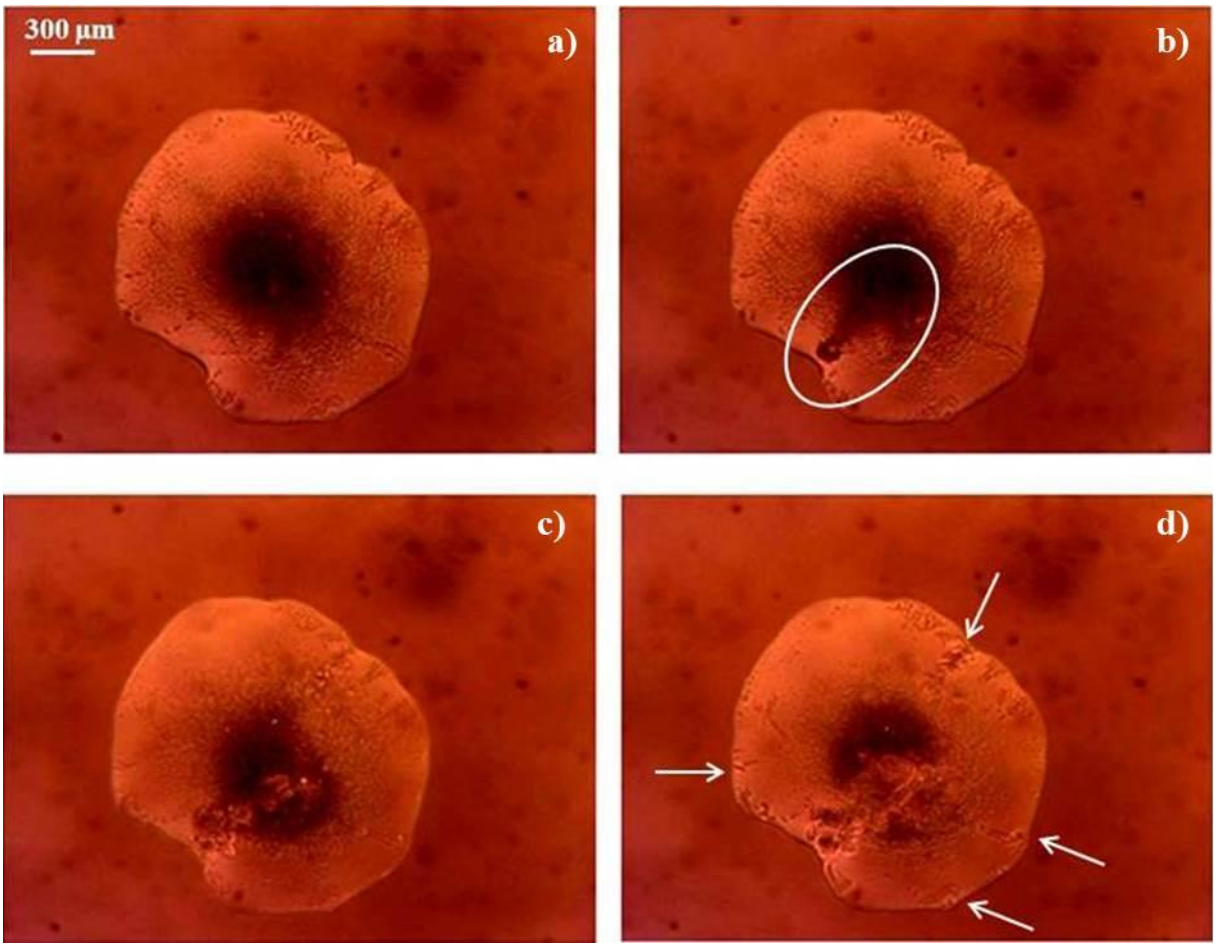

Figure 5. 10. Ejection of a nucleated crystal (white circle) in the emulsion towards the triple line (ΔT_{sub} = 3.4°C). a) t_0, b) t_0 + 8s, c) t_0 + 68s, d) t_0 + 264s. In this case, several nucleation points exist (white arrows). Bright field imaging mode. Experiment 2014/10/22.

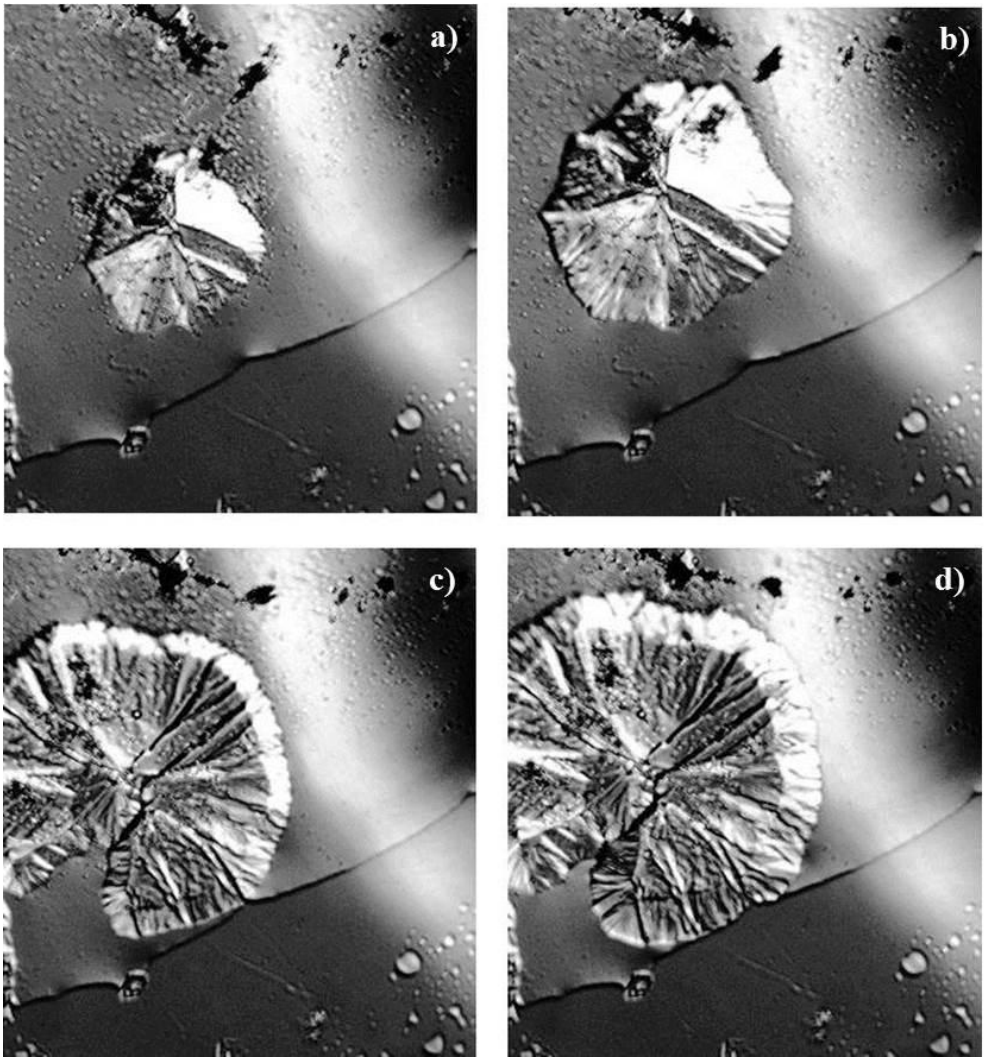

Figure 5. 11. Hydrate crust growth along the interface water/CP (T = 0°C). The hydrate crystal migrates from the emulsion to the contact line. a) 13.4s, b) 19.2s, c) 23.8s and d) 26.8s. Field of view 120µm. DIC imaging mode. Experiment 2015/07/17.

In the following sections we are going to analyze the results obtained for a high subcooling and for a low subcooling working mode. High subcooling means here a temperature equal or very slightly superior to 0°C (ΔT_{sub} ~ 7°C, see below). Low subcooling means a temperature in the range of 3.5 - 5.5°C (ΔT_{sub} = 1.5 - 3.5°C, see next section). Our results will be compared below to those of Sakemoto et al. [2], who carried out some experiments at different subcoolings in order to observe the effect of the temperature on the morphology of CP hydrate crystals. They will also be compared to those by Smelik and King [4] who found, in general and independently on the subcooling degree, two types of methane hydrate crystals: those from surface crystallization (i.e. crystallization at the water/guest interface) and small single crystals in the bulk (with sizes not exceeding 25 µm). They

observed that surface crystallization can take place in two ways: individual crystals impinging together or surface crystal fronts with drapery appearance originating from the triple line and suturing together, engulfing sometimes a single crystal that is moving over the surface. As shown in Figure 5.12 and consistent with literature results on cubic crystals (and not only structure II hydrates), it seems clear that structure II monocrystals grow in the following dominant morphologies: regular octahedral and thin platelets with hexagonal or triangular shapes. Large monocrystals are most often observed for low subcooling conditions, as further discussed below. These forms normally grow together and we do not find one without the other, so it can be said that there is not one preferential geometric form. Note that all the experiments presented and discussed here are a second or subsequent hydrate formation. We do not talk about first hydrate formation in this chapter.

Figure 5. 12. Geometrical forms of the growing monocrystals floating at the water/CP interface at low subcooling (ΔT_{sub} = 1.6°C): octahedra, pentagons, triangular, hexagons, needles. Experiment 2014/10/22.

5.3.2.1. Low subcooling

5.3.2.1.1. Hydrate growth

In pure water/CP systems, for ΔT_{sub} = 1.4 to 4.3K, Sakemoto et al. [3] typically find irregular hexagons or pentagons with a length between 0.3 mm to 1 mm. They also observe that the time required to completely cover the cyclopentane water interface with a polycrystalline crust highly depends on the subcooling degree. At a ΔT_{sub} = 1.4K, 46.5 h are

required, but the time decreases as the subcooling degree increases. For a subcooling ΔT_{sub} = 3.1K, 143 minutes are required to completely cover a surface with area ~ 50 mm^2 whereas at ΔT_{sub} = 5K just 29 minutes are needed for covering the same area. The corresponding areal velocities are shown in Table 5.1. In our case, "low subcooling" experiments are within temperatures ΔT_{sub} < 3.4°C. Our observations are made for a water drop that has a low contact angle with the substrate. This allows the calculation of the drop surface as $S = \pi R^2$, being R the radius of the contact line. The CP/water interface, i.e. the surface of our water drops, is about 2 mm^2 which is a value a lot smaller than that of the CP/water interfaces Sakemoto et al. analyzed. We have tried different ΔT_{sub} and found that at ΔT_{sub} = 1.6°C the whole water drop is completely covered by a CP hydrate crust in 55 minutes (Figure 5.13). If we increase the subcooling and set it at ΔT_{sub} = 2.2°C, the time required is around 38 minutes, whereas for a ΔT_{sub} = 3.4°C, the hydrate layer takes around 20 minutes to completely cover the drop surface (Figure 5.14). As Sakemoto et al. did, we observe that the time needed to completely cover the whole surface of the water drop decreases when ΔT_{sub} increases, i.e. when the set temperature is lower. Our measured areal velocities are in the same range, but somewhat lower than those determined by Sakemoto et al. (Table 5.1).

ΔT_{sub} (°C)	**Growth velocity ([2], mm^2/min)**	**Growth velocity (our results, mm^2/min)**
1.4	0.02	-
1.6	-	0.04
2.2	-	0.05
3.1	0.35	-
3.4	-	0.10
5	1.72	-

Table 5. 1. Time needed for the hydrate crust to cover the whole water drop surface (2 mm^2) with respect to the subcooling degree ΔT_{sub}. Comparison between literature and our results. Experiment 2014/10/22.

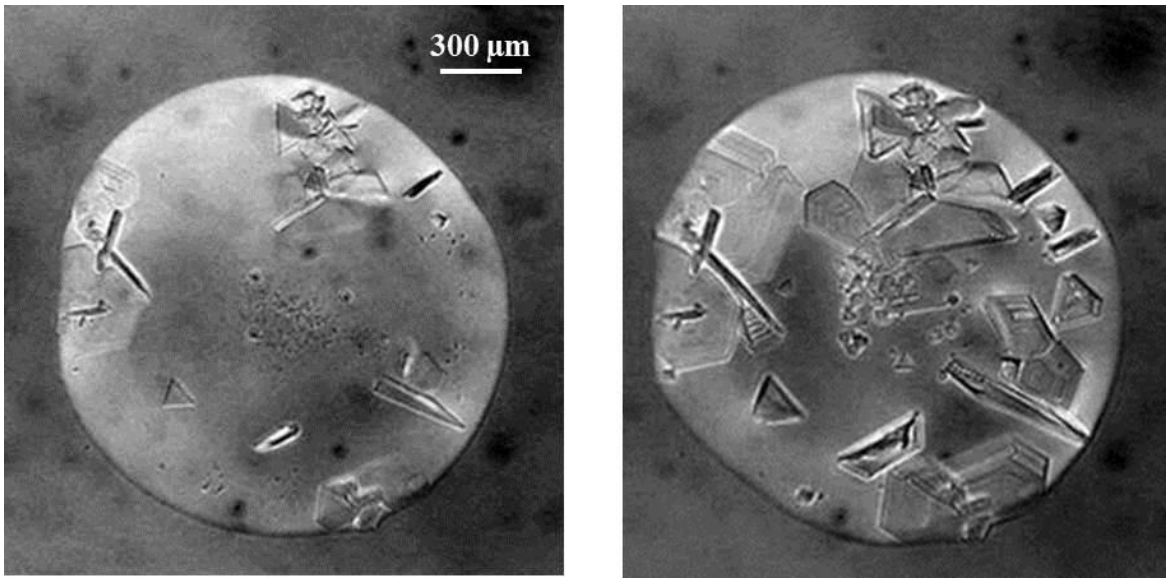

Figure 5. 13. Growth of the hydrate crust along the water surface at low subcooling (ΔT_{sub} = 1.6°C). Left: t_0 + 33 minutes. Right: t_0 + 45 minutes. Individual crystals grow and tend to form hexagons. Bright field imaging mode. Experiment 2014/10/22.

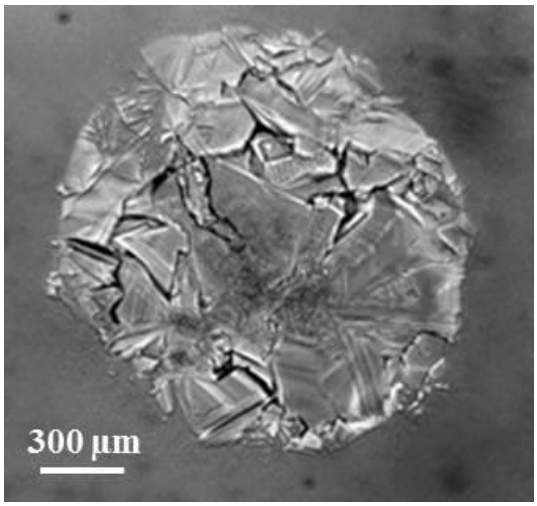

Figure 5. 14. Growth of the hydrate crust along the water surface at low subcooling (ΔT_{sub} = 3.4 °C). Image taken 20 minutes after the beginning of the crystallization. Bright field imaging mode. Experiment 2014/10/22.

5.3.2.1.2. Hydrate morphology

We have observed that depending on the subcooling degree (low or high), some morphological differences exist between the resulting hydrate crusts. As we said above, Sakemoto et al. found irregular hexagons or pentagons with a length between 0.3mm to 1mm when they worked at low subcooling (ΔT_{sub} = 1.4 to 4.3K). We did observe the same features, among other things. A lot of different crystal habits are obtained when working at this low

subcooling. Larsen et al. [5] affirm that the crystal growth planes which are exhibited macroscopically are the slowest growing planes. They studied molecular models of sII hydrate and got to state that the 6-membered rings of the large cavities all lie in the {111} planes. That suggests a possible hypothesis for the normal growth habit, appealing to a presumed higher energy barrier against producing these rings compared to 5-membered rings. It is hypothesized that the {111} plane in sII grows slowest because it contains a predominance of hexagonal faces relative to other crystal planes in sII. Crystal planes containing hexagonal faces may grow slowest because hexagonal faces are considerably more strained (120° between O-O-O angles) than are pentagonal faces (108°), relative to either the tetrahedral O-O-O angle (109°) or the water angle (H-O-H of 104.5°) [6]. This also agrees with what Smelik and King [4] say about the crystal growth of methane hydrates: "The bounding faces of any crystal generally correspond to the slowest growing directions or planes, whereas the fastest growing directions typically never develop corresponding morphologic faces and instead occur as apices or edges of the crystal". And this is why most of the polygonal forms observed tend to form hexagons.

At low subcooling, several crystal forms are observed, such as triangles, needles, pentagons and hexagons (Figures 5.13 and 5.15). By letting them grow, almost all these forms tend to form hexagons. In case of working at low subcooling, all the different forms are normally meant to be tridimensional, meaning that crystals are able to grow in order to form a completely faceted crystal [7]. This means that all the faces of the tridimensional crystals should grow at the same rate, but this is difficult to determine because an individual crystal presents different cooling gradients along its faces. The interfacial cooling is necessarily greatest near the corners, least at the face centers, and intermediate at the centers of the edges [8]. Also, the growth in the perpendicular direction to the water surface is difficult in our case due to the handicap of the mass transfer between water and CP. A modification of the crystal habit is produced and so a combination of forms different from the "conventional" ones is obtained.

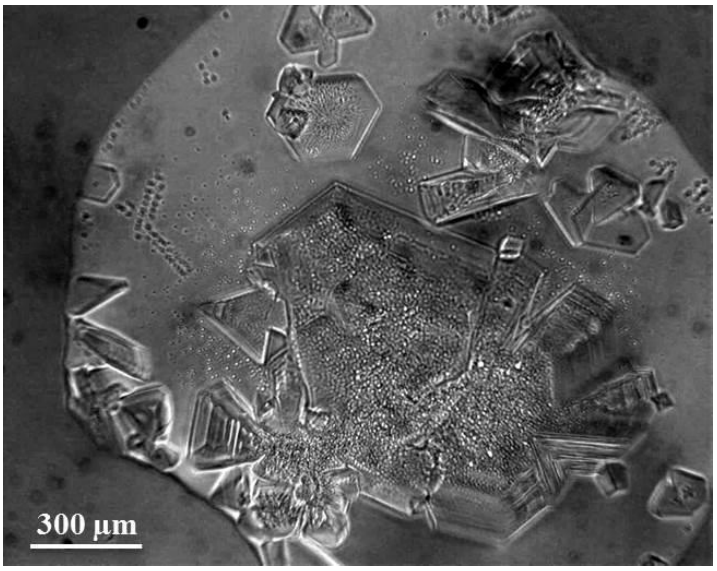

Figure 5. 15. Several crystal forms at low subcooling: triangles, needles, pentagons and hexagons (ΔT_{sub} = 3.4°C). Image taken 17 minutes after the beginning of the crystallization. Dark field imaging mode. Experiment 2014/10/22.

5.3.2.2. High subcooling

5.3.2.2.1. Hydrate growth

Sakemoto et al. also concluded that at higher subcoolings than the previous cases (typically ΔT_{sub} = 5.1K), both slender polygons, triangular and swordlike crystals of 0.1 mm to 0.2 mm are observed. Very often, these geometric forms cannot be easily identified and the crust looks smoother than the crust composed of larger monocrystals that is observed at low subcooling. Therefore, after what they observe at low subcooling they conclude that the size of hydrate crystals decreases with increasing subcooling. The "high subcooling" experiments we have carried out are at ΔT_{sub} > 3.4°C, i.e. set temperature of 6.7 - 7.2°C. For a 0.03 µl water drop (~ 3 mm^2 surface), the average time for the hydrate to cover the whole surface is between 1 – 2 minutes. This gives a growth velocity of 1.5 mm^2/min. When volumes are higher (surfaces around 6 mm^2) we obtain a hydrate crust growth velocity of 0.8 – 1mm^2/min.

The general observation is then that, when we work at high subcooling, the growth velocity of the hydrate crust varies between 0.8 and 1.5 mm^2/min. This is very different from what we observe when we work at low subcooling but consistent with what Sakemoto et al. found for subcoolings ΔT_{sub} = 5K (growth velocity of 1.72 mm^2/min). This has also been observed by Li et al. [9] for methane hydrates.

5.3.2.2.2. Hydrate morphology

For a subcooling ΔT_{sub} > 3.4°C (typically T = 6.7 - 7.2°C), the observations we make are different from those of Sakemoto et al. In our case, swordlike crystals are not observed as they are in low subcooling conditions, but tiny triangular and hexagonal crystals (as we did in low subcooling mode) that have not enough time to grow individually. What happens is that, as the subcooling is very high, there are a lot of nucleation points all over the water drop surface, so a lot of small polygonal crystals are formed, but there is no time for them to grow individually (there are a lot of them growing rapidly). The growing hydrate crystals move along the water/CP interface, find other smaller or bigger crystals nearby and are attracted to finally merge together in order to form a bigger crystal, as explained before. Several advancing hydrate fronts (Figure 5.16) are created and when the water drop is completely covered, a cracklike/mosaic structure can be easily observed (Figure 5.17).

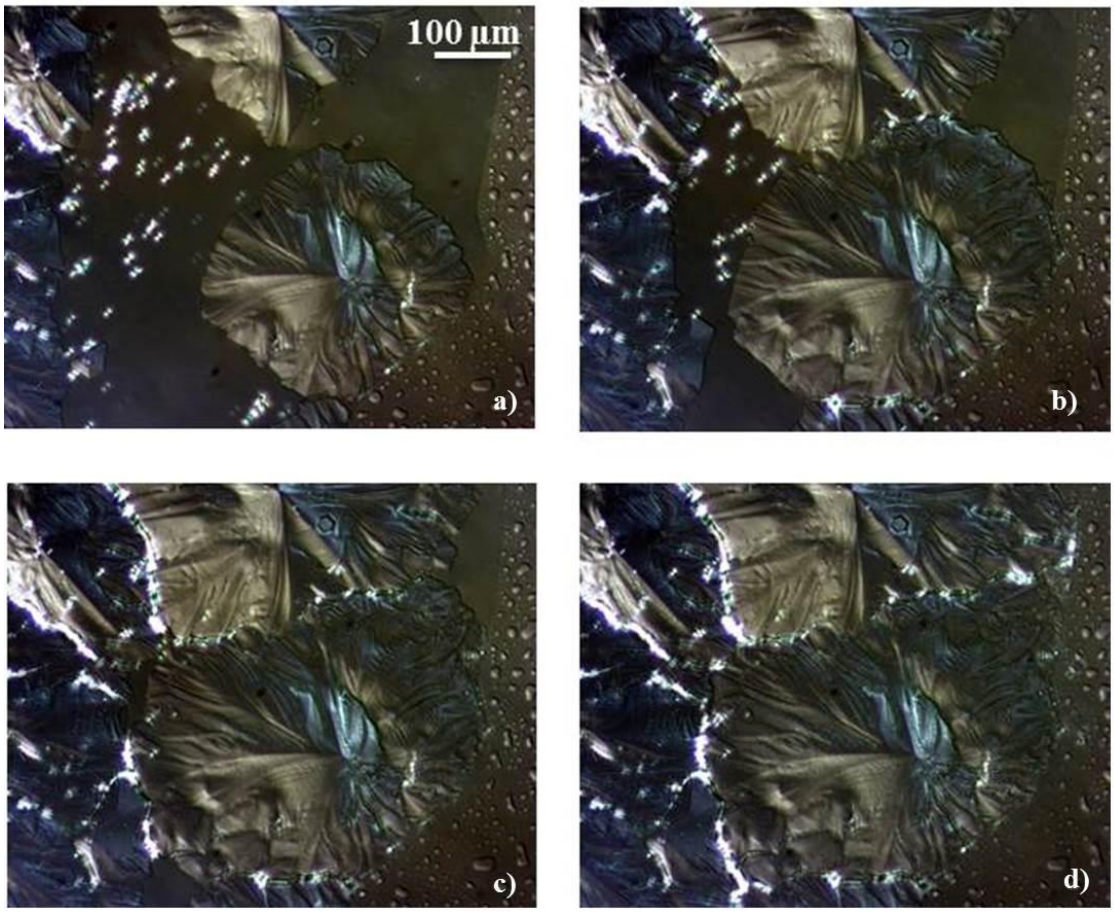

Figure 5. 16. Advancing hydrate fronts that stick together in order to form the hydrate crust (T = 0°C). a) t_0, b) t_0 + 11s, c) t_0 + 19s, d) t_0 + 31 s. Bright field imaging mode. Experiment 2014/11/17.

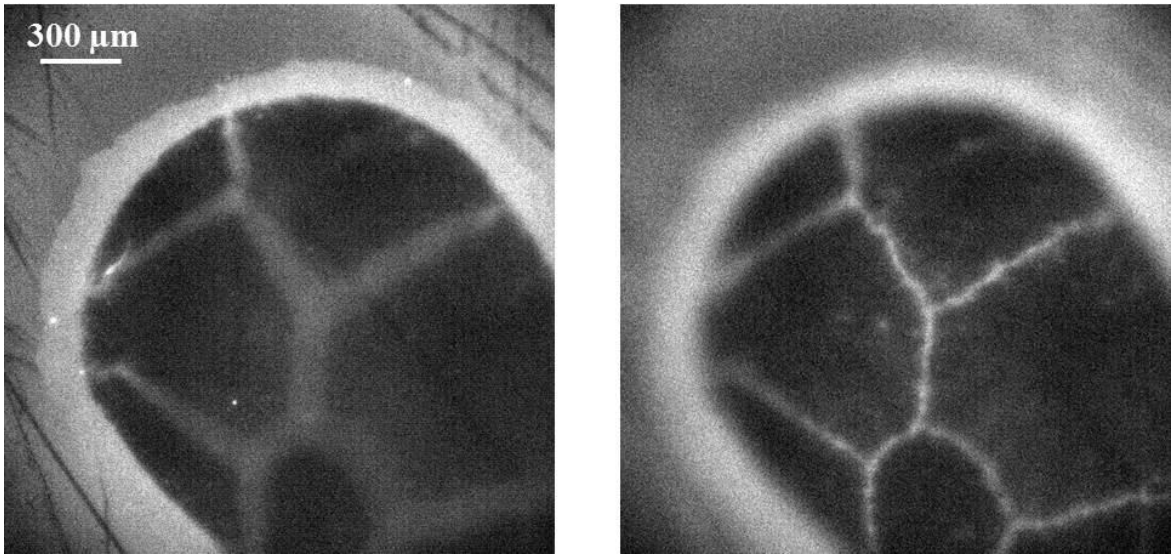

Figure 5. 17. Cracklike/mosaic structure obtained when several hydrate fronts stick together and cover the whole water drop surface. Left: focus on the substrate. Right: focus on top of the water drop. The limit of the hydrate fronts when they stick together can be distinguished (T = 0°C). Fluorescence (DASPI) imaging mode. Experiment 2014/11/25.

This agrees with what Smelik and King [4] observed. When they carried out a surface crystallization, they got crystals with hexagonal shape that would increase in size until they impinged on one another, forming what they call a surface mosaic. Sometimes they found several large fronts freezing across the water-gas interface simultaneously. Those fronts had often a drapery appearance and almost always originated near the side walls (which would be the triple line in our case). They often met another front, becoming sutured together, or sometimes they trapped floating surface crystals until the surface was completely frozen in a complex mosaic. We observe the drapery appearance of the hydrate crust in Figure 5.18 and the trapped floating surface crystals in Figure 5.19.

The individual floating polygonal crystals are mostly solid plates in the form of hexagons or triangles. A hexagonal plate is a slice through an octahedron (typical cubic form) parallel to {111}. Since the subcooling is very high now we do not let crystals grow along all their faces, and we just see one face macroscopically. All the final visible faces appear to belong to {111}.

The result is a more uniform hydrate crust (Figure 5.18 left) compared to the one formed when the decrease in temperature is slow. On the other hand, when this decrease in temperature is slower, all the nucleation places form tiny crystals that have more time to

grow, ending by sticking all together and creating a more nervured (like an insect wing) and cracklike structure (Figures 5.18 right and 5.19). This is a general observation, but more experiments will have to be carried out.

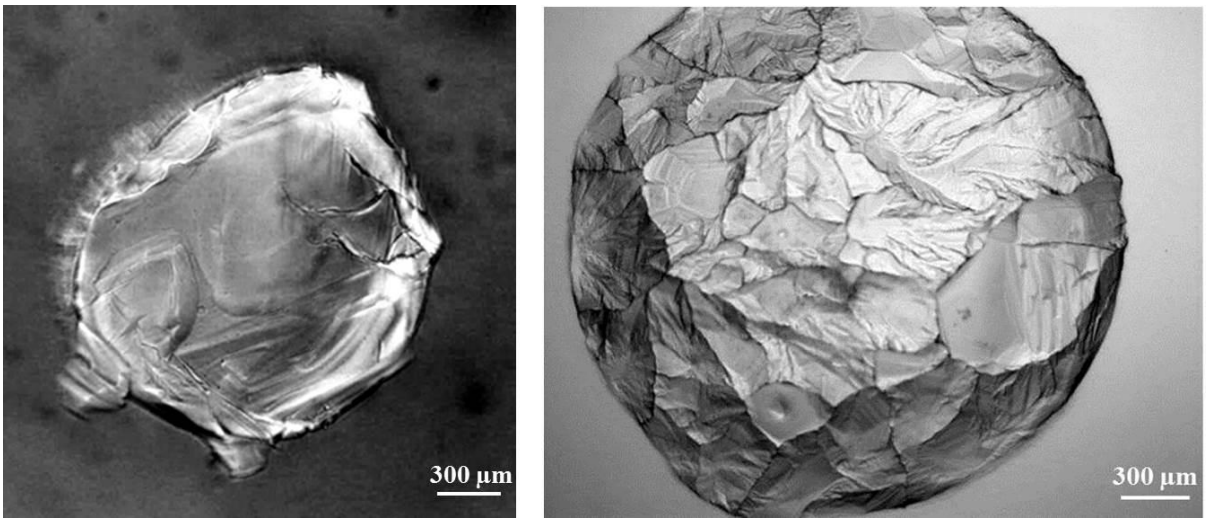

Figure 5. 18. Left: Uniform and homogeneous appearance of the hydrate crust when the temperature is decreased faster (T = 0°C). Bright field imaging mode. Experiment 2014/10/22. Right: Drapery appearance of the hydrate fronts when the hydrate crust has completely covered a 1µl water drop surface at a slower velocity (T = 0 °C). Bright field imaging mode. Experiment 2014/10/31.

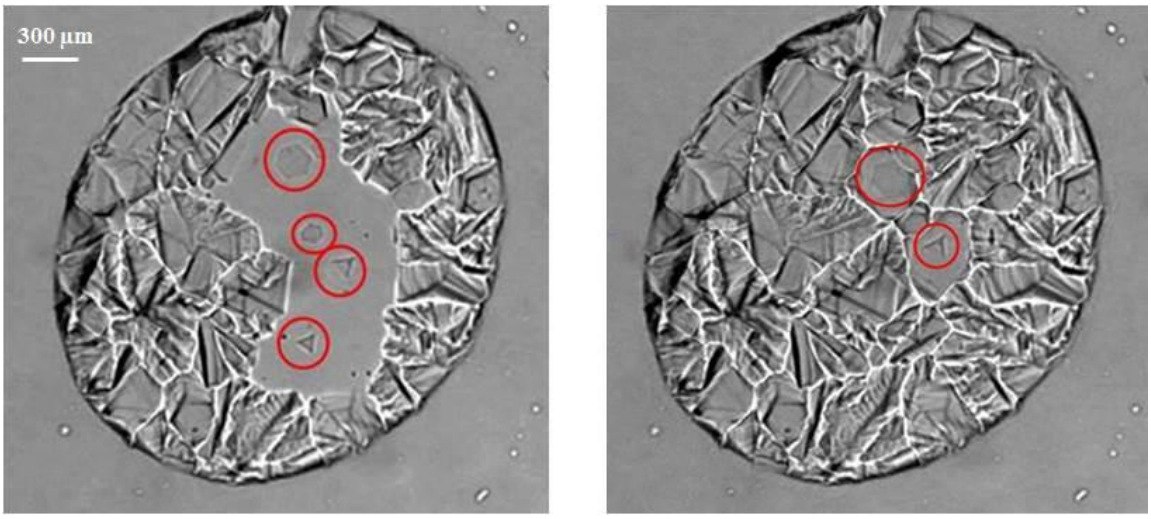

Figure 5. 19. Left: random hydrate polygonal crystals (solid plates in the form of hexagons or triangles) floating on the surface of a 0.03µl water drop at t_0 + 60s (T = 0.5°C). Right: single hydrate crystals are trapped while the hydrate crust is covering the water surface (t_0 + 80s). A drapery/mosaic structure is obtained (T = 0.5°C). Bright field imaging mode. Experiment 2014/10/24.

Another thing we have noticed is that, depending on the time we stay at 0 - 0.5°C during the first hydrate formation, more or less emulsion will be formed during the dissociation step. This higher or lower quantity of emulsion has an effect on the formation of nucleation points and on the nucleation places. When the emulsion is abundant, the main nucleation place is the emulsion, i.e. more nucleation points are possible because a lot more water/CP interfaces are present in the system. On the other hand, when less emulsion is present, less nucleation points will exist and so tiny crystals have fewer opportunities to be formed, although there are still more than when we work in the low subcooling mode, due to the higher subcooling. The nucleation places are reduced here because there is little emulsion for crystals to nucleate in it.

The selected dissociation temperature seems to have no effect on the morphology of the hydrate crust. When working at high subcooling, four different dissociation temperatures have been tested and the hydrate was left dissociating for the same time (13 minutes). These temperatures were 8.4°C, 9.2°C, 10.2°C and 11.2°C. The velocity at which we decreased the temperature to 0°C in order to reform the hydrate crust was ~ 0.05°C/s for all the experiments. All conditions led to the reformation of a CP hydrate crust on the water drop except for the last one (11.2°C during 13 minutes), where the 'memory' of previous hydrate formation was lost. The resulting morphology of the hydrate crusts was almost the same in all three cases.

In summary, the obtained structures are the result of several factors. The most important factor for having one type of structure of the other is the subcooling degree. But once we decide to work in the high subcooling mode, other factors have to be taken into account, like the quantity of emulsion formed in the previous dissociation step and/or the time needed to reach the experimental temperature.

One thing we have observed for both high and low subcooling working modes is the same as Knight and Rider did for sII tetrahydrofuran hydrates [7]. They call it the "skeletal" form of an octahedron. The 'skeletal 60° plates' are the next step of solid plates although the transition is not seen. They are composed of two or three parallel plates connected by ribs. The leading ribs where the fast growth takes place do not noticeably thicken. The thickening consists of an increase in the plate separation. This kind of structure indicates some form of aggregation or intergrowth, which is very normal in most crystalline minerals and in many crystals produced industrially [10]. The simplest form of aggregate results from a

phenomenon called parallel growth, in which individual forms of the same substance grow on the top of one another in such a manner that all corresponding faces and edges of the individuals are parallel, as shown in Figure 5.20. In this figure we see a typical structure in which regular octahedral are piled on top of one another in a column symmetrical about the vertical axis. This makes that, seen from above (or from below, in the case of our microscope), we observe the kind of stair steps showed in Figures 5.21, 5.22 and 5.23.

Figure 5. 20. Crystal parallel growth [10].

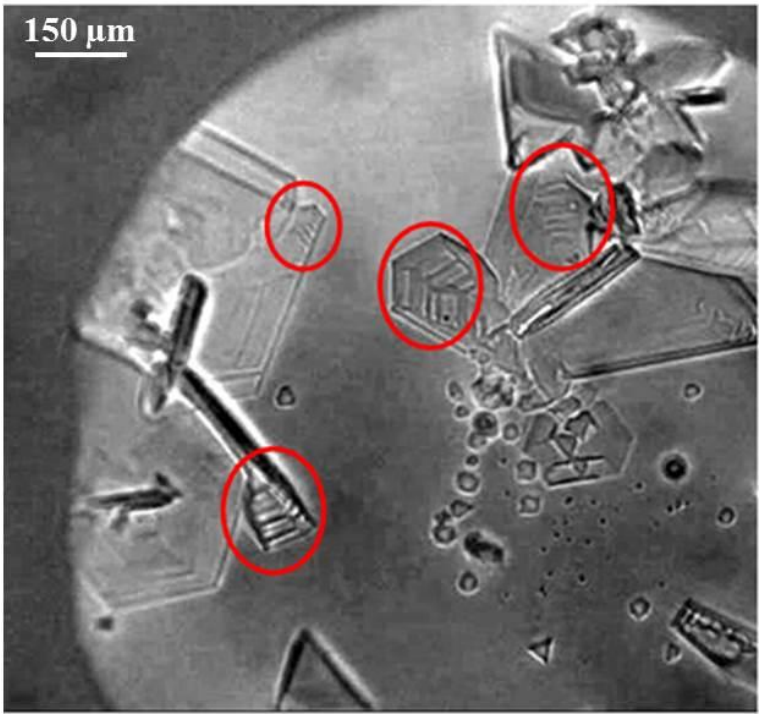

Figure 5. 21. Parallel growth observed at T = 5.6 °C (Low subcooling). Bright field imaging mode. Experiment 2014/10/22.

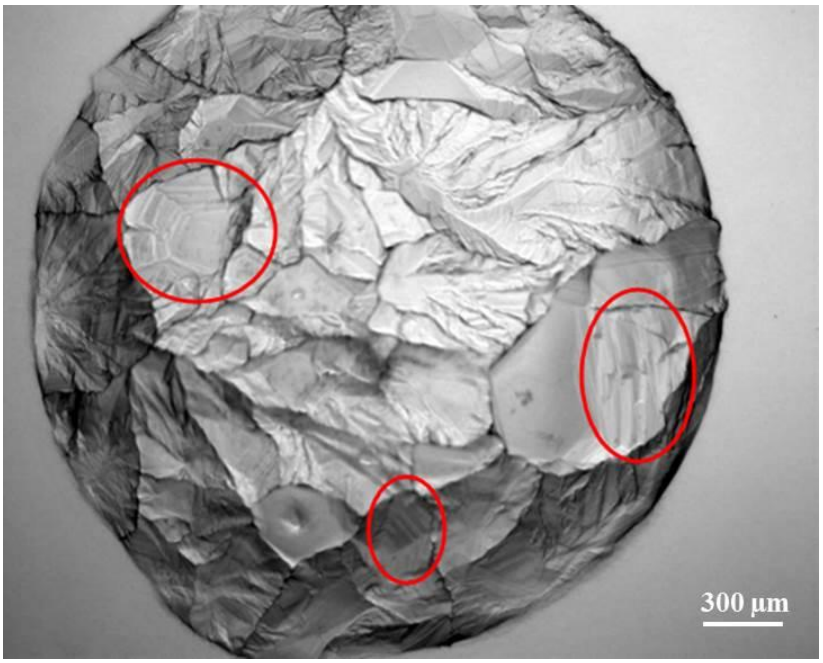

Figure 5. 22. Parallel growth observed at T = 0 °C (High subcooling). Bright field imaging mode. Experiment 2014/10/31.

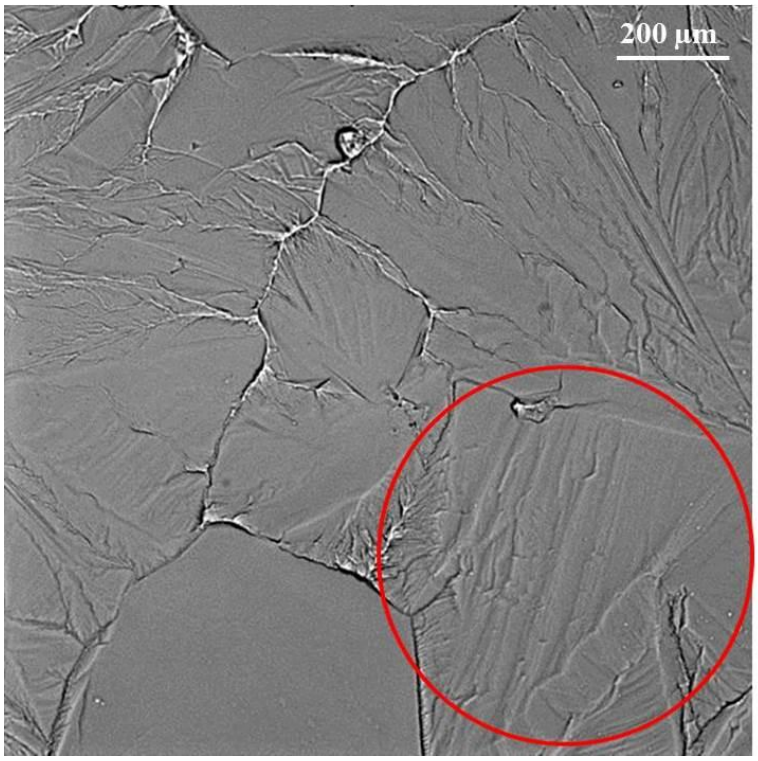

Figure 5. 23. Parallel growth observed at T = 0 °C. The limits of the hydrates fronts can also be observed. Bright field imaging mode. Experiment 2015/02/19.

5.3.3. Effect of repeated temperature cycling

In some experiments, several formation-dissociation cycles have been carried out with the same water drop. Once the first hydrate formation has taken place, we dissociate it (always at the same temperature) and do a second hydrate formation at high subcooling (0°C), and the same with a third formation, fourth and so on. We observed that the drop diameter is slightly increased during the first two or three dissociation steps, and then it remains almost constant: Table 5.2 shows the change in the diameter of the water drop. The growth velocity of the hydrate crust is almost the same in all hydrate formations, independently on the size of the water drop (the water drop spreads a little on the substrate, i.e. the contact angle slightly decreases, but it is not significant).

We conclude that the effect of cycling does not have an effect on the hydrate crust growth velocity.

Dissociation	**Diameter (mm)**
1st	1.47
2nd	1.51
3th	1.57
4th	1.60

Table 5. 2. Effect of cycling on the drop diameter. Experiment 2014/10/22.

5.4. Conclusions

In this chapter we have showed and proved the utility of a new setup designed to visualize by optical microscopy the nucleation and growth processes of a CP hydrate crust over a water drop deposited on a glass surface.

We have been able to observe three types of hydrate nucleation: at the water/CP interface, in the CP-in-water emulsion because there is a high quantity of water/CP interfaces

and/or at the glass/water/CP triple line because the formation of a crystal in there replaces three interfaces instead of one and is favored.

Also, insights into hydrate growth are obtained thanks to this system, which allows us not only to determine the growth rates of the hydrate crust but also to characterize its morphology. Depending on the nucleation place, hydrate growth occurs in one way or the other. For example, if nucleation takes place in the emulsion, at one moment crystals are ejected towards the triple line to carry on growing while crystals nucleated at the triple line stay there and grow without being ejected anywhere. Apart from other factors such as the time spent at the dissociation temperature, the quantity of emulsion present after dissociation or the time needed to reach the experimental temperature, the most important parameter that plays a role in hydrate growth and morphology is the subcooling degree. Working at low subcooling conditions (ΔT_{sub} < 3.4°C) gives large tridimensional hydrate crystals of different forms: triangles, needles, pentagons, hexagons, etc. The hydrate crust growth velocity is between 0.04 and 0.10 mm^2/min, depending on the subcooling degree. On the other hand, when we work at high subcooling conditions (ΔT_{sub} > 3.4°C) the growth velocity of the hydrate crust is between 0.8 and 1.5 mm^2/min and the morphology of the hydrate crust is less polygonal. The result is a mosaic structure. Sometimes a parallel growth is observed independently on the subcooling degree in which the crystal is formed by two or three serrated plates interconnected.

The last observation is the fact that cycling does not really change the growth velocity of the hydrate crust over the water drop surface. What we do observe is some limited spreading of the water drop during the first two or three dissociation steps.

We have noticed that this setup is versatile, practical and comfortable enough to keep using it in order to obtain more information about all these processes. In next chapters we are going to explain other observations we have made thanks to it, such as the existence of a hydrate halo around the initial water drop and CP hydrate crystallization (in the form of single crystals and/or dendrites) within a CP-in-water emulsion.

REFERENCES

[1] Sear, R. P., **2012**. The non-classical nucleation of crystals: microscopic mechanisms and applications to molecular crystals, ice and calcium carbonate. International Materials Reviews *57* (6), 328-356.

[2] Tanaka, R., Sakemoto, R., Ohmura, R., **2009**. Crystal Growth of Clathrate Hydrates Formed at the Interface of Liquid Water and Gaseous Methane, Ethane, or Propane: Variations in Crystal Morphology. Crystal Growth & Design *9* (5), 2529-2536.

[3] Sakemoto, R., Sakamoto, H., Shiraiwa, K., Ohmura, R., Uchida, T., **2010**. Clathrate Hydrate Crystal Growth at the Seawater/Hydrophobic - Guest - Liquid Interface. Crystal Growth & Design *10* (3), 1296-1300.

[4] Smelik, E. A. and King Jr., H. E., **1997**. Crystal-growth studies of natural gas clathrate hydrates using a pressurized optical cell. American Mineralogist *(82)*, 88-98.

[5] Larsen, R., Knight, C. A., Sloan, E. D., **1998**. Clathrate Hydrate Growth and Inhibition. Fluid Phase Equilibria *(150-151)*, 353-360.

[6] Sloan, E. D. and Koh, C. A., **2008**. Clathrate Hydrates of Natural Gases, 3rd edition (H. Heinemann, ed.), CRC Press, Boca Raton, Florida.

[7] Knight, C. A. and Rider, K., **2002**. Free-growth forms of tetrahydrofuran clathrate hydrate crystals from the melt: plates and needles from a fast-growing vicinal cubic crystal. Philosophical Magazine A *82* (8), 1609-1632.

[8] Frank, F. C., **1982**. Contemporary Physics *23* (1), 3-22.

[9] Li, S-L., Sun, C-Y., Liu, B., Li, Z-Y., Chen, G-J., Sum, A. K., **2014**. New Observations and Insights into the Morphology and Growth Kinetics of Hydrate Films. Scientific Reports *(4)*, 1-6.

[10] Mullin, J. W., **2001**. Crystallization, 4th edition. Butterworth-Heinemann, Oxford, U. K.

CHAPTER 6

CYCLOPENTANE HYDRATE GROWING AS A HALO ALONG A SILICEOUS SUBSTRATE

This chapter is being submitted as a regular article to Crystal Growth and Design under the title "Growth of gas hydrate halos on glass immersed in the guest fluid". The article is reproduced below.

Abstract

Gas hydrates form preferentially along interfaces between water- and guest-rich phases, where their (rapid) growth as a polycrystalline film has been thoroughly investigated. More elusive are the mechanisms of hydrate growth on solid (e.g., mineral) substrates, which are the subject of the present experimental study. We report on the growth of cyclopentane (CP) hydrate over fused silica glass, from single 'primary' drops of water deposited under CP, using methods such as differential interference contrast (Nomarski), fluorescence and confocal reflectance microscopies.

In agreement with the observations on methane hydrate by Beltran and Servio (Crystal Growth and Design, Vol. 10, pp. 4339-4347, 2010), we see CP hydrate growing along the interface

between the substrate and the guest fluid as a ‘halo’ originating from the contact line of the primary drop.

Whereas Beltran and Servio concluded that the water source of the methane hydrate halo was the primary drop, we find that, at least on strongly hydrophilic glass, most of the water feeding the growth of the CP hydrate halo comes from other sources than the primary drop. Four external sources have been identified: (i) water on the substrate including a precursor film near the contact line and microdroplets condensed from the CP in the form of breath figures; (ii) secondary droplets left behind when melting a previous hydrate halo; (iii) dissolved water present in the bulk of the CP-rich phase; (iv) microdroplets of condensed water falling out of the CP ('rain').

In agreement with the observations on methane hydrate, halo growth was sometimes observed to feed on water issuing from cracks in the hydrate crust covering the primary drop. The halo propagated at ~ < 2 µm/s over bare glass or glass with a breath figure. 'Leap-frog' propagation over secondary water drops or pre-formed hydrate accelerated propagation up to 10-15 µm/s.

No hydrate halo was detected on hydrophobic (silane-treated) glass.

6.1. Introduction

Gas hydrates are ice-like crystalline structures made of hydrogen-bonded water molecules encaging guest (hydrate-former) molecules such as light hydrocarbons or refrigerants, rare gases, CO_2, etc. Long considered a nuisance because they block hydrocarbon flow lines and their dissociation in marine sediments renders offshore platforms and pipelines unstable, gas hydrates are now also being examined as an opportunity. Huge amounts of energy resources are trapped in submarine sediments in the form of methane hydrates, and many other applications based on gas hydrates are emerging: gas separation, energy transport and storage, water desalination / purification, etc. Research in this area is booming, mostly aimed at controlling the kinetics of gas hydrate crystallization, which depending on the application needs to be either inhibited or accelerated: one method consists in adding some mineral (e.g., oxide) particles to the water/gas system, but the inhibiting/promoting mechanisms are still ill-understood [1].

For guest molecules that are sparingly soluble in water and vice-versa, hydrate formation occurs preferentially along water/guest interfaces, where a polycrystalline hydrate crust grows rapidly until full interface coverage; this (porous) crust then acts as a low-permeable barrier to the water and guest molecules, which impedes or strongly slows downs hydrate growth in a

perpendicular direction. The morphologies and lateral growth rates of these crust layers are rather well characterized and understood, at least for the most common guest fluids [2], [3], [4], [5], [6], [7], even though some questions remain as to the respective effects of heat and mass transfers [8], [9].

In this paper, we report and discuss observations of gas hydrate growing along a solid, water-wet substrate as a 'halo', a term introduced by Beltran and Servio [10]. These authors observed methane hydrate forming and growing rapidly on the surface of water drops present on a glass substrate, and then growing radially – as a halo – on the glass surface from the drop boundaries into the methane-rich phase. This halo was shown to be responsible for the 'bridge effect', i.e. the propagation of hydrate from the surface of one water drop to that of a neighboring water drop. Beltran and Servio [10] argued that such halo growth is fed by the unreacted water drawn by capillarity from the water drop (covered with a low-permeable hydrate crust) toward the 'naked glass' – more precisely, toward the glass immersed in the guest fluid.

This halo is often seen in conventional experiments, in which hydrate formation and growth at the water/gas interface are observed behind sapphire see-through windows [11], [12], [13]. Hydrate formation typically starts at the water/gas interface, which is rapidly covered with a hydrate crust, and then a halo is seen ascending along the sapphire window originating from the contact line between the window and the water/guest interface (already covered with hydrate). Interestingly, halo growth is observed to be more rapid with repeated cycles of hydrate dissociation and then reformation [13].

Understanding gas hydrate halo growth is relevant to processes of geological interest, in which gas hydrates are present in sediments in an excess of gas, e.g., when these sediments overlay a zone of high gas saturation – and low water (or brine) saturation (in a water-wet sand, this water forms pendular structures between sand grains). The halo growth investigated here is expected to be the dominant pore-scale process occurring in this so-called excess gas configuration [20]. This halo presumably acts as cement between neighboring sand grains and confers the hydrate-bearing sediment a high mechanical rigidity [21], [22].

Additionally, the understanding of growth mechanisms of this halo as a function of substrate properties (wettability, thermal conductivity, etc.) might provide clues as to why some mineral particles are better hydrate promoter than others [1].

The purpose of the high (sub-micron) resolution observations presented in this paper is to describe and discuss the mechanisms of halo growth and melting when the conditions for hydrate stability and dissociation are respectively met. Hydrates are mainly made up of water molecules (a proportion of 17/18 for structure II hydrates, the other 1/18 being the proportion of guest molecules), yet these hydrate halos grow in an environment where water is lacking: inbetween the substrate and the guest phase, in which a very small amount of water molecules is dissolved (typically, below a few mol.%). Hence, is seems reasonable to assume that most (if not all) of the water feeding the halo growth comes from the 'reservoir' of water (a water drop sitting on the substrate in Beltran and Servio's study [10] and in the present study): Beltran and Servio assumed that water flows in-between glass and the hydrate halo, but did not provide direct experimental evidence.

The experimental configuration chosen in this work is similar to that of Beltran and Servio: a drop of water on a glass substrate immersed in the guest (hydrate-former), chosen here to be cyclopentane (CP). CP hydrates are considered a proxy of natural gas hydrates because CP, similarly to low-molecular-weight alkanes, is sparingly soluble in water and forms structure II hydrates. The interest of CP hydrates, which are stable below the dissociation temperature $T_{dis} \approx 7°C$ (T_{dis} is the temperature of coexistence between CP hydrate, liquid water and liquid CP), is that they form at ambient pressure, which considerably eases the experimental work.

To investigate how the CP hydrate halo grows on the substrate, starting from the edge of the water drop, and then melts when temperature is brought respectively below and above the dissociation temperature T_{dis}, we use a combination of optical microscopy methods, including differential interference contrast (DIC), fluorescence and confocal reflectance microscopies, which to the best of our knowledge have not been used for studying gas hydrates yet.

Another novel 'tool' used in this study is provided by the fluid system itself. Upon cooling, there is a phase separation (demixing) of water from the CP initially (i.e. at room temperature) saturated with water, simply because water solubility in CP decreases with decreasing temperature [23]. This demixing occurs in the form of tiny (micron-sized) water droplets; some of these microdroplets settle on the substrate where they form arrays similar to the *breath figures* that form when moisture comes in contact with a cold substrate. The physics of breath figures is briefly reviewed in next section, together with the wetting behavior obeyed by the glass/water/CP system of interest**.** This information will be of use for interpreting the experimental observations.

Then, the rest of the paper is divided into the experimental section describing the setup and methods used for observing the CP hydrate halo growing or melting on the substrate, and the presentation and discussion of the results themselves.

6.2. Background

In this section, we remind of two topics of surface physics relevant to our study. The first topic is on the wetting behavior, referred to as pseudo-partial or frustrated-complete [24], [25], of a liquid (here, water) being strongly attracted to the substrate (glass) but unable to form a film of macroscopic thickness (complete wetting, i.e., zero contact angle) because long-range forces oppose it. The second topic is on breath figures, which refer to the phenomenon of dropwise condensation of a non-completely-wetting liquid on a substrate.

Frustrated-complete (or pseudo-partial) wetting [24], [25]. This wetting behavior is encountered in systems with antagonistic short- and long-range forces such as our glass/water/CP system. Indeed, strong attractive short-range forces exist between a hydrophilic glass substrate and water molecules, which form a film on the substrate. Yet, a water film of macroscopic thickness cannot exist on glass because long-range (van der Waals) forces oppose it: the Hamaker constant of the water film (sandwiched between glass and CP) is positive as shown in the Appendix. [Other systems exhibiting frustrated-complete wetting include alkanes on a water substrate] [26]. As a consequence, a thin water ('precursor') film is expected to expand on the substrate from the edges of a water drop deposited on a *dry* substrate - that is, a substrate with no water on it. This precursor film is thicker than a few molecular layers (say, 1-2 nm at most for small molecules) only when the water drop has a very low contact angle with the substrate [24], [25]. Another consequence is that an excess of liquid water on the substrate does not form a stable film but rather two coexisting surface states, a process called dewetting: the thin water film described above, and domains of macroscopic thickness, which often turn out to be droplets [27].

Dropwise condensation of a non-completely-wetting fluid on a substrate (breath figures). The structure and evolution of the arrays of drops (called 'breath figures') condensing from a vapor on a cold substrate (called dew if drops are water drops) are the subject of a rich physics [28], [29], [30]. Indeed, the liquid is condensing in the form of drops only if the substrate is not completely wet (non-zero contact angle). This condensation process, in which a nascent liquid appears in vapor as droplets that settle on the substrate, is equivalent to the liquid-liquid (water-CP) demixing process and settling of the nascent water droplets that we observe on glass (see below) when

cooling the CP phase (pre-saturated with water at 20°C) and also called below condensation for simplicity. Such an assembly of water drops on a substrate ('breath figure'), one of these drops, either initially present or added by the experimenter, acts as a 'humidity sink' if for some reason the vapor pressure (or the concentration of water molecules) near this drop is lower than that near the other liquid droplets. This is for example the case if this drop has been frozen as a result of a decrease in T (the other droplets remaining in supercooled liquid), or is made up of salted water (the other drops being pure water drops) [31], [32]. The flux of water towards this particular drop is responsible for the diffusive growth of a droplet-free zone on the substrate around the drop. The process in which an ice crystal born in one particular water droplet grows at the expense of the neighboring supercooled droplets, with a diffusive droplet-free zone around the crystal, is known as the Wegener-Bergeron-Findeisen (WBF) process [31].

6.3. Experimental part

6.3.1. Experimental configuration and setup

The experimental configuration is schematically depicted in Figure 6.1. A fused silica photometric absorption cell (Hellma^{TM} QS 110-2-40, path length 2 mm, volume ~ 700 µl) is filled with cyclopentane equilibrated with water at room temperature (≈ 20°C). A small drop of water (hereafter called the 'primary drop') is deposited close to the center of the lower face of the cell, using a low-flow-rate syringe pump (Aladdin^{TM}-1002X) and a syringe needle with a bent tip. The cell is loosely stoppered, so that the pressure inside the cell is atmospheric pressure. The rectangular cell is inserted with its faces horizontal, in a cylindrical aluminium (AU4G) holder (not shown in Figure 6.1) with rectangular apertures for observations on an inverted microscope. The upper face of the cell-holder is in contact with an annular Peltier element (itself cooled by a water-cooled radiator not shown in Figure 6.1). The central holes of all elements of the setup allow passage of the full aperture beams of the microscope. The Peltier element is driven by a temperature controller (Accuthermo ATEC302) and a Pt100 sensor inserted in the cell holder.

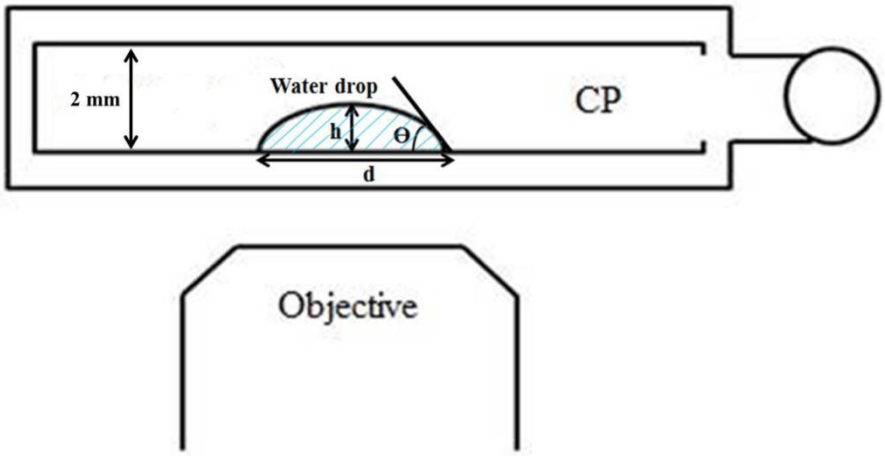

Figure 6. 1. Experimental configuration: the cell, filled with cyclopentane (CP) and a water drop (primary drop) either sitting on its lower wall (as depicted here), or hanging on its upper wall, is positioned above the objective of an inverted microscope. The cell-holder and temperature control system are not shown here. The drop is not to scale: its radius is below the millimeter range.

All the above parts are enclosed in a dry nitrogen atmosphere to prevent condensation, in an *ad hoc* plastic holder with windows on the optical axis: a standard 45 mm diameter cover slip as lower, observation window (Knittel Gläser) and an IR filter above, to prevent local heating during DIC observations (cutoff 710 nm, Edmund Optics).

In preliminary observations, we employed an AE21 inverted microscope (Motic), equipped with a Ueye SE1240 camera (IDS). Most of the data reported here were recorded on a Ti Eclipse (Nikon) with a PROEM 512B EMCCD camera (Princeton Instruments) or an ORCA 4.0 SCMOS camera (Hamamatsu). Various contrast modes were employed, principally bright field (transmission), differential interference contrast (Nomarski phase contrast, DIC) and wide field fluorescence. Confocal reflectance (λ = 532 nm, DPSS laser, Crystal Laser) was performed with a C1-Si ready laser scan head (Nikon). We used long working distance objectives ranging from x4 to x20, sometimes augmented with a x1.5 tube extender lens. The thickness of the cell and of the liquids themselves introduces strong axial smearing of the focus, so best results are obtained with objectives with a correction ring, such as the CFI SPFL ELWD x20, Nikon. Sub-micron resolution is obtained for the highest magnification (e.g., with the x20 objective and the tube extender).

6.3.2. Data Analysis

The data were analyzed with ImageJ [34] and gnuplot [34]. Micrographs shown here underwent only linear contrast enhancement to highlight specific features.

6.3.3. Chemicals

The water is ultra-pure water (resistivity > 18 MΩ·cm) produced in our laboratory by a PureLab Classic® from ELGA Labwater. CP is bought from Sigma-Aldrich (reagent grade, purity > 98%). In some experiments, DASPI (trans-4-[4-(dimethylamino)-styryl]-1-methylpyridinium iodide), a water-soluble fluorescent molecule with excitation wavelength equal to 505 nm, is added to the primary drop in small amounts ($2 \cdot 10^{-6}$ M). This molecule is a weak surfactant, i.e. it adsorbs onto the water/oil interface: the $2 \cdot 10^{-6}$ M solution lowers the water/CP interfacial tension by about 10 mN/m. The fluorescence of this dye is enhanced when its geometry is constrained to the planar form, e.g., by viscous solvents or by adsorption at solid/liquid or liquid/liquid interfaces [35]. In other experiments, Rhodamine6G-tagged PMMA nanobeads are used to exhibit the flow of water in and around the primary drop. The beads have a mean diameter of 27 nm and are stabilized in water by CTAB, a cationic surfactant. The stock suspension was diluted in deionized water, to obtain a mean average distance between particles in the range of 10 µm. The concentration of CTAB in the samples is then in the ppm range.

6.3.4. Substrate and substrate treatment

The Hellma™ cells used as substrate are fused silica of optical quality (Heraeus™, Suprasil® 2 Grade B) [36]. In the early stages of this study, we used untreated Hellma cells, which between two experiments were cleaned either by washing with a 2 wt.% alkaline solution of Hellmanex™ III in an ultrasonic bath, or by rinsing with ethanol and then deionized water, removed by drying in an oven at 70 °C. These cells had poorly reproducible contact angles θ (see Figure 6.1) lying in the range of 15°-75° (see next paragraph for a description of contact angle measurements).

Many of the results presented in this paper are obtained with the above substrates rendered either strongly hydrophilic (water-wet) by a cold plasma discharge procedure (He/1%vol. O_2), or strongly hydrophobic by treatment with silane (Sigmacote, Aldrich). The corresponding contact angles are $\theta \approx 1°$ and 145°, respectively.

6.3.5. Substrate wettability assessment: contact angle measurements

Since drop dimensions are in the millimetre range, i.e. much smaller than the capillary length $(g/\gamma\Delta\rho)^{1/2} \approx 4.5$ mm ($\gamma \approx 50$ mN/m and $\Delta\rho \approx 250$ kg/m^3 are the interfacial tension and density difference between water and CP, and $g = 9.8$ m/s^2 is the acceleration due to gravity), gravity has a negligible effect on the drop shape, which is spherical. A rough estimate of contact angle is thus

obtained from the drop diameter *d* and the difference *h* in focal plane positions of the glass surface and the top of the water drop: $\tan(\theta) = \frac{d \cdot h}{(d/2)^2 - h^2}$.

For small values of *h*, i.e. for low contact angles θ, a precise assessment of θ is obtained from the interference patterns (formed by rays reflected by the glass/water and water/CP interfaces) apparent in confocal reflectance images of the drop. The (low) contact angle is given (in radians) by dividing the elevation (= λ/2n, where λ = 532 nm and n = 1.33, the refractive index of water) by the distance between two consecutive intensity maxima or minima observed near the edge of the water drop. These interference patterns can be used to reconstruct the drop profile (Supplementary Material S1).

6.3.6. Description of a typical experiment

An experiment consists in monitoring by microscopy the changes that occur in/on the primary water drop (which is immersed in CP, see Figure 6.1) and in its vicinity while cycling T across T_{dis} = 7°C (the temperature of CP hydrate dissociation) in order to form and dissociate the CP hydrate halo on the substrate. We have carried out a series of experiments (about a dozen, summarized in Supplementary Material-Table of experiments), in which we varied the conditions of subcooling, substrate wettability, etc., and/or the domain of interest (e.g. the water drop itself or its vicinity). In this work, the focus is on the substrate in the immediate vicinity of the drop, where the hydrate halo is observed; the crystallization and dissociation events that occur on the surface of the primary drop (i.e. at the water/CP interface) are not the subject of this paper and are only briefly summarized below (see also refs. 37-39).

In order to form CP hydrate from liquid water and CP for the first time, the water has to be converted into ice, which is then melted (at T slightly above 0°C): the CP hydrate is then readily formed at the water/CP interface (see Supplementary Material S2 and ref. 39). An experiment thus entails the following steps (here we give a brief account of the observations, which are thoroughly described and discussed in next section).

6.3.6.1. Step 1: Water drop cooling and freezing

T is rapidly decreased from ambient T (≈ 20°C) down to the temperature necessary to convert the water drop into ice, which typically occurs for T ≈ -15 to -20°C. During this cooling step, water condenses from the initially water-saturated CP phase in the form of microdroplets

('rain'), some of which settle on the substrate. These microdroplets remain (supercooled) liquid owing to their very small sizes.

6.3.6.2. Step 2: Ice melting and growth of the hydrate halo

T is rapidly increased (≈ 5°C/min) to -5°C, then more slowly (1°C/min) to a value in the interval 0°C - T_{dis} ≈ 7°C (most often, in the interval 0-1°C). T is then kept constant for a few minutes. The ice melts and the primary water drop is rapidly (within a few minutes) covered with a polycrystalline hydrate crust, with thickness in the range of a few microns and to increase very slowly with time [37], leaving much of the water in the drop unconverted. At the same time, a hydrate halo emerges from the contact line and then grows on the substrate at the interface between glass and CP.

6.3.6.3. Step 3: Melting of the first hydrate halo

T is raised to above T_{dis} ≈ 7°C (typically, to T ≈ 8-9°C) and then kept constant for a few minutes. The melting of the hydrate halo occurs, shortly before that of the hydrate crust on the primary water drop, which results in an emulsion of CP droplets forming at the drop surface (see ref. 39). The melting of the hydrate halo results in a (liquid) water layer that is retracted in part into the water drop; because it is unstable, some water is left behind on the substrate in the form of water droplets ('secondary droplets'), which are much larger than the microdroplets condensed from CP in steps 1 and 2.

Then, another cycle of CP hydrate formation and dissociation (steps 4 and 5 below) is carried out, similar to steps 2 and 3 except that CP hydrate is formed at T ≥ 0°C, i.e. without prior freezing of the water; the latter CP hydrate formation is possible by virtue of the 'memory effect', i.e. because the temperature and duration of first hydrate melting (step 3) are not too large [39].

6.3.6.4. Step 4: Growth of the second hydrate halo

T is lowered down to T ≈ 0-1°C and then kept constant for a few minutes in order to form the CP hydrate again. Again, the main water drop is rapidly (within a few minutes) covered with a polycrystalline hydrate crust; a hydrate halo again emerges from the contact line, which grows on the substrate at a faster rate than in step 2, because it also fed by the secondary droplets present on the substrate (see step 3).

6.3.6.5. Step 5: Melting of the second hydrate halo

T is driven again to slightly above $T_{dis} \approx 7°C$ (e.g., to 8 - 9°C) to observe again the melting of the halo and that of the hydrate crust covering the water drop into an emulsion of CP droplets gathering at the top of the drop.

In some experiments, additional cycles of CP hydrate formation and dissociation similar to steps 4 and 5 are carried out.

6.4. Results and discussion

We first report and discuss here the observations of halo growth and melting obtained with the strongly hydrophilic (freshly plasma-treated) glass, which were more reproducible and clear-cut in comparison to those obtained with the untreated glass substrates. Most of the observed features were also observed with the untreated glass as well (some of them are reported in the Supplementary Material). Then, a few less common features are reported, which were often observed with the untreated glass (therefore not as hydrophilic as the plasma-treated glass). Finally, a short account is presented on the observations with the hydrophobic substrate, which reveal the absence of a halo.

In the following set of observations (corresponding to experiments 2015/07/17 in Supplementary Material-Table of experiments), the water drop contains $2 \cdot 10^{-6}$ M of the water-soluble fluorescent dye DASPI used as a marker of water seeping out of the drop. After placing the water drop on the lower wall of the freshly plasma-treated cell, the contact line radius is observed to be ≈ 900 μm, the drop height $h \approx 7$ μm and the contact angle $\theta \approx 1°$ (see Figure 6.2 and S1). A strongly fluorescent ring is seen outside of the contact line over a distance of ≈ 50 μm indicating the presence of a thin (precursor) film of the aqueous DASPI solution on the substrate, as expected for a system exhibiting pseudo-partial (frustrated-complete) wetting (see above). The fluorescence is caused by the confinement in a film of thickness not exceeding a few nanometers of DASPI molecules (molecular size ≈ 1.5 nm), i.e. the confinement between the glass-CP interface and the water-CP interface (adsorption occurs on the latter interface as shown by the interfacial activity of DASPI and the strong fluorescence of the emulsion of CP droplets obtained by melting the hydrate crust covering the primary drop in Step 3 of the experiment, data not shown).

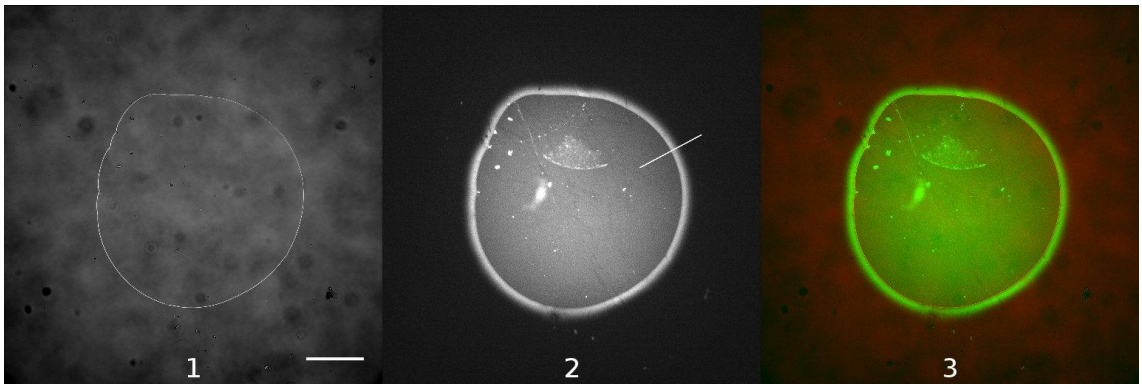

Figure 6. 2. The primary water drop viewed as soon as possible after insertion into the cell. 1, transmission showing the contact line; 2, fluorescence (excitation wavelength 505 nm); 3, superposition of 1 (red) and 2 (green), showing a bright, diffuse ring of fluorescence outside the contact line, and substrate inhomogeneities revealed as brighter or darker spots and lines. Drop diameter ~1800 µm. Scale bar: 500 µm. An analysis of fluorescence intensity across the contact line (white line in 2) shows that fluorescence outside the immediate vicinity of the contact line is uniform.

6.4.1. Cooling down to ~ -15°C: breath figures on the substrate and water drop freezing (Step 1)

Upon cooling, the CP-rich phase (i.e. the CP pre-saturated with water at 20°C) becomes cloudy as a result of the strong decrease of water solubility in CP (≈ 0.03 mol.% at 20°C and 0.01 mol.% at 0°C) [23]. A water-rich phase appears in the bulk of the CP in the form of a 'rain', with microdroplets subject to strong convection. Some of these microdroplets settle and form 'breath figures' on the substrate, as is clearly apparent in Figures 6.3 and 6.4. Their radii, which are in the µm range at T = 10°C, grow to values in the order of 2-3 µm at zero and sub-zero temperatures, where the fraction of substrate covered with these microdroplets reaches values above 20-30% (see, e.g., Figure 6.10). Interestingly, the microdroplets nearest to the primary drop coexist with the thin fluorescent film but do not exhibit any fluorescence themselves. A close view of this region in the fluorescence imaging mode reveals a leopard skin pattern of dark spots corresponding to the microdroplets making up the breath figure.

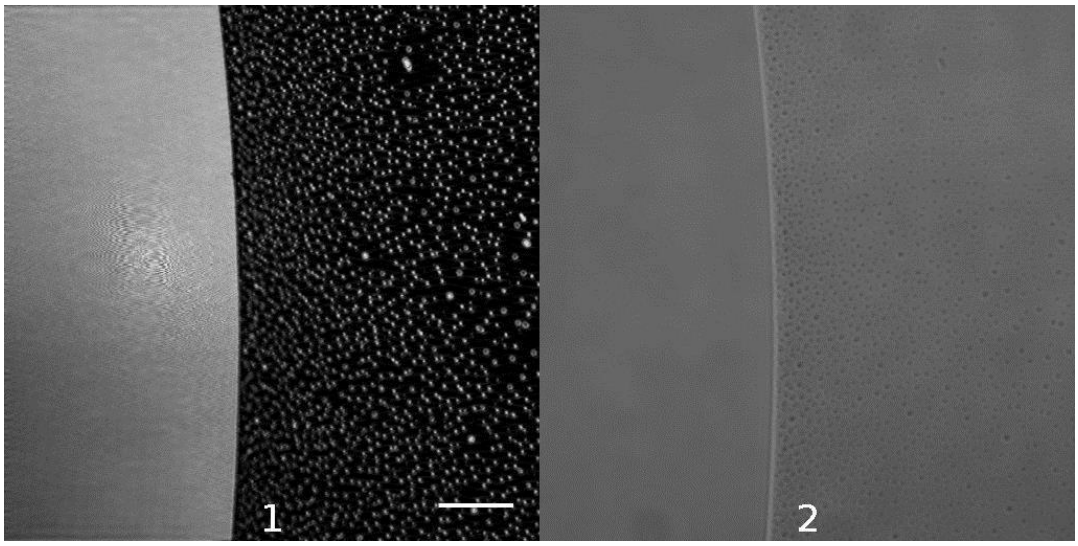

Figure 6. 3. Condensation of water from the CP-rich phase (T ~ 10°C). The main drop lies on the left. 1, confocal reflectance (λ = 532 nm) (high frequency striping due to power line electrical interference partially filtered out by Fourier transformation); 2, transmission. Scale bar 20 µm.

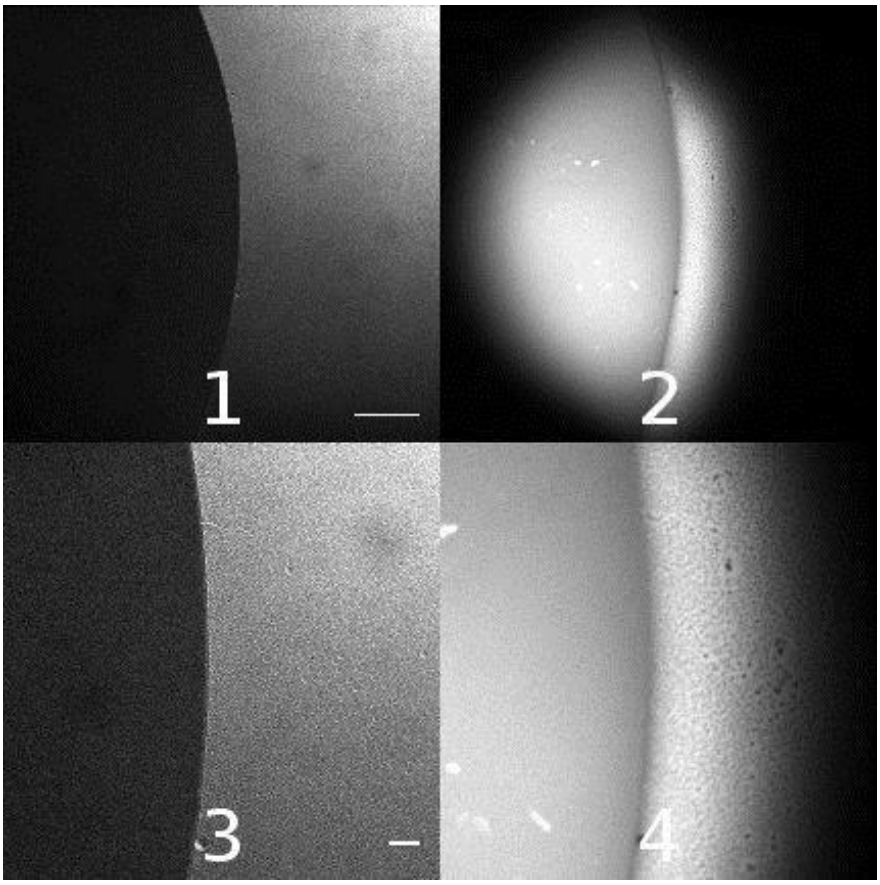

Figure 6. 4. Water condensed from the CP-rich phase is visible in fluorescence (T ~ 10°C). The primary drop lies on the left in these DIC (1, 3) and fluorescence (2,4) images of the region of the contact line. View 2 shows DASPI carried outside the contact line by water in the precursor film *cf*. Figure 6.2. Zoomed views 3 and 4 show the correlation between condensed water droplets (3, DIC) and dark spots with diminished fluorescence (4). Before condensation the spots were absent. Scale bars: 1, 2: 100 µm; 3, 4: 20 µm.

Figure 6.5 depicts the physical picture that emerges from these observations. A nanometer-thick thin film coexists with the primary drop known (*vide supra*) to be only ~ 10 µm high, for a contact line radius of about 1000 µm and a contact angle of ~ 1°. Assuming that the contact angle of the primary drop is similar to that of the condensed microdroplets of radius ~ 2-3 µm, then the latter droplets are about 20-30 nm high and therefore entirely within the depth of focus of the microscope. Therefore, the intensity variations in the leopard skin are due either (i) to differences in DASPI concentration in the bulk of the precursor film, or (ii) to differences in the environment influencing the quantum yield of DASPI. Situation (i) is highly unlikely, since molecular diffusion acting on a timescale of minutes is expected to homogenize the DASPI concentration laterally, washing out the spots. The variations in fluorescence intensity thus reflect differences in the environment of DASPI molecules, which may deform freely (and therefore are non-fluorescent) in the ~ 20-30 nm-high bumps (microdroplets), whereas they are constrained (and therefore fluorescent) in the precursor film (see above). From these observations, an upper limit of a few nanometers on the precursor film thickness can be inferred.

A further proof that the precursor film does not exceed a few nanometers in thickness is provided by the experiments conducted with a water drop loaded with a small concentration of fluorescent PMMA nanobeads with diameter 27 nm (see previous section) in place of the DASPI molecules. In all but one of these experiments, conducted with both the strongly hydrophilic and untreated glass substrates, we observed that these nanobeads remained trapped within the primary drop during all steps of the experimental procedure, including when a hydrate halo was growing on glass. The exception, which is presented later in this section, consisted in a massive breakout through a crack in the CP hydrate crust on the primary drop.

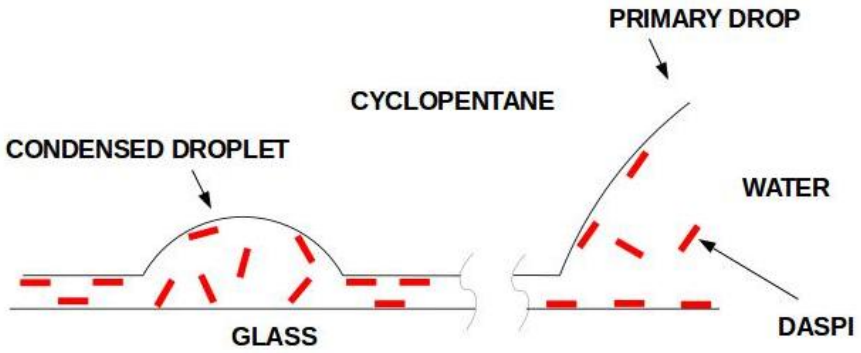

Figure 6. 5. Schematics of the primary water drop coexisting with the precursor water film on glass and the microdroplets condensed from the CP phase. The red bars represent the DASPI molecules, whose fluorescence quantum yield increases or when constrained to planar conformations (e.g., in viscous solvents, or as here, when physisorbed at solid-liquid and liquid-liquid interfaces).

When T is lowered down to -15 to -20°C, the primary drop is observed to freeze within less than 0.1 second, with air bubbles and/or CP droplets being trapped in the ice (as inclusions). Shortly (a few seconds) after, a microdroplet-free zone is observed to grow on the substrate around the contact line in a WBF-type process. Close-up views of these processes are shown in S3 not only for the experiment of Figures 6.2 to 6.4, but for other experiments with untreated (and less hydrophilic) glass. In one of these experiments, the analysis shows that the droplet-free zone grows in a diffusive manner. Ice (and hydrate as well, see below) acts in fact as a humidity sink: it pumps water molecules out of the CP-rich phase, which are driven by diffusion from the region of supercooled water microdroplets to the surface of ice (or hydrate) – this mechanism is that of the WBF process, as we will see below.

The 'breath figures' formed by the supercooled water droplets condensed from CP and the associated phenomenon of droplet depletion near ice or hydrate are observed (in the DIC mode only if the fluorescent dye DASPI is absent) on all glass substrates (some examples are given in S3), except when the CP has not been presaturated with water prior to the experiment. We have not tried to characterize the dependence with elapsed time, temperature or substrate wettability, of droplet radii and substrate coverage. With untreated glass, the latter quantity never exceeded 4-5% (see examples in S3), in contrast to the close-to-jamming coverage observed on the strongly hydrophilic substrates (see, e.g., Figure 6.10).

6.4.2. Birth and growth of the CP hydrate halo (Steps 2 and 4)

6.4.2.1. Early stages of hydrate halo growth

Prior to the hydrate halo there is the hydrate forming and growing near the contact line or as floating 'islands' at various places on the surface of the primary water drop; these pieces of hydrate at the surface ultimately merge and cover the entire surface of the drop. Figure 6.6 shows the growth of one of these 'islands', which is seen floating and attracted towards the contact line. A few seconds after touching the contact line, a hydrate halo emerges and grows on the substrate at the interface between glass and CP. In the case of a first hydrate formation (i.e. at the beginning of Step 2 of the experiment), this sequence of events is preceded by the melting of ice into water, which induces some retraction of the contact line, presumably because of the decrease in drop volume upon ice melting (see S4).

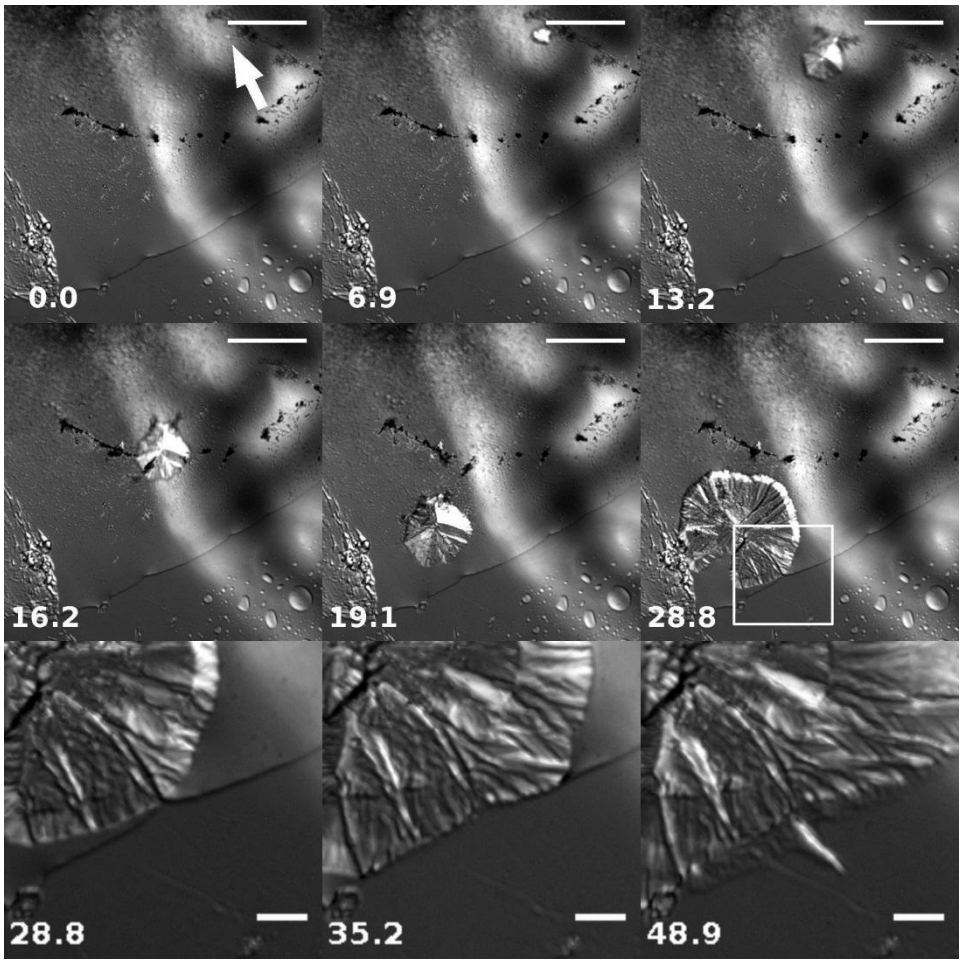

Figure 6. 6. Nucleation of the halo at the contact line. Rows 1 & 2: An 'island' of hydrate crust nucleates in the emulsion left by the previous formation-melting cycle, i.e., steps 1 to 3 (arrow, row 1). Floating at the water-cyclopentane interface, it reaches the contact line (row 2), where the halo appears after a few seconds, visible here as a dark rim outside the contact line (last image, row 3, showing the boxed region in row 2). DIC images; time shown in seconds; scale bars: rows 1&2: 50µm; row 3: 10µm.

6.4.2.2. Halo texture and stabilized growth

Once the halo has emerged at some locations on the contact line (see above), it tends to invade the gaps left in between these locations until it entirely surrounds the drop. Then it advances on the substrate in a rather compact and stable manner. In other terms, the early halo protrusions from the drop do not evolve into an unstable front (e.g., into the branches or 'seaweed' patterns often observed with creeping salt droplets) but rather into the compact structure with a stable advancing front, and a meaningful lateral velocity can thus be determined (see next paragraphs). The halo texture is that of a corrugated, finely-ridged surface, as shown in Figure 6.7. The texture of the halo just behind its leading edge correlates well with the distribution of condensation droplets on the glass, which is an indication that the halo growth is fed by the water on the substrate, rather

than by water flowing out of the primary drop. Larger droplets give rise to elongated bright streaks in the DIC images, indicating an increase in thickness of the halo at those locations.

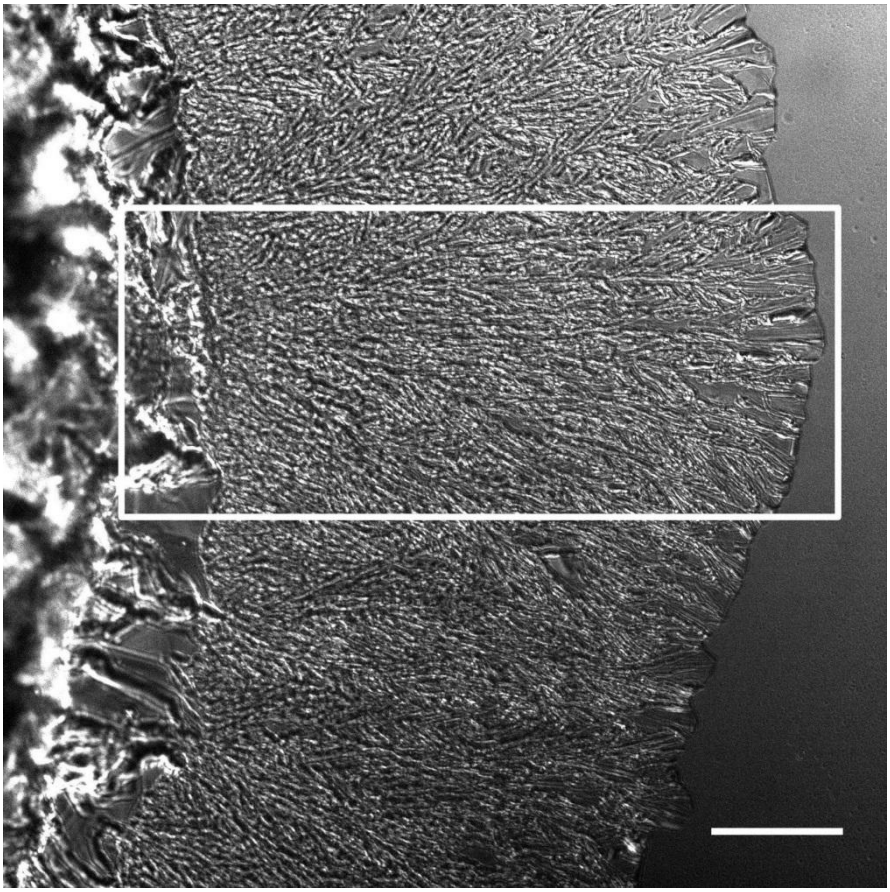

Figure 6. 7. DIC view of an extended CP hydrate halo grown for a few minutes at 0°C on the strongly hydrophilic glass substrate. The boxed area is where melting is visualized below in Figure 6.12, next section (step 2 in experiment 2015/07/17). Scale bar: 100 µm.

6.4.2.3. Halo lateral advance on the substrate

We focus here on the first propagation of the hydrate halo that occurs in step 2 of the experiment. Figure 6.8 below shows close-up views of two regions of the glass substrate with recorded growth of the hydrate halo at T = 0°C: one close to the contact line (left image), and one far from it (right image). The advance of the halo has been monitored against time at various distances from the contact line (see Figure 6.9). The rate of lateral halo growth increases away from the contact line, consistent with halo growth fed primarily by the water present on the substrate, rather than by that issuing from the primary drop. In fact, the water is present in the form of water microdroplets (condensed from the CP saturated at room temperature) forming breath figures on the

substrate, except at early times near the primary drop, where a depletion (microdroplet-free) zone due to the WBF process is clearly apparent (see, e.g., Figure 6.10, which shows enlarged images at various times of track A in Figure 6.8; and also S3). This depletion zone decreases in extent as the halo advances, and the halo accelerates when it catches up with the microdroplets (see also S5).

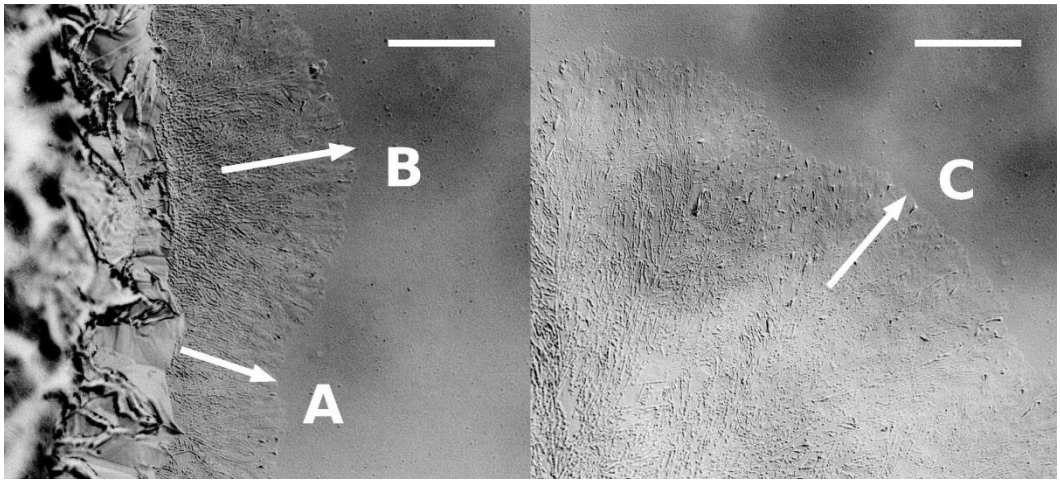

Figure 6. 8. Close-up views of the corrugated halo close to the contact line (left) and far from it (right) on a strongly hydrophilic glass. There is a large amount of water condensed on the substrate in the form of microdroplets (breath figure shown in Figure 6.10). The micrographs stacks (0.1 s/frame) were sampled randomly to construct the advance of the halo along the lines defined by arrows A, B and C. DIC images, contrast inverted for clarity. Scale bar: 100 µm.

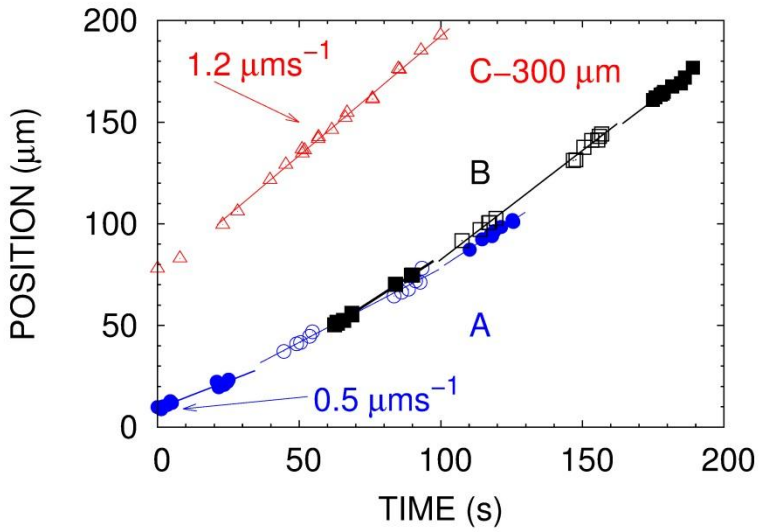

Figure 6. 9. Positions plotted against time of the leading edge of the halo along the arrows A (circles), B (squares) and C (triangles). The local speed of the halo front was determined from linear fits to sets of open or full symbols. Data silences occur during fluorescence observation; seeking DASPI carried out of the primary drop (it was not detected). Trajectory B where the halo was already some 50 µm wide in the first video frame has been shifted horizontally by 62.5 s to highlight that the speed increases with distance from the contact line. Trajectory C, from a different part of the same primary drop, has been shifted down 300 µm to fit in the graph.

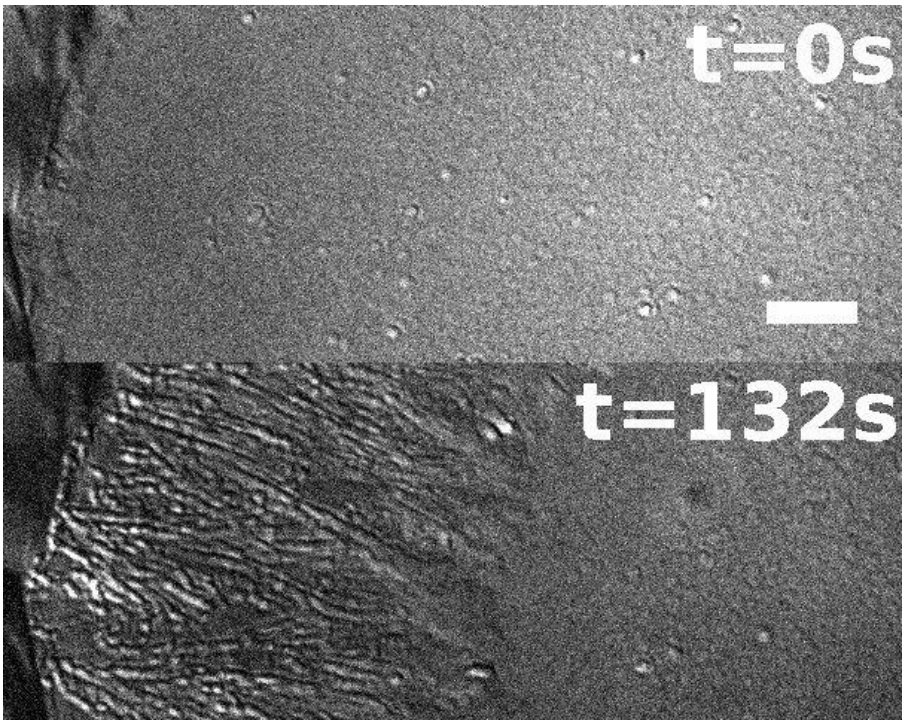

Figure 6. 10. Enlarged views of the halo along track A in Figure 6.8. Upper: the halo has emerged ~ 10 µm from the primary drop; water condensed from the CP is visible to within 50 µm of the contact line, which is surrounded by a droplet-free zone due to the WBF process. Lower: 132 s later, the droplet-free zone has receded and shrunk in extent. Bright streaks on the halo, corresponding to thicker regions, are associated with growth feeding on larger drops of condensation. DIC, scale bar: 20 µm.

6.4.2.4. Halo growth in presence of secondary droplets (Step 4)

The fact that the hydrate halo advance is primarily controlled by the water encountered on the substrate is further supported by the observations of the halo growth in presence of the secondary water droplets left on the substrate upon melting the first halo (see next section). These droplets are larger and much more heterogeneous in sizes than the microdroplets condensed from CP. Due to this additional water present on the substrate, the halo advances indeed with a higher lateral velocity, as shown for instance in the images in Figure 6.11, from which a velocity close to 2 µm/s is extracted, to be compared with values in the range of 1 to 1.5 µm/s observed when only microdroplets of condensed water are present on the substrate (see above and S6). Figure 6.11 also shows the interaction of the advancing hydrate halo with a large (~100 µm) secondary droplet. When this droplet is reached by the halo, some of the water in the droplet is sucked into the halo as seen from the movement at the droplet surface of the CP droplets left by melting a previous CP hydrate crust. At the same time, a hydrate crust starts propagating from the contact point over the droplet at a rapid rate (compared to that of the halo) in the order of 10 µm/s, and it rapidly covers the surface initially occupied by the droplet. We call ‘leap-frog’ this sequence of events. A

transmission-confocal pair of the hydrate crust shows (see S6) the irregular texture of the covered droplet and a maximum thickness in the range of 1-2 µm, consistent with its lateral extent and a contact angle ~ 1°: it is likely that some liquid water is still present beneath the hydrate crust, as it is the case in the primary water drop when covered with a hydrate crust.

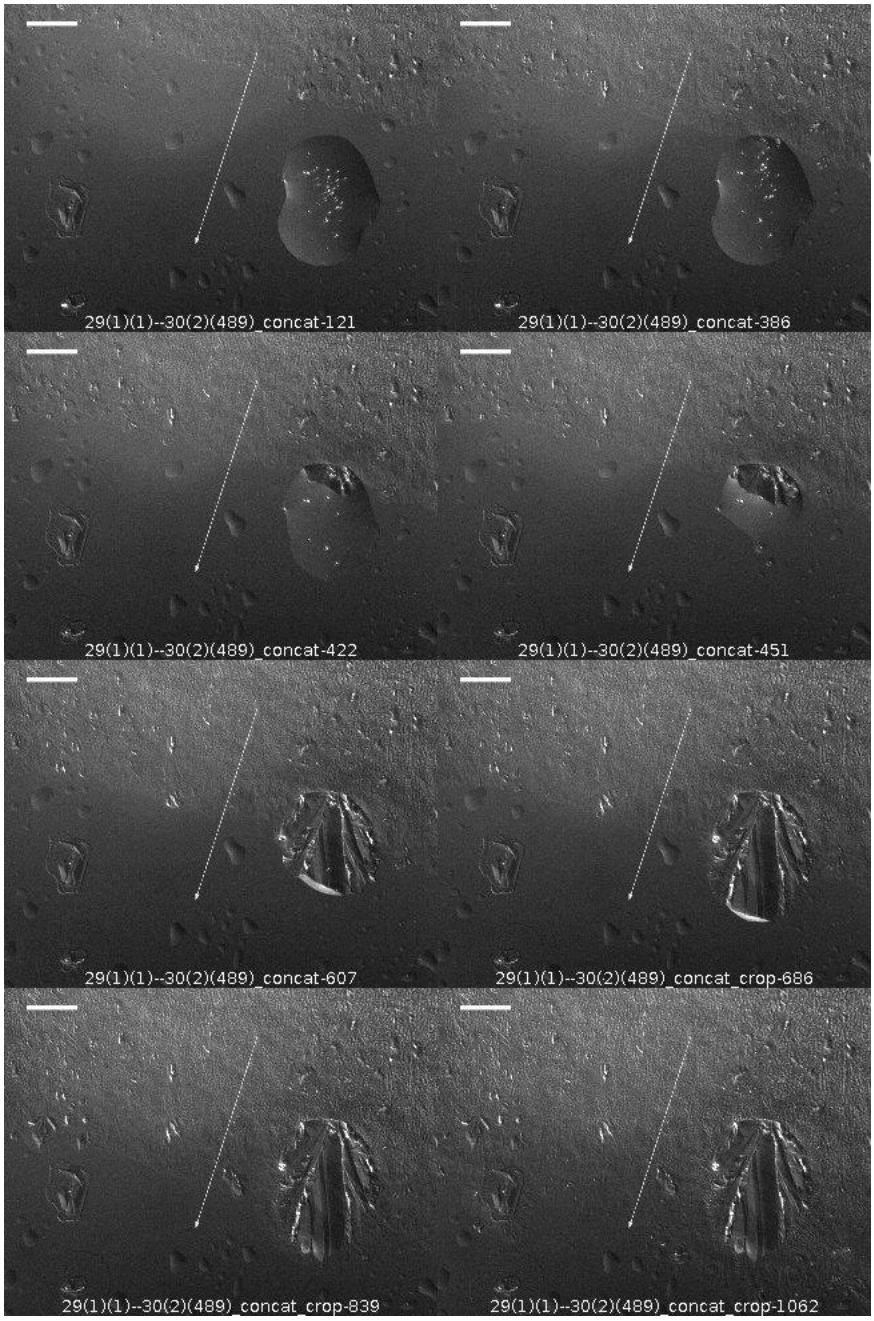

Figure 6. 11. DIC close-up views of the advancing hydrate halo in presence of secondary droplets, with a focus on the interaction of the halo with a large (100 µm) droplet. The white dots in this droplet are the CP droplets left from a previous hydrate formation/melting process. The halo velocity along the white arrow ~ 1.9 µm/s, insensitive to the leap-frog event occurring at a distance of ~ 100 µm. T = 0°C. Scale bar: 50 µm, Experiment 2017/07/17, step 4.

In conclusion, the CP hydrate halo advance on the strongly hydrophilic glass is very strongly dependent on the quantity and nature of the water present on the substrate. At T ~ 0°C the lateral halo velocity is minimum (~ 0.3 - 0.5 µm/s) on glass covered with a nanometric precursor water film, larger (~ 1.0 - 1.5 µm/s) when microdroplets of condensed water are present, and still larger (~ 2 µm/s or more) in presence of secondary droplets. When the hydrate halo hits the largest of the latter droplets, it forms at their surface a hydrate crust at a rate in the range of 10 µm/s or higher. S7 shows transmission and confocal images of a CP hydrate halo advancing on a glass substrate with all these sorts of water present: the measured lateral velocities are consistent with the values mentioned above. We recall here that all these experiments have been performed with a CP phase pre-saturated with water at room T, which therefore remains strongly supersaturated during the measurements.

6.4.2.5. Evidence for halo thickening

At the leading edge of the growing halo, the halo thickness is in the order of the thickness of the droplets present on the substrate, i.e. about 20-30 nanometers if microdroplets condensed from CP cover the substrate (strictly speaking, this thickness has to be multiplied by a factor of 1.27, the ratio of liquid water density to the density of water in CP hydrate). There are qualitative evidences, obtained, e.g., by subtracting images of a given hydrate halo taken at two different times, that the halo thickens with time. A more quantitative evidence of such thickening is provided by transmission/confocal reflectance images of the edge of the hydrate halo such as those shown in Figure 6.12, from which a halo thickening rate in the order of 5 nm/s is inferred. The water that contributes to such thickening may be the water molecules dissolved in CP and/or the microdroplets of liquid water still suspended in the bulk of the CP phase and falling on the halo. Evidences of the latter phenomenon are apparent in some videos.

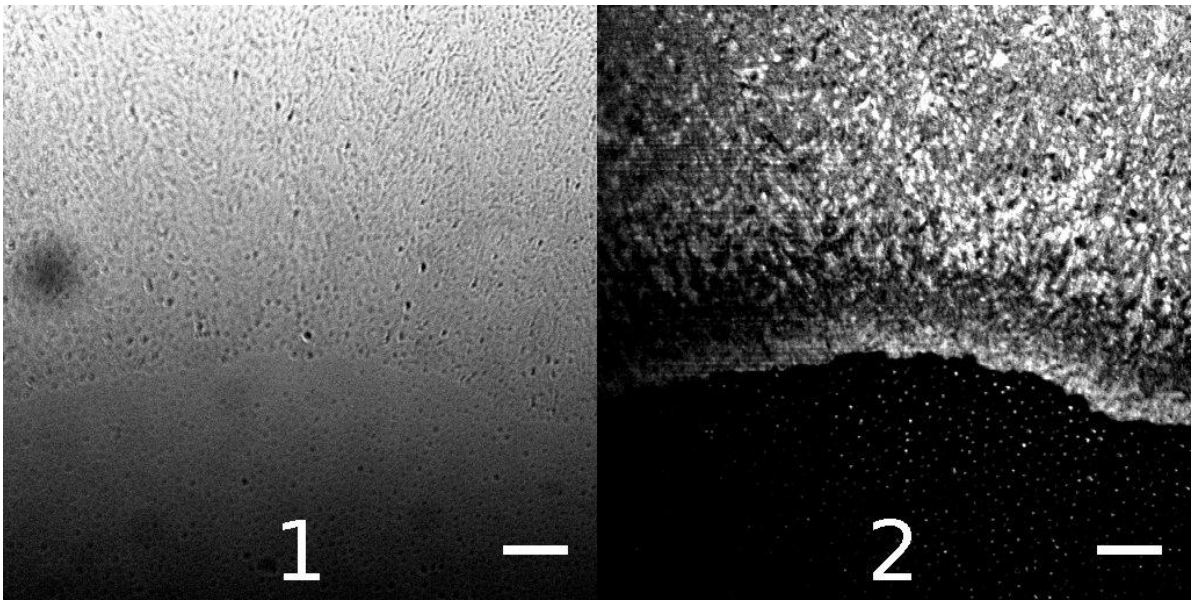

Figure 6. 12. Transmission (1)-confocal reflectance (2) pair of the leading edge of the hydrate halo on strongly hydrophilic glass, recorded at a stable temperature of ~ 0°C. The halo front was advancing at a rate of 1.5 µm/s, consistent with the presence of condensed microdroplets on the substrate. The presence in (2) of a bright edge, dark band, and then bright background behind the edge, which is due to interferences between rays reflected by the various interfaces (e.g., glass/hydrate and hydrate/CP interfaces), means that over this sequence, which extends here over ~ 60 µm, the halo thickens by λ (=532 nm)/2n ~ 200 nm (n=1.35 is the index of refraction of hydrate). The halo thus thickens at a rate of 200 nm per 60/1.5=40 seconds, or 5 nm/s. Scale bar: 20 µm.

The most compelling evidence for such thickening, however, is obtained from the analysis of the images of the melting hydrate halo, which are presented and discussed below. Hydrate halo thicknesses larger than 1 µm are inferred from this analysis (see below).

6.4.3. Melting of the CP hydrate halo (Steps 3 and 5)

6.4.3.1. Early stages of halo melting

When T is increased to above the CP hydrate dissociation temperature (~ 7°C), the hydrate halo melts as illustrated in Figure 6.13. Melting is more pronounced or starts earlier near the contact line. The first textural change is the disappearance of bright streaks oriented parallel to the previous growth direction, which leaves a finely ridged surface, visible in the enlargements given in Figure 6.14.

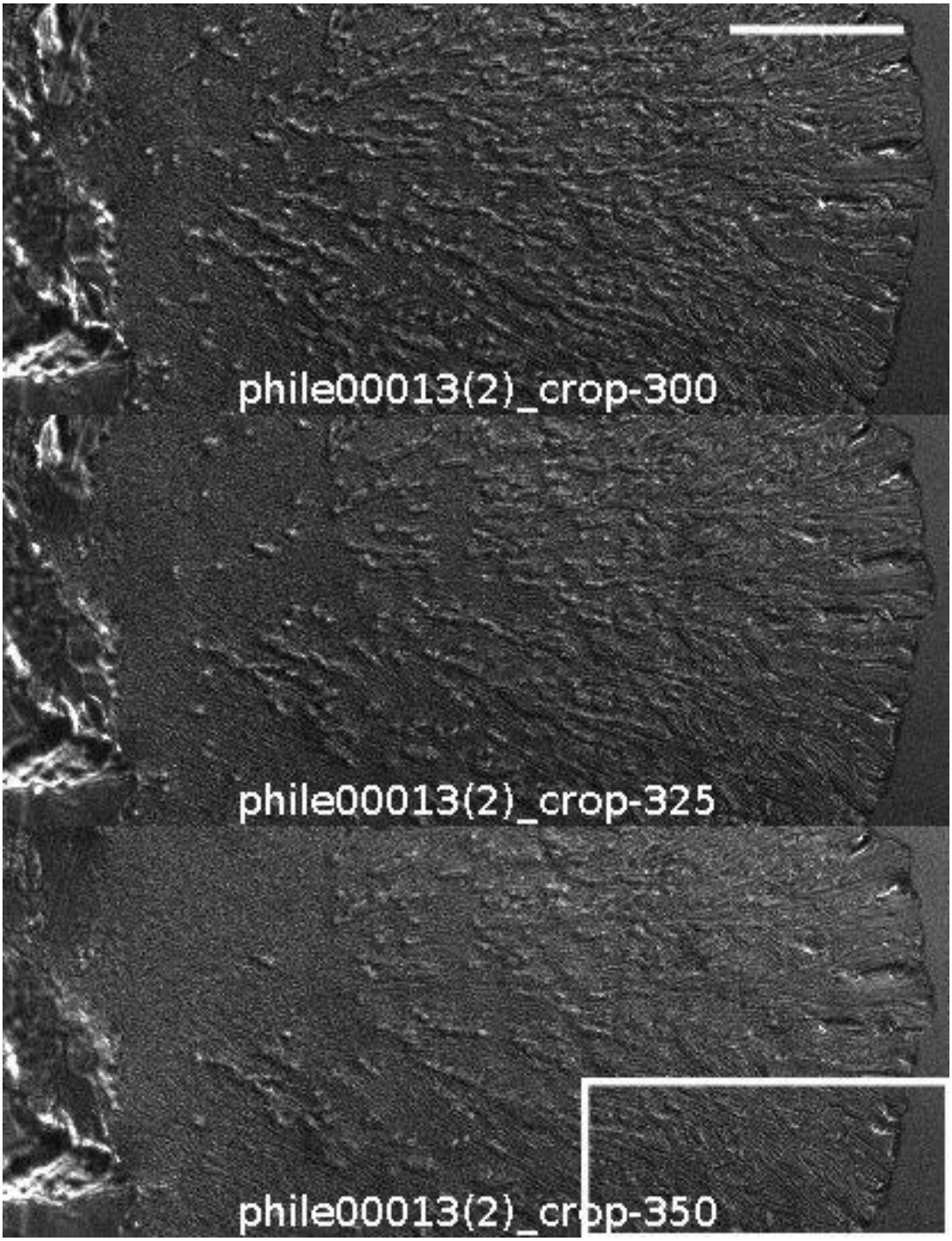

Figure 6. 13. Melting of the CP hydrate halo shown in the boxed area of Figure 6.7. The top image has been obtained 30 seconds after that in Figure 6.8 and T has reached 8°C a few seconds before. The two lower images are obtained 2.5 s and 5 s later (T = 8°C). The boxed section is enlarged in next Figure. Scale bar: 100 µm.

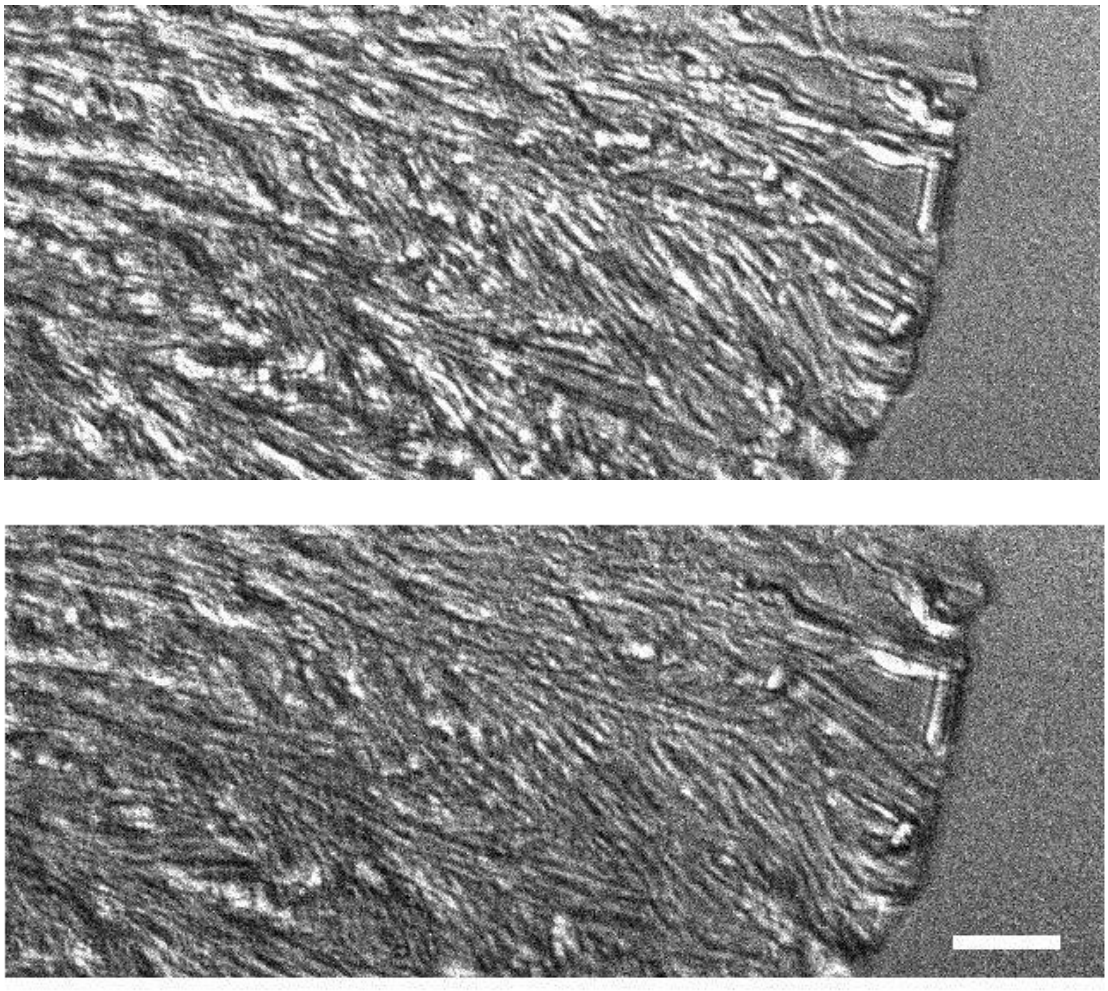

Figure 6. 14. Enlargement of the box in the upper and lower DIC images of Figure 6.13. Scale bar: 20µm.

We recall that DIC shows contrast in thickness and/or refractive index. The brighter lines in the top view are likely to be thicker parts of the halo resting on the substrate, which disappear first upon melting. Indeed, as shown in Figure 6.15, the finely grooved areas visible in the lower photo are progressively pushed out of focus by water invading from the left, and they eventually dislocate and rotate as solids, suggesting they are indeed floating on some liquid (melt water).

.

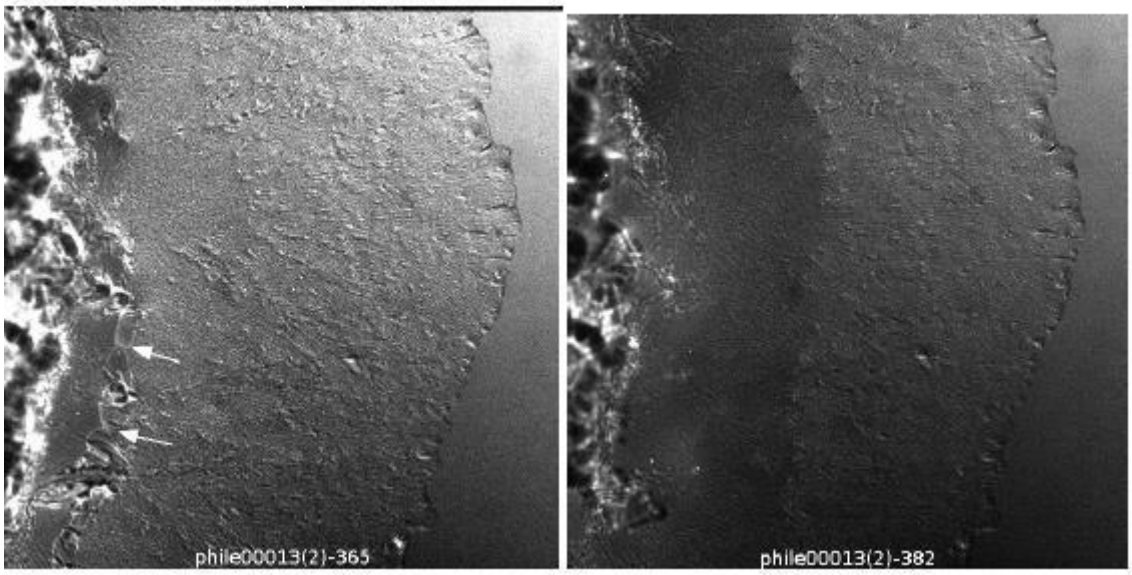

Figure 6. 15. Water from the main drop flooding under the hydrate halo melting at T = 8°C. The hydrate halo was initially (t = 0) that shown in Figure 6.7 (same field of view). Left: 36.5 s, water entering (arrows show a meniscus entering from the left). Right: the halo (viewed from below) is lifted off the substrate. The thin halo on the right eventually breaks up. The corresponding video shows that the halo then floating on a liquid film, with pieces of it rotating as solids.

6.4.3.2. Late stages of halo melting

The melt water that results from the melting of the CP hydrate halo does not form a stable film in-between the glass substrate, as expected from the pseudo-partial wetting character of water on glass in presence of CP, but rather undergoes a transition towards a situation where water droplets coexist on the surface with a nanometer-thick water film. In this process, which lasts a few tens of seconds as illustrated in Figure 6.16, part of the water resulting from halo melting is retracted towards the primary drop, and the other part is left on the substrate in the form of secondary droplets with sizes typically varying from a few tens to hundreds of microns. The heights of the transient hills or valleys and the heights of the secondary droplets at the end of the process (see Figure 6.16) can be estimated by counting the number of interference fringes and multiplying this number by $\lambda/2n_W$ ~ 200 nm (λ = 532 nm and n_W =1.33 is the index of refraction of water). An equivalent water film thickness (if this film were stable following hydrate melting) can be guessed from the images of the transient states (such as the one at 188.8 s in the Figure below). In the example shown here and in other examples, we observed that the equivalent film thickness is larger than 1 µm, whereas the quantity of water remaining on the substrate in the form of secondary water droplets at the end of the process is somewhat lower – the equivalent film thicknesses are in the

order of a few tens to hundreds of nanometers, typically (the latter quantity is obtained by image analysis of the secondary drops, assuming their contact angle is similar to that of the primary drop).

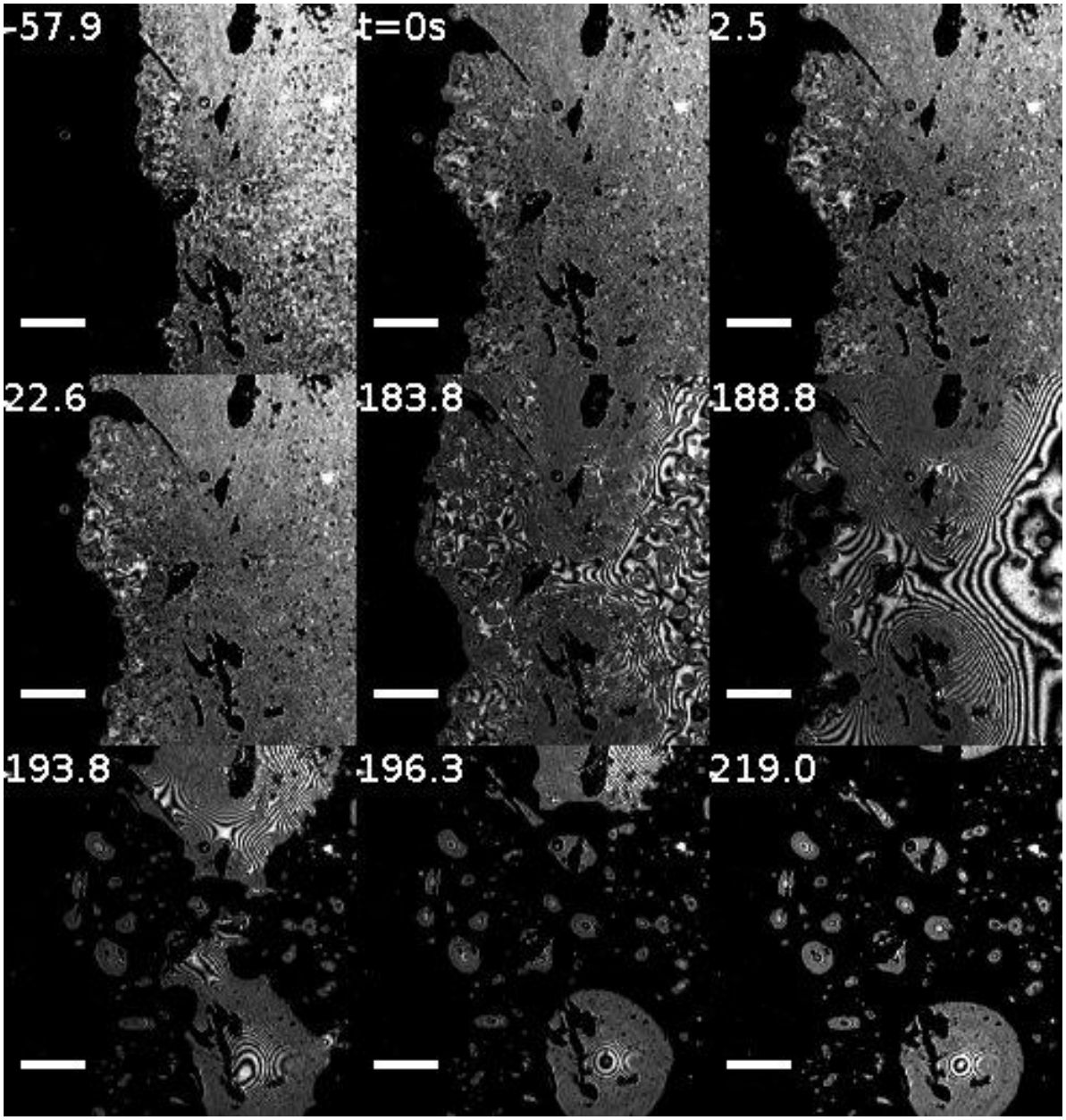

Figure 6. 16. Sequence of confocal reflectance images (λ = 532 nm) of the hydrate halo from the moment of greatest extent and onset of melting (t = 0s) to the late stages of the melting process. It shows moving interference fringes due to reflections from the glass-water and the water-CP interfaces. Phase inversion at the latter interface (due to the refractive indices for glass, CP and water in the order $n_G > n_{CP} > n_W$) should lead to a *dark* fringe at vanishing thickness. The nanometer-thick water film on the substrate should be dark for the same reason (*cf.* Newton black films). However, the edge of the halo is grey, implying finite thickness at the edge. The thickness of the water film at the *m*th *dark* (resp. bright) fringe is $m\lambda/(2n_W)$ (resp. $(m-½)\lambda/(2n_W)$). The zeroth-order dark fringe appears to extend ~5 μm into the halo front in the image at t = 2.5s, surrounding an isolated bright fringe; from which the thickness is about 100 nm. Scale bar 10μm. Time shown in seconds.

6.4.4. Observations with untreated glass substrates

Most of the features described above have also been encountered with untreated (hence, less hydrophilic) glass substrates. Some experiments with untreated glass substrates have also been conducted with a CP phase not pre-saturated with water; the quantity of water solubilized in CP is unknown, however.

As already pointed out above, the radii of the water microdroplets condensed from CP were observed to be similar on untreated and plasma-treated glass, while the fraction of the glass substrate covered by the these microdroplets was much smaller on the untreated - typically, in the range of a few percent. Some breath figures and images of droplet depletion near the ice are shown in S3.

6.4.4.1. Halo growth from water issuing from cracks in the hydrate crust covering the primary drop

This feature is more likely to be observed with drops sitting on untreated glass because of the height of the primary drop (a higher contact angle means a larger height h for a given drop volume, see Figure 6.1). This height provides a larger hydrostatic pressure and facilitates the exit of water out of the drop. In one experiment with untreated glass conducted with fluorescent (Rhodamine6G-tagged) nanobeads present in the primary water drop, we did observe a ‘massive breakout’ of the water with its fluorescent particles through a crack in the hydrate crust at one point in the contact line. An illustration is provided by the DIC and fluorescence images extracted from the same movie and shown in Figure 6.17. The DIC images show the halo protruding from the contact line along one preferential path and the fluorescence images show that this path is that of substrate striations. The fluorescent nanobeads initially present in the water drop are seen escaping with a high velocity to the expanding halo through a narrow point on the contact line – the rest of the contact line is sealing, at least to the 27 nm-sized beads. Outside the water drop, the beads are seen flowing inbetween the halo and the substrate in the growth direction, which is here that of substrate striations.

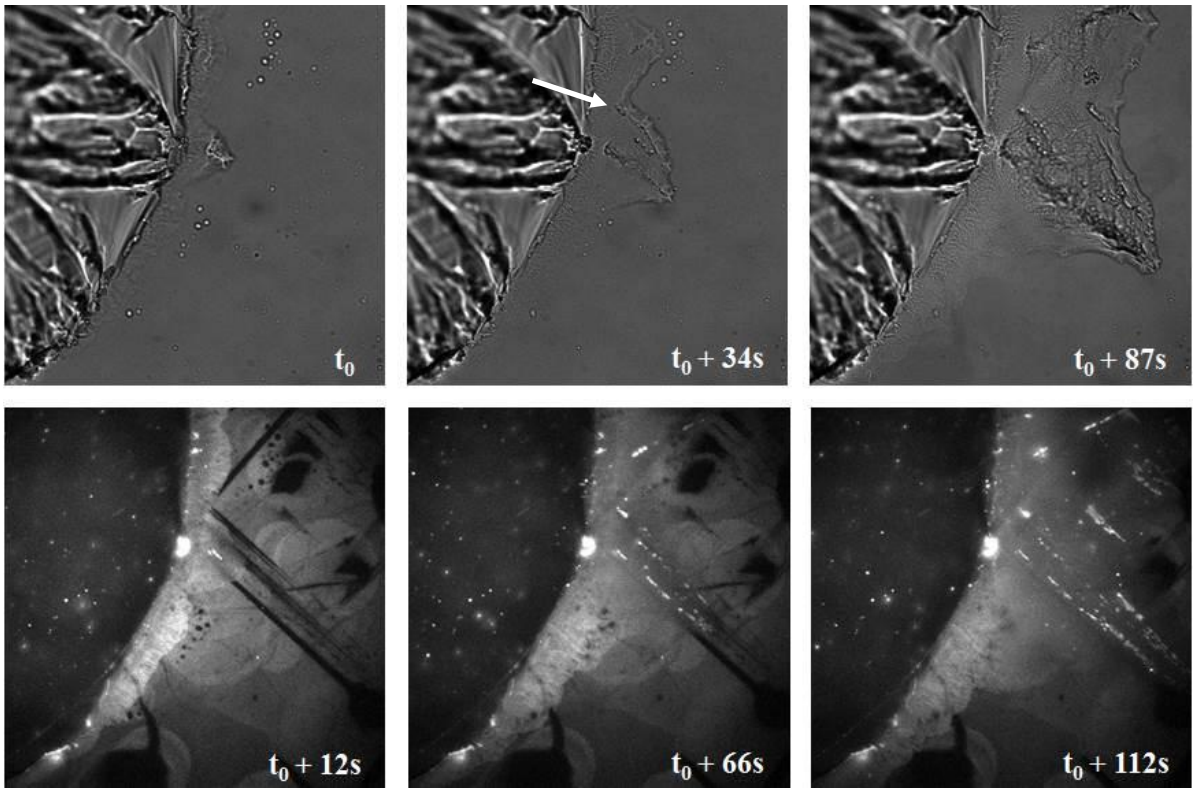

Figure 6. 17. Images in DIC (top row) and fluorescence (bottom row) mode of the early stages of the hydrate halo growth. T ≈ 0.5°C, second hydrate formation (step 4). The fluorescent beads escape the interior of the water drop by crossing the contact line (white arrow) and then follow substrate striations. The few white dots outside the drop at the beginning of the movie (at t_0) presumably correspond to the beads entrained and left on the substrate during the first formation and melting of the halo (steps 2 and 3 of the experiment 2015/04/30).

6.4.4.2. Evidence for slow diffusive water transport through the CP phase to the hydrate halo

In another experiment with untreated glass (2015/02/20), in which the CP phase was not pre-saturated with water, a strong slowing down in the growth of the first hydrate halo (step 2 of the experiment) was noted as the halo advanced on a substrate with no water microdroplets present. The analysis of the movie (with some snapshots shown in Figure 6.18), which shows 400 seconds of a CP hydrate halo advancing from the edge of the primary water drop at T ≈ 0°C on glass, indicates a 20-fold decrease in halo velocity, from about 0.5 µm/s when the halo front is close (within less than 50 µm) from the contact line of the water drop (beginning of the movie) to ≈ 0.02 µm/s when the halo extension is maximum (end of the movie). The same movie shows that, next to the advancing hydrate halo, there is a droplet-free zone on the substrate; as the hydrate halo advances, the water droplets nearest to the halo disappear, in such a way that the extension of the droplet-free zone remains approximately constant (and equal to 100 µm). This WBF-type process is similar to that observed with ice and described in S3: the water in the droplets at the edge of this zone dissolve

into the CP phase and is transported by diffusion along the water concentration gradient, i.e., from the region of liquid/liquid coexistence (CP + metastable liquid water droplets) to the region of liquid CP/hydrate coexistence (i.e. to the edge of the CP hydrate halo). The quasi-arrest of the CP hydrate halo on the substrate shows that the diffusive WBF-type mechanism of CP hydrate growth is a very slow process, at least when the CP phase is subsaturated with water. Unfortunately, the degree of subsaturation of the CP phase is not known here. This feature, namely a very slow advance of the CP hydrate halo inbetween glass and subsaturated CP, is also expected with a strongly hydrophilic glass. Additionally, these observations confirm that, at least for hydrate halo extending over a few hundreds of microns, the contribution to halo growth of the water coming from the primary water drop is extremely small.

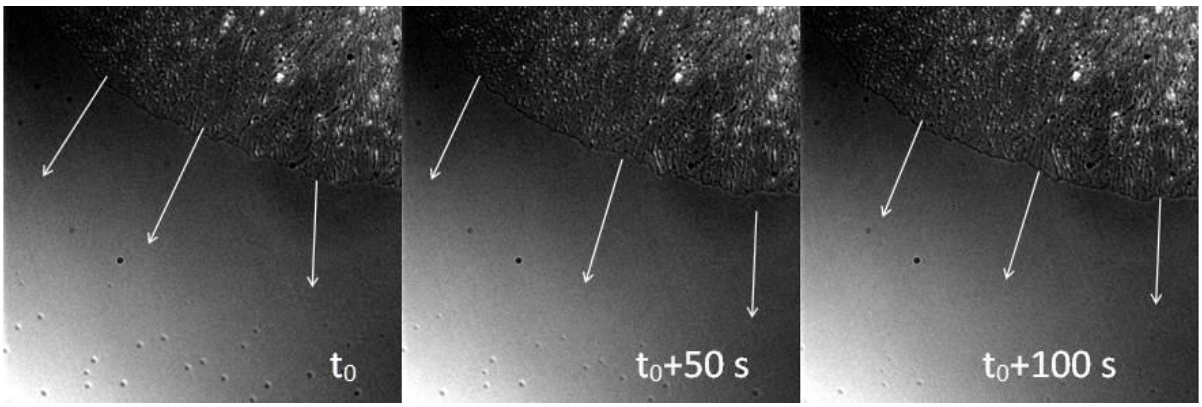

Figure 6. 18. Close-up views of an advancing (first) hydrate halo on glass (T = 0.5°C): the arrows indicate the direction of halo growth. The tiny water droplets closest to the halo disappear as the halo advances: the extent of the droplet-free zone stays in the range of 100 µm. Field of view: 403 µm. Experiment 2015/02/20.

6.4.5. Observations with a hydrophobic glass substrate

The image on the left of Figure 6.19 is that of a water drop on the silane-treated glass wall following step 3 of the experiment: first, the drop has been frozen at ~ -15°C (step 1), then the first CP hydrate has been formed by heating to T ~ 0°C (step 2), and finally this hydrate has been melted at ~ 8°C (step 3). The dark central disk is the (out of focus) emulsion floating at the top of the drop; the irregular bright line is the contact line; and the regular outer dark ring surrounded by a cusp is the drop equator (out of focus). The image on the right shows the same water drop during step 4 of the experiment a few minutes after T has been lowered to 0°C and the water drop surface has been

covered with CP hydrate. The aspect of the drop does not change during the following minutes (data not shown): in particular, there is no halo growing on the substrate from the contact line.

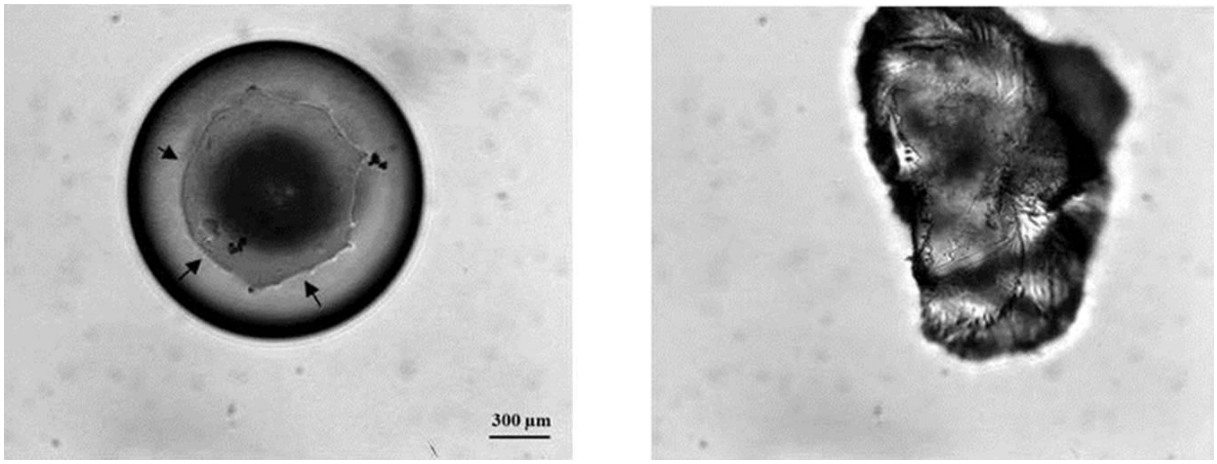

Figure 6. 19. CP hydrate formation on a water drop sitting on a hydrophobic glass substrate (see text) (T = 0°C). Experiment 2015/11/06.

6.5. Summary, prospects and conclusions

The growth properties of a cyclopentane hydrate halo advancing from the contact line of a (primary) water drop deposited under cyclopentane on glass along the interface between this substrate and cyclopentane have been observed by using methods such as differential interference contrast (Nomarski), fluorescence and confocal reflectance microscopies.

Contrary to expectation, this hydrate halo grows laterally and thickens on the glass substrate by water sources external to the primary water drop. These sources include the (supercooled) liquid contained in the precursor film near the water drop and in the microdroplets of water condensed out of the cyclopentane pre-saturated with water at a higher temperature; some of these microdroplets settle on the substrate in the form of breath figures, and the others remain suspended in the bulk of the cyclopentane phase for a while. Another source is provided by the larger ‘secondary’ droplets left on the substrate by a previous sequence of halo formation and melting. Finally, the water molecules dissolved in the bulk of the cyclopentane phase contribute to hydrate halo growth, particularly by transporting the water molecules from droplets of (supercooled) liquid water to the hydrate in a Wegener-Bergeron-Findeisen type process.

The preliminary results presented in this paper show the impact on hydrate halo growth of factors such as substrate wettability and the water oversaturation of the cyclopentane phase. The hydrate halo could not be detected on a hydrophobic (silane-treated) glass, and the hydrate halo grows quicker when the cyclopentane phase is oversaturated with water at the temperature of interest, which is achieved in this work by pre-saturating the CP with water at room temperature (20°C). Another factor that is expected to play an important role and is worth being investigated in the future is the subcooling degree, i.e. the distance to the temperature of dissociation.

The phenomenon of hydrate halo growth has similarities (and differences) with frosting and, more specifically, with the frost halos growing around a freezing water drop on a substrate, as well as with the so-called creeping of evaporating salt solutions. Frosting occurs either via ablimation (the reverse process to sublimation, that is, the direct vapor - solid phase transition) or via condensation (i.e. the direct transformation of supercooled liquid microdroplets into ice), in a manner that depends on substrate wettability, vapor humidity and temperature. Ablimation frosting is similar in our system to dissolved water molecules directly transforming into hydrate, whereas condensation frosting would correspond to the water droplets being incorporated into the halo. Frost halos forming on substrate near a freezing water drop are the results of a complex process which involves the evaporation of water from the freezing water drop (due to the released heat), the condensation on the cold substrate of subcoooled water microdroplets and then frost propagation from the frozen water drop through these microdroplets, in a manner that depends on water vapor concentration, substrate thermal conductivities and wettability [14]. Evaporating salt solutions give rise to salt crystallites growing on the substrate (usually glass) well beyond the extent of the initial aqueous drop. The observed growth patterns are diverse and depend in a complex manner on the type of salt, the water evaporation rate, the various surface energies involved, etc. The growth process is ensured by transport of fresh aqueous solution from the ‘reservoir’ to the tip of the creeping crystallites, which occurs either aside and on top of the crystallites (top supplied creeping), or in the narrow space between the crystallites and the substrate (bottom supplied creeping). This topic, which had received little attention since the early works by Wahsburn [15] and Hazlehurst et al. [16], is now experiencing a revival of interest [17], [18], [19]. In conclusion, some progress is to be expected from the consideration of the similarities and differences between hydrate and frost halos as well as creeping salt solutions.

REFERENCES

[1] Nesterov, A. N., Reshetnikov, A. M., Manakov, A. Y., Rodionova, T. V., Paukshtis, E. A., Asanov, I. P. , Bardakhanov, S. P., Bulavchenko, A. I., **2015**. Promotion and inhibition of gas hydrate formation by oxide powders. Journal of Molecular Liquids *204*, 118-125.

[2] Sun, C. Y., Peng, B. Z., Dandekar, A., Ma, Q. L., Chen, G. J., **2010**. Studies on hydrate film growth. Annual Reports on the Progress of Chemistry, Section C (Physical Chemistry) *106*, 77-100.

[3] Saito, K., Kishimoto, M., Tanaka, R., Ohmura, R., **2011**. Crystal Growth of Clathrate Hydrate at the Interface between Hydrocarbon Gas Mixture and Liquid Water. Crystal Growth & Design *11*, 295-301.

[4] Kitamura, M. and Mori, Y. H., 2013. Clathrate hydrate film growth along water/methane phase boundaries- an observational study. Crystal Research and Technology *48*, 511-519.

[5] Li, S. L., Sun, C. Y., Liu, B., Feng, X. J., Li, F. G., Chen, L. T., Chen, G. J., **2013**. Initial thickness measurements and insights into crystal growth of methane hydrate film. AIChE Journal *59*, 2145-2154.

[6] Li, S. L., Sun, C. Y., Liu, B., Li, Z. Y., Chen, G. J., Sum, A. K., **2014**. New Observations and Insights into the Morphology and Growth Kinetics of Hydrate Films. Scientific Reports *4*, 4129.

[7] Daniel-David, D., Guerton, F., Dicharry, C., Torré, J. P., Broseta, D., **2015.** Hydrate growth at the interface between water and pure or mixed CO_2/CH_4 gases: Influence of pressure, temperature, gas composition and water-soluble surfactants. Chemical Engineering & Science *132*, 118-127.

[8] Mochizuki T. and Mori H. Y., **2006**. Clathrate-Hydrate Film Growth along Water/Hydrate-Former Phase Boundaries-Numerical Heat Transfer Study. Journal of the Crystal Growth *290*, 642-652.

[9] Saito, K., Sum, A. K., Ohmura, R., **2010**. Correlation of hydrate-film growth rate at the guest/ liquid-water interface to mass transfer resistance. Industrial & Engineering Chemistry Research *49*, 7102-7103.

[10] Beltran, J. G. and Servio, P., **2010**. Morphological Investigations of Methane−Hydrate Films Formed on a Glass Surface. Crystal Growth & Design *10*, 4339-4347.

[11] Ricaurte, M., Torré, J. P., Diaz, J., Dicharry, C., **2014**. In situ injection of THF to trigger gas hydrate crystallization: Application to the evaluation of a kinetic hydrate promoter. Chemical Engineering Research & Design *9*, 1674-1680.

[12] Fandino, O. and Ruffine, L., **2014**. Methane hydrate nucleation and growth from the bulk phase: Further insights into their mechanism. Fuel *117*, 442-449.

[13] Sundramoorthy, J. D., Sabil, K. M., Lal, B., Hammonds, P., **2015**. Catastrophic Crystal Growth of Clathrate Hydrate with a Simulated Natural Gas System during a Pipeline Shut-In Condition. Crystal Growth & Design *15*, 1233-1241.

[14] Jung, S., Tiwari, M. K., Poulikakos, D., **2012**. Frost halos from supercooled water droplets. Proceedings of the National Academy of Sciences *109* (40), 16073–16078.

[15] Washburn, R., **1927**. The creeping of solutions. The Journal of Physical Chemistry *31*, 1246-1248.

[16] Hazlehurst Jr., T. H., Martin, H. C., Brewer, L., **1936**. The creeping of saturated salt solutions. The Journal of Physical Chemistry *40*, 439-452.

[17] Van Enchevort, W. J. P. and Los, J. H., **2013**. On the creeping of saturated salt solutions. Crystal Growth & Design *13*, 1838-1848.

[18] Fairhurst, D., **2015**. Droplets of ionic solutions in Droplet Wetting and Evaporation: From Pure to Complex Fluids (D. Brutin, ed.). Academic Press.

[19] Shahidzadeh, N., Schut, M. F. L., Desarnaud, J., Prat, M., Bonn, D., **2015**. Salt stains from vaporating droplets. Scientific Reports *5*, 10335.

[20] Pinkert, S. and Grozic, J. L. H., **2015**. Failure Mechanisms in Cemented Hydrate-Bearing Sands. Journal of Chemical & Engineering Data *60*, 376−382.

[21] Spangenberg, E., Priegnitz, M., Heeschen, K., Schicks, J. M., **2015**. Are Laboratory-Formed Hydrate-Bearing Systems Analogous to Those in Nature? Journal of Chemical & Engineering Data *60*, 258−268.

[22] Waite, W. F., Santamarina, J. C., Cortes, D. D., Dugan, B., Espinoza, D. N., Germaine, J., Jang, J., Jung, J. W., Kneafsey, T. J., Shin, H., Soga, K., Winters, W. J., Yun, T. S., **2009**. Physical properties of hydrate-bearing sediments. Reviews of Geophysics *47*, RG4003.

[23] Shaw, D. G., Maczynski, A., Goral, M., Wisniewska-Goclowska, B., Skrzecz, A., Owczarek, I., Blazej, K., Haulait-Pirson, M. C., Hefter, G. T., Kapuku, F., Maczynska, Z., Szafranski, A., **2005**. IUPAC-NIST Solubility Data Series. 81. Hydrocarbons with Water and Seawater Revised and Updated. Part 7. C_8H_{12}–C_8H_{18} Hydrocarbons with Water. Journal of Physical and Chemical Reference Data *34*, 2261.

[24] Brochard-Wyart, F., di Meglio, J. M., Quéré, D., de Gennes, P.G., **1991**. Spreading of non-volatile liquids in a continuous picture. Langmuir *7*, 335-338.

[25] Bonn, D., Eggers, J., Indekeu, J., Meunier, J., Rolley, E., **2009**. Wetting and Spreading. Review of Modern Physics *81*, 739-805.

[26] Bonn, D., Bertrand, E., Shahidzadeh, N., Ragil, K., Dobbs, H.T., Posazhennikova, A. I., Broseta, D., Meunier, J., Indekeu, J. O., **2001**. Complex wetting phenomena in liquid mixtures: frustrated-complete wetting and competing intermolecular forces. Journal of Physics: Condensed Matter *13*, 4903-4907.

[27] Sharma, A. and Khanna, R., **1998**. Pattern Formation in Unstable Thin Liquid Films. Physical Review Letters *81*, 3453.

[28] Beysens, D. and Knobler, C. M., **1985**. Growth of breath figures. Physical Review Letters *57*, 1433-1437.

[29] Beysens, D., **1995**. The formation of dew. Atmospheric Research *39*, 215-237.

[30] Beysens, D., **2006**. Dew nucleation and growth. Comptes Rendus Physique *7*, 1082-1100.

[31] Pruppacher, H. R. and Klett J. D., **1997**. Microphysics of Clouds and Precipitations (Kluwer Academic Publishers), p. 549. The Netherlands.

[32] Guadarrama-Cetina, J., Narhe, R. D., Beysens, D. A., González-Viñas, W., **2014**. Droplet pattern and condensation gradient around a humidity sink. Physical Review E *89*, 012402.

[33] Schneider, C. A., Rasband, W. S., Eliceiri, K. W., **2012**. NIH Image to ImageJ: 25 years of image analysis. Nature Methods *9*, 671-675.

[34] Williams, T. and Kelley, C. gnuplot 4.6, an Interactive Plotting Program, http://gnuplot.sourceforge.net.

[35] Jee, A. J., Bae, E., Lee, M., **2010**. Internal motion of an electronically excited molecule in viscoelastic media. Journal of Chemical Physics *133*, 014507.

[36]http://heraeusquarzglas.com/media/webmedia_local/downloads/broschren_mo/DataandProperties_Optics_fusedsilica.pdf

[37] Taylor, C. J., Miller, K. T., Koh, C. A., Sloan, E. D. Jr., **2007**. Macroscopic investigation of hydrate film growth at the hydrocarbon/water interface. Chemical Engineering & Science *62*, 6524-6533.

[38] Sakemoto, R., Sakamoto, H., Shiraiwa, K., Ohmura, R., Uchida, T., **2010**. Clathrate Hydrate Crystal Growth at the Seawater/Hydrophobic−Guest−Liquid Interface. Crystal Growth & Design *10*, 1296–1300.

[39] Martinez de Banos, M. L., Carrier, O., Bouriat, P., Broseta, D., **2015**. Droplet-based millifluidics as a new tool to investigate hydrate crystallization: Insights into the memory effect. Chemical Engineering & Science *123*, 564–572.

[40] Israelachvili, J. N., **2011**. Intermolecular and Surface Forces, 3rd edition. Chapter 13 (Associated Press).

Appendix. Van der Waals analysis of water film stability on quartz

This analysis is a classic of film physics, which is applied here to the system of interest: a water film sandwiched between glass and cyclopentane (CP). We consider a water film with thickness at most a few tens of nanometers and neglect retardation effects. The contribution of van der Waals forces to the disjoining pressure (the net force per unit area between the two -glass/water and water/CP - interfaces) can be estimated as a function of film thickness *d* as:

$$\Pi(d) = -\frac{6\pi A}{d^3}$$

where *A* is the Hamaker constant, which depends on the dielectric properties of the three phases involved: glass, water and CP. The film is stable (complete wetting) when the disjoining pressure is positive (i.e. the Hamaker constant is negative) and unstable when the disjoining pressure is negative (i.e. the Hamaker constant is positive).

In the standard approximation [40], the three phases are assumed to possess the same single absorption frequency in the ultra-violet range; the Hamaker constant is the sum of two contributions, a zero - frequency (static) contribution arising from the permanent and induced dipoles:

$$A_{\nu=0} = \frac{3}{4}kT\frac{(\varepsilon_{glass} - \varepsilon_{water})(\varepsilon_{CP} - \varepsilon_{water})}{(\varepsilon_{glass} + \varepsilon_{water})(\varepsilon_{CP} + \varepsilon_{water})},$$

where k is the Boltzmann's constant, *T* is the temperature and ε_i is the static dielectric constant of phase *i*, and a dispersion term arising from all other frequencies:

$$A_{\nu>0} = \frac{3h\upsilon_e}{8\sqrt{2}}\frac{(n_{glass}^2 - n_{water}^2)(n_{CP}^2 - n_{water}^2)}{(n_{glass}^2 + n_{water}^2)(n_{CP}^2 + n_{water}^2)[(n_{glass}^2 + n_{water}^2) + (n_{CP}^2 + n_{water}^2)^{1/2}]},$$

where *h* is the Planck's constant, $\upsilon_e = 3\cdot10^{15}$ s^{-1} the common absorption frequency, and n_i the refractive index of phase *i*. The dielectric constants and refractive indices of (fused) quartz, water and CP are tabulated in the literature; their values at 20°C are given in the Table below.

	ε	n_D **(sodium D ray)**	**source**
Glass	3.7	1.485	Suprasil 2 grade B, ref. 36
Water	80.37	1.33283	Handbook of Physics
CP	1.965	1.4065	Handbook of Physics

Using these values, we find $A_{\upsilon=0} = 2.635 \cdot 10^{-21}$ Joule and $A_{\upsilon>0} = 2.49 \cdot 10^{-21}$ Joule, that is, the Hamaker constant $A = 5.1 \cdot 10^{-21}$ Joule is positive: the water film sandwiched between glass and CP is unstable. The same calculation carried out with air in place of CP leads to a negative $A \approx 10^{-20}$ Joule (see ref. 40, chapter 13, Table 13.3 in Israelachvili's book): water films are stable on glass, as is sometimes observed.

CHAPTER 7

CYCLOPENTANE HYDRATE FORMATION IN A 2D CP-IN-WATER EMULSION

7.1. Introduction

The oil/brine effluents from offshore wells have a risk to plug the transport lines by forming hydrates from water and the lighter components dissolved in the oil (and, to a lesser extent, in brine). Understand the kinetics of hydrate formation in these emulsions will help in tailoring flow processes and additives (inhibitors) to prevent hydrate plugging.

We have already explained that when the hydrate-former (guest) molecule is sparingly soluble in water, hydrate formation and growth happen preferentially (and initially) at the interfaces between the water-rich and the guest-rich phases. First, a polycrystalline hydrate film grows laterally at a high rate along this interface. Once this interface is fully covered with

the hydrate film, the low permeability (to water and hydrate-former) of this film inhibits/delays further growth in a direction perpendicular to the interface. As we explained in chapter 5, this polycrystalline film can start being formed either in the emulsion and/or at the triple line and its structure and growth rate strongly depend on the subcooling degree. But sometimes and depending on where the emulsion is placed, there are additional hydrate crystallization 'collective' phenomena.

These collective phenomena are the topic of this chapter, which presents an investigation by video-microscopy of hydrate formation and growth in CP-in-water emulsions. The purpose of this chapter is to shed some light on the physics of hydrate formation in guest-in-water emulsions and how it is similar / different from that in other simpler systems like ice formation from a cloud of subcooled water drops. By slightly modifying the experimental procedure described and used in Chapters 5 and 6, we are able to generate a 2D cyclopentane-in-water (hereafter CP-in-water) emulsion, in which we observe the hydrate crystallization process by means of optical microscopy.

7.2. Experimental procedure

The modification of the experimental procedure used in the two previous chapters consists in working with a water drop hanging from the upper wall of the measurement cell (Figure 7.1) instead of sitting on the lower wall. The CP-in-water emulsion generated at the water/CP interface (cf. chapters 3 and 5) by dissociating the CP hydrate previously formed is driven away from the interface by buoyancy (CP droplets are lighter than water). These CP droplets therefore accumulate in the plane just beneath the upper window of the Hellma cell: this plane is now the observation plane.

In this kind of experiments the glass substrate does not interfere with the crystallization process because the contact angle in the CP phase is high, i.e. equal to 180°-θ, where θ is the (low) value of the contact angle in the water phase. In fact, the droplets hardly touch the surface and are subject to some weak Brownian agitation. They constitute a 2D emulsion, allowing the in-plane hydrate crystallization to be visualized and characterized (Figure 7.2). The absence of CP droplets at the water/CP interface has for consequence that the nucleation of the hydrate crust at this interface is delayed, as these droplets are one of the favoured places for the nucleation of the hydrate phase (cf. chapter 5). This feature will

facilitate the observation of hydrate crystallization in the 2D assembly of CP droplets, which will start long (several minutes) before that occurring at the water/CP interface.

To the best of our knowledge, this very simple experimental procedure, which allows the production of a 2D oil-in-water emulsion, has never been documented before. The only requirement is that the oil must be a hydrate-former.

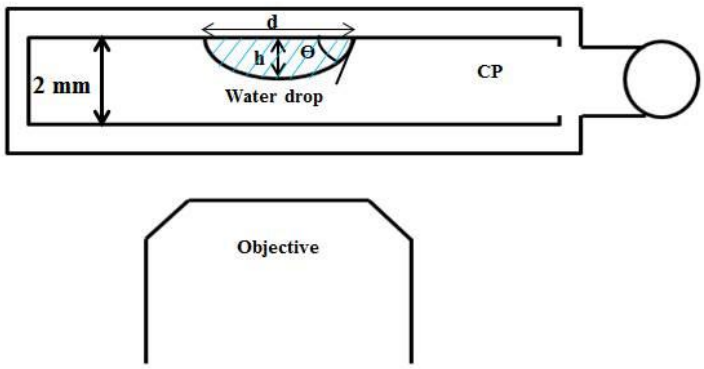

Figure 7. 1. Experimental setup adapted to a microscope, where a water drop is introduced in a Hellma cell filled with CP. In contrast to the setup used in chapter 5 and 6, in this case the water drop is hanging from the upper wall of the cell.

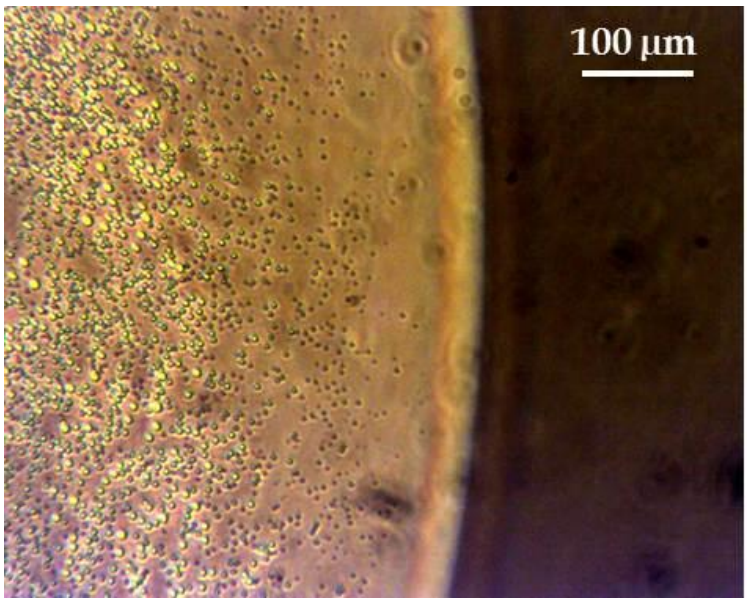

Figure 7. 2. 2D CP-in-water emulsion after first hydrate dissociation (T = 8°C). Dark field imaging mode. Experiment 2014/11/03.

7.3. Results and discussion

We observe two modes of hydrate crystallization in these 2D CP-in-water emulsions: the conventional mode, in which isolated hydrate crystals nucleate and then grow at the expense of the neighboring CP droplets, and a non-conventional mode consisting in the propagation of a crystallization front in the assembly of CP droplets. These two processes are analogous to processes that occur when ice forms and grows in an assembly of supercooled water droplets in air: this analogy will be discussed below.

7.3.1. Conventional hydrate crystallization in the emulsion

The phenomenon investigated in this section is analogous to ice growth in an assembly of supercooled water droplets in air (i.e. a cloud at sub-zero temperature) known by meteorologists as the Wegener – Bergeron – Findeisen (WBF) process [1]. In this process, the ice crystal grows at the expense of the neighboring water droplets (Figure 7.3), which vaporize into the atmosphere. The vaporized water molecules are driven from the region of supercooled water droplets to the growing ice crystal because the vapour pressure is lower over ice than over liquid water (in the regions in-between the ice crystal and the water droplets the ambient vapour pressure falls in-between these two saturation pressures and the environment is subsaturated for liquid water but supersaturated for the ice crystal). The ice crystal grows through vapour deposition in a process called antisublimation.

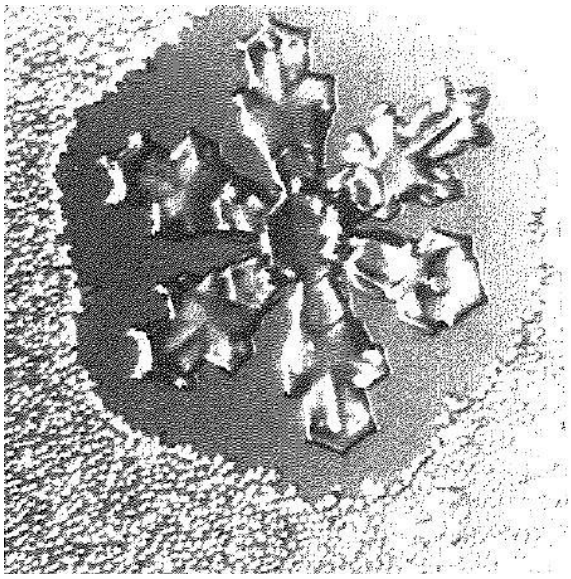

Figure 7. 3. The Wegener – Bergeron – Findeisen process illustrated by means of a snow crystal of 400 µm growing at the expense of the neighboring supercooled water droplets [1].

The analogy with the system of interest here is the following. The ice crystal corresponds to the CP hydrate crystal, water droplets to the CP droplets, the atmosphere to liquid water and water molecules in air correspond to CP molecules dissolved in water.

In our experiments, the most spectacular feature is the build-up of a layer depleted in CP droplets in the neighborhood of the growing crystal (Figure 7.4). Similarly to the WBF process depicted in Figure 7.3, in our system the crystal and its surrounding layer both grow with elapsed time by means of the following diffusion process: the CP molecules dissolved in water flow from the region of CP droplets to the CP hydrate crystal because the CP solubility in the liquid water phase containing the CP droplets is higher [2] than that near the CP hydrate (unfortunately, the latter solubility is not known). This process is very similar to the antisublimaton process described above: the CP molecules, after having been solubilized into the water from the CP droplets, feed the hydrate growth.

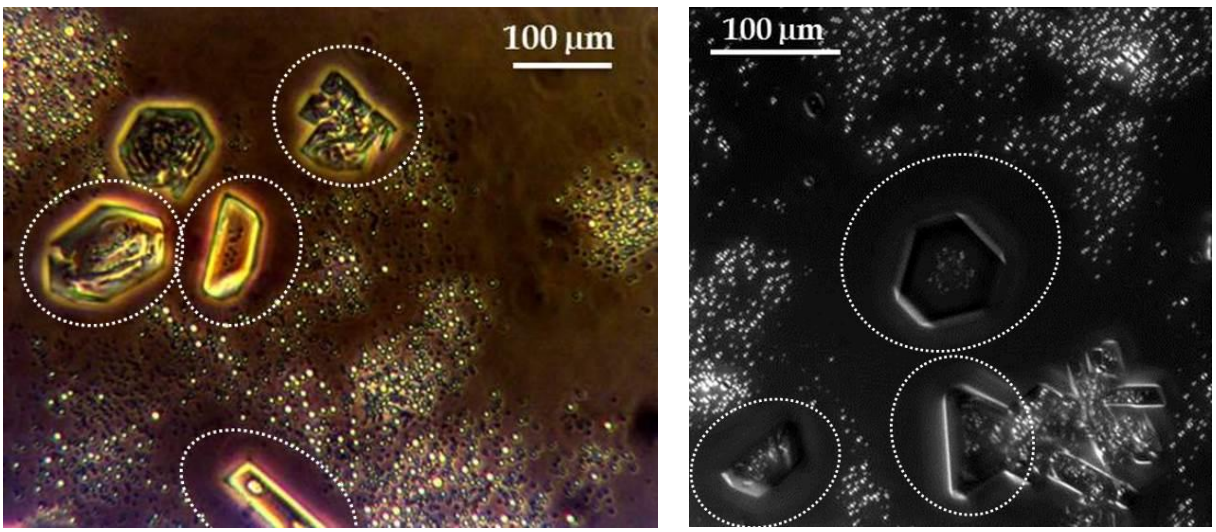

Figure 7. 4. Layer depleted in CP droplets in the neighborhood of the growing crystals. Left: T = 0°C. Dark field imaging mode. Experiment 2014/11/03. Right: T = 1°C. DIC. Experiment 2015/03/31.

The growth of the hydrate crystal and the buildup of a depletion layer are shown in Figures 7.5 and 7.6, the latter figure emphasizing the differences between two images at different times of a growing crystal and its depleted layer.

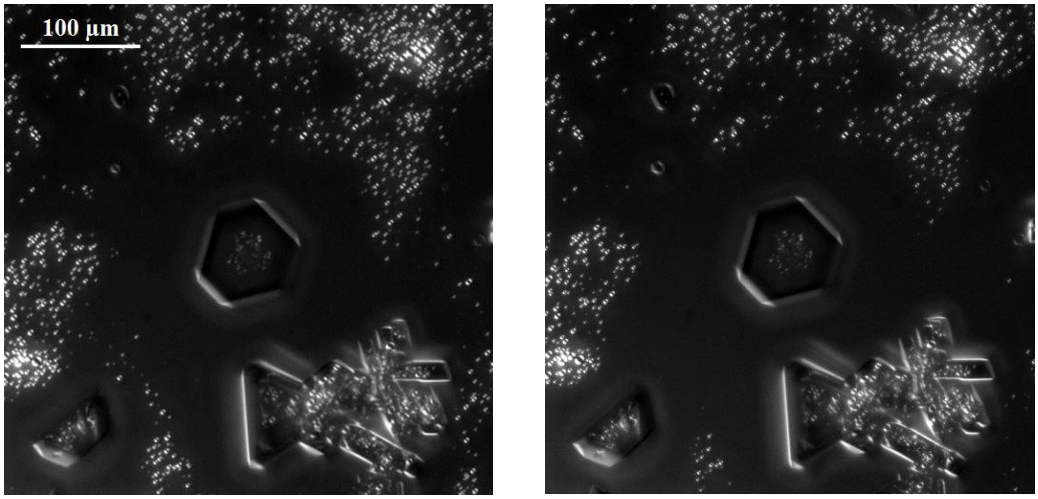

Figure 7. 5. Evolution with elapsed time of a growing CP hydrate crystal in a CP-in-water emulsion. Note the depletion of CP droplets around the crystal as the hydrate crystal grows (T = 1°C). Left: t_0. Right: t_0 + 1h 30min. DIC. Experiment 2015/03/31.

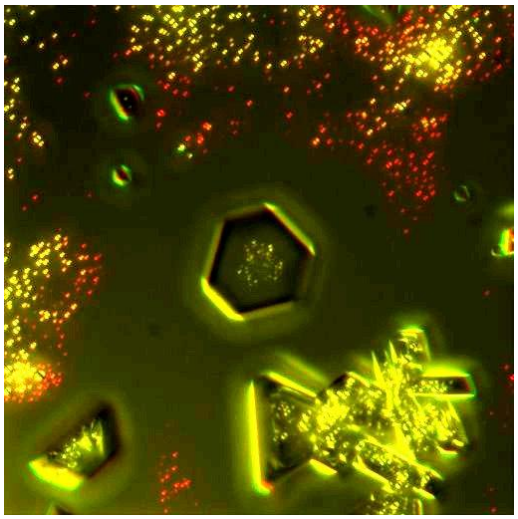

Figure 7. 6. Composite image of both left and right images from Figure 7. 5. What we observe at t_0 is in red and at t_0 + 1h 30min is in green. A lot of CP droplets were there at t_0 (red) but are not here any longer at t_0 + 1h 30min due to the crystal growth process. The green edges of the hydrate crystals highlight the growth in size in 1h 30min. Yellow parts are the common features found in both images. Experiment 2015/03/31.

The above is true as long as the hydrate crust has not covered the water/CP interface, because when it does, crystal growth stops and the CP droplets disappear, probably at the expense of the hydrate crust (Figure 7.7): the diffusion process mentioned above acts in favour of the crust growth in the vertical direction. Most of our results below are obtained before there is a hydrate crust covering the water/CP interface. This feature is also observed when the CP droplets have crystallized as aggregates, as studied in next section.

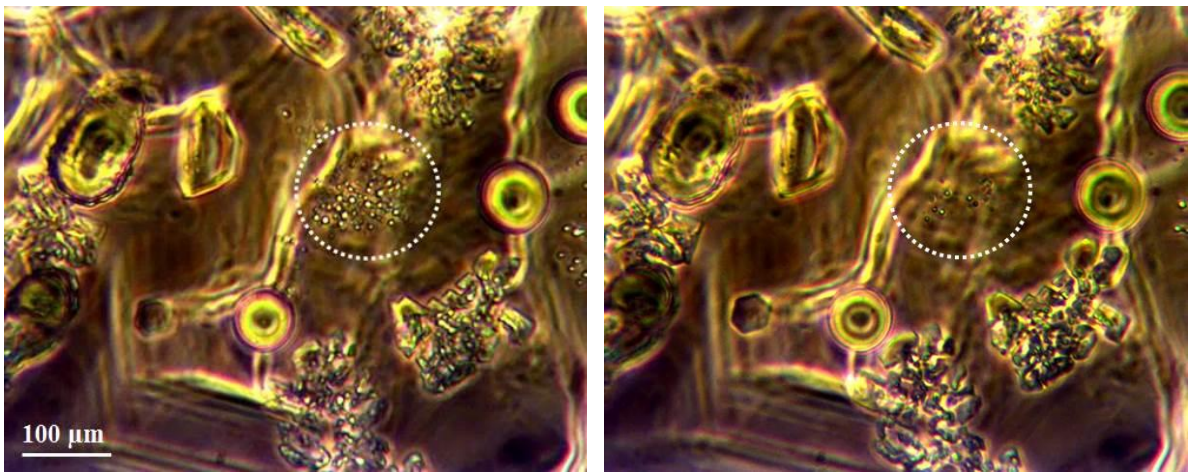

Figure 7. 7. The CP droplets disappear when the hydrate crust covers the water drop surface (T = 0°C). Left: t_0. The hydrate crust has just covered that zone. Right: t_0 + 2 min. The CP droplets disappear completely with time. Dark field imaging mode. Experiment 2014/11/03.

7.3.2. Percolation-like crystallization in the emulsion

Another type of growth process, analogous to the frost growth process recently identified by Guadarrama et al. [3], is observed. Petit and Bonaccurso observed something similar [4]. These authors observed the following process: one of the supercooled water droplets in an assembly of such droplets (sitting on a substrate) crystallizes and then a dendrite sprouts from it towards a neighboring water drop. The latter droplet starts evaporating when the first droplet crystallizes and therefore it decreases in size. There is a competition between dendrite growth and droplet evaporation. If the droplets are close enough, then the dendrite hits the neighbor droplet before it has been completely vaporized. This process is expected when there is a high initial quantity of water droplets, and especially when the droplets are close to jamming conditions.

We have also observed this percolation-type growth process in experiments where the CP droplets were initially very close to each other (or even in contact). As seen in Figures 7.8 and 7.9, hydrate nucleation starts in one CP droplet which then elongates slightly to reach the neighboring CP droplet, etc., similar to what Guadarrama et al. and Petite and Bonaccurso observed. The same bridging process is observed in Figure 7.9.

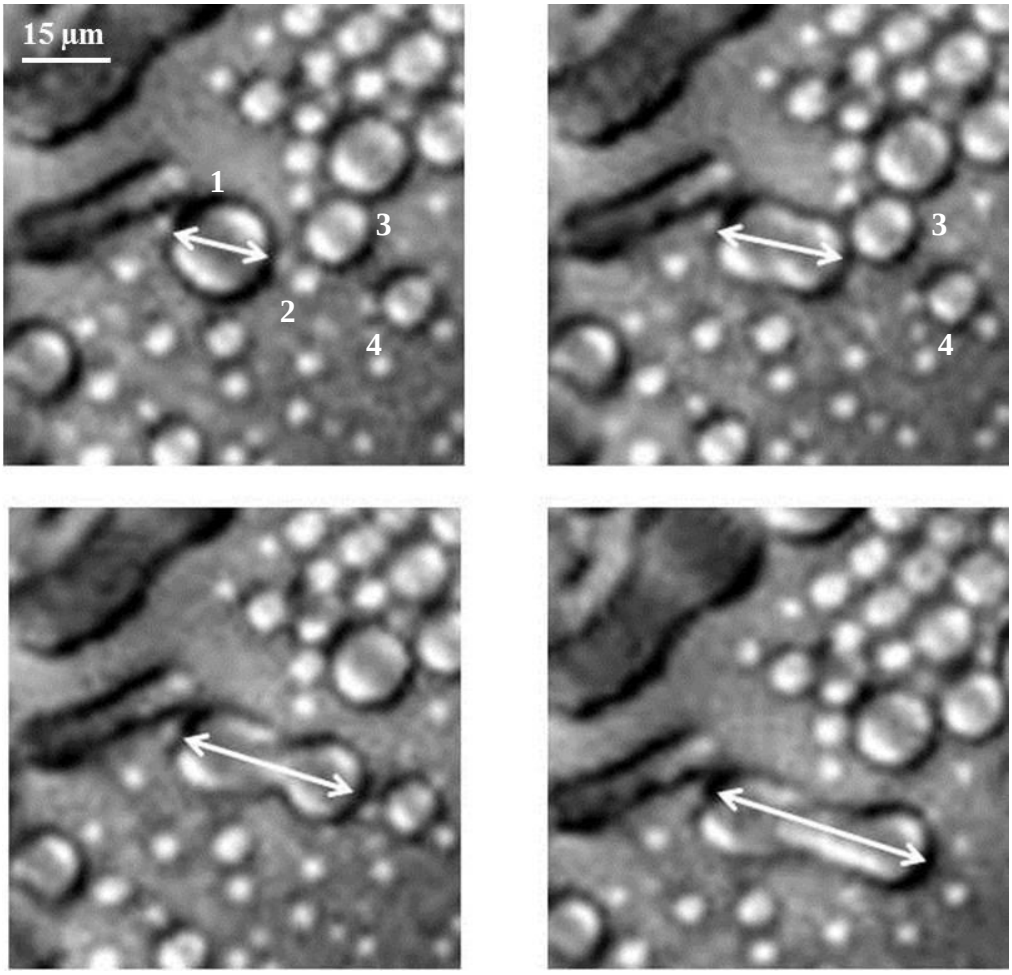

Figure 7. 8. Percolation-type growth process (T = 0°C). The CP hydrate nucleates on a given droplet 1; the droplet elongates to reach droplet 2, which is incorporated into the growing crystal. A further elongation results in the incorporation of droplets 3 and 4 in the growing hydrate. The elongation is approximately linear with elapsed time. Times: t_0, t_0 + 2.5s, t_0 + 5s, t_0 + 8s. DIC. Experiment 2015/03/31.

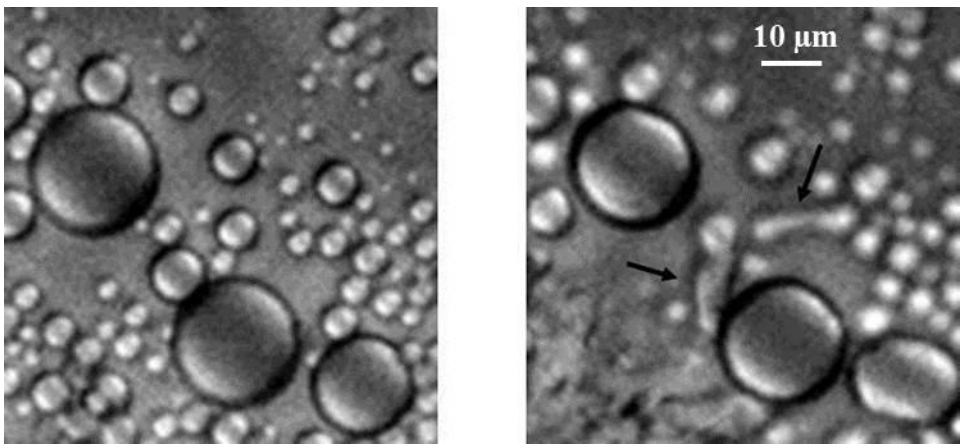

Figure 7. 9. Beginning of the percolation-type process in an assembly of CP droplets (T = 0°C). We can clearly observe the bridge formed between one CP droplet that acts as a sink of another neighboring one in order to incorporate it to the structure. There is 1 minute between both images. Experiment 2015/03/31.

We have followed the evolution of some of the droplets while the percolation-type structure (hereafter percolation aggregate) is approaching (Figure 7.10). In this figure the decrease in size of the droplets is apparent, which leads to the complete disappearance of two of them by the time they are reached by the percolation aggregate.

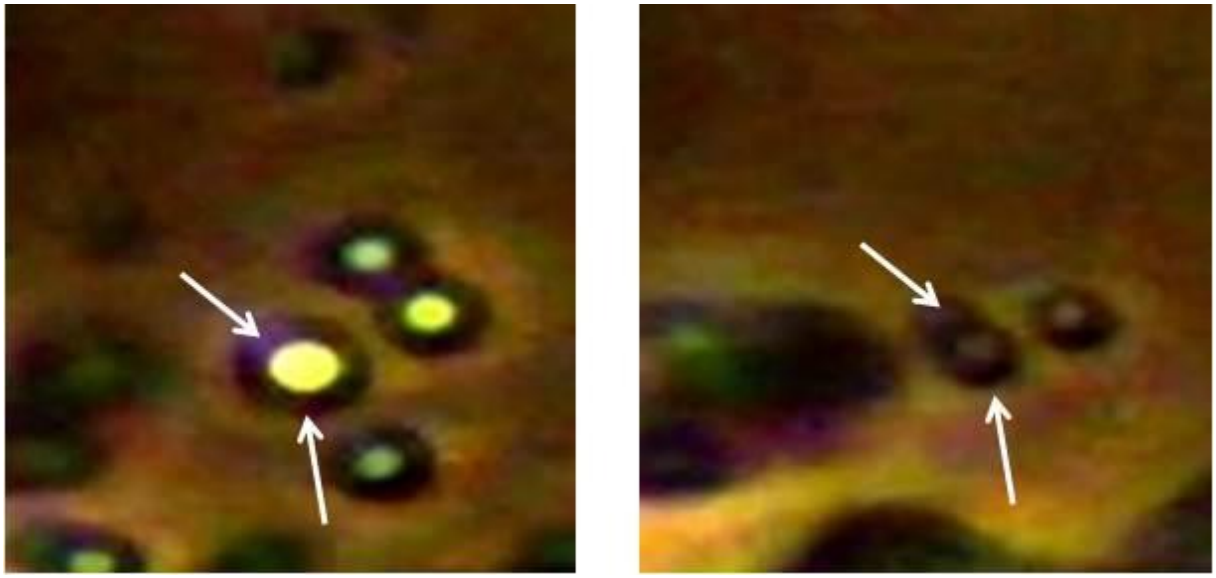

Figure 7. 10. Close-up view of CP droplets near a growing hydrate front: they shrink in size (T = 0°C). Two of the droplets have disappeared before being reached by the growing hydrate structure, while the two others are incorporated into the structure (data not shown). There are 26s between both images. Experiment 2014/11/03.

Two processes are in competition in the neighborhood of the CP hydrate crystal nucleating on a liquid CP droplet: (i) this droplet, although it is (probably) covered with CP hydrate, is able to deform and elongate in order to approach another droplet in its neighborhood and (ii) the neighboring droplets are subjected to a dissolution process due to the diffusion of CP molecules from these CP droplets to the CP hydrate crystal. If the two CP droplets are initially close enough, then the merging will occur into the percolation aggregate. If they are not close enough, the second droplet disappears (it dissolves completely) thus initiating the formation of a droplet-free zone (depleted zone) near the growing crystal. The latter case corresponds to the situation examined in section 7.3.1, whereas the former case (high density of CP droplets close to jamming conditions) is examined in this section.

In some situations we observe a percolation aggregate with a limited extent, corresponding to an assembly of CP droplets that were initially separated from other CP

droplets that are too far to be reached by the growing structure. Once all the CP droplets of the assembly are incorporated to the aggregate (if they have not disappeared before), the latter continues growing very slowly, fed only by CP molecules flowing by diffusion from CP droplets that are far away from the aggregate. A droplet-free zone thus grows around this percolation aggregate, as seen in Figure 7.11.

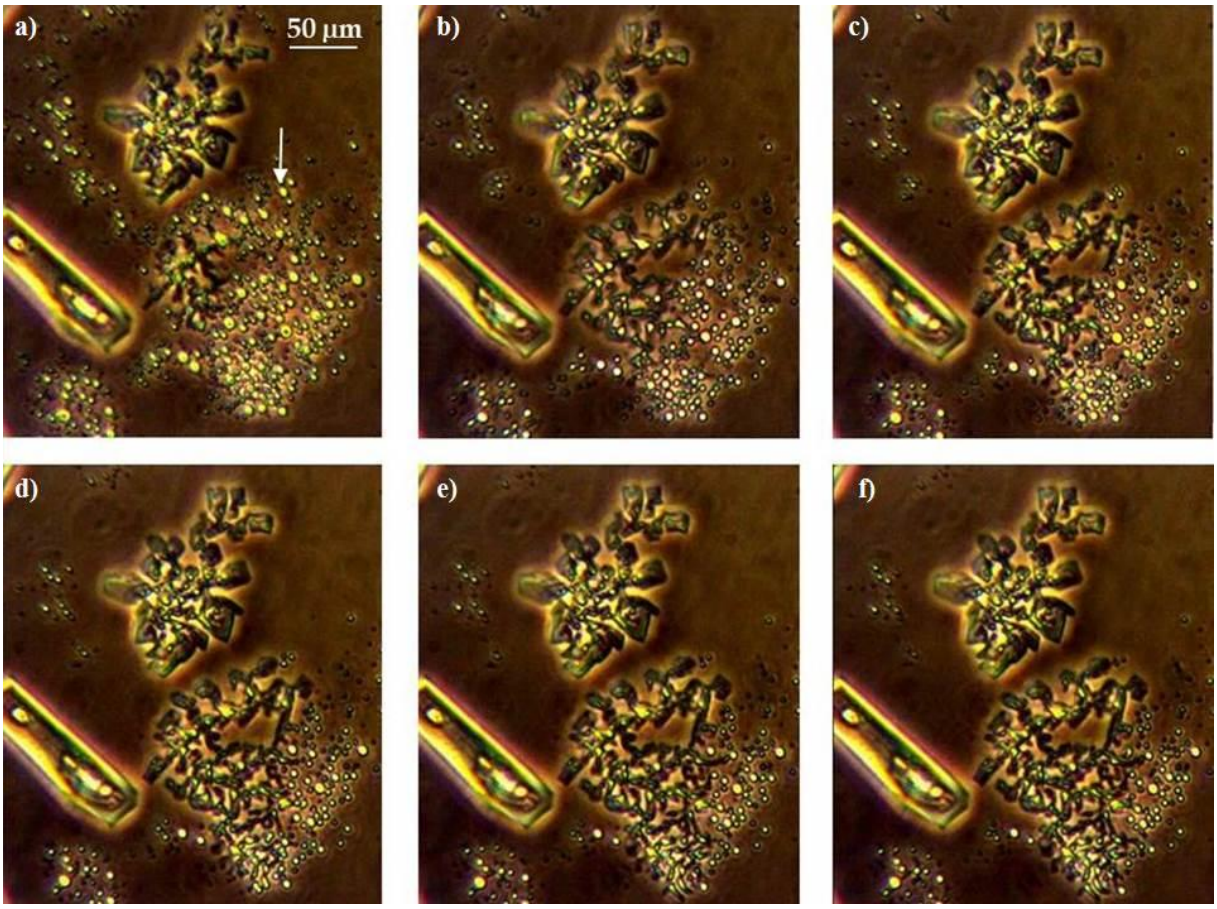

Figure 7. 11. Percolation-type growth process of the CP hydrate by incorporating CP droplets that have previously decreased in size (see the droplets shown by the white arrow in the first image and how they evolve in the following images). A droplet-free zone grows around the percolation aggregate (T = 2 °C). a) t_0, b) t_0 + 29s, c) t_0 + 36s, d) t_0 + 46s, e) t_0 + 52s, f) t_0 + 55s. Dark field imaging mode. Experiment 2014/11/03.

In Figure 7.12, a percolation aggregate that coexists with the hydrate crust at the water/CP interface is shown. The CP droplets far from the aggregate (e.g., in the left top corner of the images) are observed to shrink in size and then disappear, probably because of the proximity of the hydrate crust. The CP droplets that are closer to the aggregate disappear at the expense of the growing aggregate (center of the image).

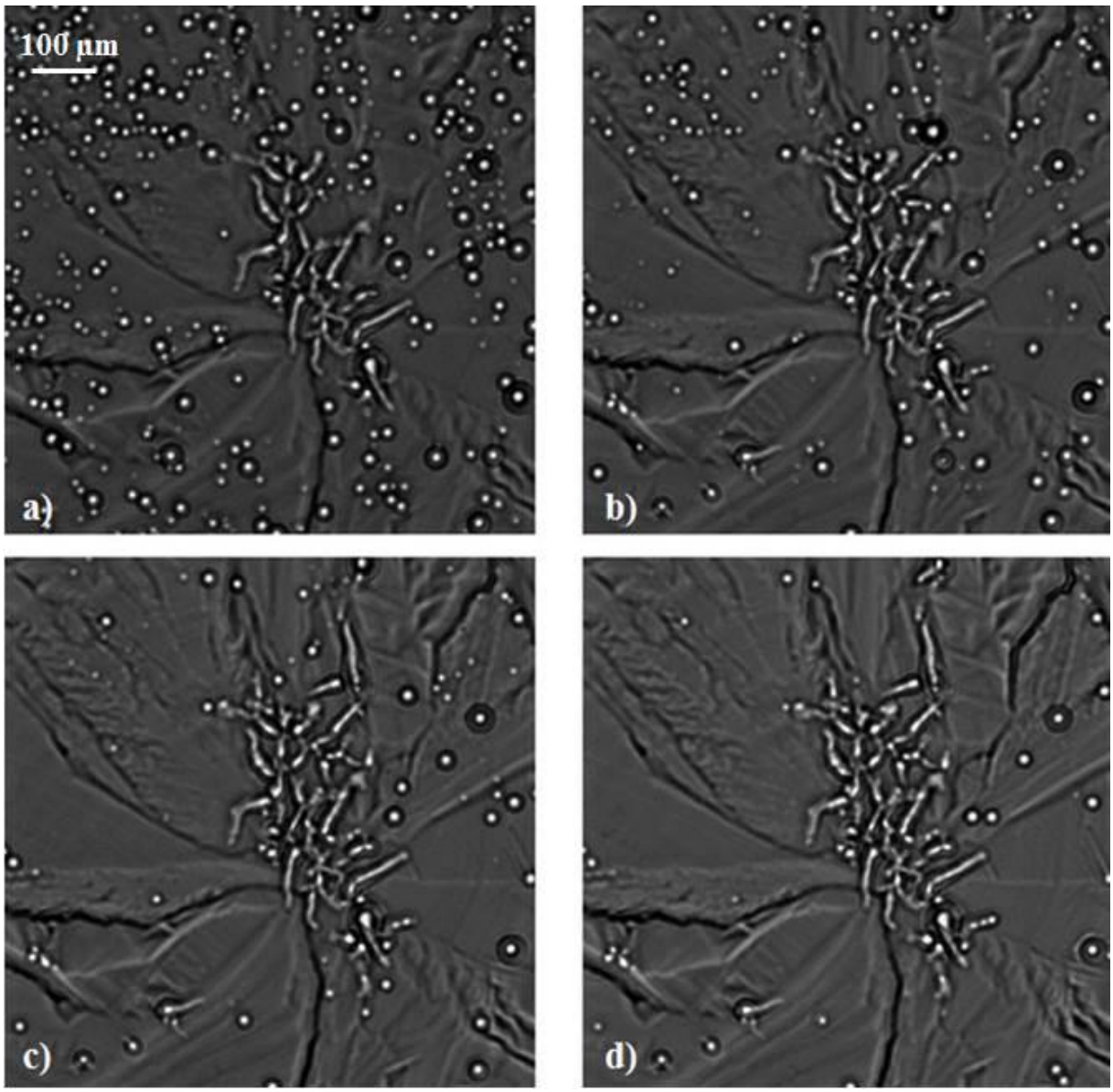

Figure 7. 12. CP droplets disappear at the expense of the hydrate crust (e.g., in the left top corner) and of the growing aggregate (e.g., in the center of the field of view) (T = 0°C). a) t_0, b) t_0 + 20 s, c) t_0 + 40 s, d) t_0 + 60 s. DIC. Experiment 2015/02/19.

Note that the two types of crystallization presented and discussed above are sometimes observed to occur simultaneously in nearby locations (Figure 7.13). They are observed before the hydrate crust is formed.

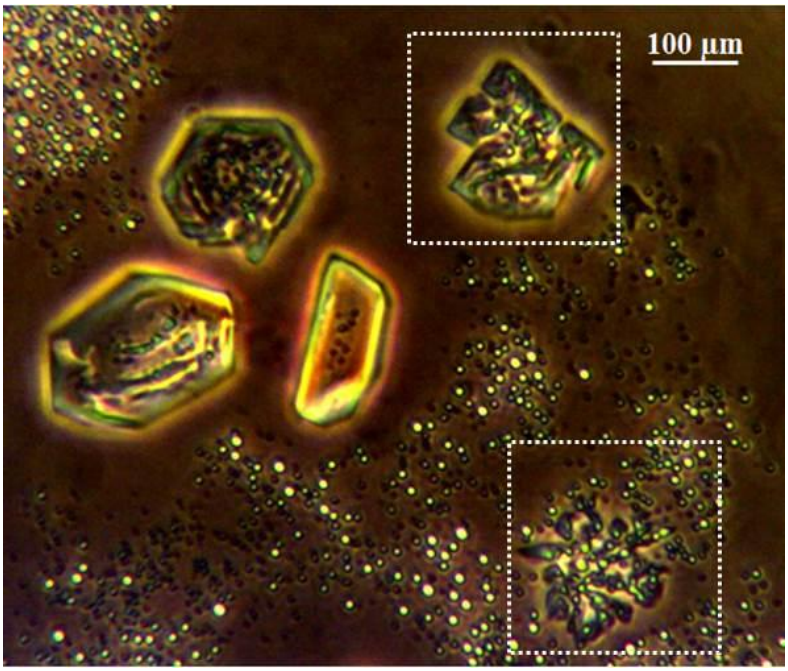

Figure 7. 13. Both types of crystals: single and percolation aggregates (dotted white squares), are observed at the same time but in different places of the 2D emulsion and before the hydrate crust is formed (T = 1 °C). Dark field imaging mode. Experiment 2014/11/03.

7.3.3. Dissociation and second formation of the two crystal structures

As has been reported and discussed in chapter 3, the second hydrate formation is easier when the hydrate has been previously formed: this is the memory effect. Interestingly, we observe a similar effect for percolation aggregates. There seems to be a memory of the aggregate structure: when a CP hydrate crystal aggregate melts, the resulting CP droplets are distributed similarly to how they were distributed before; the ensuing crystallization produces a CP crystal aggregate very similar in shape and extent (Figure 7.14).

A single crystal that melts also produces an assembly of droplets close to jamming conditions (Figure 7.15) and, therefore, when temperature is lowered again to form the CP hydrate, the crystal structure that arises is no longer that of a single crystal but that of a percolation aggregate (Figure 7.16). In other words, a single crystal is observed only once.

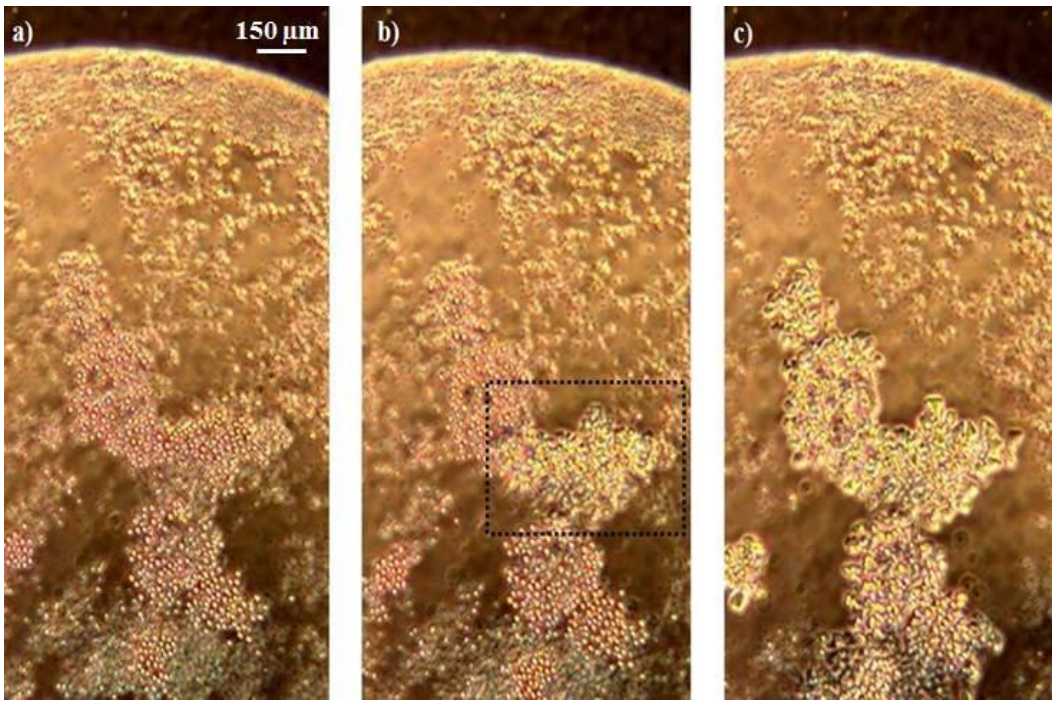

Figure 7. 14. Percolation aggregate formation after melting of a previous aggregate of the same characteristics. a) CP droplets coming from a dissociated percolation-like crystal (T = 8°C), b) beginning of a second percolation aggregate formation (T = 2°C), c) percolation aggregate completely formed (T = 0°C). Dark field imaging mode. Experiment 2014/11/03.

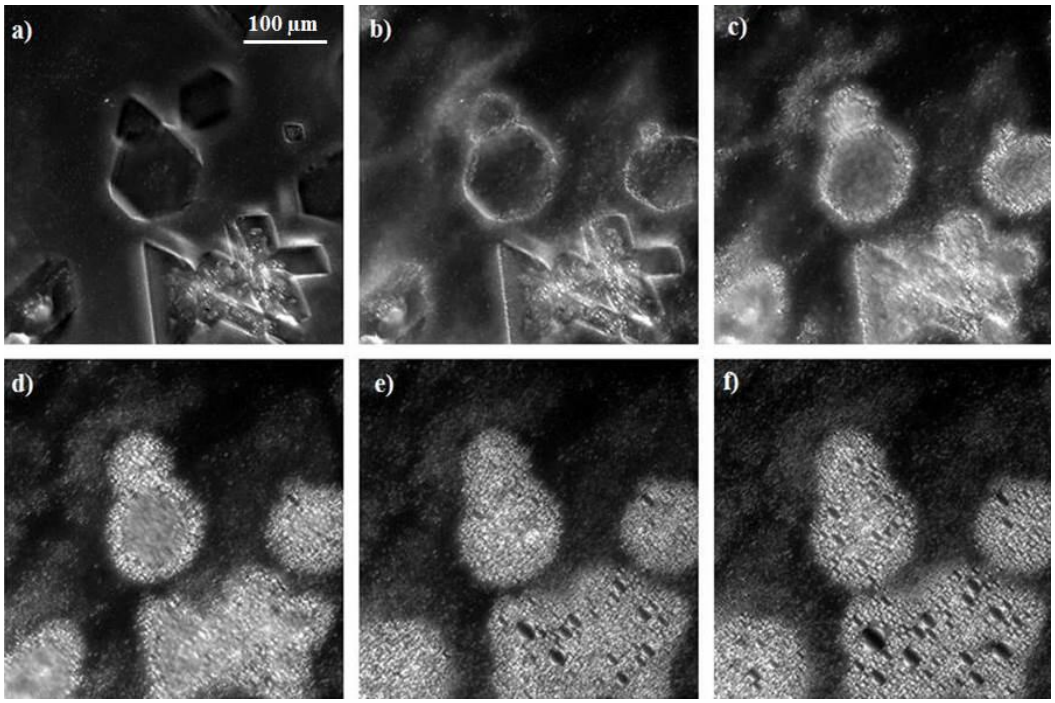

Figure 7. 15. Dissociation of a single CP hydrate crystal. In f) a CP-in-water emulsion close to jamming conditions is observed. The formation of a percolation aggregate will be favored in that place when temperature is decreased. a) t_0, T = 7.7 °C; b) t_0 + 27 s, T = 8.5 °C; c) t_0 + 50 s, T = 9 °C; d) t_0 + 81s, T = 9 °C; e) t_0 + 137 s, T = 9 °C; f) t_0 + 480s, T = 9°C. DIC. Experiment 2015/03/31.

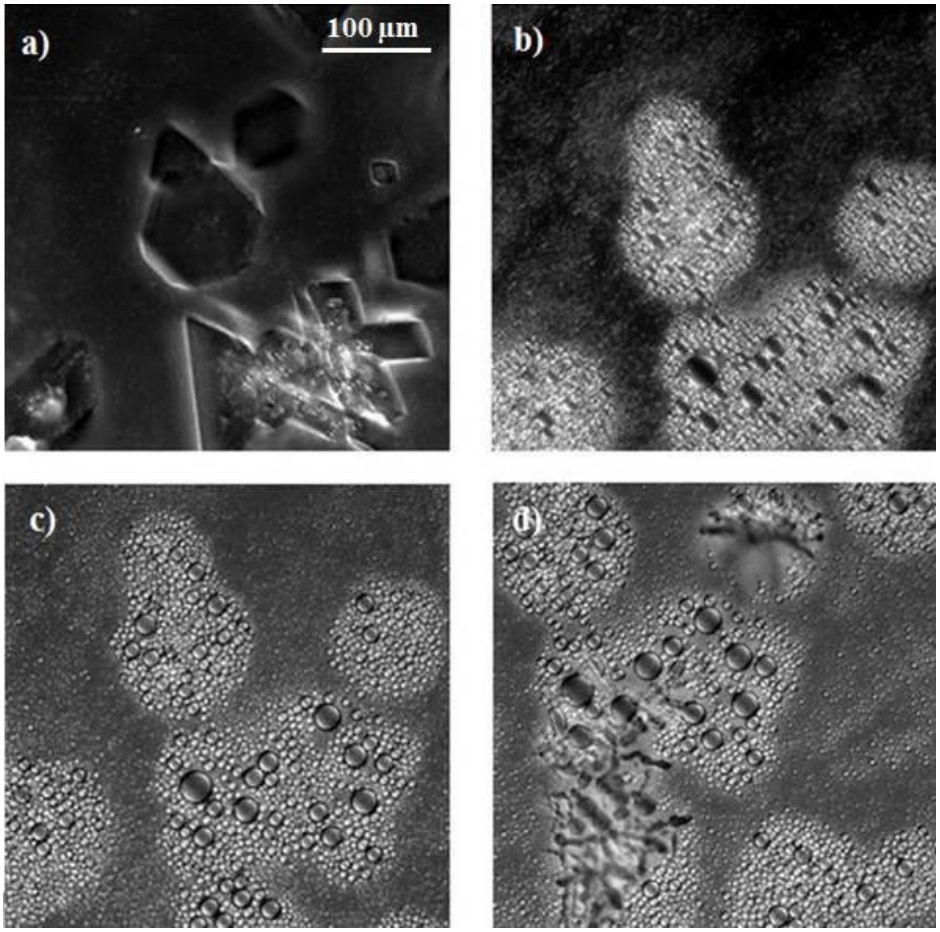

Figure 7. 16. Percolation-aggregate growth instead of single crystal during second hydrate formation. a) Single CP hydrate crystal (T = 7.7 °C), t_0 = 0. b) CP-in-water emulsion (T = 9 °C), t_0 + 8 min. c) CP-in-water emulsion close to jamming conditions (T = 9 °C), t_0 + 22 min. d) Percolation aggregate. The blurred zones are out of focus (T = 0°C), t_0 + 42 min. DIC. Experiment 2015/03/31.

7.4. Conclusions

In this chapter we have operated the experimental setup presented in chapters 5 and 6 in a slightly different manner - by placing the water drop hanging from the upper wall - in order to form a 2D CP-in-water emulsion just after melting the hydrate crust. In this CP-in-water emulsion we have observed, in addition to the conventional crystallization process generating single crystals, a non-conventional type of hydrate crystallization.

In the conventional hydrate crystallization, a layer depleted in CP droplets is observed close to the growing single CP hydrate crystal thanks to a diffusive process, driven by the difference in CP solubilities when the hydrate is present or not. These individual hydrate crystals stop growing when the hydrate crust covers the water surface: the CP droplets disappear in order to feed the growing hydrate crust.

The other type of crystallization is a percolation-type growth process, in which a crystallization front (percolation aggregate) propagates from one CP droplet to neighboring ones that slowly dissolve in water. The crystallized droplets are capable of deforming in the direction of a neighboring CP droplet. If the droplets are close enough, the latter droplet has not time to dissolve completely and the percolation aggregate propagates in the assembly of CP droplets.

Sometimes both types of crystallization are observed at the same time but in different locations in the water drop.

We have also observed that it is a lot easier to perform a second formation when a first percolation aggregate has existed before. This second aggregate formation occurs at the same place and has the same overall shape. In contrast to this, when single crystals are dissociated they do not form again. As the CP droplets that appear upon melting of these single hydrate crystals are very close to each other, a percolation aggregate growth is favored and it forms where the single hydrate crystals were placed before.

REFERENCES

[1] Pruppacher, H. R. and Klett, J. D., **2010**. Microphysics of Clouds and Precipitation, volume 18 (Chapter 13), 2nd revised and enlarged edition (SpringerLink ed.), Kluwer Academic Publishers, The Netherlands.

[2] Shaw, D. G., Maczynski, A., Goral, M., Wisniewska-Goclowska, B., Skrzecz, A., Owczarek, I., Blazej, K., HaulaitPirson, M. C., Hefter, G. T., Kapuku, F., Maczynska, Z., Szafranski, A., **2005**. Hydrocarbons with Water and Seawater. IUPAC-NIST Solubility Data Series. 81. Revised and Updated. Part 7. C_8H_{12}-C_8H_{18} Hydrocarbons with Water. Journal of Physical and Chemical Reference Data *34* (4), 2261-2298.

[3] Guadarrama-Cetina, J., Mongruel, A., González-Viñas, W., Beysens, D. A., **2013**. Percolation-induced frost formation. Europhysics Letters *101* (1), 16009.

[4] Petit, J. and Bonaccurso, E., **2014**. General Frost Growth Mechanism on Solid Substrates with Different Stiffness. Langmuir *30* (4), 1160-1168.

IV. CONCLUSIONS

CONCLUSIONS AND PERSPECTIVES

All along this work we have tried to shed some light on the mechanisms of formation and dissociation of cyclopentane (CP) hydrates by means of novel experimental methods which, to the best of our knowledge, had never been implemented before in the context of gas hydrate research. These methods are droplet-based millifluidics and optical microscopy in the differential interference contrast (DIC), fluorescence and confocal reflectance modes. Cyclopentane was chosen as the guest phase because, similarly to natural gases, it is sparingly soluble in water and forms a structure II hydrate; the formation conditions are from 0 to 7°C and atmospheric pressure, which eases the experimental work.

In a first series of experiments, a droplet-based millifluidic setup and procedure have been elaborated (i) to investigate the hydrate formation and dissociation processes in an assembly of millimetric-sized water droplets surrounded by the guest (CP) phase, each droplet behaving as an independent reactor for hydrate crystallization, and (ii) to visualize these processes at the scale of a single drop by means of a zoom system. By monitoring on a large number of droplets (or reactors) the hydrate formation events, some insights have been gained into the elusive ‘memory effect’: these events occur more easily, i.e. for a lesser subcooling,

in a water/guest system which has previously been experiencing a sequence of hydrate formation and melting. The impact of the melting conditions on the hydrate reformation process has been investigated: the milder the melting conditions, the easier the reformation. Working in the zoom mode, hydrate birth and growth events can be followed, the formation of guest-in-water emulsions upon hydrate melting is identified, as well as the mechanisms at work in presence of a very small amount (100 ppm) of polymer inhibitors (PVCap, VP/VCap, PVP). These mechanisms are also effective in stabilizing the hydrate phase a few degrees above 7°C: a polymer is as good at inhibiting the growth of hydrate crystals when lowering the temperature T as at preventing the melting of these crystals when raising T. The water drops in these experiments are in contact with a hydrophobic (fluorinated) substrate (i.e. tubing) that does not interfere with the hydrate formation and melting processes.

In a second series of experiments, optical microscopy is used to investigate CP hydrate formation and dissociation at an extremely high resolution, down to a few nanometers when using the microscope in the differential interference contrast or fluorescence modes. The water droplet is placed in contact with a hydrophilic substrate (glass), which induces a novel phenomenon: hydrate growth as a halo originating from the contact line and growing inbetween the glass and CP. Contrary to expectations and to what has been published so far, we observe that the growth of the halo on a strongly hydrophilic substrate is mainly controlled by the water present outside the water droplet from which the halo originates, e.g., the water condensed on the substrate or dissolved in the CP. This halo is absent on a hydrophobic substrate.

We have also examined: (i) the growth and morphologies of the hydrate crust formed at the surface of the water droplet, i.e. at the water/CP interface and (ii) the hydrate crystallization process in an assembly of CP droplets dispersed in water.

(i) Growth velocity of the hydrate crust is primarily controlled by the subcooling degree (the lower the subcooling the slower the hydrate crust grows), which also controls morphologies (the lower the subcooling the more polygonal are the crystals). Due to the high resolution, hydrate nucleation events have been identified at the water/CP interface, along the contact line (glass/water/CP) and in the CP-in-water emulsion that forms following a sequence of hydrate formation and dissociation; nucleation in the emulsion is the most frequent.

(ii) Hydrate crystallization in a 2D assembly of CP droplets in water (this assembly is obtained from the dissociated hydrate crust by working with a droplet hanging on the upper wall of the experimental cell. Two types of hydrate growth are observed: single crystal growth, which occurs at the expense of the neighboring CP droplets, and a percolation-type growth, in which crystallization proceeds from one CP droplet to the neighboring one.

The two experimental setups and methodologies designed, constructed, tested and optimized are novel, very versatile and can be utilized for studying a variety of hydrate-related issues. What is very interesting in this work is that the dimensions at which we perform the experiments are such that very low quantities of chemicals are required and, as we can have a high resolution, processes that have not been seed before are observed and studied in detail.

We think that a huge research field has been opened with this thesis and perspectives are listed here:

- The effect of inhibitors could be studied with the second experimental setup in more detail.

- Promoters of hydrate formation and other types of inhibitors (thermodynamic or antiagglomerants) could be studied.

- The study of other hydrate forming (liquid-liquid) systems and even gas-liquid hydrate forming systems if the experimental setup is adapted to high pressures.

- Other substrates apart from glass or quartz can be studied. We expect the effect on hydrate halo growth and structure of the material thermal conductivity wettability, surface roughness, etc., to be very important. There are at least two ramifications of these studies. One relates to the behavior of gas hydrate in sediments, and the other to the promoting character of mineral particles.

V. ANNEXES

A. Supplementary material Chapter 3

Detection of the apparent onset and end of hydrate formation in a single water drop

The procedure for determining the onset of hydrate formation in a given water drop consists in monitoring the grey level intensities (from 0 = black to 255 = white) along a longitudinal axis of the drop. The apparent onset corresponds to the moment when there is an abrupt change in the grey level profile, which usually occurs at one apex of the drop. This is illustrated in Figure A.1 that shows, respectively, a quarter of the spiral capillary at two consecutive acquisition times t_1 and t_2 (one image per 7 seconds, i.e., $t_2 = t_1 + 7s$) and the corresponding grey level intensities measured in a given single drop along the longitudinal axis marked in the two figures below by a white segment. The peak(s) that are apparent at t_1 at one drop apex correspond to reflections, which disappear when hydrate covers the apex (at t_2). In this example, the onset time is intermediate between t_1 and t_2. The end of hydrate formation is determined in a similar manner when there is an abrupt change in grey level intensities at the other apex.

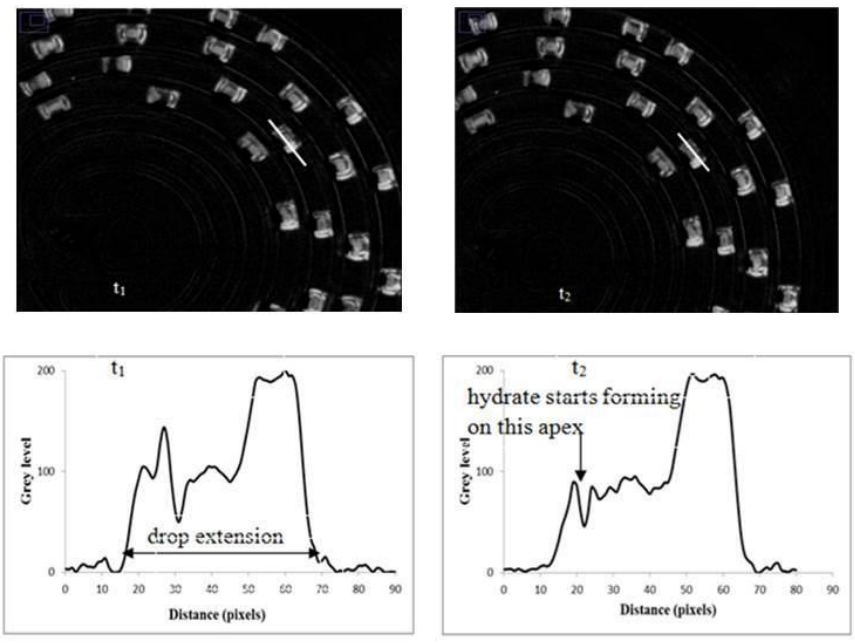

Figure A. 1. A quarter of the spiral capillary at two consecutive acquisition times t_1 and $t_2 = t_1 + 7$ s, and the corresponding grey level intensities measured in a given single drop along the longitudinal axis marked in the two figures below by a white segment. The peak(s) that are apparent at t_1 at one drop apex correspond to reflections, which disappear when hydrate covers the apex (at t_2).

B. Supplementary material Chapter 4

Morphology of hydrate crusts

Here we separate the two groups of inhibitors used in this thesis: 1) PVP, which forms a homogeneous layer over the surface and 2) VP/VCap and PVCap, which adsorb to the surface by 'patches', in a very irregular way.

1) PVP: it forms a monolayer over the surface. In the end, a hydrate crust gets to be formed, but less thick than the case of the pure system, which has no impediment to form. Both hydrate crusts are quite homogeneous in morphology, but we can see that the pure system hydrate film is thicker, more continuous and smoother (Figure B.1 left). We affirm the hydrate film is thicker for the pure system because it is more translucent than the PVP hydrate layer, which is more transparent. Also, when experiments are carried out, the film formation is visually seen *in situ* more easily than that with PVP. On the other hand, we could say that the hydrate film for the system with PVP is homogeneous, thin and more faceted than that of the pure system. We can see a lot more 'fractures' all over the surface (Figure B.1 right).

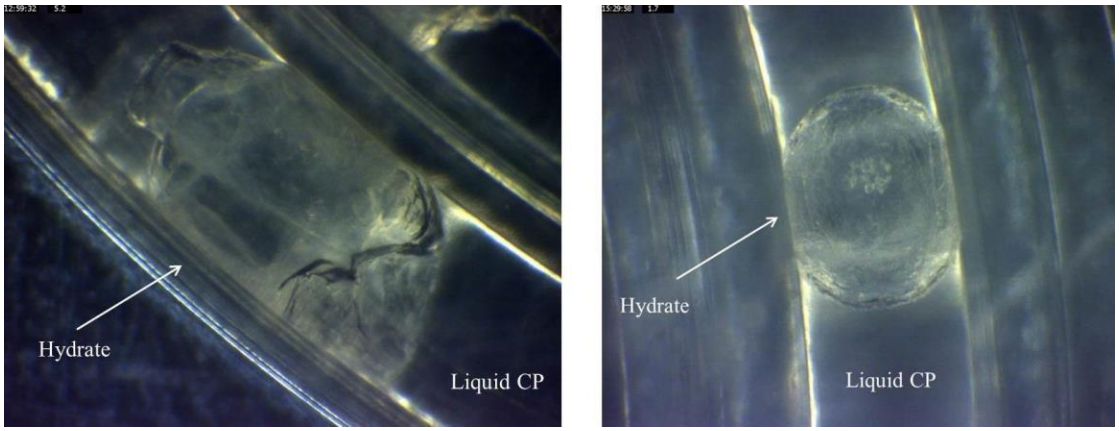

Figure B. 1. Morphologic differences of hydrate layers after 1st hydrate formation. Left: pure system. Right: PVP.

2) VP/VCap and PVCap adsorb to the hydrate surface by forming a thicker layer than that of PVP as seen in the adsorption experiments. Although the thickness of the VP/VCap film adsorbed on the hydrate surface is lower than that of PVCap, we think the adsorption

mechanism is the same. This is why no big differences in the morphology are observed between them, except from the central part of the 'hydrate drop', which is smooth and flat for VP/VCap and rougher and less homogeneous for PVCap (Figure B.2b and B.2c). We also observe some differences with respect to the pure system (Figure B.2a) mainly at both sides of the 'hydrate drop'. The solid/liquid interfaces present some irregularities, wrinkles or mountains and inhomogeneous parts for both inhibitors. This is in agreement with what Bruusgaard et al. observed in their study of the effect of VP/VCap, among others, on the morphology of methane hydrates (cf. [2] chapter 4). They found that the inhibitor does not completely cover the hydrate surface at a uniform concentration. The hydrate growth pattern is then composed of sections of higher thickness separated by areas of a thinner hydrate layer. They suggest that this variation in thickness is directly related to the local presence of inhibitor and indicates that VP/VCap has large local concentration gradients repeated across the surface. This can be in agreement with the 'patches' or 'clumps' we observe for both VP/VCap and PVCap in the adsorption experiments.

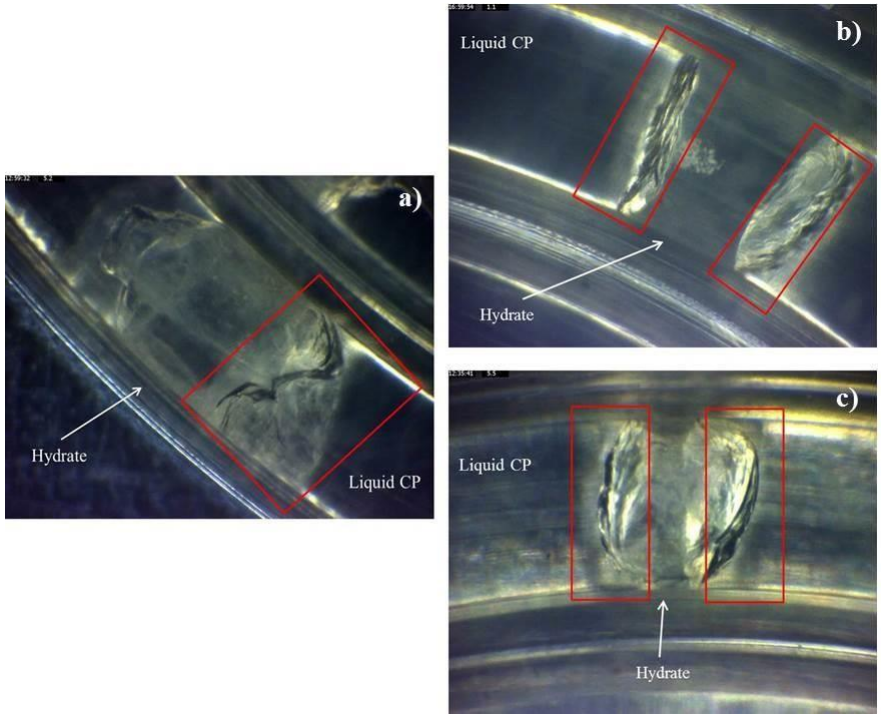

Figure B. 2. Morphologic differences of hydrate layers after 1st hydrate formation: a) Pure system, b) VP/VCap and c) PVCap. The central part of the drop is different between the system with VP/VCap (smooth) and with PVCap (rough). The red squares show the edges of the 'hydrate drops', which are different from the pure system (a) to the system with inhibitors (b and c).

C. Supplementary material Chapter 6

S1. Determination of the drop contact angle and contour by confocal reflectance image analysis

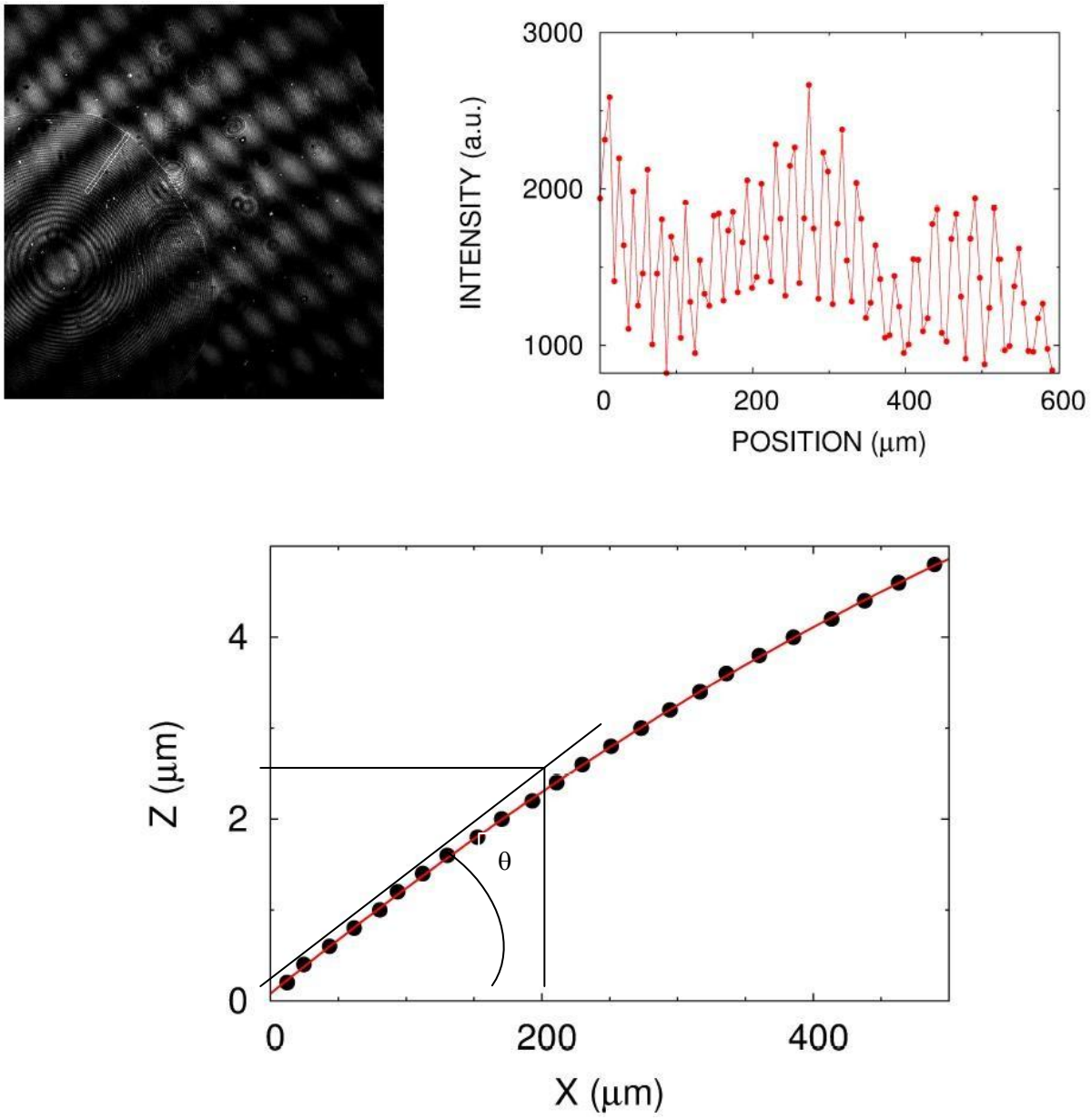

Figure S1. 1. Determination of the drop contact angle and contour. Top left: confocal reflectance image of the water drop sitting of the plasma-treated glass substrate. Top right: section through the image in the top right corner of the drop (cf. white line). Bottom: reconstructed profile and fit to a circle. The contact angle is here equal to $\theta \sim 1°$.

S2. The figure below shows that the water drop in CP needs to be frozen first in order to be transformed into CP hydrate at its surface by raising T to slightly above 0°C

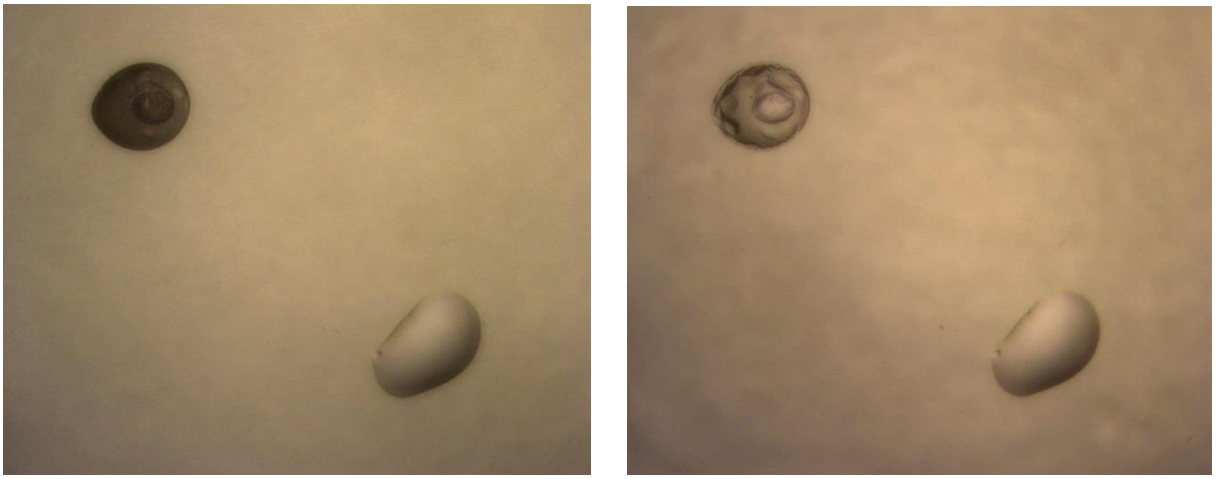

Figure S2. 1. Step 1 of the experiment. Photographs of two water drops in CP sitting on a glass substrate taken just after one of the drops (the one in the upper left corner) has been frozen at T ≈ -15°C (left image) and then transformed into CP hydrate at its surface by raising T just above 0°C (right image). The other water drop remains in a (metastable) liquid state.

S3: Breath figures on the cooled glass substrate. Build-up of a droplet-free zone near ice acting as a humidity sink

We show below three images or sets of images from three different experiments showing supercooled water microdroplets condensed from the CP on the glass substrate near the primary water drop, which has previously been transformed into ice by freezing at T = -15 to -20°C. Near the ice, a droplet-free zone is apparent that grows diffusively: an attempt is made to relate the effective diffusion coefficient to the molecular diffusion coefficient of water in CP, the solubility of water in CP and the substrate coverage of the water microdroplets.

The following two DIC images show close-up views of the water drop on plasma- treated glass (Experiment 2015/07/17) just after it has been transformed into ice (t = 0, left) and about 6 minutes later (t = 367 s, right). The absence of microdroplets near the ice is apparent in the latter image (scale bar: 50 µm).

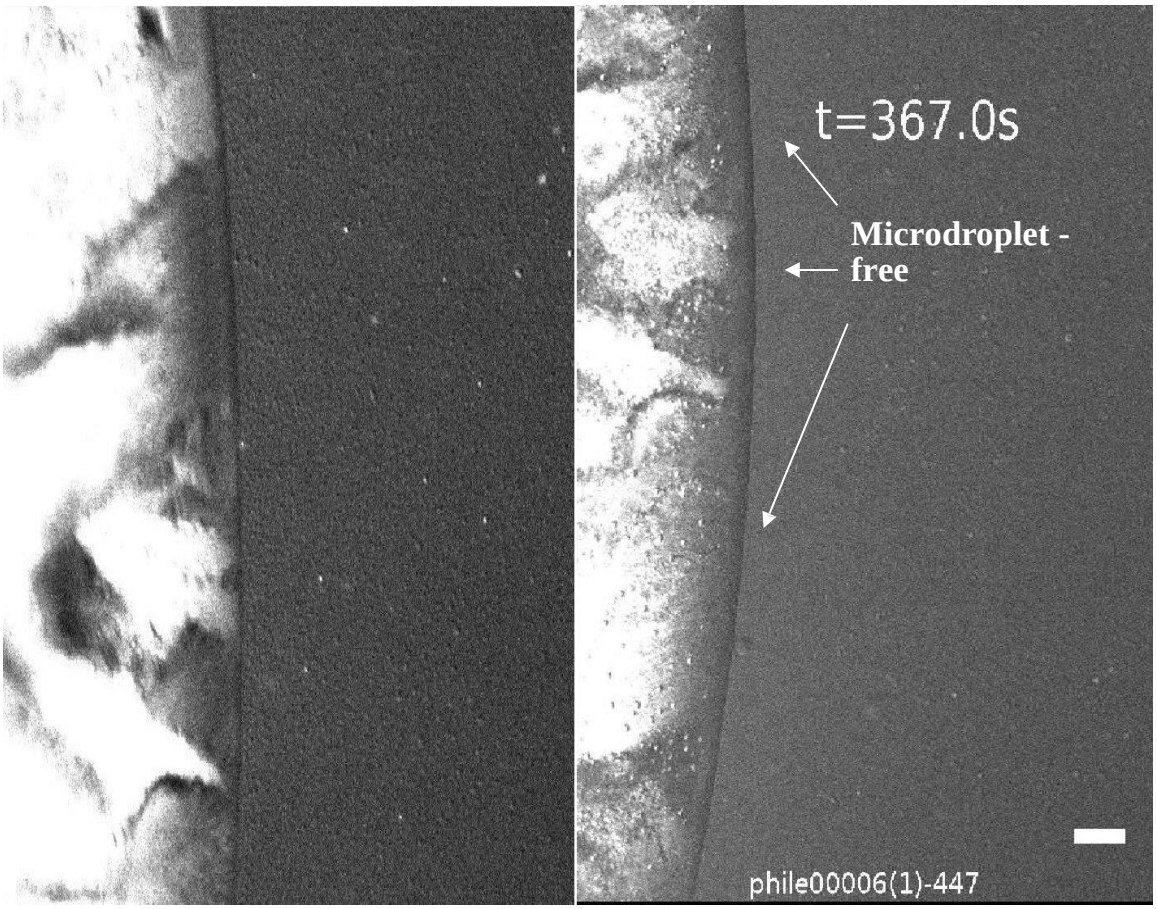

The following image is taken from another experiment (2015/02/20) with untreated glass, in which the microdroplets of supercooled water droplets and their substrate coverage are somewhat larger than those of the previous experiment. A droplet-free zone is clearly visible near the ice border.

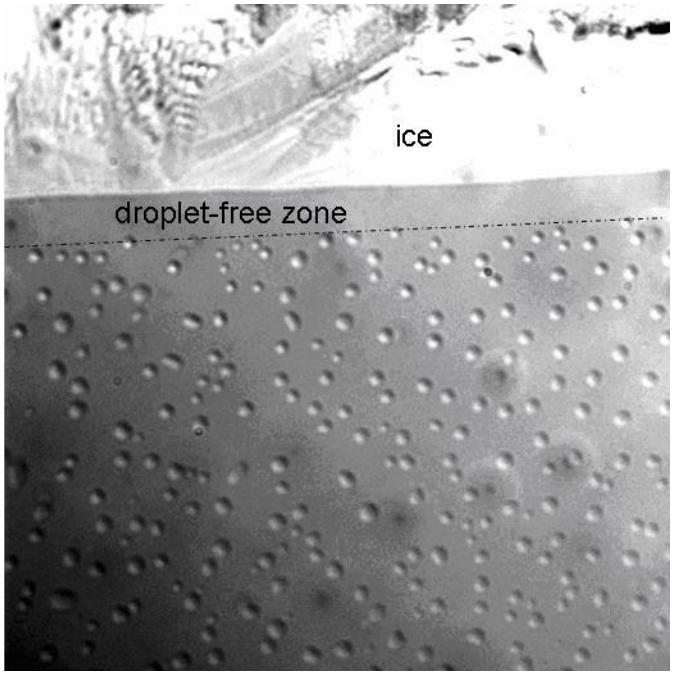

Field of view: 403 µm

Lastly, the following images show the region near the ice border (apparent at the top of the images) at different times following t_0 when the primary drop has been transformed into ice; T is below 0°C over the time interval of about 7 minutes (Experiment 2015/03/31). The expansion of the depletion zone is well within the limits of diffusion in the WBF process (assuming an order of magnitude molecular diffusion constant of $D = 5 \cdot 10^{-5}\,cm^2/s$).

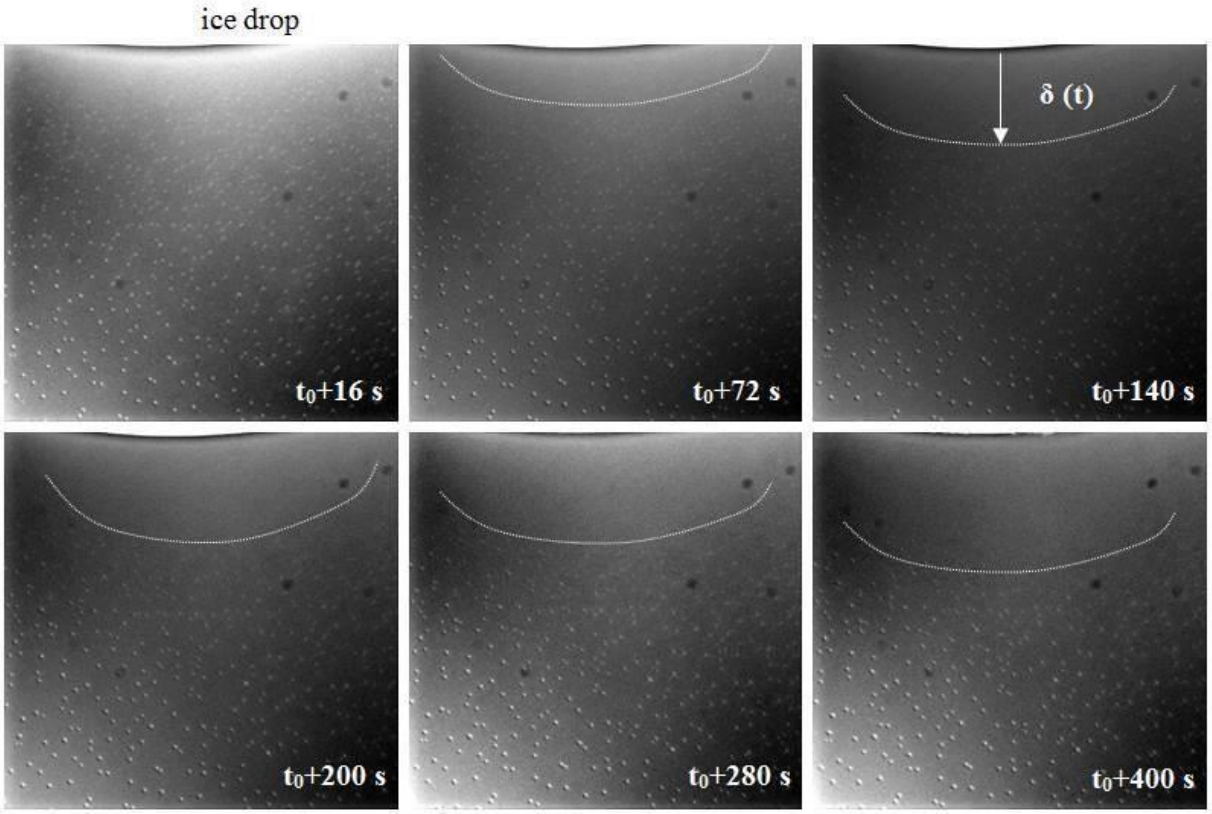

Field of view: 271 µm

S4. Nucleation of the hydrate halo from hydrate crystals formed on the primary water drop along the contact line after ice melting (early stages of Step 2)

We reproduce and discuss here two sets of images illustrating the early stages of halo formation and growth on a strongly hydrophilic glass substrate. Each set corresponds to a different primary drop (Experiment 2015/07/17). In the first set of images (this and the two following pages) polygonal, plate-like hydrate crystals are observed on the primary drop shortly after ice melting, first floating in the melt water close to the contact line.

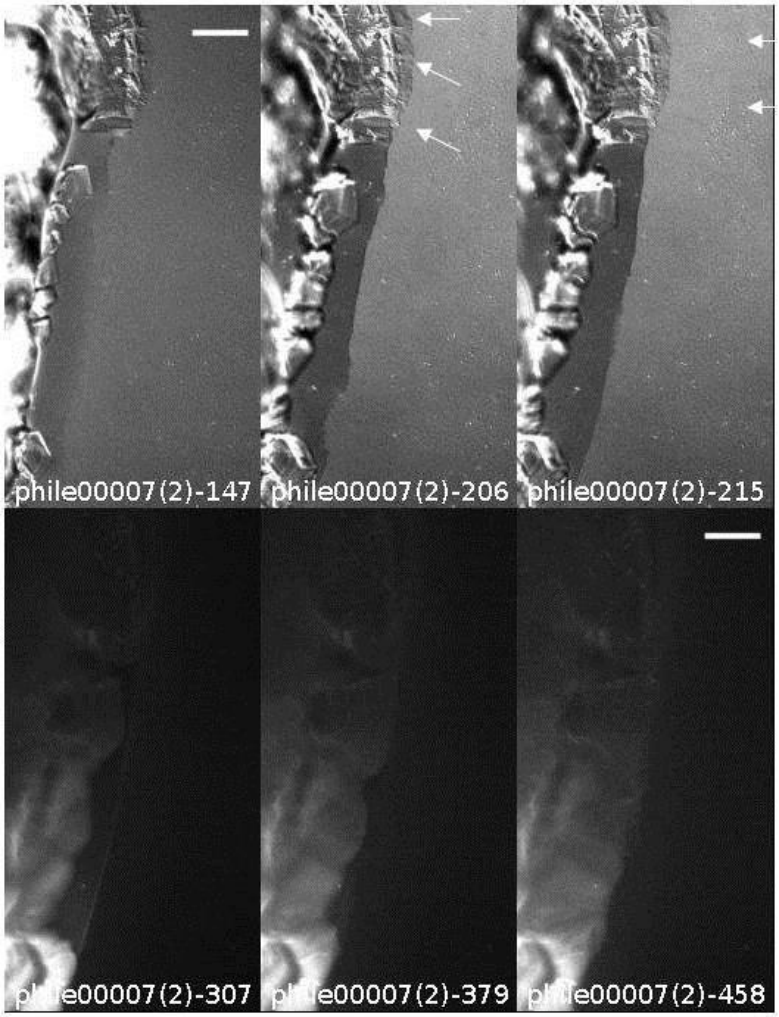

Intervals between images approx. 6, 1, 10, 7 and 8 s. Top row: DIC. Bottom: fluorescence. Scale bars: 50 µm. The white arrows show the growing hydrate halo. The (hydrophilic) surface of the crystals appears strongly fluorescent, probably due to adsorbed DASPI.

Shortly after one of these crystals has touched the contact line, the hydrate halo starts growing from that part of the contact line on the substrate (see also Figure 6.6 in the main text).

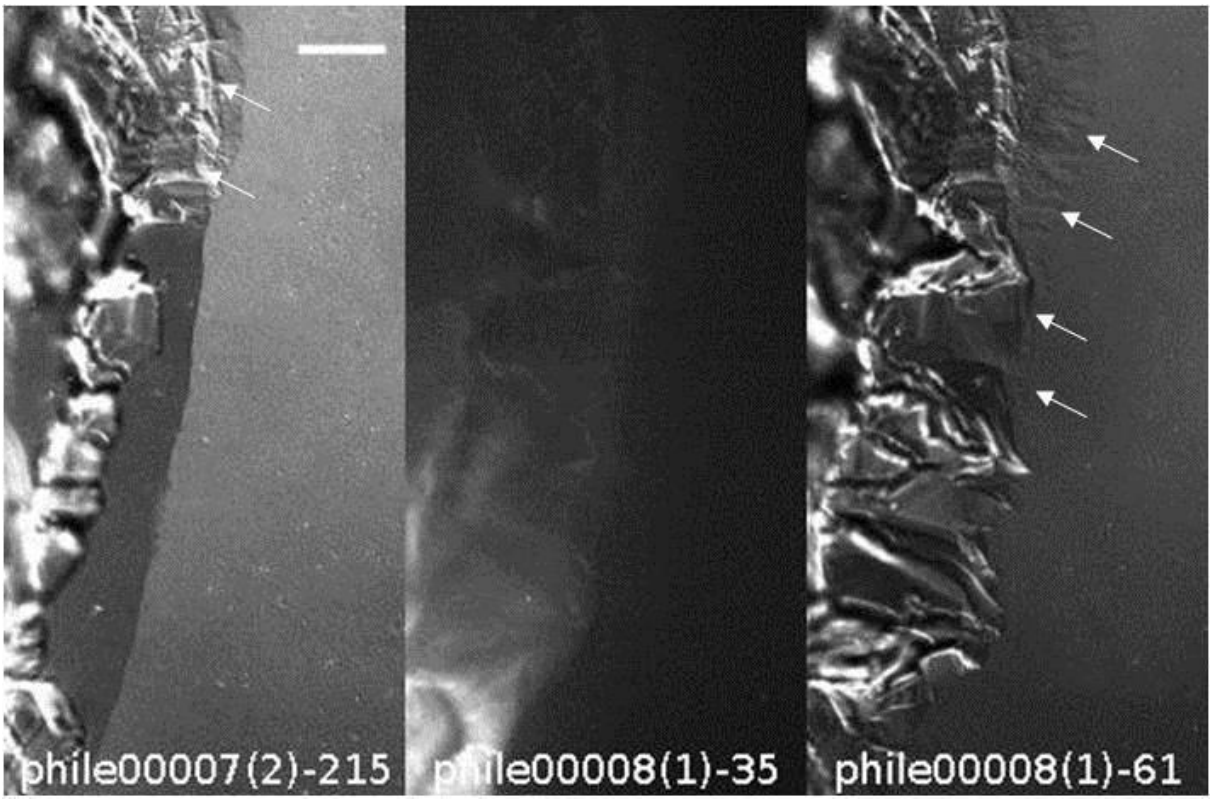

Views 1 and 3: DIC; 2: fluorescence. Intervals between the images: ~33 and 3s. Same caption as in previous page. More conspicuous 'teeth' grow on the lower part of the contact line, and the hydrate halo (white arrows) grows and extends along the contact line.

Finally (see next page), a peripheral, highly corrugated (width ~ 2-3µm, length ~ 10µm) halo develops. Views 1 and 3: DIC; 2 and 4: fluorescence. The corrugation increases with ageing. Fluorescence is not detected much beyond the initial extent of the precursor film. Intervals between the images: ~ 3, 50 and 1s. Scale bar: 50µm.

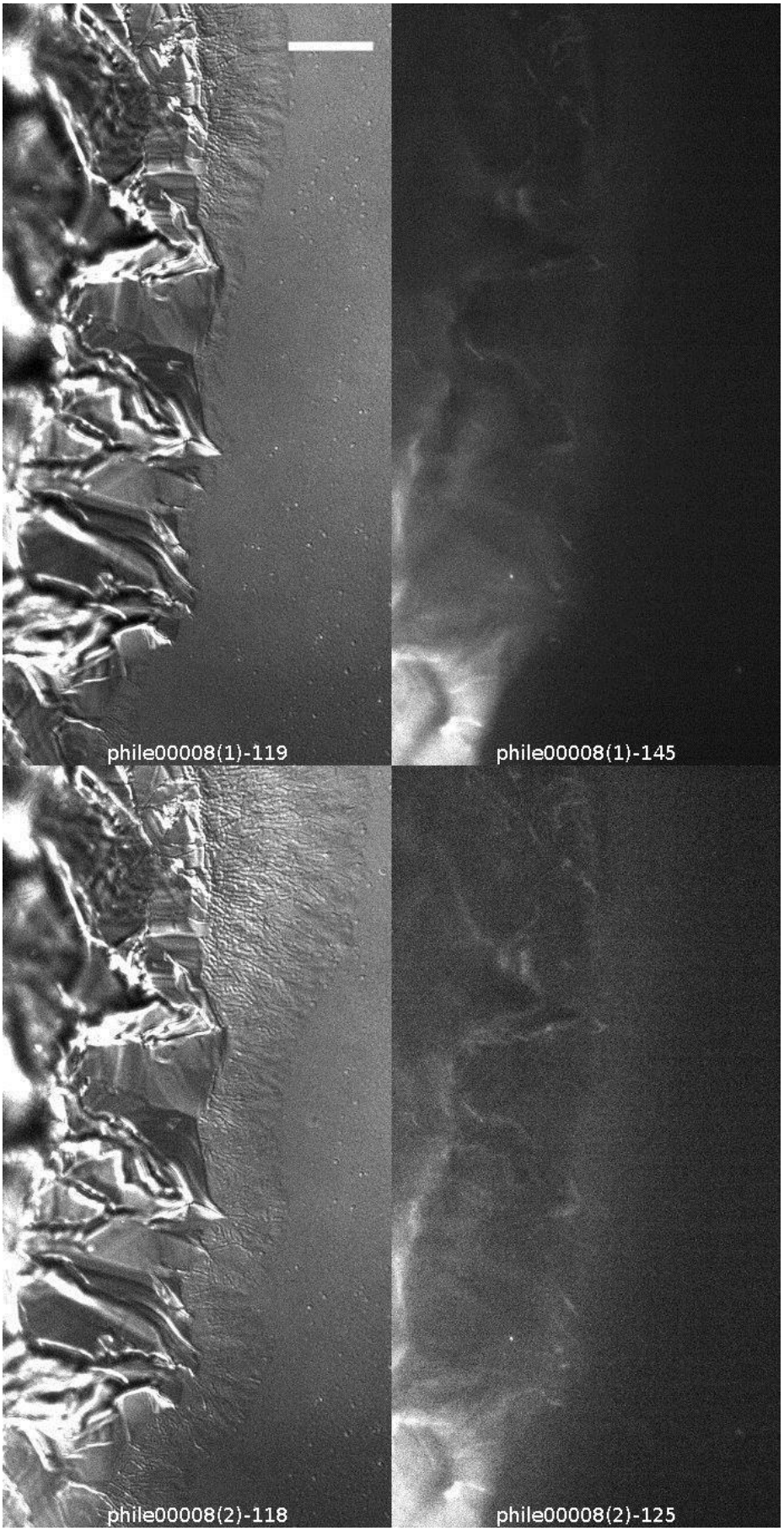
phile00008(1)-119
phile00008(1)-145
phile00008(2)-118
phile00008(2)-125

In the 2nd set of images shown below (corresponding to a different drop on the same substrate), the contact line recedes (to the right, initial position highlighted by red dots) as the ice melts, leaving a bare area of substrate and a thin sheet of water, visible in the upper right image between the dots and the melting ice. Then, polygonal crystals (yellow arrows) grow outwards in the thin sheet of water and expand as far as the original contact line, but not beyond. DIC, scale bar 20 µm.

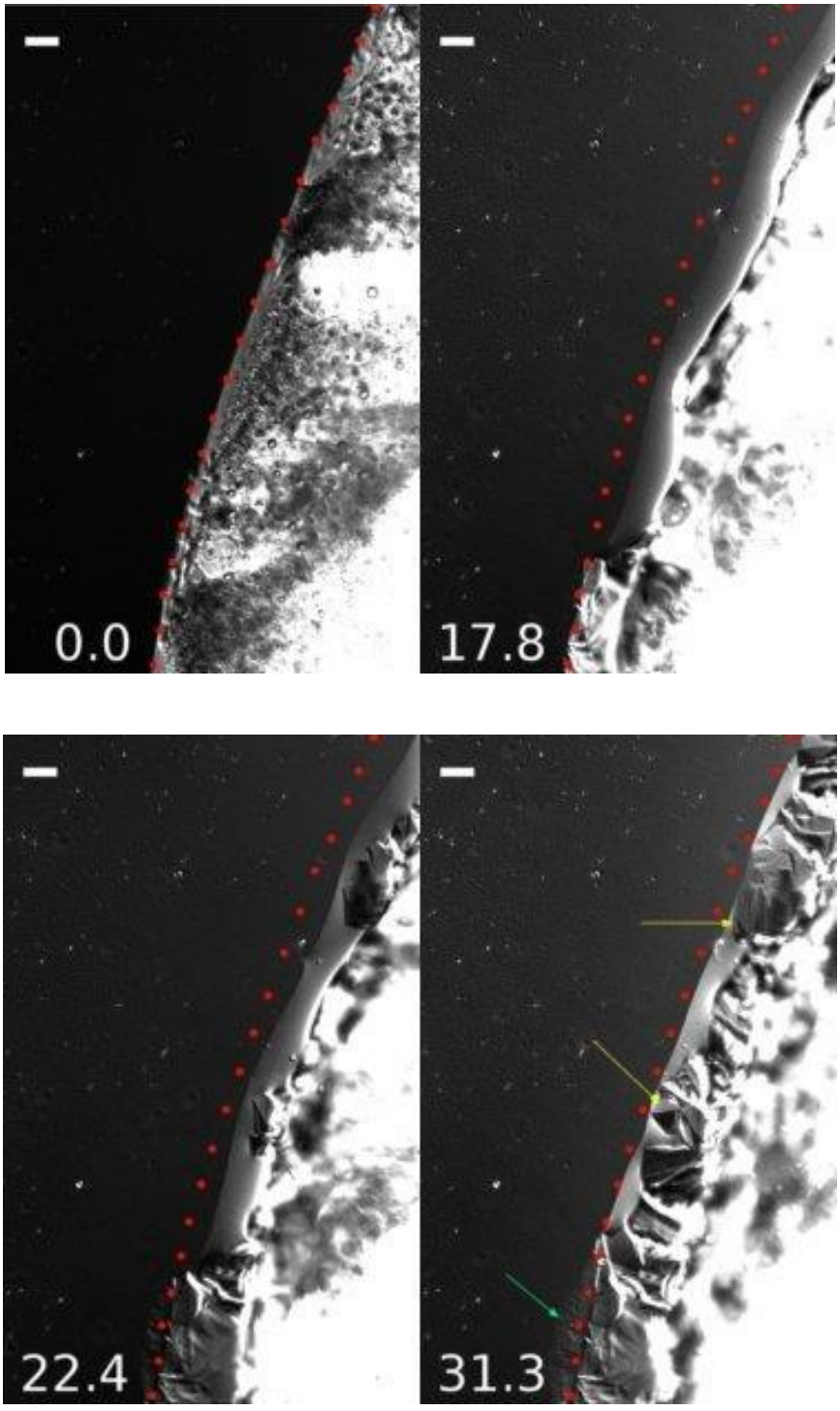

These crystals are conspicuous in the fluorescence image on the right (see below), since they are growing over the primary drop. Their lower face adsorbs and enhances the fluorescence of DASPI. Growth of the polygonal crystals is arrested at the contact line; they are replaced by a halo of hydrate with a different texture (DIC image on the left, green arrow). The halo front is marked by reduced emission of DASPI in the fluorescence image on the right (red arrow). Condensation droplets near the halo front have disappeared and emission at the contact line has also diminished.

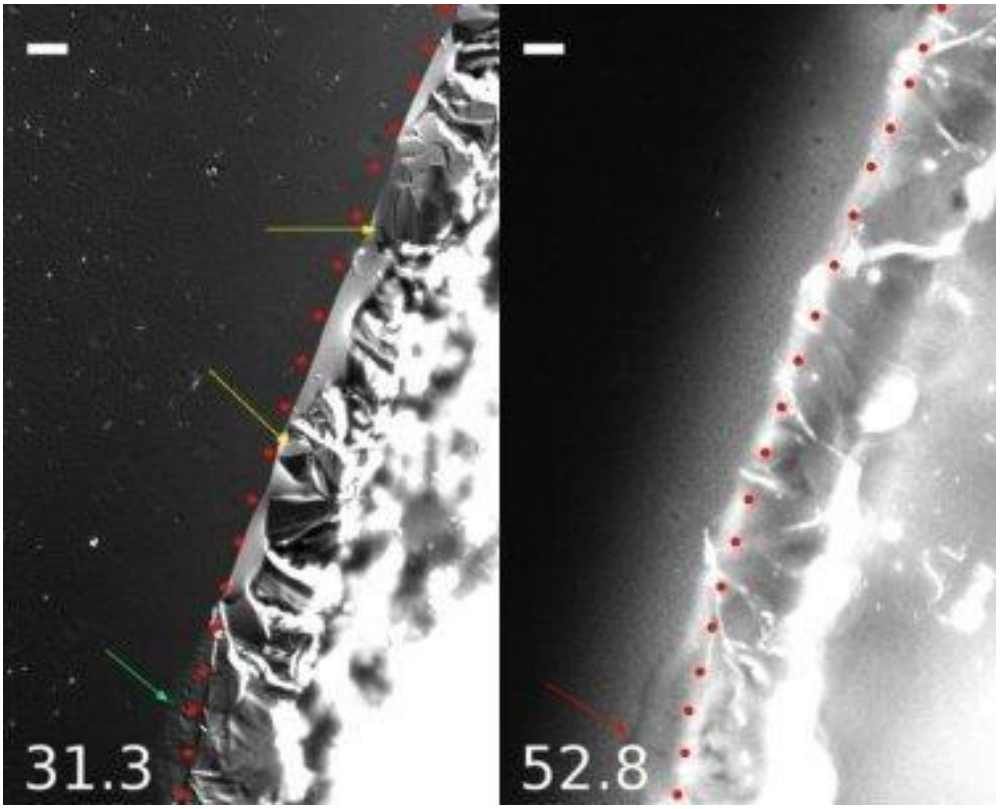

Finally, the hydrate halo grows over the substrate (green arrows in the DIC image):

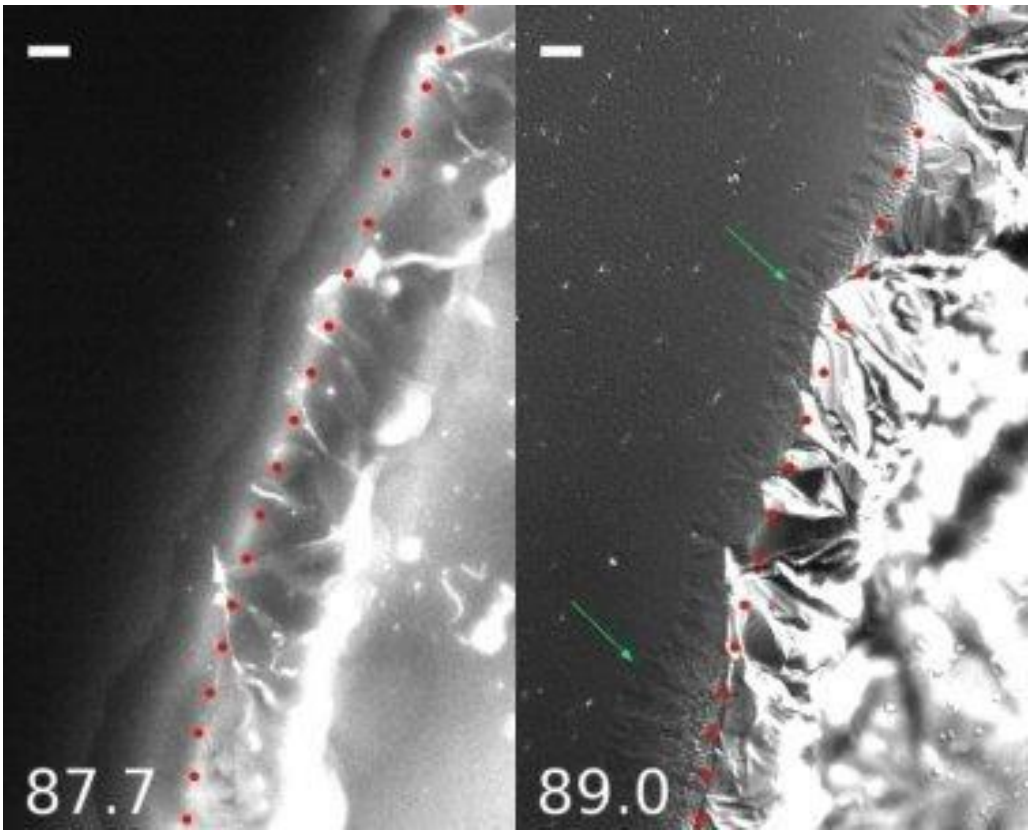

S5. Hydrate halo growth on a strongly hydrophilic substrate: complementary data

The fluorescence image below has been obtained shortly after the hydrate halo has started to grow (in the first cycle, from ice) on the strongly hydrophilic glass substrate (step 2 of the experiment). The intensity profiles along the arrow, averaged laterally over the boxed region, reveal a dip that radiates out with the halo front. DASPI was not detected outside the original precursor film of the liquid primary drop. In the region of the precursor film, an increase of the fluorescence signal ahead of the front and a drop behind it show that the halo is displacing DASPI, hence is growing in contact with the substrate.

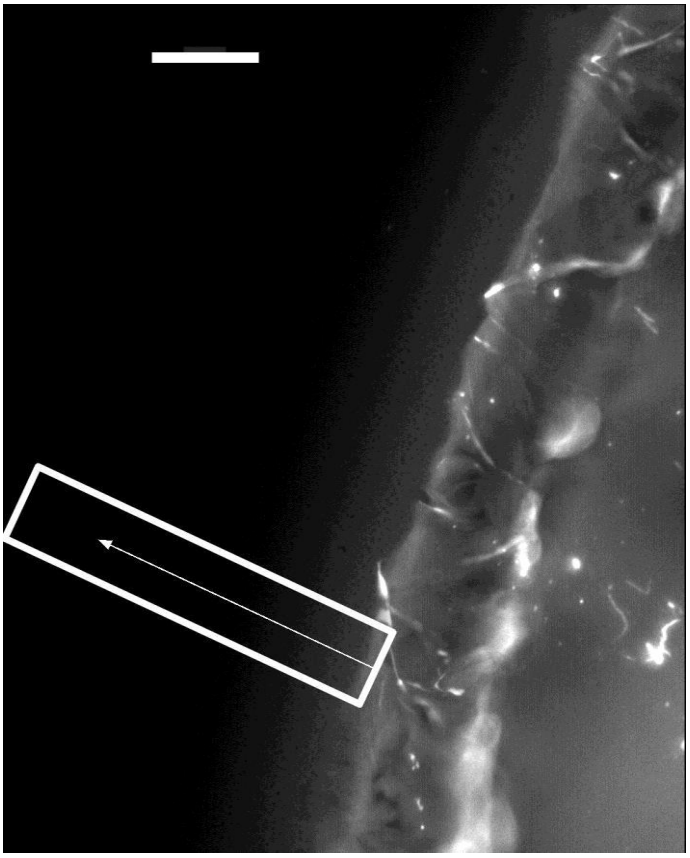

Scale bar: 50 µm

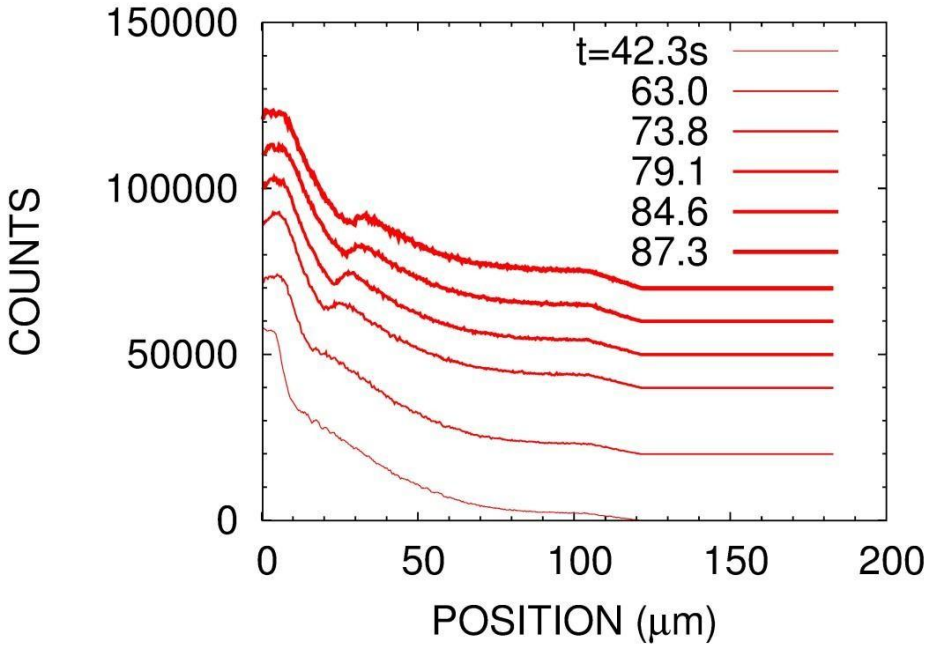

Successive curves offset vertically for clarity.

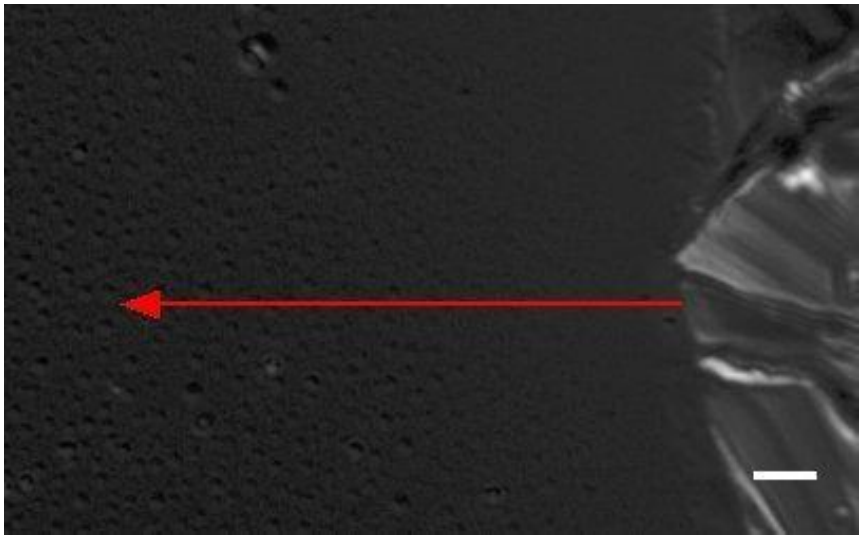

Enlargement of a region of the contact line at the initiation of the halo (fluorescence). The crust has just covered the primary drop on the right, the halo is apparent at the root of the red arrow and is growing towards the left, across a zone of the substrate free of microdroplets (no fine condensation) due to the WBF process, as seen from DIC views, not shown here). DIC image. Scale bar 10 µm.

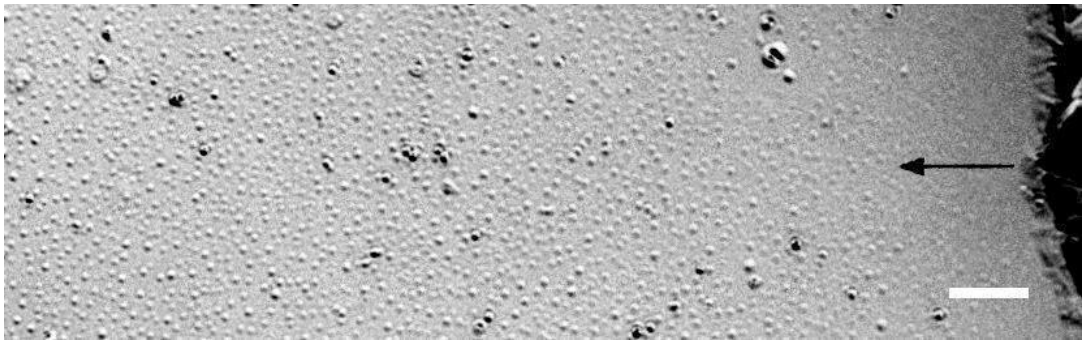

DIC image (inverted contrast for clarity) showing the depletion of condensation in the vicinity of the contact line by the WBF process. Scale bar 20 µm.

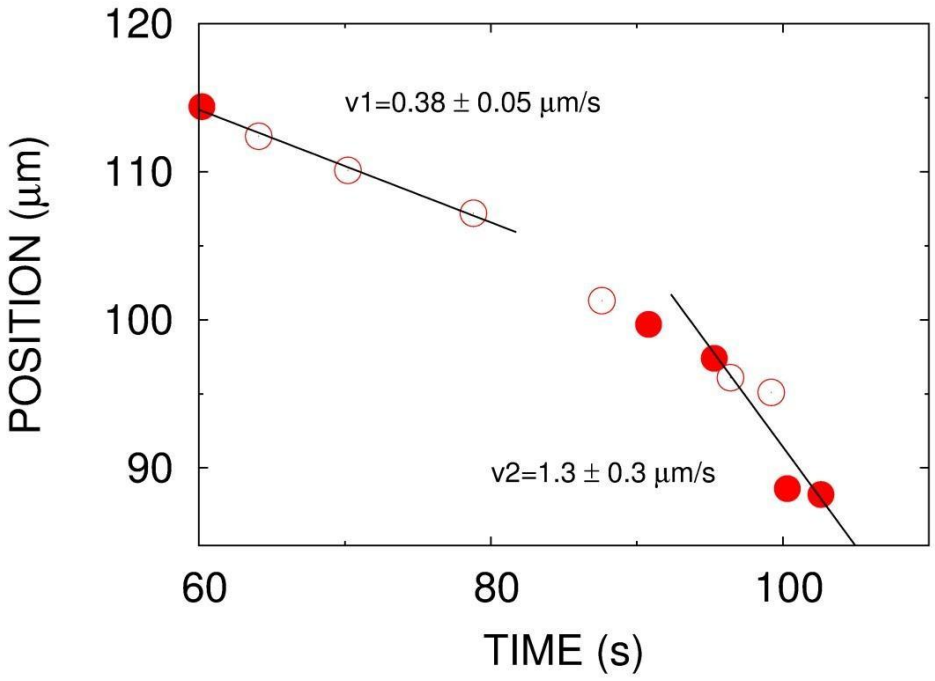

The condensation continues to recede as the halo advances, but is caught up, at which point, the halo grows faster. Data from DIC and fluorescence images are shown as full or open symbols.

The next DIC image shows a hydrate halo in step 4 of the experiment on a strongly hydrophilic substrate in a region where only the water microdroplets condensed from the CP are present (the secondary droplets left by the melting of a previous halo have not been reached by the growing halo yet). The hydrate lateral velocity measured along the red arrow (see graph) is in the range of 1 µm/s. Scale bar: 50 µm

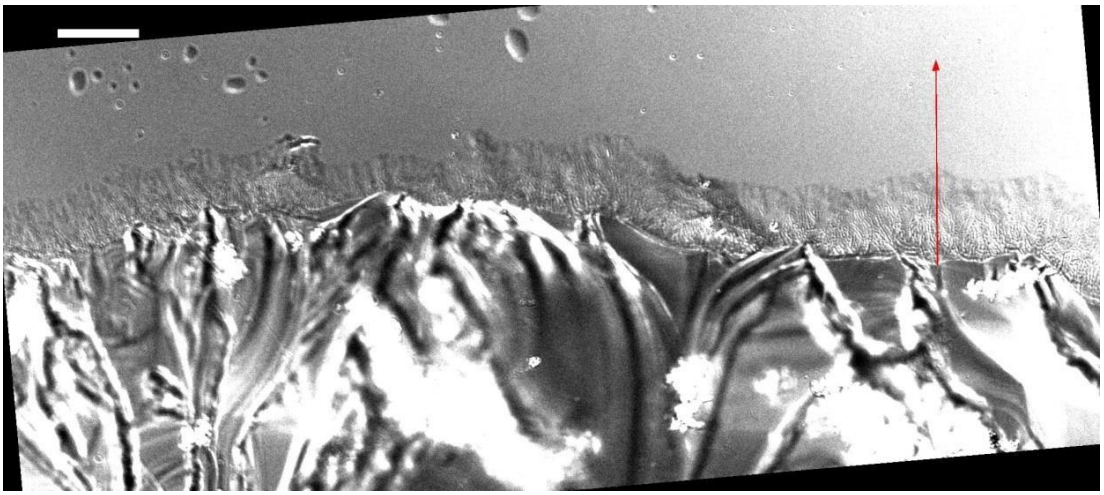

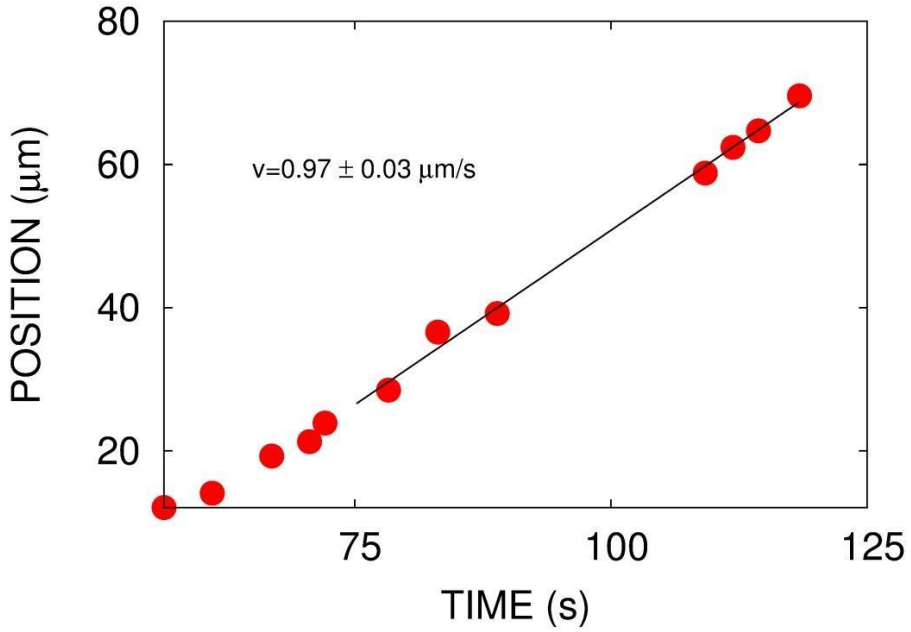
80
60
40
20
POSITION (µm)
v=0.97 ± 0.03 µm/s
75
100
125
TIME (s)

S6.

Transmission and confocal pairs of the secondary water droplet following the 'leap-frog' event described in Figure 6.11 (see main text). Scale bar: 50 µm.

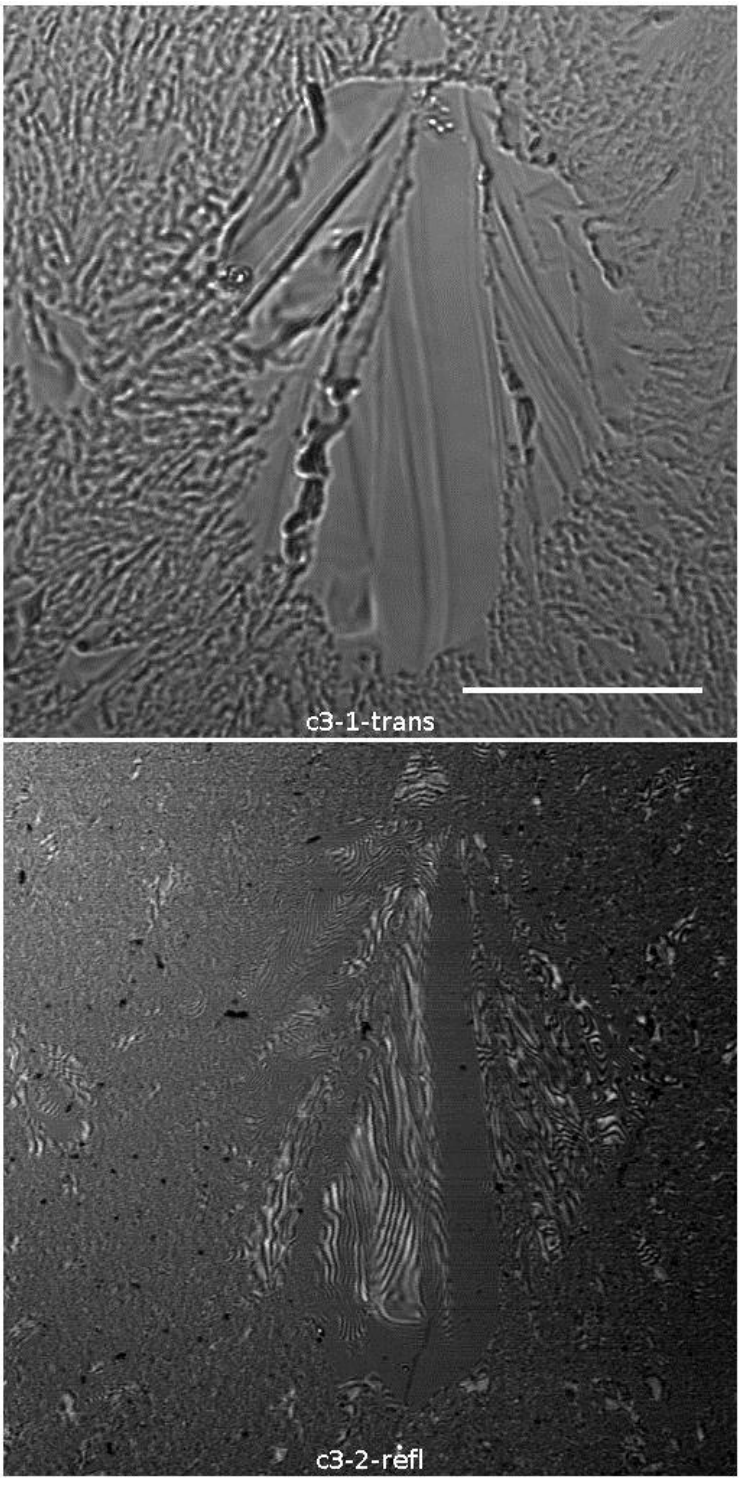

S7. Effect of the water present on a strongly hydrophilic substrate on the lateral velocity of the CP hydrate halo

The growth of the hydrate halo is monitored by transmission and confocal reflectance in the red box (see next page). The DIC image below is the initial state after two cycles of formation and melting (steps 1 to 5 of the experiment), just before freezing to ~ 0°C in order to form the CP hydrate halo. An array of irregular 'secondary', intermediate-sized drops has been left on the substrate upon melting the previous halo. Their diameter is in the 10 - 100 µm range, much larger than the microdroplets condensed from CP (not visible at this magnification – the scale bar is 500 µm). The CP-in-water emulsion resulting from the melting of the hydrate crust is visible as dark spots within both the primary drop and the largest of the secondary droplets.

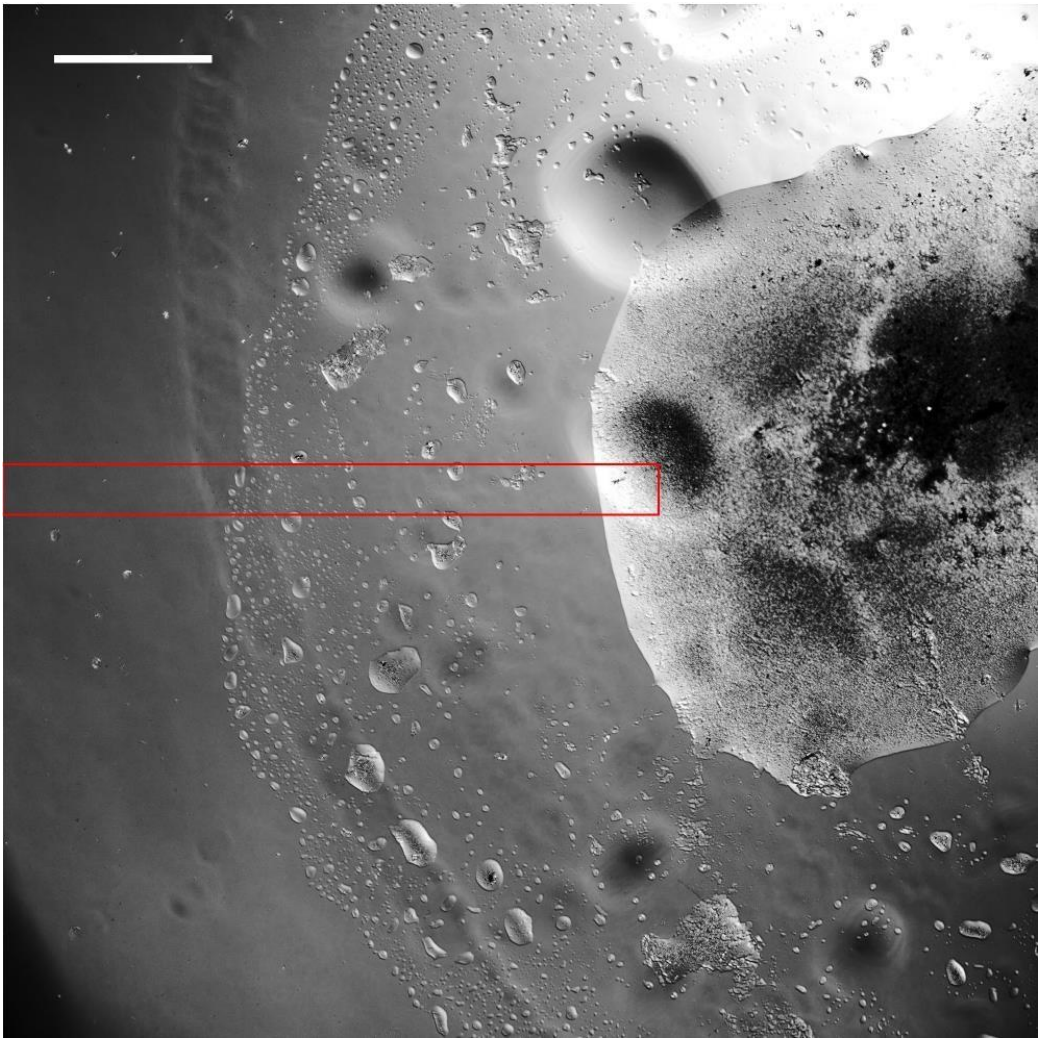

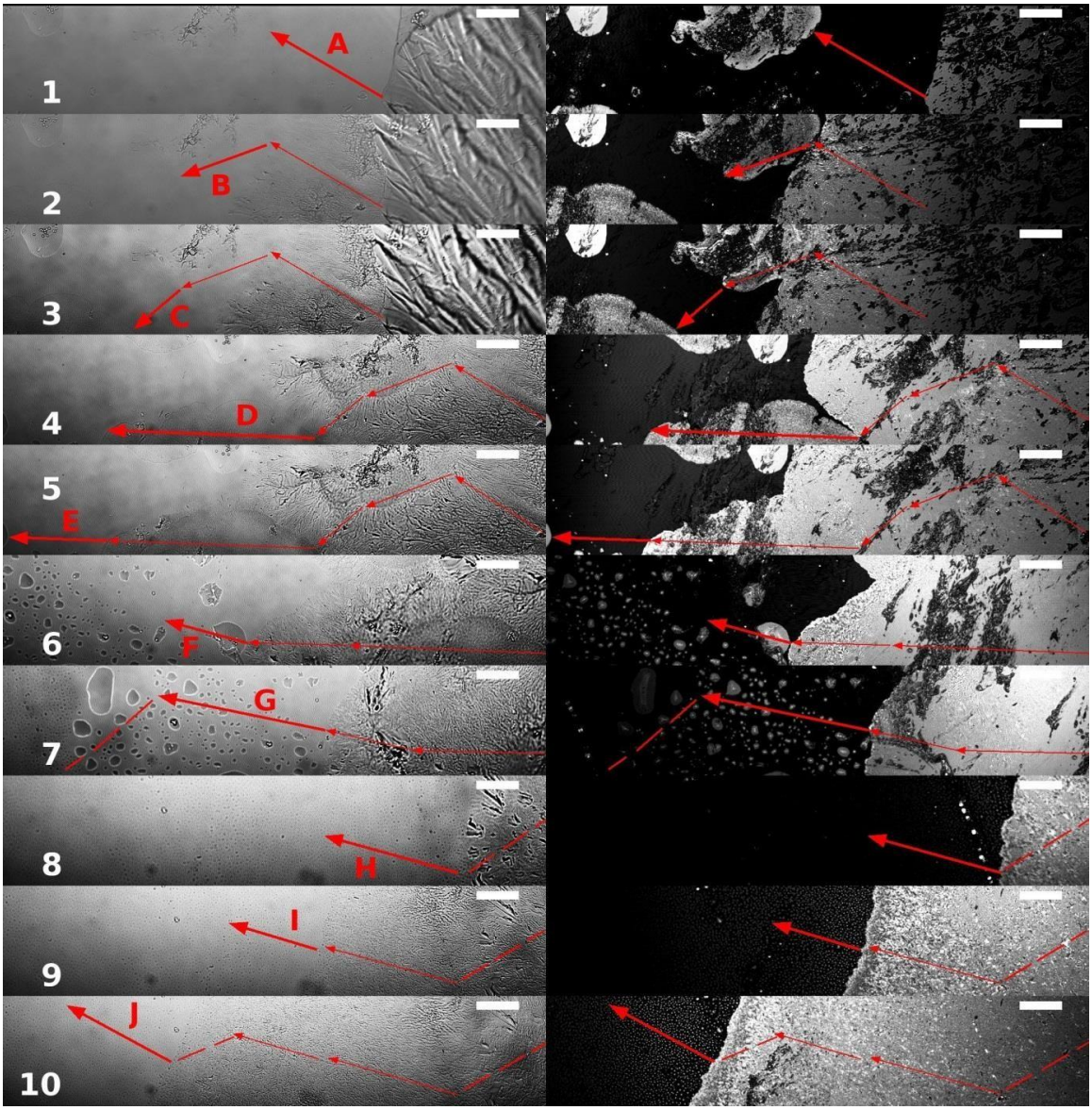

The growth of the halo at T ~ 0°C is observed simultaneously in transmission (left) and in confocal reflection (right) in a 640 µm x 130 µm window (stepped left across the red box in the preceding wide field image), as the halo expands, between rows 3 and 4, 5 and 6, 6 and 7, 7 and 8. The table below shows the speed of halo growth (measured perpendicular to the local halo front) as it swept out each of the line segments labelled as A to J. In each row, the halo has just reached the root of the labelled segment. Scale bars: 50 µm.

Row	T (°C)	Halo lateral velocity (µm/s)	Comments
1	0	1.63 ±0.02	Halo sprouts from contact line
2	0	21.0 ±0.9	Halo grows over pre-formed hydrate
3	0	1.65 ±0.05	Progress over 'bare' glass
4	0	15.2 ±2.0	Halo grows over pre-formed hydrate
5	0	1.78 ±0.07	Progress over 'bare' glass
6	0	2.9 ±0.8	'Leap-frog' over secondary droplet
7	0	1.64 ±0.1	Halo reaches secondary droplets
8	0	1.19±0.02	'Bare' glass beyond
9	0	1.11±0.01	Halo reaches condensed µdroplets
10	0 to 8	0.9±0.02	Starts melting; growth constant however

NB:

1) Error margins correspond to the particular trajectory chosen. Obviously the spread of values for a given 'state' of the glass substrate is greater when comparing different trajectories, e.g., due to specifics of the sample history at each point. However, the orders of magnitude are representative.
2) The initial spread over bare glass (~ 1.6 µm/s) is higher than reported elsewhere here (~ 0.5 µm/s). It is in part determined by a breakout of water from the main drop, noticed from hydrate debris entrained out of the primary drop.

Table of experiments (from 2015/04/8 the CP phase was systematically pre-saturated with water. Unless otherwise specified the temperatures are all 0 - 0.5°C).

Expt #	Substrate : fused quartz, unless otherwise specified	drop sitting or hanging, citing figure	Water +	T of halo growth (0-1°C, unless otherwise specified)	drop radius, µm	θ	First halo velocity, µm/s (second figure: velocity of the 2nd halo)	Comments
2014/10/22		Sitting, Fig. 5.9			nd	nd	nd	Ejection of a crystal from the emulsion to the triple line
2014/10/22		Sitting, Fig. 5.10 and 5.12		3.8°C				Crust crystallization at low subcooling
2014/10/22		Sitting, Fig. 5.11, 5.19		5.6°C				Crust crystallization at low subcooling
2014/10/23		Sitting, Fig. 5.8 right			nd	nd	nd	Competition between nucleation at the triple line or in the emulsion
2014/10/24		2 sitting drops, Fig. S1, 5.16, 5.17			nd	nd	nd	Fig. 5.16, 5.17: high subcooling
2014/10/31		Sitting, Fig. 5.4						CP-in-water emulsion after 1st dissociation
2014/10/31		Sitting, Fig. 5.8						Nucleation at the triple line
2014/10/31		Sitting, Fig. 5.15						Mosaic appearance of the hydrate crust
2014/10/31		Sitting, Fig. 5.20						Parallel growth
2014/11/03		Hanging, Fig. 7.2		8°C	nd	nd	nd	2D CP-in-water

								emulsion
2014/11/03		Hanging, Fig. 7.4						Growth of individual hydrate crystals
2014/11/03		Hanging, Fig. 7.7						Disappearance of CP droplets when hydrate crust covers the water surface
2014/11/03		Hanging, Fig. 7.8		2°C				Dendritic growth by incorporating CP droplets that have decreased in size
2014/11/03		Hanging, Fig. 7.12						Simultaneous conventional and dendritic crystallization in different places
2014/11/03		Hanging, Fig. 7.13						Simultaneous conventional and dendritic crystallization in the same place
2014/11/03		Hanging, Fig. 6.8		8°C				Halo retraction when melting. Water droplets are left behind.
2014/11/06		Hanging, Fig. 7.14		8°C-2°C-0°C				Memory effect of the dendrite
2014/11/06		Hanging, Fig. 6.6bis (color)						Advancing halo covering the water droplets left after

								the 1st dissociation
2014/11/17		Sitting		4-5°C	340	70	1.1/3.1 0.3	
2014/11/17		Sitting, Fig. 5.5, 5.6, 5.13			340	70		Fig. 5.5, 5.6: Nucleation at water/CP interface Fig. 5.13: hydrate fronts
2014/11/25		Sitting, Fig. 5.14	DASPI		230 340	3 50	0.2 0.15	Mosaic hydrate structure (hexagons)
2014/12/02		Sitting, Fig. 2.16	DASPI		550	80	nd	Fluorescent hydrate crystals starting to grow
2015/02/18		Sitting, Fig. 6.4			510	25+-10	2.8	Halo growth (3µm/s)
2015/02/19		Hanging, Fig. 6.2, 5.21		Fig. 6.2: -15°C	220	65	0.1	Fig. 6.2: droplet-free zone near the ice Fig. 5.21: parallel growth
2015/02/19		Hanging, Fig. 7.11						Diffusion of CP droplets towards the dendrite and the hydrate crust
2015/02/20		Sitting, Fig. 6.5			700	15+-10	0.45/1.6	Depleted zone between the advancing halo and the water droplets condensed from the CP
2015/03/06		Sitting, Fig. 6.6						Tiny droplets disappear as the

								halo gets closer. Large water drop disappears in 1s
2015/03/30		Hanging, Fig. 6.9		8°C	xx	nd	0.25	Halo melting and retraction. CP droplets left on the substrate.
2015/03/31		Hanging, Fig. 6.7		6°C	850	15	9.8 <0.03	Halo thickening
2015/03/31		Hanging, Fig. 7.5						Diffusion of CP droplets at the expenses of the growing hydrate crystal
2015/03/31		Hanging, Fig. 7.9, 7.10						Dendritic growth of the hydrate from the emulsion. Bridges between CP droplets
2015/03/31		Hanging, Fig. 7.15, 7.16		Fig. 7.15: 7.7°C-8.5°C-9°C-9°C-9°C-9°C Fig. 7.16: 4°C				Melting of individual crystals to give an emulsion. Coalescence of some of the CP droplets
2015/03/31		Hanging, Fig. 7.17		7.7°C-9°C-9°C-0°C				Growth of a dendritic hydrate where there was an individual crystal before
2015/04/30		Sitting, Fig 6.3	Fluorescent beads/DIC		470	75	< 0.5	Beads escaping the interior of the water

								drop
2015/06/03		Sitting, Fig. 5.7			340	65	0.6	Nucleation at the triple line
2015/06/25	plasma treated		fluorescent beads		1139	30	Hamamatsu	
2015/07/15	hydrophobic				561	145	no halo apparent	
2015/07/17	plasma treated	Sitting	DASPI		912	66	Hamamatsu	

nd : not determined

ÉCOLE DOCTORALE DES SCIENCES EXACTES ET LEUR APPLICATIONS (ED SEA)

LABORATOIRE DES FLUIDES COMPLEXES ET LEURS RÉSERVOIRS (LFC-R)

UNIVERSITÉ DE PAU ET DES PAYS DE L'ADOUR